ELECTROCHEMICAL STUDY OF PROTON EXCHANGE MEMBRANE FUEL CELLS AND DEVELOPMENT OF PT BASED CATALYSTS FOR ELECTRO-OXIDATION OF ETHANOL

GUANGCHUN LI

Electrochemical Study of Proton Exchange Membrane Fuel Cells and Development of Pt Based Catalysts for Electro-Oxidation of Ethanol

By

Guangchun Li

A thesis submitted to the School of Graduate Studies in partial fulfillment of the requirements for the degree of Doctor of Philosophy

Department of Chemistry
Memorial University of Newfoundland
St. John's, Newfoundland, Canada
December 2005

Abstract

This research includes three related parts: Investigation of the effects of Nafion loading in the cathode catalyst layer on the performance of hydrogen fuel cells, designing a DHE (dynamic hydrogen electrode) reference electrode to resolve cell performance into individual electrode behaviors, and developing Pt based binary and ternary catalysts for electro-oxidation of ethanol.

It was found that Nafion content and distribution in the cathode catalyst layer had a strong influence on cell performance. There was an optimum Nafion loading for the best cell performance, which is due to the fact that a balance has to be made between ionic conductivity and O_2 transport resistance.

By simulating experimental impedance data, reasonable conductivity profiles and resistance values for the cathode catalyst layer have been extracted, and they provide insights into the understanding of cathode behavior.

A novel DHE reference electrode has been designed to analyze cell performance losses. The special feature of this DHE reference electrode is that it can be conveniently fitted into a commercial cell without the need of any modifications. Polarization measurements and impedance spectroscopy have demonstrated that it was quite stable during measurements.

With the aid of the DHE reference electrode, we have separated cell performance losses into anode performance losses and cathode performance losses. For hydrogen fuel cells, it was found that at low current densities, the cell performance was mainly determined by cathode performance, while at high current densities, the anode

performance contributed significantly to the cell performance. For methanol fuel cells, it was found that at low current densities, cell performance losses were due to both cathode performance losses and anode performance losses, while at high current densities, the rapid decrease of cell performance was mainly due to cathode performance losses. It was also found that the anode performance was improved at a higher concentration of methanol, whereas the cathode performance decreased significantly at a higher concentration of methanol.

In order to develop direct ethanol fuel cells, a variety of Pt based binary and ternary catalysts have been prepared for electro-oxidation of ethanol. It was found that carbon supported Pt/Sn (4:1) and carbon supported Pt/Ru/Pb (1:1:0.15) catalysts have significantly enhanced catalytic activities for electro-oxidation of ethanol relative to Pt. Preliminary fuel cell tests have shown these two catalysts to be quite promising.

Finally, a simplified equivalent circuit has been built to simulate the impedance behavior of PEMFC electrodes. The excellent fit between the experimental data and simulation data indicates that the circuit is reasonable. Meaningful resistance values have been extracted by simulation, and these values shed light on understanding cell performance losses under different operating conditions.

Acknowledgements

I would like to express my deepest appreciation to Dr. Peter Pickup for his guidance, support, and kindness throughout the duration of my program.

I would also like to thank my supervisory committee, Dr. R. W. Davis and Dr. K. M. Poduska for all their comments, advice, and help.

I am grateful for the help from Dr. Pickup's research group. In particular, I would like to thank Dr. E. Bradley Easton for his kind help during the initial stage of this work.

Financial support from the School of Graduate Studies, the Chemistry Department, and Dr. Pickup's NSERC grants are gratefully acknowledged.

Finally, I would like to thank my wife, my family and friends for all their support and encouragement throughout my studies.

Table of Contents

List of Abbreviations and Symbols

AFC – alkaline fuel cell

C – capacitance

C_{dl} – double layer capacitance

CFP – carbon fiber paper

CV – cyclic voltammetry or cyclic voltammogram

DEFC – direct ethanol fuel cell

DEMS – differential electrochemical mass spectroscopy

DHE – dynamic hydrogen electrode

DMFC – direct methanol fuel cell

E – potential

EIS – electrochemical impedance spectroscopy

EDX – energy dispersive X-ray emission analysis

I – current

i_o – exchange current

j – current density

MEA – membrane electrode assembly

MCFC – molten carbonate fuel cell

OCP – open circuit potential

PAFC – phosphoric acid fuel cell

PEM – proton exchange membrane

PEMFC – proton exchange membrane fuel cell

PTFE – polytetrafluoroethylene

R – resistance

$R_{s,C}$ – cathode side resistance of the membrane

$R_{s,A}$ – anode side resistance of the membrane

RT – room temperature

SEM – scanning electron microscopy

SHE – standard hydrogen electrode

SOFC – solid oxide fuel cell

SSCE – saturated sodium chloride calomel electrode

TEM – transmission electron microscopy

W_o-R_C – ionic resistance in the cathode catalyst layer

W_o-R_A – ionic resistance in the anode catalyst layer

XPS – X-ray photoelectron spectroscopy

XRD – X-ray diffraction

Z – impedance

η - overpotential

ω - angular frequency

List of Tables

List of Figures

Chapter 1 General Review of Fuel Cells

1.1 Introduction to Fuel Cells

A fuel cell is an electrochemical device that directly converts the chemical energy of an externally supplied fuel into electrical energy. In a fuel cell, the anode is fed with a fuel such as hydrogen and the cathode is fed with air or oxygen. When the cell is put into use, the fuel is oxidized on the anode, oxygen is reduced on the cathode, and the electrons flow from the anode to the cathode through the load. The most distinguishing feature of a fuel cell is that the fuel and oxygen are continuously supplied to the cell externally, rather than stored in the cell. This endows the cell with much longer life than a battery, since the life of a battery is limited by the amount of the stored electrochemically active materials.

Because chemical energy is directly converted into electrical energy in fuel cells, fuel cells have the advantages of high energy efficiency and low emissions over internal combustion engines. When a fuel cell is operated with hydrogen as the fuel, the only product is water. Thus, a hydrogen fuel cell can be considered zero emission.

Fuel cells have gone through more than one and a half centuries of development since Sir William Grove's invention in 1839 [1]. Interestingly, Grove discovered the principle of fuel cells accidentally when he disconnected the battery from an electrolyzer and connected the two electrodes together. He observed a current flowing in the opposite direction and consumption of hydrogen and oxygen.

Although many famous electrochemists have devoted great effort to the study of fuel cells, the development of fuel cells was quite slow over the first hundred years due to the limited knowledge of materials science. In the 1950s, however, a great advance was

achieved by Bacon, who successfully realized the first practical alkaline fuel cell by using porous electrodes [2]. In the 1960s, fuel cells found historical applications in the NASA space program, successfully providing electricity for Gemini and Apollo missions. This opened a new era of fuel cell development by demonstrating their power and advantages [3-4]. In the 1970s, Kordesch built a car powered by a hybrid of fuel cells and batteries that operated for three years [4]. In recent years, fuel cells have received tremendous attention and significant progress has been made, especially in proton exchange membrane fuel cells. The impetus of the recent development of fuel cells is due to the oil crisis of the 1970s and the increasing awareness of environmental protection.

Fuel cells have great potential to be used in a variety of areas, ranging from powering portable devices such as cellular phones and laptop computers, to powering vehicles and residential heating and utility systems. Fuel cells have attracted almost all major automakers in the world to develop fuel cell powered vehicles due to their fascinating advantages of high efficiency and low emission. Fuel cell powered cars have been successfully demonstrated and marketed by many car companies. In addition, more than 2500 fuel cell systems have been installed in the world to provide primary power and backup [5].

At the moment, the widespread application of fuel cells is impeded by high costs. However, with the advance of technology, the high cost should be greatly reduced and fuel cells should have a bright commercial future. Theoretically, there are no insurmountable technical problems [6].

1.2 Proton Exchange Membrane Fuel Cells

1.2.1 Introduction

Proton exchange membrane fuel cells (PEMFCs), also called polymer electrolyte membrane fuel cells, have attracted huge attention in recent years. A PEMFC is a type of thin layer cell with a proton exchange membrane as the electrolyte. The key part of a PEMFC is the membrane electrode assembly (MEA). The structure of a MEA is shown in Figure 1.1. It consists of carbon fiber paper (CFP) or carbon cloth backings, catalyst layers and a piece of membrane. Generally, a MEA is prepared by hot-pressing the cathode and the anode onto each side of the membrane. The main advantages of MEAs are the low resistance and high mass transport rate associated with their thin layer dimensions, their low weight, and the ease with which they can be scaled up to form compact fuel cell stacks.

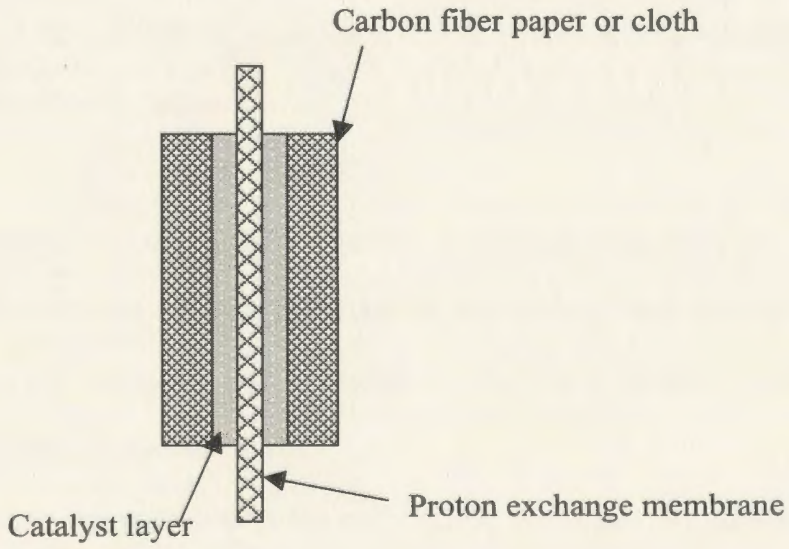

Figure 1.1. A schematic diagram of a MEA.

1.2.2 Electrochemical Processes

The primary electrochemical processes occurring in a PEMFC are hydrogen oxidation on the anode, oxygen reduction on the cathode, hydrogen and oxygen transport in the backing and catalyst layers, water transport in the cell, and hydrogen ion transport in the catalyst layers and the electrolyte.

Hydrogen oxidation on the anode (Equation 1.1) is generally considered as reversible, and therefore, little attention has been paid to this reaction in the fuel cell study.

$$H_2 = 2H^+ + 2e^- \quad (1.1)$$

However, recently, Andreaus and coworkers [7] have found that there is a significant overpotential for hydrogen oxidation on the anode at high current densities. This was explained by the authors as being due to dehydration of the catalyst layer caused by the electro-osmotic drag of water from the anode to the cathode.

Oxygen reduction on the cathode is quite complex. It involves both electron and proton transport as expressed in Equation 1.2.

$$O_2 + 4H^+ + 4e^- = 2H_2O \quad (1.2)$$

Compared with hydrogen oxidation, the kinetics of oxygen reduction are much slower. The exchange current for oxygen reduction is ca. 10^{-5} of that for hydrogen oxidation on Pt catalysts [8]. Also, oxygen reduction on Pt is a 4 electron multi-step process and it involves several pathways [9-10].

The slow kinetics of oxygen reduction is the main factor that limits the performance of a PEMFC [11]. Therefore, a great deal of effort has been devoted to study the reaction mechanism of oxygen reduction. Several models have been proposed to depict the reaction mechanism [12-16]. Figure 1.2 shows one of the proposed mechanisms [16]. It is

generally agreed that the first step of oxygen reduction on a Pt catalyst is the adsorption of oxygen on the catalyst surface. Therefore, the structure and size of the catalyst can strongly influence the kinetics of oxygen reduction [17-18].

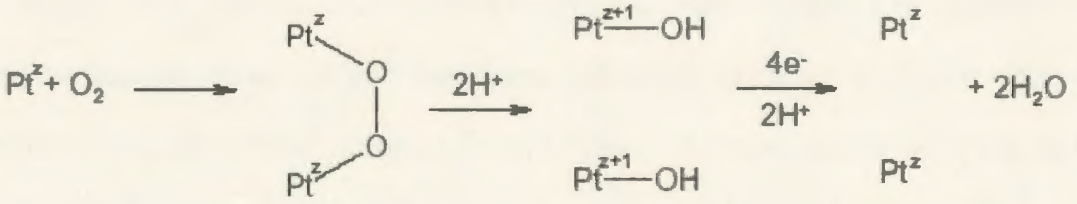

Figure 1.2. The bridge model of oxygen reduction on a Pt catalyst, where z represents the oxidation state of surface Pt sites.

Water and proton transport also play an important role in the performance of a PEMFC [18,19]. In an operating cell, protons migrate from the anode to the cathode, which drags water from the anode to the cathode. This can result in dehydration of the anode catalyst layer and the membrane. As a consequence, hydrogen gas must be humidified before entering the cell to compensate for the dehydration of the anode catalyst layer and the membrane. However, too much water in the cathode can cause cathode flooding which increases the resistance to oxygen transport to the cathode catalyst. In addition, water can diffuse back from the cathode to the anode. All these processes make management of water content and distribution in a cell a key issue for obtaining high performance [20]. Several models have been proposed to model water transport in a cell [21-23].

1.2.3 Proton Exchange Membranes

The proton exchange membrane (PEM) is a crucial part of a PEMFC. It serves both as the electrolyte and a separator between the fuel and oxidant. Although many kinds of membranes have been developed, Nafion membranes invented by DuPont in the 1970s are still the most widely used membrane [24].

Figure 1.3 shows the general structure of Nafion. It consists of a polytetrafluoroethylene (PTFE) backbone and short perfluorinated side chains with terminating sulfonic acid groups ($-SO_3H$). The Teflon-like backbone endows Nafion membranes with excellent chemical, thermal, and mechanical stability, while the sulfonic acid groups ($-SO_3H$) provides them with relatively high proton conductivity when well hydrated [25].

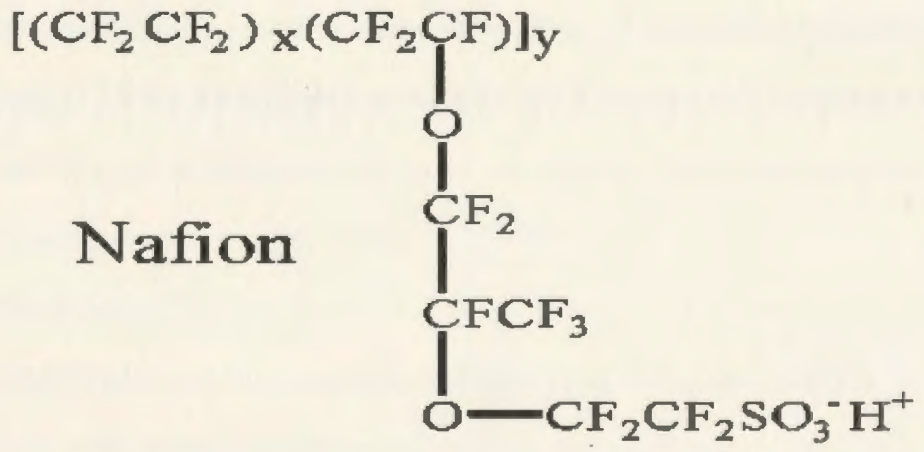

Figure 1.3. The general structure of Nafion.

The detailed configuration and geometry of Nafion are still not very clear [26], although there have been many studies [27-30]. It is generally believed that there are two

phases at a nanometer scale in a Nafion membrane: one is a hydrophobic phase consisting of the PTFE backbone, and the other is hydrophilic clusters consisting of the sulfonate groups and water which are involved in the proton transport [31].

The proton conductivity of a Nafion membrane strongly depends on its water content. In the dry state, Nafion is a poor proton conductor. This dependence greatly limits the operational temperature of a Nafion membrane. When the temperature exceeds 100 °C, water evaporates very fast, resulting in dehydration of the Nafion membrane. Consequently, the proton conductivity of the membrane decreases significantly. Therefore, Nafion membranes are regarded as not suitable for use at temperatures above 100 °C. Another drawback of Nafion membranes is that they are very expensive.

Considerable effort has been made to develop new membranes that can be used at elevated temperatures. The approaches include designing Nafion-based composite membranes [32-33] and making other new kinds of membrane [34-36]. Savinell and coworkers [37] have developed a phosphoric acid doped polybenzimidazole membrane which can be used at temperatures up to ca. 150 °C. This membrane also has a zero electro-osmotic drag number for water.

1.2.4 Electrodes

A PEMFC electrode is essentially a kind of gas diffusion electrode. It consists of a porous carbon fiber paper (or carbon cloth) backing and a catalyst layer. It is also reported that inserting a diffusion layer between the backing and the catalyst layer can increase the catalyst utilization by preventing the catalyst entering too deeply into the pores of the backing [38].

A PEMFC electrode can be prepared by directly applying a catalyst ink onto the backing or by applying the catalyst ink onto the membrane and then pressing the backing onto the membrane during cell assembly [39-40]. Catalyst inks are generally prepared by dispersing a carbon black supported catalyst and Nafion solution in iso-propanol by sonication. Several techniques such as screen printing, spraying, brush painting, and rolling have been developed to prepare a PEMFC electrode [41].

The structure of the catalyst layer is crucial to the performance of an electrode and is quite complex [4]. The catalyst layer is a heterogeneous four-phase mixture, including the carbon support, the catalyst, the recast Nafion, and gas filled pores. The catalyst layer must have hydrophobic channels to allow gas access to the catalyst and inhibit water condensation. It must also have good electronic and ionic conductivities. Electronic conductivity is provided by the carbon support, while ionic conductivity is due to the recast Nafion. Optimization of the structure of PEMFC electrodes and the composition of their catalyst layers for the best electrode performance has been the subject of intensive study [3,42-44].

1.2.4.1 Anodes

PEMFC anodes employ platinum (or Pt based alloys) as the catalyst. Platinum has been shown to be the best catalyst for hydrogen oxidation [45-46]. The kinetics of hydrogen oxidation on Pt are very fast and the mechanism of hydrogen oxidation on Pt involves the two steps expressed in Equations 1.3 and 1.4 [4]. The first step includes chemisorption of hydrogen on the Pt catalyst, followed by the dissociation of the H_2 molecules.

$$2\,Pt + H_2 \rightarrow Pt\text{-}H_{ads} + Pt\text{-}H_{ads} \quad (1.3)$$

$$Pt\text{-}H_{ads} \rightarrow H^+ + e^- + Pt \qquad (1.4)$$

Unfortunately, there is no natural pure hydrogen resource on the earth. Thus, hydrogen must be produced by electrolysis, or by reforming other resources such as natural gas, methanol and gasoline [47]. The reformed hydrogen normally contains small amounts of CO, which can poison the Pt catalyst readily by blocking its active sites for hydrogen adsorption. It is reported that less than 25 ppm CO in hydrogen can result in a large decrease in cell performance [48]. Several approaches have been taken to address this issue: one is to use an "air bleed" that involves mixing reformed hydrogen with small amounts of oxidants such as air or hydrogen peroxide to oxidize the adsorbed CO so that the Pt active sites are available for hydrogen adsorption [49-50]. The problem with this method is that it wastes fuel. The more intensively studied method is to develop CO tolerant catalysts. A number of Pt based Pt/M (M represents the second metal) alloy catalysts have been shown to be more CO tolerant than Pt alone. These catalysts include Pt/Ru [51-55], Pt/Sn [56-62], Pt/Mo [63-65] and other Pt based binary catalysts. In addition, Pt based ternary catalysts have also been investigated. $Pt/Ru/WO_x$ was reported more active than Pt/Ru for oxidation of reformed hydrogen [66].

Several mechanisms have been proposed to explain the promotion effect of the second metal. The most accepted mechanism is the bifunctional mechanism [64]. It is believed that the additional metal can activate water to form adsorbed OH at lower potentials compared with Pt [59, 67], and that OH_{ad} can oxidize CO_{ad} to CO_2, and therefore, release Pt active sites for hydrogen oxidation. It is also reported that the additional metal can have electronic promotion effects for hydrogen oxidation on Pt [68].

1.2.4.2 Cathodes

The performance of a PEM fuel cell cathode is mainly limited by the slow kinetics of oxygen reduction on the Pt catalyst. In addition, proton and oxygen transport in the electrode also play important roles in the cathode performance. A great deal of effort has been devoted to improve the performance of cathodes. Some researchers have focused on developing new and more active catalysts, while others have endeavored to optimize the compositions and structures of cathodes.

Platinum is the most commonly used catalyst for oxygen reduction. However, oxygen reduction on the platinum catalyst is far from satisfactory. Also, platinum is a precious metal and earth's resource is quite limited [69]. Two strategies have been taken to address these issues: one is to develop non-precious metal catalysts for oxygen reduction; another is to modify platinum with other metals to increase its activity for oxygen reduction. It is reported that iron (II) produced by high temperature pyrolysis of its organic compounds shows good catalytic activity for oxygen reduction [69, 70]. A number of researchers have found that platinum based alloys such as Pt/Cr, Pt/Ni, and Pt/Co show enhanced catalytic activities for oxygen reduction compared with Pt alone [71-73].

Oxygen reduction on the cathode takes place at the three-phase interface of the catalyst, gas, and the recast Nafion [74]. High performance cathodes not only require highly active catalysts but also require good electronic and ionic conductivities. Because catalytic activities, electronic conductivities, and ionic conductivities are provided by different materials, the structure and composition of the cathode is crucial to its performance [75]. Increasing the ionic conductivity of the cathode catalyst layer has been shown to be an effective way to improve cathode performance. Pickup and coworkers

[76-77] have found that cathode performance can be improved by increasing the hydrophilic properties of the carbon support. Also, cathode performance is improved significantly by introducing recast Nafion into the catalyst layer to increase its ionic conductivity [78-80]. In addition, optimization of the composition and structure of the cathode can also result in Pt loading being decreased without lowering cell performance [80].

Because the transport of oxygen, water, and protons influence each other within the catalyst layer, the picture of how they work together and their integrated effects on cell performance is still not very clear. A number of models have been developed to describe the operation of PEMFC catalyst layers over the past decade [21, 81-88]. The most accepted model is the thin-film flooded agglomerate model [89]. According to this model, catalyzed carbon particles flooded with the electrolyte form agglomerates covered with a thin film of electrolyte. The catalyst layer consists of macro-micro porous interconnected hydrophobic regions to allow the reactant gas access to the surface of agglomerate regions, then the reactant gas diffuses through the electrolyte film to the catalyst, where the redox reaction takes place. The thin-film flooded agglomerate model is very successful in explaining oxygen diffusion in PEMFC electrodes.

Treatments by Perry and coworkers [88] and Jaouen and coworkers [90] have provided useful diagnostic criteria. They concluded that cathodes controlled by either Tafel kinetics and oxygen diffusion in the agglomerate regions or Tafel kinetics and proton transport in the catalyst layer result in a double Tafel slope. If controlled by Tafel kinetics, oxygen diffusion, and proton transport together, a quadruple Tafel slope will appear. The total current density due to Tafel kinetics and oxygen diffusion is

proportional to the catalyst layer thickness and relatively insensitive to the humidity of the oxygen. However, in the Tafel kinetics and proton transport region it is independent of thickness and much more sensitive to humidity.

Recently, Passalacqua and coworkers [91] developed a quite intuitive percolation model. According to this model, if the Nafion content is too low, there will not be good ionic conductivity in the catalyst layer, therefore the performance of the cathode will be poor. On the other hand, too much Nafion will cut off the percolation path for electron transfer between catalyst particles resulting in worse electronic conduction, and also hinder gas access to the reactive sites. So there is an optimum Nafion content for best cathode performance. Although the percolation model is simple and intuitive, the drawback of this model is that it can not yet provide kinetic information.

The classical models all consider the composition of the catalyst layer to be uniform and then take the whole layer into account. However, Bultel and coworkers [87] have developed a model at the discrete nano-particle level. They confirmed that the discrete distribution of the catalyst as isolated nano-particles could have an important influence on mass and charge transport in the catalyst layer.

1.3 Direct Alcohol Fuel Cells

1.3.1 Introduction

The principle of direct alcohol fuel cells (DAFCs) is much like that of PEMFCs, both using a proton conducting membrane as the electrolyte. In a DAFC, a low molar mass alcohol, rather than hydrogen, is used as the fuel. Several alcohols such as methanol [92], ethanol [93-94], ethylene glycol [95-96], and propanol [97-98] have been studied as fuels for DAFCs. Among them, methanol is the most studied fuel.

Compared with hydrogen fuel cells, DAFCs have many advantages such as ease of storage and transport of fuel, high energy densities, simple systems, and low cost. In addition, the existing gasoline transport system can be easily adapted to deliver alcohols [99]. Moreover, low molar mass alcohols can be easily produced from a variety of resources such as natural gas and biomass. DAFCs are therefore drawing increasing attention [100].

Although DAFCs are very promising as power sources for portable devices and vehicles, currently, there are two major hurdles that impede their commercialization: one is the slow kinetics of electro-oxidation of alcohols on state-of-the-art catalysts; another is the crossover of alcohols from the anode to the cathode. Their slow anode kinetics limit the power and efficiency of DAFCs, while alcohol crossover not only wastes fuel but also causes depolarization of the cathode, resulting in poor performance of the cell [101]. To address these two issues, considerable effort has been devoted to developing highly active catalysts for electro-oxidation of alcohols and to developing membranes that have less permeability to alcohols.

1.3.2 Direct Methanol Fuel Cells (DMFCs)

1.3.2.1 DMFC Anodes

In a DMFC, aqueous methanol is pumped into the anode compartment and oxidized on the anode. The thermodynamic equilibrium potential for methanol oxidation on the anode (Equation 1.5) is ca. 0.02 V *vs* SHE, very close to that of hydrogen oxidation [102]. However, the kinetics of electro-oxidation of methanol are very sluggish compared with those of hydrogen oxidation.

$$CH_3OH + H_2O \rightarrow CO_2 + 6\,H^+ + 6e^- \quad (1.5)$$

Pt has been shown to be the most active and stable catalyst for adsorption of methanol and breaking of the C-H bonds in acid media at low temperatures [100,103]. However, it is found that Pt is quickly poisoned by the reaction intermediates, particularly CO, when potentials are below 0.6 V *vs* SHE, and therefore, becomes inactive for methanol oxidation in the potential region of fuel cell interest. In order to increase the activity of the Pt catalyst, other metals are added. A number of Pt based binary and ternary alloy catalysts such as Pt/Ru, Pt/Sn, Pt/Mo, and Pt/Ru/W have shown enhanced activities for methanol oxidation compared with Pt alone. To date, the Pt/Ru binary catalyst has been shown to be the best catalyst for methanol oxidation [104].

The promoting effect of Ru on methanol oxidation on Pt catalysts has been explained by the bifuntional mechanism plus ligand effects [105-106]. The bifunctional mechanism proposed by Watanabe and Motoo [67] (Equations 1.6 to 1.8) proposes that Ru can activate water at lower potentials (ca. 0.2 V *vs* SHE) than Pt does, and that the activated water can oxidize adsorbed CO and therefore liberate Pt active sites for methanol oxidation; while the ligand effect proposes that the addition of Ru can change the electronic structure of Pt, resulting in weakening of the Pt-CO bond.

$$CH_3OH + Pt \rightarrow Pt\text{-}CO + 4\,H^+ + 4e^- \quad (1.6)$$

$$H_2O + Ru \rightarrow Ru\text{-}OH + H^+ + e^- \quad (1.7)$$

$$Pt\text{-}CO + Ru\text{-}OH \rightarrow CO_2 + Pt + Ru + H^+ + e^- \quad (1.8)$$

There is controversy in the literature concerning the optimum ratio of Pt to Ru for the best performance. Some believe that 30% Ru is optimum, while others claim that 50% Ru is best [100, 107]. Also, there is inconsistency in the literature regarding which oxidation state of Ru is better for the oxidation of methanol on Pt catalysts. Rolison and coworkers

[108] reported that hydrous ruthenium oxide, rather than ruthenium, plays an important role in the oxidation of methanol on Pt/Ru catalysts, while other researchers believe that alloys of Pt and Ru are best for methanol oxidation [109].

1.3.2.2 DMFC Membranes

Currently, most DMFCs employ Nafion membranes as the electrolyte. However, Nafion membranes are permeable to methanol, resulting in high methanol crossover, which is a serious problem for DMFCs. Another limitation of Nafion membranes is that they cannot be used at temperatures over 100 °C which are needed for efficient methanol oxidation. Obviously, new kinds of membranes with low methanol permeability are greatly needed.

Many alternative membranes have been developed in recent years. For example, sulfonated poly(ether ketone) and poly(ether sulfone) based membranes [110-111] have been shown to be less permeable to methanol than Nafion membranes. Recently, polyaryl type membranes have been reported to have excellent chemical and thermal stability, good proton conductivity, and promising performances in DMFCs [112]. Another approach is to modify Nafion membranes so that they have lower methanol permeability or can be used at elevated temperature. Pickup and coworkers [113-114] have developed polypyrole modified Nafion composite membranes. These membranes show much less methanol crossover compared with unmodified Nafion membranes. Incorporation of silica into Nafion membranes has also been shown to be an effective way to reduce methanol crossover and to increase water retention in the membrane at temperatures as high as 150 °C [115-117].

1.3.2.3 DMFC Cathodes

The performance of cathodes in DMFCs is much lower than in PEMFCs due to methanol crossover [118]. To address this issue, a number of methanol tolerant catalysts have been developed. For example, a $Mo_2Ru_5S_5$ catalyst shows superior activity to Pt for oxygen reduction in the presence of methanol [4]. Also, the performance of cathodes can be significantly improved by operating the cell at optimum conditions. Thomas and coworkers [119] claimed that the performance of Pt cathodes in DEFCs was not much lower than in PEMFCs when the cell was operated at optimum conditions. In addition, water management also takes a critical role in the performance of cathodes. Every effort has been made to prevent cathode flooding.

1.3.3 Direct Ethanol Fuel Cells (DEFCs)

Ethanol is another attractive fuel and it has many advantages over methanol [100, 120]. First, ethanol is much less toxic than methanol. Second, ethanol can be considered as a renewable fuel since it can be easily produced in large quantity from fermentation of biomass. Third, ethanol can be called a green fuel because the CO_2 produced by DEFCs is consumed by biomass growth. In addition, the thermodynamic data for electro-oxidation of ethanol are quite promising. For example, the thermodynamic equilibrium potential for ethanol oxidation is 0.084 *vs* SHE, close to that of hydrogen. Also, the theoretical energy density for ethanol oxidation is ca. 8.0 kWh/kg, comparable to that of gasoline [100].

However, the kinetics of electro-oxidation of ethanol are quite slow and more complex than those of methanol, involving many steps. Many products such as carbon dioxide, acetaldehyde, and acetic acid have been detected during electro-oxidation of

ethanol [121]. The complete oxidation of ethanol to carbon dioxide is preferred for high energy efficiency and involves the transfer of 12 electrons as expressed in Equation 1.9.

$$C_2H_5OH + 3H_2O \rightarrow 2CO_2 + 12H^+ + 12e^- \quad (1.9)$$

The key to electro-oxidation of ethanol is to find active catalysts to break the C-C bond. To date, Pt has been found to be the best catalyst for electro-oxidation of ethanol in acid media [122]. However, Pt catalysts are readily poisoned by reaction intermediates such as CO and become inactive in the potential region of fuel cell interest. Thus, a number of Pt based catalysts have been investigated for electro-oxidation of ethanol. Pt/Ru [121, 123-126] and Pt/Sn [122,126,127-128] have exhibited significantly enhanced catalytic activity for ethanol oxidation compared with Pt alone.

Although electro-oxidation of ethanol has drawn considerable attention, only a few attempts have been made to realize DEFCs. Wang and coworkers [93] claimed that there was no significant difference between the performance of DEFCs and DMFCs at a high operating temperature of 170 °C when Pt/Ru was used as the anode catalyst, while Arico and coworkers [94] reported that the performance of DEFCs was not as good as that of DMFCs at a operating temperature of 145 °C with Pt/Ru as the anode catalyst. It is also reported that Pt/Sn was more active than Pt/Ru when they were used as the anode catalyst in DEFCs [126,129]. Obviously, with such a promising fuel, more research effort should be made to realize DEFCs.

1.4 Other Types of Fuel Cell

Besides PEMFCs and DAFCs, four other types of fuel cell have been developed and they are generally classified according to the electrolyte used. They are alkaline fuel cells (AFCs), phosphoric acid fuel cells (PAFCs), molten carbonate fuel cells (MCFCs), and

solid oxide fuel cells (SOFCs) [4, 130-131]. The main characteristics of these cells are summarized in Table 1.1.

Table 1.1. Characteristics of four types of fuel cell

Type	AFC	PAFC	MCFC	SOFC
Electrolyte	Aqueous solution of KOH soaked into a matrix	Liquid H_3PO_4 Soaked into a matrix	Liquid solution of Li_2CO_3, Na_2CO_3 soaked into a matrix	Solid yttria stabilized zirconia
Operating temperature	90-100 °C	175-200 °C	600-1000 °C	600-1000 °C
Anodes and reactions	Pt/C or Pt/Ni $H_2 + 2OH^- \rightarrow 2H_2O + 2e^-$	Pt/C $H_2 \rightarrow 2H^+ + 2e^-$	Ni/Al or Ni/Cr $H_2 + CO_3^{2-} \rightarrow H_2O + CO_2 + 2e^-$	Ni/YSZ $H_2 + O^{2-} \rightarrow H_2O + 2e^-$
Cathodes and reactions	Pt/C or Pt/Ag $O_2 + 2H_2O + 4e^- \rightarrow 4\ OH^-$	Pt/C $O_2 + 4H^+ + 4e^- \rightarrow 2H_2O$	NiO $O_2 + 2CO_2 + 4e^- \rightarrow 2CO_3^{2-}$	Sr/$LaMnO_3$ $O_2 + 4e^- \rightarrow 2O^{2-}$
Fuels	H_2	H_2 and reformate gas	H_2 and natural gas	H_2 and natural gas
Advantages	High performance	The most commercially advanced systems	Cheap catalysts and various fuels	Cheap catalysts and various fuels
Disadvantages	Need for removal of CO_2	Need Pt catalysts, large size	Corrosion of cell components	Corrosion of cell components
Applications	Space, military	Electric utility, transportation	Electric utility	Electric utility

1.5 Electrochemistry of Fuel Cells

1.5.1 Principles

A fuel cell is a type of galvanic cell. The electrochemistry of the cell involves both charge transfer and mass transport. The voltage that a cell can provide is given by Equation 1.10 as follows:

$$\Delta G = -nFE_{cell} \qquad (1.10)$$

where n is the number of moles of electrons involved in the reaction per mole of the fuel, F is the Faraday constant, and E_{cell} is the cell voltage.

The cell voltage is determined by the potential of the cathode $E_{cathode}$, potential of the anode E_{anode}, and cell resistance R as expressed in Equation 1.11:

$$E_{cell} = E_{cathode} - E_{anode} - iR \qquad (1.11)$$

The potential of an individual electrode is determined by the equilibrium potential of the electrode E_{eq}, the kinetic overpotential $\eta_{kinetic}$ (representing kinetic polarization), and the concentration overpotential η_{conc} (representing concentration polarization) as given in Equation 1.12:

$$E_{individual} = E_{eq} - \eta_{kinetic} - \eta_{conc} \qquad (1.12)$$

where $E_{individual}$ represents $E_{cathode}$ or E_{anode}, E_{eq} is the equilibrium potential of the cathode or the anode, which is governed by the Nernst equation. For example, the equilibrium potential of O_2 reduction on the cathode (Equation 1.2) is expressed as follows:

$$E = E^o + (RT/4F) \ln(P_{oxygen} [a_{H^+}]^4) \qquad (1.13)$$

Where E^o is the standard potential of O_2 reduction, P_{oxygen} is the partial pressure of O_2, and a_{H^+} is the activity of hydrogen ions.

The kinetic polarization of an electrode is due to the resistance of charge transfer at the electrode and can be represented by the Tafel equation as follows.

$$\eta_{kinetic} = a + b \log(j) \qquad (1.14)$$

where a is a constant, b is the Tafel slope, and j is the current density. A typical Tafel slope is 118 mV/n at room temperature. From the Tafel equation we can see that a b mV increase of overpotential can result in ten fold increase of current density. This means that the rate of charge transfer can be greatly increased by increasing the overpotential. However, this will result in significant decrease in the cell voltage.

Concentration polarization is due to the mass transport resistance of the fuel or oxygen in the cell and it is significant at large current densities.

An Ohmic polarization (iR) also plays an important role in the performance of a cell. The higher the resistance R, the lower is the cell performance. The Ohmic resistance polarization is due to the electrolyte resistance, electronic resistances, and cell contact resistances, but is mainly determined by the electrolyte resistance. Obviously, an electrolyte with a smaller resistance is preferred.

1.5.2 Polarization Measurements

Polarization measurements (V *vs* j curves) are the most common way to evaluate a cell's performance. The kinetic polarization, Ohmic resistance polarization, and concentration polarization are reflected in different regions of a polarization curve as shown in Figure 1.4. Generally, the kinetic information is reflected in the low overpotential region and can be analyzed with the Tafel equation. The Ohmic resistance polarization is reflected in the medium current density region and it is governed by Ohm's law. The concentration polarization is reflected in the high current density region and the typical feature of concentration polarization is that the cell voltage drops sharply in the high current density region, eventually reaching a limiting current.

The Tafel kinetic parameters in the lower overpotential region and Ohmic resistance in the linear region of the polarization curve can be evaluated by fitting the polarization curve to Equation 1.15 until the end of the linear region in the polarization curve [132].

$$E = E_o - b \log i - Ri \qquad (1.15)$$

where b is the Tafel slope, R is the approximately Ohmic resistance responsible for the linear variation of the polarization curve, and E_o is a constant and is given by Equation 1.16:

$$E_o = E_{max} + b \log i_o \qquad (1.16)$$

where E_{max} is the theoretical open circuit cell voltage, and i_o is the exchange current at the equilibrium potential.

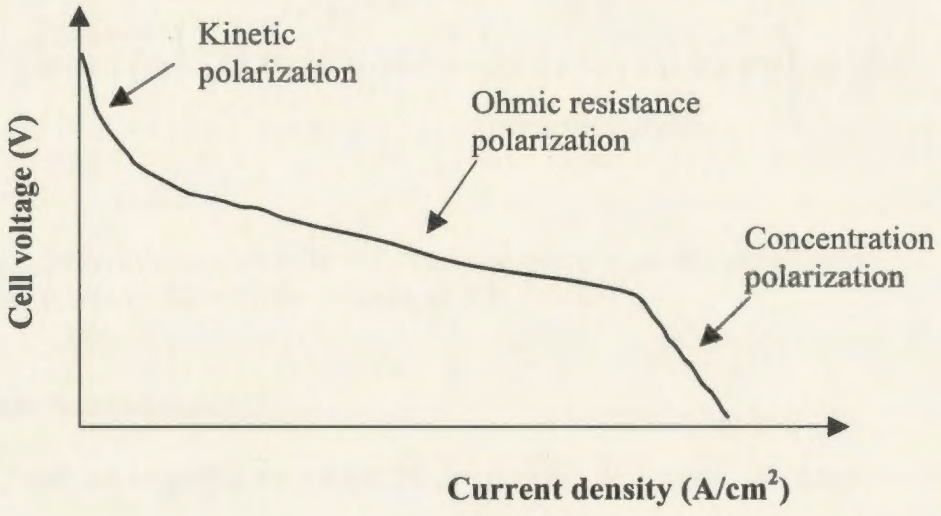

Figure 1.4. A typical polarization curve for a cell.

With the aid of a reference electrode (RE), the cell polarization curve can be resolved into the individual electrode polarization curves as shown in Figure 1.5. Separate polarization information for the anode and the cathode is crucial to improving the cell performance and optimizing the cell's operating conditions.

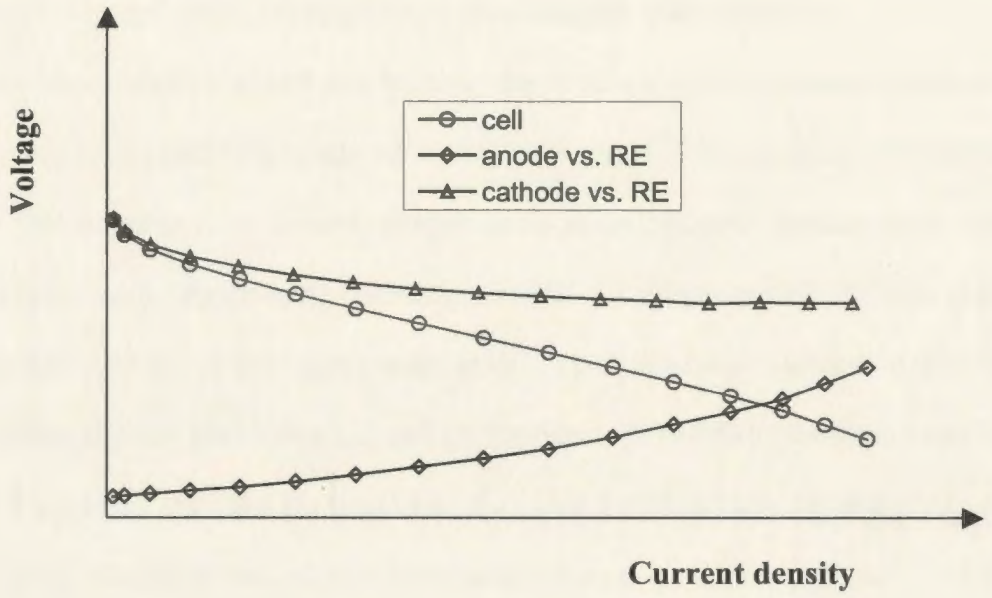

Figure 1.5. A polarization curve for a fuel cell, together with the polarization curves of the anode *vs* RE and the cathode *vs* RE.

1.5.3 Impedance Spectroscopy

Impedance Z can be regarded as a kind of generalized resistance. It consists of the resistance R and the capacitive reactance X_c as expressed in Equation 1.17:

$$Z = R - jX_c \qquad (1.17)$$

The capacitive reactance of a capacitor is analogous to the resistance of a resistor. However, it is frequency dependent as expressed in Equation 1.18:

$$X_c = 1/(2\pi fC) \qquad (1.18)$$

where f is the frequency in Hz and C is the capacitance. At extremely high frequencies, X_c approaches zero and a capacitor essentially becomes a conductor. In contrast, at very low frequencies, a capacitor is actually an insulator. The dependence of capacitive reactance on frequency indicates that impedance also changes with frequency.

An electrochemical cell can be considered as a kind of impedance, when a small ac excitation is applied. The study of variation of the impedance of an electrochemical cell with the frequency is termed electrochemical impedance spectroscopy (EIS) [133]. Compared with steady-state techniques, EIS is dynamic and it can provide more information than steady-state techniques. This dynamic method can also provide diagnostic criteria for evaluating cell performance [134-143]. The main advantage of EIS as a diagnostic tool for investigating fuel cell behavior are its ability to separate the individual contributions of the interfacial charge transfer resistances, mass transport resistances in the catalyst layer and backing diffusion layer, and ion and electron transport resistances [134,140].

The main contributors to the impedance of a fuel cell include interfacial charge transfer resistances, membrane resistance, cell contact resistances, oxygen transport resistances, proton transport resistances, and fuel transport resistances. It also includes double layer capacitances and Faradaic pseudo capacitances. There are several formats commonly used to describe the impedance behavior of a cell:

(a) Complex plane impedance plots (Nyquist plots)

Complex plane impedance plots are the most commonly used way to depict impedance. They can provide valuable information about electrochemical processes occurring in a fuel cell. For example, the sum of the cell contact and electrolyte resistances ($R_{\Omega} = R_{contact} + R_{membrane}$) can be conveniently determined by the intercept of the impedance plots with the x-axis at high frequency. Generally, the charge transfer resistance R_{ct} is reflected in the plot in the high frequency region as a semicircle as shown in Figure 1.6, while the mass transport resistance is represented in the low frequency region. However, it is more often than not that the charge transfer resistance and the mass transport resistance fall in the same frequency region, and therefore, it is difficult to separate them directly from the plot. Under such circumstances, a special experimental design or simulation is needed to separate the charge transfer resistance from the mass transport resistance.

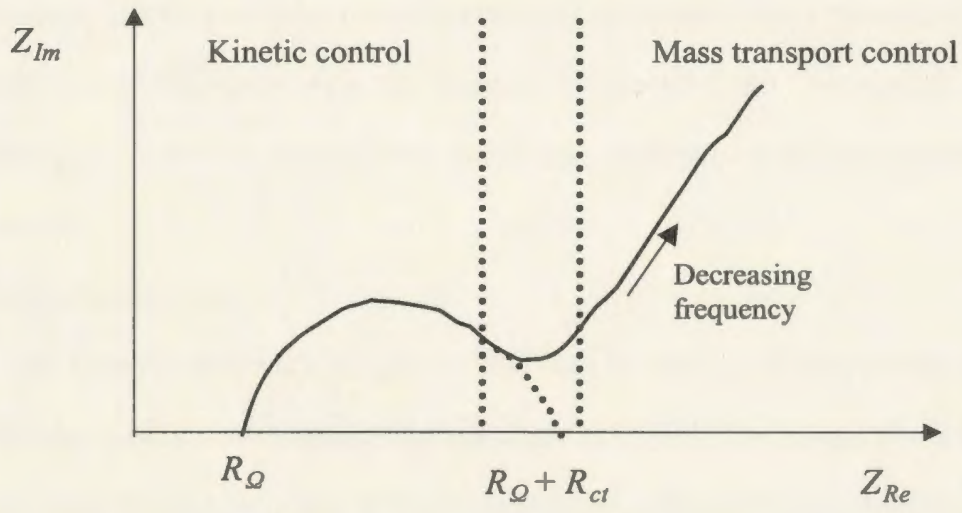

Figure 1.6. Complex plane impedance plot for a typical cell.

If we are interested in studying mass transport resistances, we can use large overpotentials to increase the rate of charge transfer so that the charge transfer resistance becomes insignificant compared with the mass transport resistance. On the other hand, if we want to investigate charge transfer resistances, we can study the electrochemical process at low overpotentials or alternatively, increase the rate of mass transport so that the mass transport resistance is relatively unimportant in the whole impedance. Another commonly used way to separate the charge transfer resistance and mass transport resistance is simulation. The charge transfer resistance and the mass transport resistance are obtained by simulation of the experimental data based on an equivalent circuit [138,140]. The problem with this method is that the same plot may be simulated with different equivalent circuits and consequently, different values of parameters can be obtained [144].

(b) Bode plots

Bode plots show magnitude and phase angles of the impedance as a function of frequency. Because different electrochemical processes have their own characteristic frequencies [140], measuring the change of characteristic frequencies with different potentials can provide insights into the change of electrochemical processes at different potentials.

(c) Capacitance plots

The series capacitance of an electrode can be used as a reasonable measure of the electrochemically active area of the electrode [76,145]. The bigger the magnitude of the series capacitance, the larger is the electrochemically active area. Measuring changes in capacitance as a function of potential at low frequencies is especially useful for studying

the activity of catalysts at different potentials [145-146]. The series capacitance of an electrode is calculated by the following equation:

$$C = -1/(Z''\omega) \quad (1.19)$$

where C is the capacitance, Z'' is the imaginary impedance, and $\omega = 2\pi f$ is the angular frequency.

1.6 Thesis Objectives

The main objectives of this thesis include investigating the effects of Nafion loading on the performance of PEMFC cathodes, designing reference electrodes to resolve cell performance into the individual electrode behaviors, and developing anode catalysts for DEFCs.

Oxygen reduction on cathodes involves both electron and proton transport, and proton transport is provided by Nafion. Therefore studies of the effects of Nafion loading on the performance of PEMFC cathodes are of significant importance. The effects of Nafion loading on the performance of PEMFC cathodes have been investigated by impedance spectroscopy, cyclic voltammetry, and polarization measurements. With these techniques plus simulations, it was found that optimum Nafion loading is determined by the balance between oxygen transport and proton conduction. This is the first time that impedance spectroscopy has been applied to this problem. By using this technique, conductivity profiles of PEMFC cathode catalyst layers were obtained. This work has been published in J. Electrochem. Soc. [147], although additional analysis of the impedance data is presented in this thesis.

Resolving cell performance to the individual electrode behaviors can provide valuable information for optimization of cell performance and cell operation conditions,

and this can only be done with the aid of a reference electrode. A dynamic hydrogen reference electrode (DHE) for thin layer cells has been designed, and it was found that reliable single electrode potentials and impedances can be obtained in both hydrogen and methanol cells. This work has been published, in part, in Electrochimic Acta [148].

Ethanol is a promising fuel. The key to developing direct ethanol fuel cells is to find active anode catalysts. It was found that Pt/Sn and Pt/Ru/Pb catalysts are very promising for use as the anode catalysts for direct ethanol fuel cells.

1.7 References

[1] W. R. Grove, Philos. Mag. 14 (1839) 127.

[2] A. M. Adams, F. T. Bacon, R. G. H. Watson, in: Fuel Cells, W. Mitchell Jr., Ed., Academic Press, New York, 1963, P. 129.

[3] G. J. K. Acres, J. Power Sources 100 (2001) 60.

[4] L. Carrette, K. A. Friedrich, and U. Stimming, ChemPhysChem 1 (2000) 162.

[5] http://www.fuelcells.org/fcapps.htm.

[6] M. L. Perry and T. F. Fuller, J. Electrochem. Soc. 149 (2002) S59.

[7] B. Andreaus, A. J. McEvoy, and G. G. Scherer, Electrochim. Acta 47 (2002) 2223.

[8] H. S. Wroblowa, Y. C. Pan, and G. Razumney, J. Electroanal. Chem. 69 (1976) 195.

[9] M. Watanabe, H. Sei, and P. Stonehart, J. Electroanal. Chem. 261 (1989) 375.

[10] A. J. Appleby, F. R. Foulkes, A Fuel Cell Handbook, 2nd Ed., Kreiger Publishing: New York, 1993, p22.

[11] T. E. Springer, M. S. Wilson, and S. Gottesfeld, J. Electrochem. Soc. 140 (1993) 3513.

[12] A. Damjanovic, M. A. Grenshaw, and J. O'M. Bockris, J. Chem. Phys. 45 (1966) 4057.

[13] H. S. Wroblowa, Y. C. Pan, and G. Razumnet, J. Electroanal. Chem. 69 (1976) 195.

[14] A. J. Appleby and M. Savy, J. Electroanal. Chem. 92 (1978) 15.

[15] R. W. Zurilla, R. K. Sen, and E. Yeager, J. Electrochem. Soc. 125 (1978) 1103.

[16] E. Yeager, Electrochim. Acta 29 (1984) 1527.

[17] L. J. Bregoli, Electrochim. Acta 23 (1978) 489.

[18] G. J. M. Janssen and M. L. J. Overvelde, J. Power Sources 101 (2001) 117.

[19] J. J. Baschuk and X. Li, J. Power Sources 86 (2000) 181.

[20] W. Masahiro, U. Hiroyuki, and E. Masaomi, J. Phys. Chem. B 102 (1998) 3129.

[21] T. E. Springer, T. A. Zawodzinski, and S. Gottesfeld, J. Electrochem. Soc. 138 (1991) 2334.

[22] D. M. Bernardi and M. W. Verbrugge, J. Electrochem. Soc. 139 (1992) 2477.

[23] T. Okada, G. Xie, and M. Meeg, Electrochim. Acta 43 (1998) 2141.

[24] P. D. Beattie, F. P. Orfino, V. I. Basura, K. Zychowska, J. Ding, C. Chuy, J. Schmeisser, and S. Holdcroft, J. Electroanal. Chem. 503 (2001) 45.

[25] N. Miyake, J. S. Wainright, and R. F. Savinell, J. Electrochem. Soc. 148 (2001) A898.

[26] A. V. Anantaraman and C. L. Gardner, J. Electroanal. Chem. 414 (1996) 115.

[27] C. Gavach, G. Pamboutzoglou, N. Nedyalkov, and G. Pourcelly, J. Membr. Sci. 45 (1989) 37.

[28] H. L. Yeager and A. Steck, J. Electrochem. Soc. 128 (1981) 1880.

[29] A. Eisenberg, B. Hird, and R. B. Moore, Macromolecules, 23 (1990) 4098.

[30] T. D. Gierke, G. E. Munn, and F. C. Wilson, J. Polym. Sci. Polym. Phys. Ed.19 (1981) 1687.

[31] F. N. Buchi and G. G. Scherer, J. Electrochem. Soc. 148 (2001) A183.

[32] K. A. Mauritz, I. D. Stefanithis, S. V. Davis, R. W. Scheetz, R. K. Pope, G. L. Wilkes, and H. H. Huang, J. Appl. Polym. Sci. 55 (1995) 181.

[33] K. T. Adjemian, S. J. Lee, S. Srinivasan, J. Benziger, and A. B. Bocarsly,

J. Electrochem. Soc. 149 (2002) A256.

[34] I. Honma, S. Hirakawa, K. Yamada, and J. M. Bae, Solid State Ionics 118 (1998) 29.

[35] K. D. Kreuer, J. Membr. Sci. 185 (2001) 29.

[36] H. Nakajima, S. Nomura, T. Sugimoto, S. Nishikawa, and I. Honma, J. Electrochem. Soc. 149 (2002) A953.

[37] J. T. Wang, R. F. Savinell, J. Wainright, M. Litt, and H. Yu, Electrochim. Acta 41 (1996) 193.

[38] E. Passalacqua, F. Lufrano, G. Squandrito, A. Patti, and L. Giorgi, Electrochim. Acta 43 (1998) 3665.

[39] V. A. Paganin, E. A. Ticianelli, and E. R. Gonzalez, J. Appl. Electrochem. 26 (1996) 297.

[40] M. S. Wilson, J. A. Valerio, and S. Gottesfeld, Electrochim. Acta 40 (1995) 355.

[41] T. R. Ralph and M. P. Hogarth, Platinum Metals Rev. 46 (2002) 3.

[42] S. D. Lin, T. C. Hsiao, J. R. Chang, and A. S. Lin, J. Phys. Chem. B 103 (1999) 97.

[43] X. Cheng, B. Yi, M. Han, J. Zhang, Y. Qiao, and J. Yu, J. Power Sources 79 (1999) 75.

[44] O. Teschke, J. Electrochem. Soc. 131 (1983) 1095.

[45] H. Yu, Z. Hou, B. Yi, and Z. Lin, J. Power Sources 105 (2002) 52.

[46] R. Venkataraman, H. R. Kunz, and J. M. Fenton, J. Electrochem. Soc. 150 (2003) A278.

[47] G. A. Camara, E. A. Ticianelli, S. Mukerjee, S. J. Lee, and J. McBreen, J. Electrochem. Soc. 149 (2002) A748.

[48] H. F. Oetjen, V. M. Schmidt, U. Stimming, and F. Trila, J. Electrochem. Soc. 143 (1996) 3838.

[49] S. Gottesfeld and J. Pafford, J. Electrochem. Soc. 135 (1998) 2651.

[50] V. M. Schmidt, H. F. Oetjen, and J. Divisek, J. Electrochem. Soc. 144 (1997) L237.

[51] H. A. Gasteiger, N. Markovic, and P. N. Ross, J. Phys. Chem. 99 (1995) 17757.

[52] M. M. P. Janssen and J. Moolhuysen, Electrochim. Acta 21 (1976) 869.

[53] T. V. Choudhary and D. W. Goodman, Catal. Lett. 59 (1999) 93.

[54] A. S. Arico, E. Modica, I. Ferrara, and V. Antonucci, J. Appl. Electrochem. 28 (1998) 881.

[55] J. Y. Kim, Z. G. Yang, C. Chang, T. I. Valdez, S. R. Narayanan, and P. N. Kumta, J. Electrochem. Soc. 150 (2003) A1421.

[56] B. N. Grgur, N. M. Markovic, and P. N. Ross, Electrochim. Acta 43 (1998) 3631.

[57] H. A. Gasteiger, N. M. Markovic, and P. N. Ross, J. Phys. Chem. 99 (1995) 8945.

[58] M. R. Andrew, B. D. McNicol, R. T. Short, and J. S. Drurry, J. Appl. Electrochem. 7 (1977) 153.

[59] N. M. Markovic, A. Widelov, P. N. Ross, O. R. Monteiro, and I. G. Brown, Catal. Lett. 43 (1997) 161.

[60] J. Arana, P. Ramirez de la Piscina, J. Llorca, J. Sales, N. Homs, and J. L. G. Fierro, Chem. Mater. 10 (1998) 1333.

[61] A. E. Aksoylu, M. M. A. Freitas, and J. L. Figueiredo, Catal. Today 62 (2000) 337.

[62] E. M. Crabb, R. Marshall, and D. Thompsett, J. Electrochem. Soc. 147 (2000) 4440.

[63] T. Ioroi, K. Yasuda, Z. Siroma, N. Fujiwara, and Y. Miyazaki, J. Electrochem. Soc. 150 (2003) A1225.

[64] E. I. Santiago, G. A. Camara, and E. A. Ticianelli, Electrochim. Acta 48 (2003) 3527.

[65] B. N. Grgur, N. M. Markovic, and P. N. Ross, J. Phys. Chem. B 102 (1998) 2494.

[66] C. He, H. R. Kunz, and J. M. Fenton, J. Electrochem. Soc. 150 (2003) A1017.

[67] M. Watanabe, S. Motoo, J. Electroanal. Chem. 60 (1975) 275.

[68] J. Davies, B. E. Hayden, and D. J. Pegg, Electrochim. Acta 44 (1998) 1181.

[69] F. Jaouen, S. Marcotte, J. P. Dodelet, and G. Lindbergh, J. Phys. Chem. B 107 (2003) 1376.

[70] M. Lefevre, J. P. Dodelet, and P. Bertrand, J. Phys. Chem. B 104 (2000) 11238.

[71] E. Antolini, R. R. Passos, and E. A. Ticianelli, Electrochim. Acta 48 (2002) 263.

[72] U. A. Paulus, A. Wokaun, G. G. Scherer, T. J. Schmidt, V. Stamenkovic, N. M. Markovic, and P. N. Ross, Electrochim. Acta 47 (2002) 3787.

[73] L. Xiong, A. M. Kannan, and A. Manthiram, Electrochem. Commun. 4 (2002) 898.

[74] J. Fleig and J. Maier, J. Electrochem. Soc. 144 (1997) L302.

[75] P. Gode, F. Jaouen, G. Lindbergh, A. Lundblad, and G. Sundholm, Electrochim. Acta 48 (2003) 4175.

[76] N. Jia, R. B. Martin, Z. Qi, M. C. Lefebvre, and P. G. Pickup, Electrochim. Acta 46 (2001) 2863.

[77] E. B. Easton, Z. Qi, A. Kaufman, and P. G. Pickup, Electrochem. Solid-State Lett. 4 (2001) A59.

[78] I. D. Raistrick, in Diaphragms, Separators, and Ion Exchange Membranes, J. W. Van Zee, R. E. White, K. Kinoshita, and H. S. Burney, Eds. Electrochemical Society, Pennington, NJ, 1986, p172.

[79] M. S. Wilson, and S. Gottesfeld, J. Electrochem. Soc. 139 (1992) L28.

[80] S. J. Lee, S. Mukerjee, J. McBreen , Y. W. Rho, Y. T. Kho, and T. H. Lee, Electrochim. Acta 43 (1998) 3693.

[81] G. Murgia, L. Pisani, M. Valentini, and B. D'Aguanno, J. Electrochem. Soc. 149 (2002) A31.

[82] E. A. Ticianelli, J. Electroanal. Chem. 387 (1995) 1.

[83] K. Broka and P. Ekdunge, J. Appl. Electrochem. 27 (1997) 281.

[84] O. Antoine, Y. Bultel, R. Durand, and P. Ozil, Electrochim. Acta 43 (1998) 3681.

[85] Y. Bultel, P. Ozil, and R. Durand, J. Appl. Electrochem. 28 (1998) 269.

[86] C. C. Boyer, R. G. Anthony, and A. J. Appleby, J. Appl. Electrochem. 30 (2000) 777.

[87] Y. Bultel, P. Ozil, and R. Durand, J. Appl. Electrochem. 30 (2000) 1369.

[88] M. L. Perry, J. Newman, and E. J. Cairns, J. Electrochem. Soc. 145 (1998) 5.

[89] T. E. Springer and I. D. Raistrick, J. Electrochem. Soc. 136 (1989) 1594.

[90] F. Jaouen, G. Lindvbergh, and G. Sundholm, J. Electrochem. Soc. 149 (2002) A437.

[91] E. Passalacqua, F. Lufrano, G. Squadrito, A. Patti, and L. Giorgi, Electrochim. Acta 46 (2001) 799.

[92] A. Heinzel and V. M. Barragan, J. Power Sources 84 (1999) 70.

[93] J. Wang, S. Wasmus, and R. F. Savinelll, J. Electrochem. Soc. 142 (1995) 4218.

[94] A. S. Arico, P. Creti, P. L. Antonucci, and V. Antonucci, Electrochem. Solid-State Lett. 1 (1998) 66.

[95] E. Peled, V. Livshits, and T. Duvdevani, J. power Sources 106 (2002) 245.

[96] E. Peled, T. Duvdevani, A. Aharon, and A. Melman, Electrochem. Solid-State Lett. 4 (2001) A38.

[97] Z. Qi and A. Kaufman, J. Power Sources 110 (2002) 65.

[98] D. Cao and S. H. Bergens, J. power Sources 124 (2003) 12.

[99] C. Lamy, E. M. Belgsir, and J. M. Leger, J. Appl. Electrochem. 31 (2001) 799.

[100] C. Lamy, A. Lima, V. Lerhun, F. Delime, C. Coutanceau, and J. M. Leger, J. Power Sources 105 (2002) 283.

[101] X. Ren, T. E. Springer, T. A. Zawodzinski, and S. Gottesfeld, J. Electrochem. Soc. 147 (2000) 466.

[102] T. Iwasita, Electrochim. Acta 47 (2002) 3663.

[103] K. W. Park, J. H, Choi, B. K. Kwon, S. A. Lee, Y. E. Sung, H. Y. Ha, S. A. Hong, H. Kim, and A. Wieckowski, J. Phys. Chem. B 106 (2002) 1869.

[104] Y. H. Chu, Y. G. Shul, W. C. Choi, S. I. Woo, and H. S. Han, J. Power Sources 118 (2003) 334.

[105] F. Vigier, C. Coutanceau, F. Hahn, E. M. Belgsir, and C. Lamy, J. Electroanal, Chem. 563 (2004) 81.

[106] H. Hoster, T. Iwasita, H. Baumgartner, and W. Vielstich, Phys. Chem. Chem. Phys. 3 (2001) 337.

[107] H. A. Gasteiger, M. Markovic, P. N. Ross and E. Cairns, J. Electrochem. Soc. 141 (1994) 1795.

[108] D. R. Rolison, P. L. Hagans, K. E. Swider, and J. W. Long, Langmuir 15 (1999) 774.

[109] A. Pozio, R. F. Silva, M. D. Francesco, F. Cardellini, L. Giorgi, Electrochim. Acta 48 (2002) 255.

[110] J. Kerres, A. Urllich, T. Haring, W. Preidel, M. Baldauf, and U. Gebhardt, J. New Mater. Electrochem. Syst. 3 (2000) 229.

[111] R. Nolte, K. Ledjeff, M. Bauer, and R. Mulhaupt, J. Membr. Sci. 82 (1993) 221.

[112] L. Jorissen, V. Gogel, J. Kerres, and J. Garche, J. Power Sources 105 (2002) 267.

[113] N. Jia, M. C. Lefebvre, J. Halfyard, Z. Qi, and P. G. Pickup, Electrochem. Solid-State Lett. 3 (2000) 529.

[114] E. B. Easton, B. L. Langsdorf, J. A. Hughes, J. Sultan, Z. Qi, A. Kaufman, and P. G. Pickup, J. Electrochem. Soc. 150 (2003) C735.

[115] N. Miyake, J. S. Wainright, and R. F. Savinell, J. Electrochem. Soc. 148 (2001) A898.

[116] K. T. Adjemian, S. J. Lee, S. Srinivasan, J. Benziger, and A. B. Bocarsly, J. Electrochem. Soc. 149 (2002) A256.

[117] P. Staiti, A. S. Aricon, V. Baglio, F. Lufrano, E. Passalacqua, and V. Antonucci, Solid State Ionics 145 (2001) 101.

[118] X. Ren, T. E. Springer, and S. Gottesfeld, J. Electrochem. Soc. 147 (2000) 92.

[119] S. C. Thomas, X. Ren, S. Gottesfeld, and P. Zelenay, Electrochim. Acta 47 (2002) 3741.

[120] V. Klouz, V. Fierro, P. Denton, H. Katz, J. P. Lisse, S. Bouvot-Mauduit, and C. Mirodatos, J. Power Sources 105 (2002) 26.

[121] A. O. Neto, M. J. Giz, J. Perez, E. A. Ticianelli, and E. R. Gonzalez, J. Electrochem. Soc. 149 (2002) A272.

[122] F. Delime, J-M. Leger, and C. Lamy, J. Appl. Electrochem. 29 (1999) 1249.

[123] E. V. Spinace, A. O. Neto, and M. Linardi, J. Power Sources 124 (2003) 426.

[124] A. O. Neto, E. G. Franco, E. Arico, M. Linardi, and E. R. Gonzalez, J. European Ceramic Soc. 23 (2003) 2987.

[125] N. Fujiwara, K. A. Friderich, and U. Stimming, J. Electroanal. Chem. 472 (1999) 120.

[126] W. J. Zhou, B. Zhou, W. Z. Li, Z. H. Zhou, S. Q. Song, G. Q. Sun, Q. Xin, S. Douvartzides, M. Goula, and P. Tsiakaras, J. Power Sources 126 (2004) 16.

[127] F. Vigier, C. Coutanceau, F. Hahn, E. M. Belgsir, and C. Lamy, J. Electroanal. Chem. 563 (2004) 81.

[128] M. J. Gonzalez, C. T. Hable, and M. S. Wrighton, J. Phys. Chem. B 102 (1998) 9881.

[129] W. Zhou, Z. Zhou, S. Song, W. Li, G. Sun, P. Tsiakaras, and Q. Xin, Appl. Catal. B 46 (2003) 273.

[130] www.education.lanl.gov/resources/fuelcells.

[131] E. B. Easton, Ph. D. Thesis, Memorial University of Newfoundland, 2003.

[132] S. Srinivasan, D. J. Manko, H. Koch, M. A. Enayetullah, and A. J. Appleby, J. Power Sources 29 (1990) 367.

[133] A. J. Bard and L. R. Faulkner, Electrochemical Methods, 2nd ed., John Wiley & Sons, New York, 2001.

[134] T. E. Springer, T. A. Zawodzinski, M. S. Wilson, and S. Gottesfeld, J. Electrochem. Soc. 143 (1996) 587.

[135] M. Eikerling and A. A. Kornyshev, J. Electroanal. Chem. 475 (1999) 107.

[136] M. C. Lefebvre, R. B. Martin, and P. G. Pickup, Electrochem. Solid-State Lett. 2 (1999) 259.

[137] J. M. Song, S. Y. Cha, and W. M. Lee, J. Power Sources 94 (2001) 78.

[138] V. A. Paganin, C. L. F. Oliveira, E. A. Ticianelli, T. E. Springer, and E. R. Gonzalez, Electrochim. Acta 43 (1998) 3761.

[139] T. J. P. Freire and E. R. Gonzalez, J. Electroanal. Chem. 503 (2001) 57.

[140] M. Ciureanu and R. Roberge, J. Phys. Chem. B 105 (2001) 3531.

[141] T. Romero-Castanon, L. G. Arriaga, and U. Cano-Castillo, J. Power Sources 118 (2003) 179.

[142] Y. Bultel, L. Genies, O. Antoine, P. Ozil, and R. Durand, J. Electroanal. Chem. 527 (2002) 143.

[143] O. Antoine, Y. Bultel, and R. Durand, J. Electroanal. Chem. 499 (2001) 85.

[144] X. Wang, I. M. Hsing, Y. J. Leng, and P. L. Yue, Electrochim. Acta 46 (2001) 4397.

[145] R. E. Melnick and G. T. R. Palmore, J. Phys. Chem. B 105 (2001) 1012.

[146] T. Iwasita, X. H. Xia, H. D. Liess, W. Vielstich, J. Phys. Chem. B 101 (1997) 7542.

[147] G. Li and P. G. Pickup, J. Electrochem. Soc. 150 (2003) C745.

[148] G. Li and P. G. Pickup, Electrochim. Acta 49 (2004) 4119.

Chapter 2 Experimental

2.1 Chemicals and Materials

Except for Nafion membranes, all chemicals and materials were used as received. Nafion membranes were cleaned according to the following procedures: Nafion 115, 117, or 112 membranes were immersed in ca. 3% H_2O_2(aq) for two hours at 80 °C with stirring, then immersed in deionized water for one hour at 80 °C with stirring, followed by immersion in 1 M H_2SO_4(aq) for two hours at 80 °C with stirring. Finally, the membranes were further immersed in deionized water for one hour at 80 °C with stirring, then washed with a copious amount of deionized water and stored in deionized water.

2.2 Preparation of Electrodes

Electrodes were prepared by applying either a catalyst ink or paste onto carbon fiber paper (Toray, 0.26 mm), then drying in a fume hood overnight at ambient temperature. In order to prevent loss of the catalyst ink and define the area over which the ink could spontaneously spread, the carbon fiber paper was clamped in a Teflon holder. The ink or the paste was prepared by thoroughly dispersing the catalyst (E-Tek In.) in an appropriate mixture of 5% Nafion solution (Aldrich) and iso-propanol by sonication for 30 min.

2.3 Preparation of MEAs

MEAs were prepared by hot-pressing the electrodes onto each side of a Nafion membrane at a pressure of 200 kg/cm^2 and a temperature of 135° for 30 min by using a Carver laboratory press. In order to align the cathode and the anode, the electrodes and the membrane were fixed in a stainless steel die during pressing.

2.4 Preparation of Catalysts

A number of Pt based binary and ternary catalysts have been prepared and the details of preparation will be described in the relevant chapters.

2.5 Electrochemical Measurements

Electrochemical experiments were conducted with a Solartron 1286 electrochemical interface coupled with a 1250 frequency response analyzer or with an EG&G PAR 273 potentiostat/galvanostat coupled with a 5210 lock-in amplifer. Locally-made 1 cm^2 cells or commercial 5 cm^2 cells (one was made by Fuel cell Technology Inc. and another was made by ElectroChem. Inc.) were used to perform fuel cell tests. The humidification of gases was achieved by passing them through water filled bubblers at the specified temperature with the gas flow rate controlled by flow meters (made by Cole-Parmer Inc.) The details of cell operation conditions can be found in the relevant chapters.

2.6 Scanning Electron Microscopy and X-Ray Emission Analysis

Scanning electron microscopy (SEM) images and X-ray emission analysis (EDX) data were acquired with an Hitachi-570 scanning electron microscopy coupled with a Tracor Northern 5500 energy dispersive X-ray analyzer. X-ray analysis data were analyzed with Tracor Northern's Software (SQ) for standardless analysis.

2.7 Transmission Electron Microscopy

Transmission electron microscopy (TEM) images were acquired with a Zeiss 109 high resolution TEM at 70 keV. Samples for TEM measurements were prepared as follows: 2 mg of the catalyst were dispersed in 500 μl of ethanol by sonication for 30 min. A drop of the resulting ink was then deposited onto a carbon coated copper grid and dried at room temperature.

2.8 X-Ray Diffraction

X-ray diffraction (XRD) patterns for catalysts were obtained on a X-ray diffracometer (Rigaku D/Max-2200V-PC) using a Cu K_α source (λ = 1.5418 Å) at a scan rate of 1.5 degrees per minute. The scan range was from 20 degrees to 120 degrees. Samples were ground in a mortar before measurements.

2.9 Measurements of Ethanol Crossover

Ethanol crossover was measured by following the same procedure as that for measurements of methanol crossover [1]. One side of the cell was fed with aqueous ethanol while the other side was fed with humidified N_2. Ethanol permeating through the membrane to the N_2 side was oxidized electrochemically. The limiting ethanol oxidation current was used as a measure of ethanol crossover. In these experiments the cathode (ethanol side) evolves H_2 and approximates a dynamic hydrogen reference electrode.

Figure 2.1 shows an example of ethanol oxidation current as a function of potential. It can be seen that limiting current was reached at potentials above ca. 0.75 V. Thus, the limiting ethanol permeation current was routinely measured at a cell voltage of 0.9 V and data were collected after ca. 10 min of applying of the potential.

2.10 Analysis of DEFC Products

DEFC anode products were collected as shown in Figure 2.2. The anode outlet solution was collected in a glass tube bathed in ice to reduce the volatility of the solution and the CO_2 was absorbed in an aqueous NaOH trap. The CO_2 was determined by a two-step titration of the aqueous NaOH solution with standardized HCl [2-3]. The first step, with the phenolphthalein as the indicator, converts sodium carbonate to sodium bicarbonate and consumes the excess NaOH. The second step, with methyl orange as the

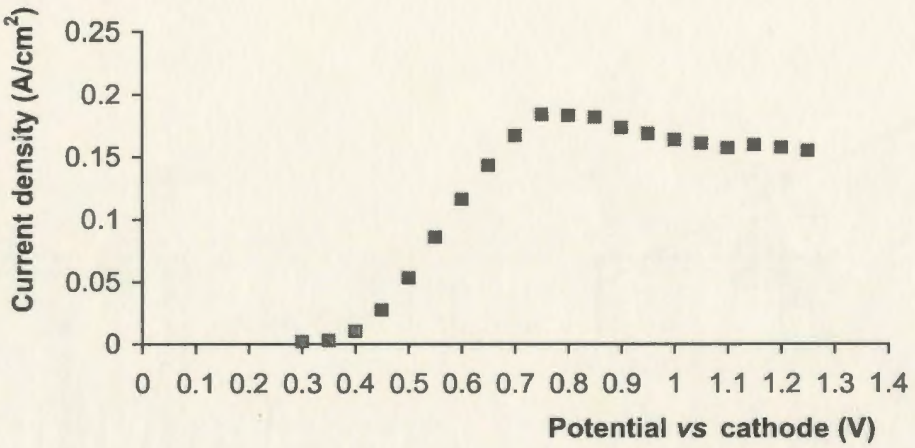

Figure 2.1 Ethanol permeation current as a function of potential on a Pt/Ru (1:1, 5.47mg/cm^2) catalyst in a 5 cm^2 cell. The cell was operated with one side fed with 2 M ethanol(aq) and the other side fed with humidified N_2 at a temperature of 80 °C. A Nafion 115 membrane was used as the electrolyte.

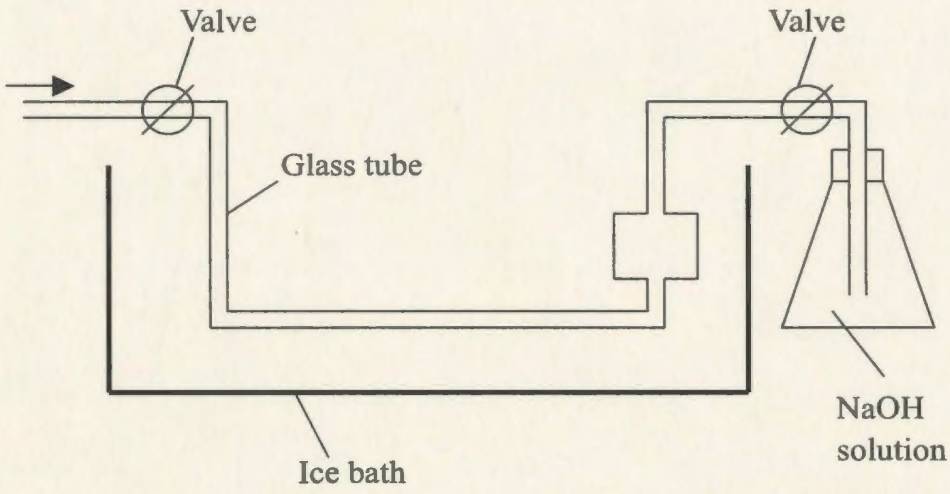

Figure 2.2. Schematic diagram of the equipment for collecting the anode outlet solution.

indicator, converts sodium bicarbonate to carbonic acid. The moles of sodium bicarbonate equals the moles of the CO_2 produced by the anode of the DEFC. Non-volatile acids (mainly acidic acid) in the anode outlet solution were determined by titrating the solution with standardized NaOH. It was found that purging the solution collected in the glass tube with N_2 did not significantly influence either the amount of CO_2 collected, or the acid content of the solution.

2.11 References

[1] X. Ren, T. E. Springer, and S. Gottesfeld, J. Electrochem. Soc. 147 (2000) 92.

[2] C. M. Davis and M. C. Mauck, J. Chem. Educ. 80 (2003) 552.

[3] K. M. Keener, J. D. LaCrosse, and J. K. Babson, Poultry Sci. 80 (2001) 983.

Chapter 3 Effects of Nafion Loading in the Cathode Catalyst Layer on the Performance of PEMFCs

3.1 Introduction

Proton exchange membrane fuel cells (PEMFCs) have attracted huge interest in recent years due to their high efficiency and friendliness to the environment. Significant improvement of cell performance has been achieved by using Nafion membranes as the electrolyte and mixing the catalyst with solublized Nafion [1-3]. However, the high costs of platinum based catalysts and the Nafion electrolyte are still major barriers to the commercialisation of the PEMFCs. Generally, there are two approaches to address this problem: one is to try to find cheaper catalysts and membranes [4]; another is to increase utilization of platinum and Nafion in the catalyst layer without lowering the cell performance [5-7]. In order to accomplish these goals, a deeper knowledge of the electrochemical processes, and the structure, composition, and morphology of electrodes is a prerequisite. Unfortunately, the structure of the electrodes and mass transport properties in the electrodes are still not very clear [8].

Oxygen reduction at the cathode of a PEMFC requires both electron and proton transport as shown in equation 3.1.

$$O_2 + 4e^- + 4H^+ = 2H_2O \quad (3.1)$$

Electron transport is provided by the carbon support, while Nafion incorporated into the catalyst layer transports protons to the active Pt sites. Oxygen reduction in the catalyst layer is a quite complex process, taking place at three-phase interfaces of the catalyst, gas, and electrolyte [9]. High performance for oxygen reduction requires good accessibility of oxygen to the active sites of the cathode, fast interfacial electron transfer kinetics, fast

electron transport through the hydrophobic carbon support, and facile proton transport through the hydrophilic Nafion. Since the electron transport resistance is normally negligible compared with the proton transport resistance [10], the limiting factors for oxygen reduction in a PEMFC are the interfacial electron transfer kinetics, the oxygen transport resistances in the catalyst layer and backing diffusion layer, and the proton transport resistance in the catalyst layer [10].

Intensive research has been devoted to optimize the structure and composition of cathodes for good oxygen accessibility and facile proton transport in the catalyst layer [11-14]. Some studies have focused on the effects of Nafion loading on the performance of cathodes. Pioneering work was accomplished by Raistrick and coworkers [15], who first introduced Nafion into the catalyst layer by impregnating it with a Nafion solution. The loading of platinum required was greatly reduced by this method without lowering cell performance. Further improvement was achieved by Gottesfeld and coworkers [7] by mixing the catalyst with a Nafion solution. Lee and coworkers [16] showed that by impregnating the catalyst layer with Nafion solution the activity of cathodes increased rapidly with increasing Nafion loading up to a loading of 1.3 mg/cm^2 followed by a more gradual change with a maximum at 1.9 mg/cm^2 (ca. 35-40 mass %) for both oxygen and air reduction (platinum loading 0.4 mg/cm^2). Passalacqua and coworkers [13] found that the optimum Nafion loading for cathodes prepared by mixing the catalyst with Nafion solution is 33 mass %.

Less attention has been paid to the effects of Nafion distribution on the performance of cathodes. For the impregnation method, the Nafion distribution is unlikely to be even. That is why there is a difference in optimum Nafion loading between the impregnation and mixing methods. Since proton transport is one of the limiting factors for better

cathode performance and Nafion is the only proton transport provider, fully understanding the effects of Nafion loading and distribution on the cell performance is crucial to optimising electrodes and operating conditions.

Because the transport of oxygen, water, and protons influence each other within the catalyst layer, the picture of how they work together and their integrated effects on the cell performance is still not very clear. However, a number of models have been proposed to depict oxygen reduction in PEMFC cathode catalyst layers [10, 17-19]. The most accepted model is the thin-film flooded agglomerate model [18]. This model is very successful in explaining oxygen diffusion in the hydrophobic pores and electrolyte thin films. Another interesting model is the percolation model, which is quite simple and intuitive [19]. The details of these models are described in section 1.2.4.2 of chapter one.

Impedance spectroscopy is a powerful technique in fuel cell studies. This dynamic method can provide more information than steady-state experiments and can provide diagnostic criteria for evaluating PEMFC performance [20-23]. The main advantage of impedance spectroscopy as a diagnostic tool for dissecting fuel cell behaviour is its ability to separate the individual contributions of the interfacial charge transfer resistance, mass transport resistances in the catalyst layer and backing diffusion layer, and ion and electron transport resistances [20]. Generally, the high frequency region of an impedance spectrum reflects the charge transfer resistance, whereas the medium and low frequency regions represent the mass transport resistance [24]. The contributors to the impedance of a PEMFC include the interfacial charge transfer resistances, membrane resistance, contact resistances, oxygen transport resistances, proton transport resistances, and fuel transport resistances. It also includes double layer capacitances and Faradaic pseudo capacitances. The impedance of a PEMFC is quite complicated in most cases, because the charge

transfer resistance and the mass transport resistance fall in the same frequency region [20, 23]. However, the impedance strongly depends on the cell voltage. At high cell voltages, where the mass transport resistance is not significant, the main contributor to the impedance is the interfacial charge transfer resistance; at low cell voltages (high current densities), the oxygen transport resistance and/or fuel transport resistance become dominant, especially when air is used as the oxidant [23]; at medium cell voltages, protons, oxygen, and fuel can contribute significantly to the total impedance of the cell.

Useful information can be acquired from impedance spectroscopy by simulating the experimental data [20]. However, the complexity of the system makes this difficult to do accurately, unless many parameters are already known. It is therefore of importance to develop methodology for experimentally isolating the contributions of the various components of the cell. To this end, Pickup and coworkers [21, 25] have investigated the ionic resistance in the catalyst layers of PEMFC cells by running impedance experiments under a nitrogen atmosphere. They obtained conductivity profiles for the cathode catalyst layer by simulating the impedance data using a transmission-line equivalent circuit.

The aim of the work described in this chapter was to elucidate more clearly the effects of Nafion loading in the cathode catalyst layer. To this end, a variety of cathodes with different Nafion loadings and different Nafion distributions were prepared. A number of diagnostic tests such as polarization experiments, cyclic voltammetry, impedance spectroscopy and electron microscopy have been performed to analyse the performance and structure of these cathodes. In addition, the impedance data were simulated based on different equivalent circuits, so that conductivity profiles and resistance values of the cathode catalyst layer were obtained.

Since publication of this work [26], there have been a number of complementary

publications by other groups [27-28]. Liu and coworkers [27] found that the optimal Nafion distribution is a linearly increasing function from the gas diffusion layer side to the membrane side. Makharia and coworkers [28] showed that the measured catalyst layer electrolyte resistance increased with decreasing Nafion content in the cathode.

3.2 Experimental

3.2.1 Chemicals and Materials

20 mass % Pt on XC-72 carbon (E-Tek Inc.), carbon fibre paper (Toray, 0.26 mm), electrodes (4 mg/cm^2 Pt black on carbon paper, supplied by Ballard Power Systems), and 5% Nafion solution (Aldrich) were used as received. Nafion 115 membranes (DuPont) were cleaned according to the procedure described in section 2.1 of chapter two.

3.2.2 Preparation of Cathodes and MEAs

A catalyst ink was prepared by mixing the catalyst (20% Pt on C; ca. 2-4 nm Pt particle size) and 5% Nafion solution (Aldrich) with isopropyl alcohol by sonication for 30 min. The ink was poured onto carbon fibre paper clamped in a Teflon holder which defined the area over which the ink could spread (spontaneously). The ink was allowed to dry at room temperature in a fume hood overnight. The electrodes were then sintered in an oven at 135 $^{\circ}$ C for 30 min, and 1 cm^2 discs were cut and used as the cathode. In some experiments, a second catalyst layer was applied to the sintered electrode in the same manner to prepare bilayer cathodes (Pt and Nafion loadings are based on the masses of catalyst and Nafion used to prepared the ink). Cathode Pt loadings were 0.4 mg/cm^2 in all cases.

MEAs were prepared by hot-pressing a 1 cm^2 cathode and a standard 1 cm^2 anode (Ballard electrode) onto each side of a Nafion 115 membrane at a pressure of 200 kg /cm^2 at 135 $^{\circ}$C for 90 s.

3.2.3 Electrochemistry

Electrochemical measurements were made in a 1 cm^2 active area fuel cell at ambient temperature (23 ± 3 °C) and pressure. Before measurements were taken, the cell was operated with humidified H_2 on the anode and dry O_2 on the cathode at a cell voltage of 0.5 V until a steady current was obtained.

Measurements were made with a Solartron 1286 electrochemical interface and 1250 frequency response analyser. Impedance measurements were conducted with a perturbation amplitude of 5 mV over a frequency range of 65 kHz to 0.1 Hz. For measurement of ionic conductivities in the cathode catalyst layer, the impedance measurements were carried out immediately following a H_2/O_2 polarization experiment, and therefore should provide a good approximation of the characteristics of the operating cathode.

Voltammetric measurements (2 electrode mode) were conducted, following purging of the cathode compartment with N_2, to determine the electrochemically active areas of the cathodes. The anode served as a pseudo reference electrode and counter electrode in these experiments.

3.2.4 Scanning Electron Microscopy and X-Ray Emission Analysis

Scanning electron microscopy (SEM) is a powerful technique to study the structure and morphology of a MEA. Generally, a cross-section of a MEA is prepared for SEM observation by cutting or fracturing. However, these methods can lead to distortion of the surface of the cross-section. In order to prevent this, the MEA was first mounted in epoxy, and then polished it until a clear cross-section was obtained.

The distribution of Nafion in catalyst layers was investigated using X-ray emission analysis (EDX) line scans of the cross-section of a half MEA. The half MEA was

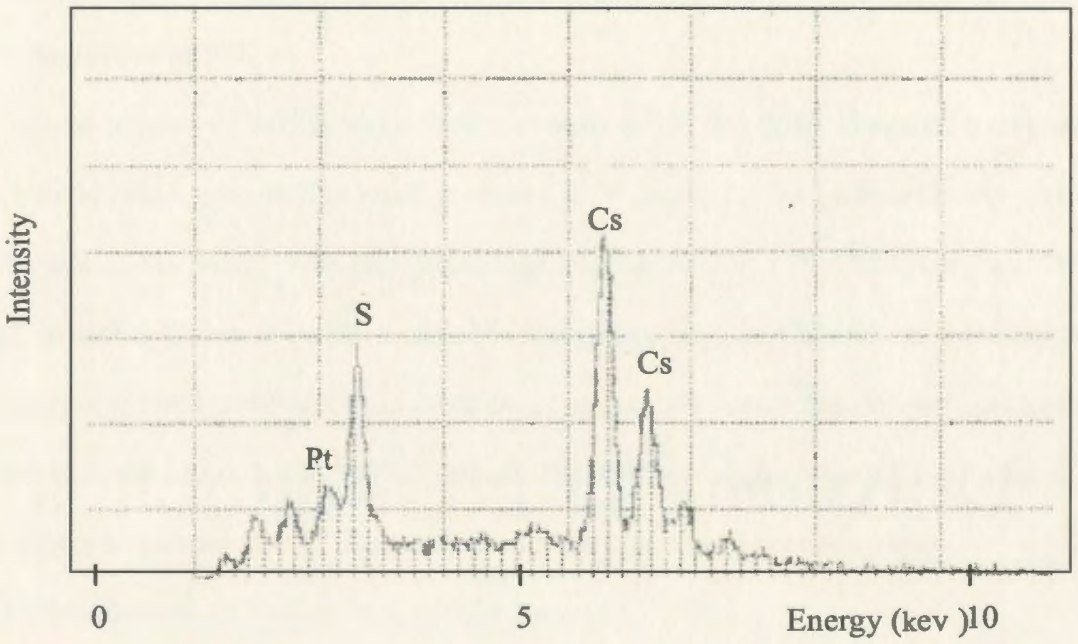

Figure 3.1. An EDX spectrum of a catalyst layer following ion-exchange with Cs^+.

prepared by hot-pressing the cathode onto one side of a Nafion 115 membrane. Cesium ions were incorporated into the half MEA by ion-exchanging with 0.1 M aqueous $CsClO_4$ at room temperature for 15 hours with stirring. The distribution of Nafion in the catalyst layer was represented by the cesium ion concentration profiles. Figure 3.1 clearly shows that Cs ions were incorporated into the half MEA and the Cs ion peak is well separated from the Pt and S peaks.

3.3 Results and Discussion

3.3.1 Structure of MEAs

The structures of MEAs were observed with SEM. An SEM image of a crosssection of a typical MEA used in this work is shown in Figure 3.2. The picture clearly shows the five layers of the MEA. The grey central area is the Nafion 115 membrane, and the dark areas on each side are the carbon paper backing. The very bright areas in between are the Pt containing catalyst layers. It is clear that the catalyst layers are not very uniform. The variation in thickness between the thinnest and thickest regions is about a factor of two. This is due to penetration of the catalyst into the pores of the carbon paper.

3.3.2 Distribution of Nafion in Catalyst Layers

Because Nafion contains pendant $-SO_3H$ groups, Nafion distribution in catalyst layers can be represented by sulfur concentration profiles in the catalyst layer [29] However, there is ca. 5000 ppm (weight) of sulfur in the E-Tek Vulcan-72 carbon catalyst support [30]. Also, the sulfur peak is quite close to the platinum peak in the EDX spectrum as shown in Figure 3.1. Therefore, cesium ion concentration profiles were chosen to represent Nafion distributions in the catalyst layer. Figure 3.3 shows the cesium concentration profile of a half MEA that has been ion exchanged with cesium ions. The cathode consisted of two layers of catalyst with different Nafion loading. The layer in

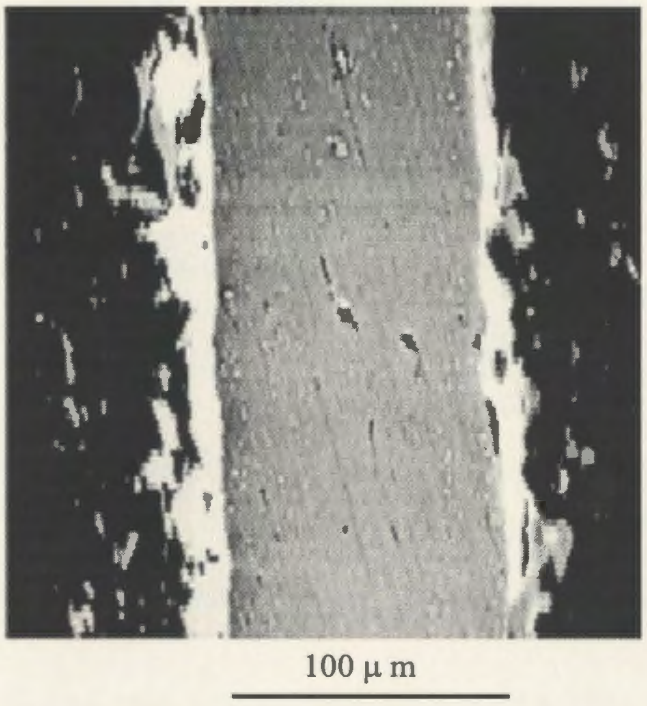

Figure 3.2. A SEM image of a MEA. The MEA consists of an anode of 4 mg/cm^2 Pt, a Nafion 115 membrane, and a cathode of 0.9 mg/cm^2 Nafion and 0.4 mg/cm^2 Pt.

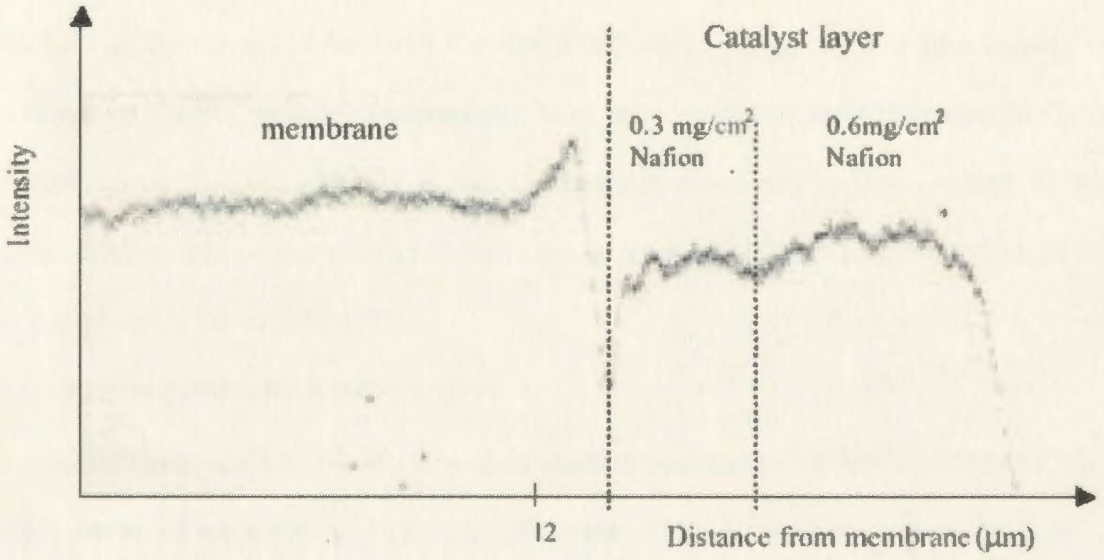

Figure 3.3. A Cs EDX line scan across a half MEA with a bilayer cathode. The half MEA was ion exchanged with Cs^+.

contact with carbon fibre paper contained 0.6 mg/cm^2 of Nafion, while the layer in contact with the Nafion membrane contained 0.3 mg/cm^2 of Nafion. The cesium concentration profile clearly reflects the Nafion distribution in the half MEA. The highest plateau represents the Nafion membrane. The second highest plateau reflects the Nafion distribution in the layer next to the CFP (0.6 mg/cm^2), and the plateau in the middle represents the layer next to the membrane with a Nafion loading of 0.3 mg/cm^2. The sharp minimum in the Cs signal between the membrane and catalyst layer is presumably due to delamination during sample preparation. Also, it is seen that the difference in Cs signal between the two layers was not as big as expected, since the Nafion content in the first layer is double that in the second layer. This is presumably due to penetration of Nafion into the pores of the carbon paper.

3.3.3 Electrochemically Active Areas

Cyclic voltammetry has been widely used to estimate the electrochemically active surface areas of catalysts in fuel cell electrodes [31]. Normally, cyclic voltammetry is taken with the cathode fed with nitrogen and the anode fed with hydrogen, and the hydrogen fed anode is assumed to act as a reversible hydrogen reference electrode. The coulombic charge for hydrogen adsorption on the cathode under a nitrogen atmosphere is used to calculate the active surface area of platinum by assuming that 210 μC/cm^2 is needed to produce a monolayer of adsorbed H on polycrystalline platinum [32].

Although the method is quite simple, the results obtained by different authors on commercial Pt/C catalysts are quite variable [33].

Figure 3.4 shows cyclic voltammograms for three cathodes with different Nafion loadings. It can be seen that the hydrogen adsorption peaks (cathodic peaks) change significantly with the different Nafion loadings. Electrochemically active areas of Pt in

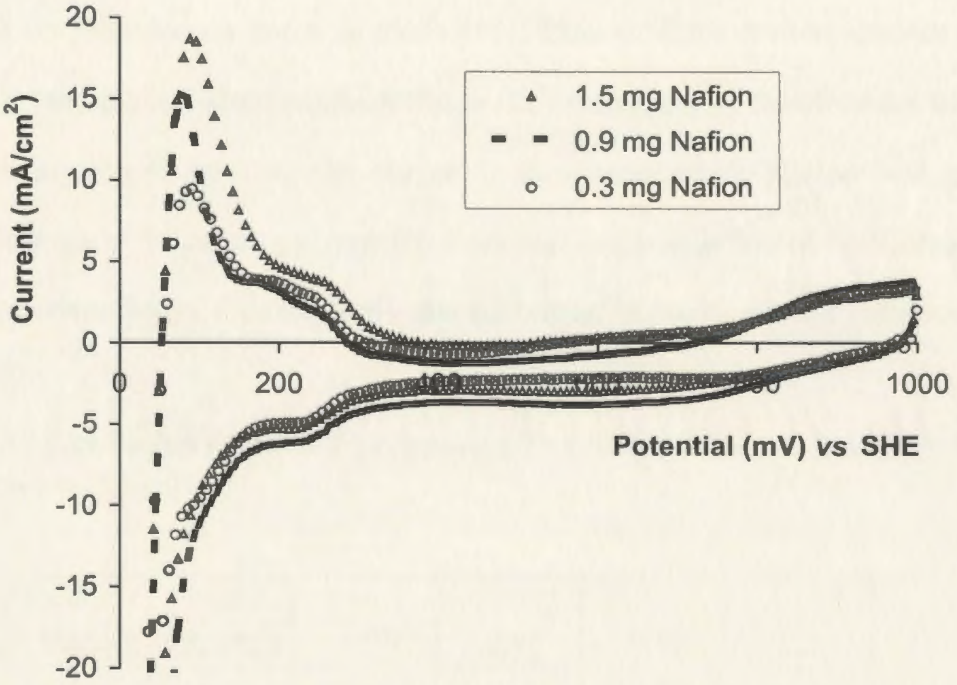
20
15
10
5
0
-5
-10
-15
-20
Current (mA/cm^2)
0
200
1000
Potential (mV) *vs* SHE
1.5 mg Nafion
0.9 mg Nafion
0.3 mg Nafion

each cathode (plus two others not included in Figure 3.4 for clarity) estimated from the charges for hydrogen adsorption are listed in Table 3.1, together with the Pt utilization. The Pt utilization is calculated as the electrochemically active area of the Pt catalyst divided by the total surface area of the Pt. The total surface area was determined by assuming that the surface area of Pt was 87 m^2/g for the catalyst employed [34].

Table 3.1 indicates that there is an optimum Nafion loading for the maximum electrochemically active area of the Pt catalyst. This can be explained by the model proposed by Passalacqua and coworkers [19]. That is, if the Nafion content is too low, there will not be good ionic conductivity in the catalyst layer; therefore the utilization of the Pt catalyst will be low. On the other hand, too much Nafion will cut off the percolation path for electron transfer between catalyst particles, resulting in worse electronic conductivity. Consequently, the utilization of the Pt catalyst will also be low.

Table 3.1. Electrochemically active areas of Pt cathode catalysts and their utilizations from cyclic voltammetry

Nafion loading (mg/cm^2)	0.30	0.60	0.90	1.2	1.5
Active Pt area (m^2/g)	48	52	66	59	56
Pt utilization	55%	60%	76%	68%	64%

The best Pt utilization was 76%, indicating that 24% of the catalyst is isolated either

ionically or electronically from the rest of the catalyst layer. This is probably mainly due to penetration of the catalyst into the pores of the carbon fibre paper backing (see Figure 3.2). It was reported that catalyst utilizations could be increased by application of the catalyst directly onto the membrane [7], or use of a carbon black sub-layer to fill the pores in the backing [6,35].

3.3.4 Conductivities of Cathode Catalyst Layers

Impedance spectroscopy has been shown to be a useful tool to investigate proton transport in the cathode catalyst layer [21,25]. For measurement of the conductivity of the cathode catalyst layer by impedance spectroscopy, the gas feed to the cathode was switched to dry N_2 immediately after a polarization experiment on H_2/O_2. Since the currents passed are small, the H_2 anode behaves as a reversible hydrogen electrode at low current densities, and therefore, the cell impedance is determined overwhelmingly by the cathode [20,23]. In addition, the applied potential during impedance measurements should be close to the open circuit potential for O_2/H_2O to minimize the Faradaic impedance due to reduction of trace O_2. Under these conditions, impedance spectra in the medium and low frequency region mainly reflect the proton transport resistance and double layer capacitance of the catalyst/Nafion binder interface.

Figure 3.5 shows impedance spectra for cathodes with different Nafion loadings. It is seen that the real resistance at low frequency decreases significantly with increasing Nafion loading. This indicates that the ionic resistance of the cathode catalyst layer decreases with increasing Nafion loading.

Another interesting finding is that there are small variations in the high frequency intercepts (see inset of Figure 3.5). These variations are likely due to experimental uncertainty such as variability of the membrane and cell contact resistances, since the

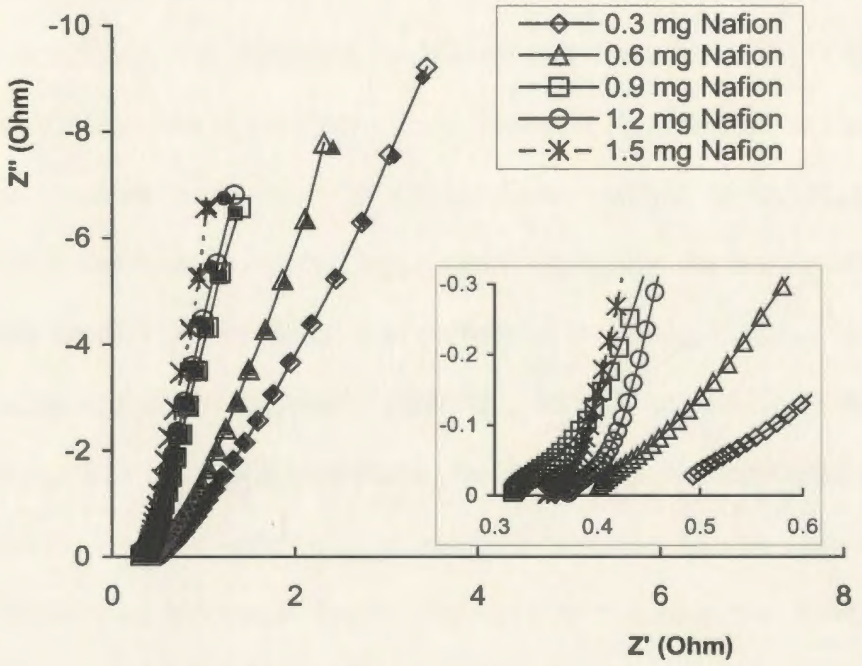

Figure 3.5. Complex plane impedance plots (open points) for nitrogen-bathed cathodes with various Nafion loadings, together with simulated plots (solid points). The inset shows an expansion of the high-frequency region of the plots.

high frequency real resistance intercept is mainly determined by the membrane and cell contact resistances.

It is difficult to obtain accurate ionic conductivity values for the cathode catalyst layer due to the uncertainty of the thickness of the catalyst layer (see Figure 3.2). However, approximate conductivity profiles of the catalyst layer can be acquired by simulating the impedance data.

The simulation was proposed by Pickup and coworkers [25], and is based on the finite transmission-line equivalent circuit shown in Figure 3.6. In the circuit, $R_{electronic}$ represents electron conduction in the cathode catalyst layer, R_{ionic} represents ion conduction in the cathode catalyst layer, and C represents the double-layer capacitance of the catalyst layer. The simulation was performed by setting $R_{electronic}$ at zero, $R_{membrane}$ at the experimental high frequency intercept, and C at the low frequency limiting capacitance. Fitting to each impedance spectrum was accomplished by changing the parameters in a power series plus exponent expression for the resistance profile. The Solver function in Microsoft Excel was used to optimise the fitting. The simulated impedance spectra are shown in Figure 3.5. It can be seen that the fitting is excellent, indicating that the simulation is reasonable. Figure 3.7 shows the conductivity profiles obtained by simulation. It is seen that the proton conductivity of the catalyst layer increases with increasing Nafion loading. This is expected and consistent with the experimental results (see Figure 3.5). It is also found that the conductivities for the three electrodes with high Nafion loading are quite uniform in the half of the layer closer to the membrane and drop sharply closer to the carbon paper backing.

The sharp drop of conductivity close to the carbon paper backing can be explained by penetration of Nafion into pores in the carbon paper (see Figure 3.2), because the

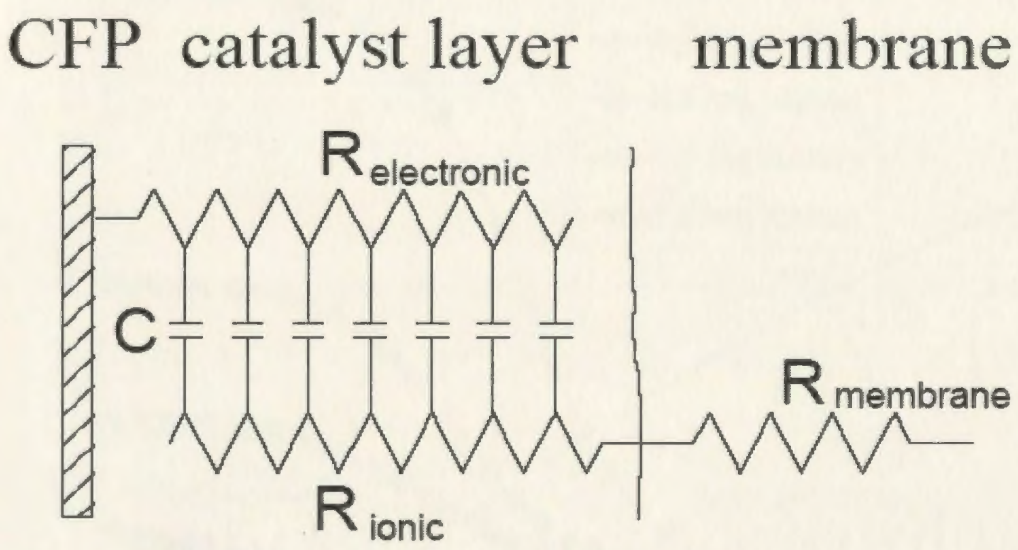

Figure 3.6. The finite transmission-line equivalent circuit used to simulate the impedance of the cathode under a nitrogen atmosphere.

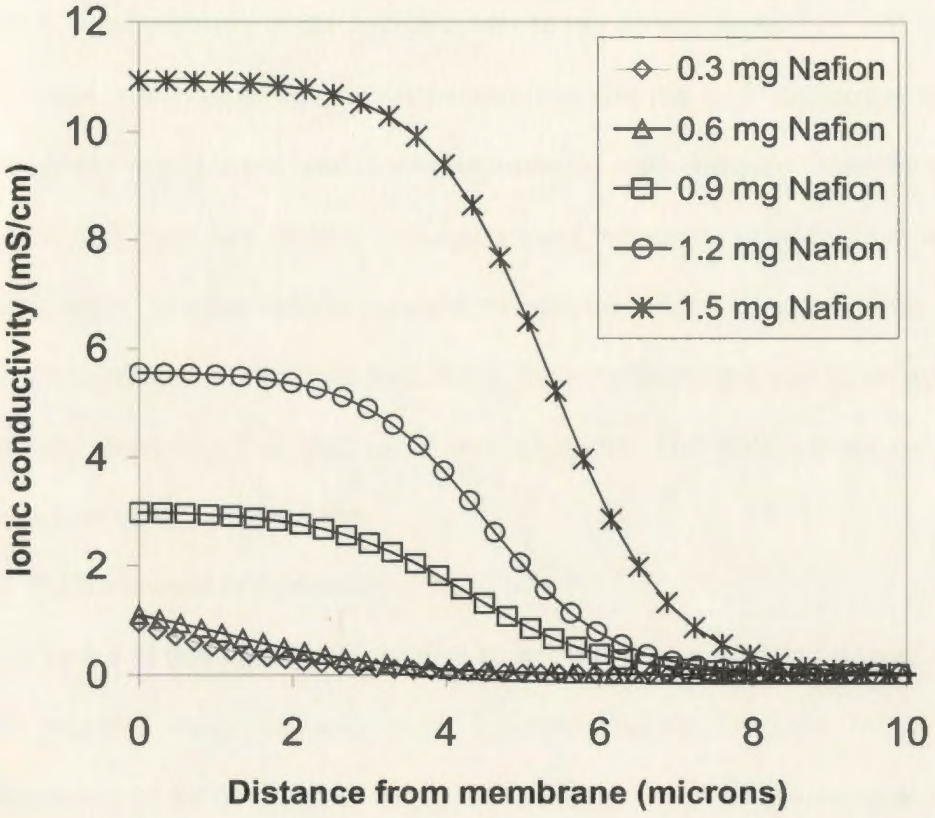

Figure 3.7. Conductivity profiles used to simulate the impedance data shown in Figure 3.5.

penetration can result in the loss of Nafion in the region close to the carbon paper andtherefore makes the region in poor ionic contact with the rest of the layer. Another possible reason is the formation of gradients of hydration in the catalyst layer caused by the dry N_2 stream, since the passage of dry N_2 through the back of the carbon paper can result in less hydration of the region closer to the carbon paper.

It was also found that the conductivities for the two electrodes with low Nafion loadings are much lower and drop continuously with distance from the membrane. This suggests that these low Nafion loadings are not enough to provide ionic connection in the catalyst layer. In other words, the catalyst particles are isolated ionically. This can lead to poor performance of the cathode, since high performance cathodes require both good electronic conductivities and facile ion transport. The polarization measurements (see below) confirm this conclusion.

3.3.5 Performance of Cathodes

In order to test the effects of Nafion loading on the performance of cathodes, MEAs were prepared with cathodes with different Nafion loadings. It is found that the performance of the cathodes strongly depended on the Nafion loading as shown in Figure 3.8. Also, there is an optimum Nafion loading of 0.9 mg/cm^2 for the best cell performance. The initial increase of cell performance with increasing Nafion loading can be attributed to the increasing ionic conductivities of the cathode catalyst layers at higher Nafion loadings. However, the decrease of cell performance with increasing Nafion loading after the Nafion loading exceeding 0.9 mg/cm^2 indicates that, at high Nafion loadings, other factors such as the O_2 transport resistance become more significant and begin to influence the cell performance (see below).

It was also found that the optimum Nafion loading is the same as the value that gives

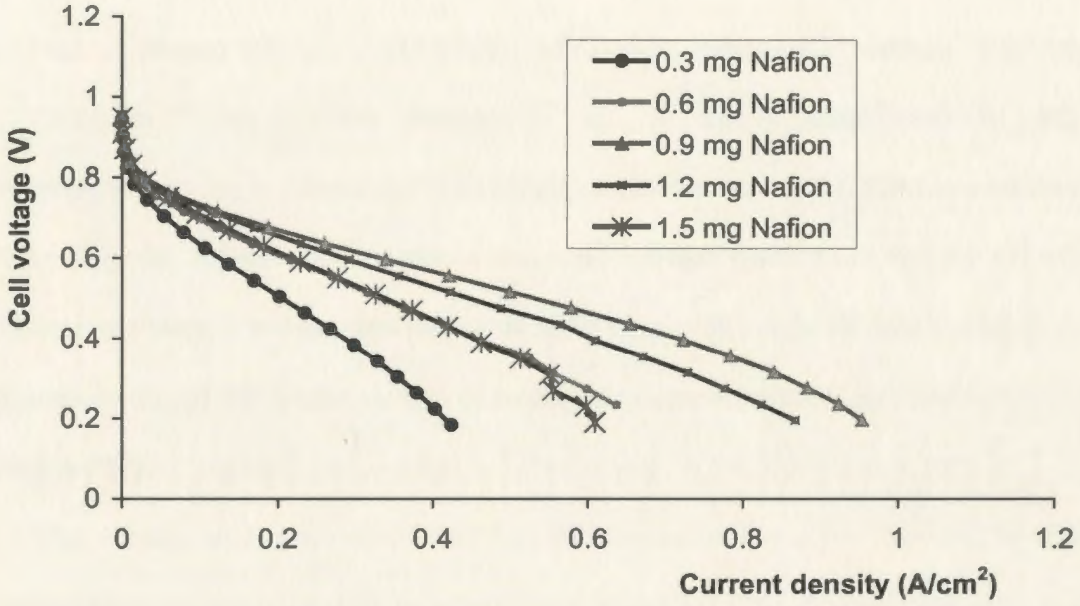

Figure 3.8. Polarization curves for cells with cathodes with various Nafion loadings. The cell was operated at ambient temperature and pressure with an anode feed of humidified H_2 and a cathode feed of O_2.

the highest catalyst utilization (Table 3.1). However, the difference in utilization is orders of magnitude too small to account for the large differences in the polarization curves observed in Figure 3.7. Something else must be more significant. From Figure 3.7 we can see that the slope of the linear region of the polarization curve changes significantly with Nafion loading. This indicates that Ohmic resistances are responsible for the large differences in cell performance.

The total Ohmic resistance mainly includes the membrane resistance, cell contact resistances, proton transport resistance, and oxygen transport resistance. The membrane resistance and cell contact resistances can be easily determined by impedance spectroscopy at high frequency. The major contributors to the Ohmic resistance after subtracting the membrane resistance and cell contact resistances should be the proton transport resistance and oxygen transport resistance in the cathode catalyst layer, since the resistances due to the anode should be negligible compared with the resistances due to the cathode [23].

The Ohmic resistance and Tafel kinetic parameters can be obtained by fitting the experimental polarization data to equations 1.6 and 1.7 [36]. Fitting was performed in an Excel spreadsheet by using the Solver function to minimize the sum of the squares of the difference between the experimental and calculated currents. The best fitting values are listed in Table 3.2.

It can be seen that the Tafel slope is ca. 70 mV/dec for all of the cathodes, being almost independent of Nafion loading. This indicates that the mechanism of oxygen reduction is not influenced significantly by the Nafion loading. Similar results were reported by Passalacqua and coworkers [19]. It is believed that if O_2 reduction is controlled

Table 3.2. Kinetic parameters for cathodes with various Nafion loadings

Nafion loading (mg/cm^2)	b (mV/dec)	i_o (mA/cm^2)	R (Ω cm^2)
0.3	68	0.74×10^{-4}	1.1
0.6	73	1.9×10^{-4}	0.63
0.9	68	1.5×10^{-4}	0.42
1.2	65	1.1×10^{-4}	0.53
1.5	71	2.7×10^{-4}	0.70

both by kinetics and mass transport, the Tafel slope will assume a higher value than 60 mV/dec [37]. Thus, the Tafel slope of ca. 70 mV/dec means that there was a mass transport limitation for oxygen reduction on the cathodes. The mass transport limitation can come from the proton transport resistance, the O_2 transport resistance, or from both.

Figure 3.9 shows the Ohmic resistance of the cell after subtracting the membrane resistance and cell contact resistances as a function of Nafion loading. The interesting finding is that the Ohmic resistance decreases with increasing Nafion loading at first, but when the Nafion loading exceeds 0.9 mg/cm^2, the Ohmic resistance increases with increasing Nafion loading. Also, the Ohmic resistance was lowest at a Nafion loading of 0.9 mg/cm^2. This correlates well with the fact that the cell has best performance at a Nafion loading of 0.9 mg/cm^2. Since the ionic resistance of the cathode catalyst layer decreases with increasing Nafion loading (Figure 3.5), the increase of the Ohmic resistance with Nafion loadings above 0.9 mg/cm^2 must be due to an increase of the oxygen transport resistance. The clear conclusion from Figure 3.9 is that at lower Nafion loading, the ionic resistance in the catalyst layer is more significant than the oxygen transport resistance for the cell performance. However, at higher Nafion loading, Nafion

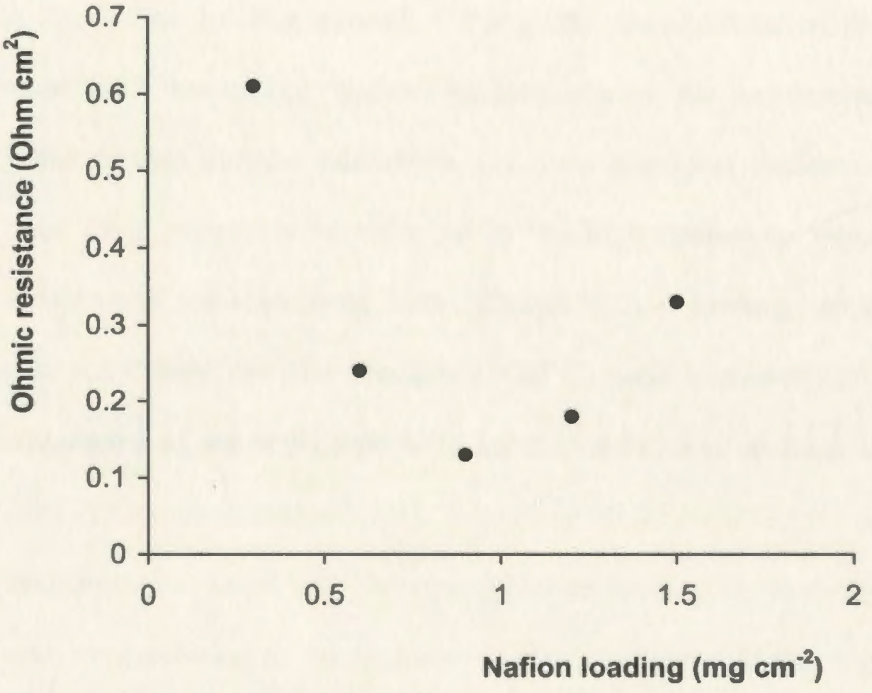

Figure 3.9. Ohmic resistances from fitting of the polarization data in Figure 3.8, after subtraction of the high frequency resistance from impedance spectroscopy.

blocks oxygen transport in the catalyst layer, and the oxygen transport resistance becomes more and more important with increasing Nafion loading.

Figure 3.10 shows impedance spectra for cells with cathodes with different Nafion loadings, the cells being operated with humidified H_2 on the anode and O_2 on the cathode at a cell voltage of 0.8 V. It is seen that all of the impedance spectra present a single semicircle, and the diameter of the semicircle changed significantly with Nafion loading. At first, the diameter of the semicircle decreased rapidly with increasing Nafion loading. However, when the Nafion loading exceeds 0.9 mg/cm^2, the diameter of the semicircle began to increase with increasing Nafion loading. Since the semicircle reflects a combination of the charge transfer resistance, O_2 mass transport resistance and ionic resistance, and the ionic resistance is reflected in the high frequency region [28], the change of the diameter of the semicircle with different Nafion loadings must be mainly due to changes in the charge transfer resistance and O_2 mass transport resistance. The decrease of the diameter of the semicircle with increasing Nafion loading indicates that the charge transfer resistance decreased with increasing Nafion loading, because the O_2 mass transport resistance increased with increasing Nafion loading as we discussed before. This decrease can be attributed to an increase in Pt active sites at the higher Nafion loadings. The increase of the diameter of the semicircle with increasing Nafion loading suggests that the O_2 mass transport resistance became significant at high Nafion loadings, and this is consistent with the results shown in Figure 3.9.

Depending on different operation conditions, several different equivalent circuits have been proposed to explain the impedance behaviour of PEMFC cathodes [23, 28, 38]. Here, we propose the simplified equivalent circuit shown in Figure 3.11 to explain the cathode impedance behaviour. In the equivalent circuit, R_s represents the membrane

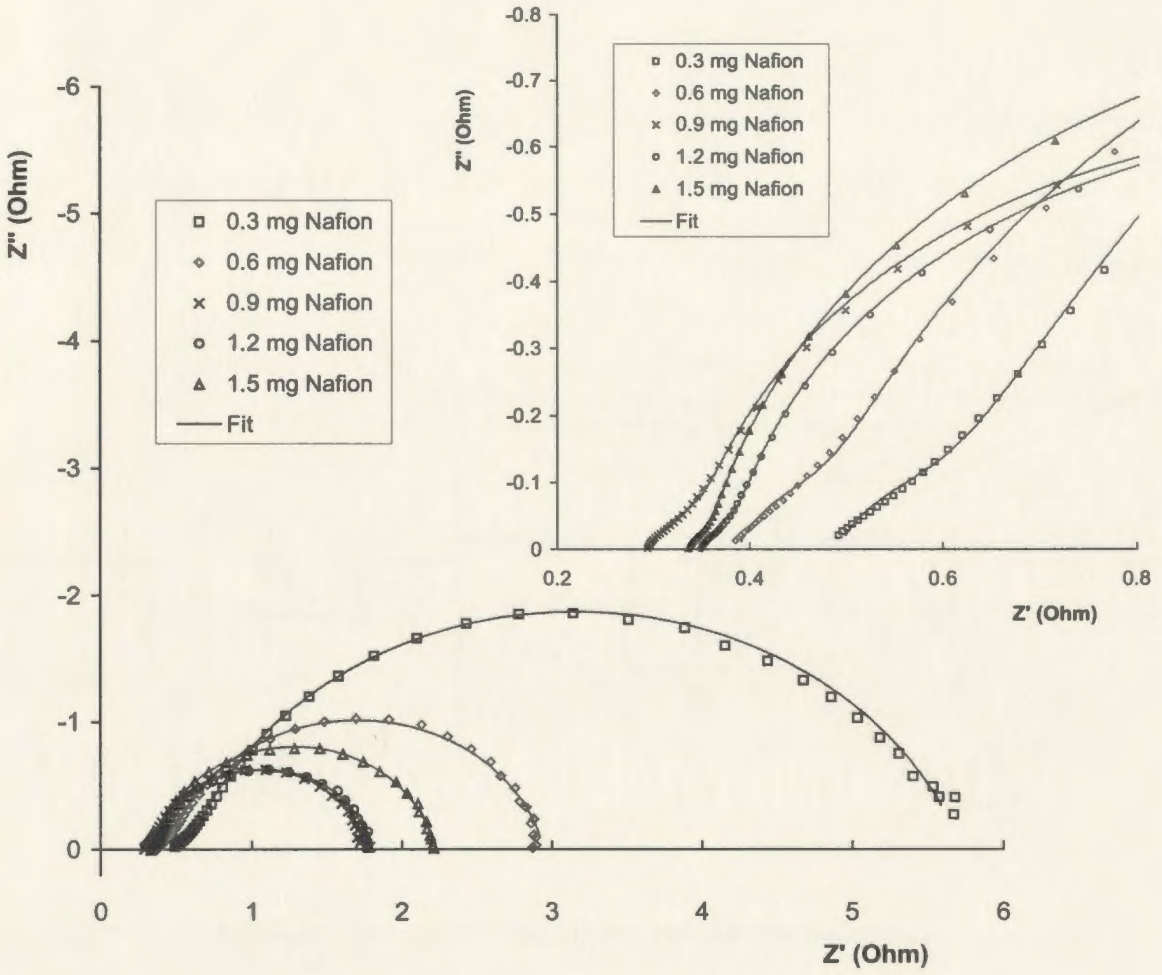

Figure 3.10. Complex plane impedance plots for cells with cathodes with different Nafion loadings at a cell voltage of 0.8 V. The cell was operated at ambient temperature and pressure with an anode feed of humidified H_2 and a cathode feed of O_2. The inset shows an expansion of the high frequency region of the plots.

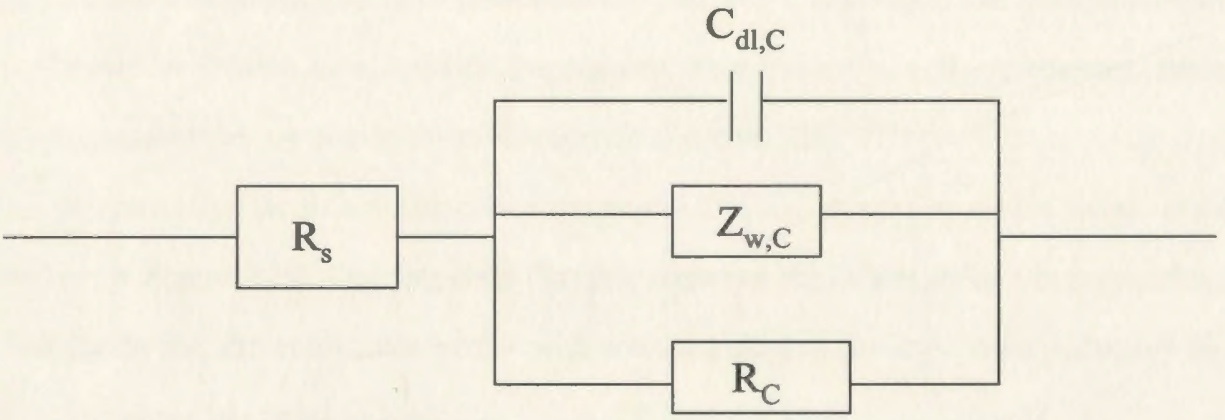

Figure 3.11. An equivalent circuit describing cathode impedance.

resistance plus contact resistances, and it is reflected by the high frequency intercept with the real axis; $Z_{w,C}$ is a Warburg impedance that represents the ionic resistance in the cathode catalyst layer, and it is reflected in the high frequency region by a characteristic 45 degree slope [28]; $C_{dl,C}$ represents the double layer capacitance due to catalyst in contact with the membrane; R_C represents the charge transfer resistance for O_2 reduction plus the O_2 transport resistance, and the magnitude of R_C is reflected by the diameter of the semicircle. Note that an open circuit terminus finite length Warburg was used in the circuit, and it is defined by three parameters: W_o-R, W_o-T, and W_o-P. The simulation was performed in Zview. Also, cathode impedances were treated as cell impedances, since anode impedances are negligible at low current densities [23].

It is seen that the fit between the experimental data and simulation data is excellent as shown in Figure 3.10. This suggests that the proposed equivalent circuit is reasonable. Parameters for the equivalent circuit with different Nafion loadings were extracted by simulation and are listed in Table 3.3.

Table 3.3. Parameters for the equivalent circuit in Figure 3.11 as a function of Nafion loading

Nafion loading (mg/cm^2)	0. 3	0. 6	0.9	1.2	1.5
R_s ($\Omega\ cm^2$)	0. 495	0. 389	0.296	0.352	0.337
$C_{dl,C}$ (F/cm^2)	0. 00094	0. 00173	0.00321	0.00444	0.00547
W_o-R ($\Omega\ cm^2$)	0. 467	0. 449	0. 258	0. 191	0. 130
W_o-T	0. 00263	0. 00336	0. 00340	0. 00245	0. 00185
W_o-P	0. 396	0. 435	0. 461	0. 461	0. 446
R_C ($\Omega\ cm^2$)	5. 23	2. 55	1. 45	1. 43	1. 88

From Table 3.3 we can see that R_C changed greatly with Nafion loading. At low Nafion loadings, R_C decreased significantly with increasing Nafion loading. At high Nafion loadings, R_C increased with increasing Nafion loading. It can be seen that the change of R_C with Nafion loading totally matches the change of the diameter of the semicircle. It is also found that the ionic resistance (W_o-R) decreased with increasing Nafion loading as expected. We can also see that the double layer capacitance increased greatly from low Nafion loadings to high Nafion loadings, suggesting that some catalyst particles were isolated at low Nafion loadings.

For comparison, the impedance data were also simulated based on the finite transmission line equivalent circuit shown in Figure 3.12. This finite transmission line equivalent circuit is provided by the Zview software and it has been used to simulate cathode impedance data [28]. During simulation, we found that the double layer capacitor had to be substituted by a constant phase element. Otherwise, the fit between the experimental data and the simulation data are poor. The reason for this substitution is due to the inhomogeneity of porous electrodes [23].

Table 3.4 lists the resistance values extracted by using this finite transmission line equivalent circuit. It is seen that the resistance values are quite close to those listed in Table 3.3. This again suggests that the proposed equivalent circuit shown in Figure 3.11 is reasonable.

Table 3.4. Resistance values for the finite transmission line equivalent circuit in Figure 3.12 as a function of Nafion loading

Nafion loading (mg/cm^2)	0. 3	0. 6	0.9	1.2	1.5
R_{ionic} (Ω cm^2)	0. 47	0. 36	0. 21	0. 15	0. 10
$R_{membrane}$ (Ω cm^2)	0. 43	0. 34	0. 27	0. 33	0. 32
R_C (Ω cm^2)	5. 1	2. 5	1. 4	1. 4	1. 9

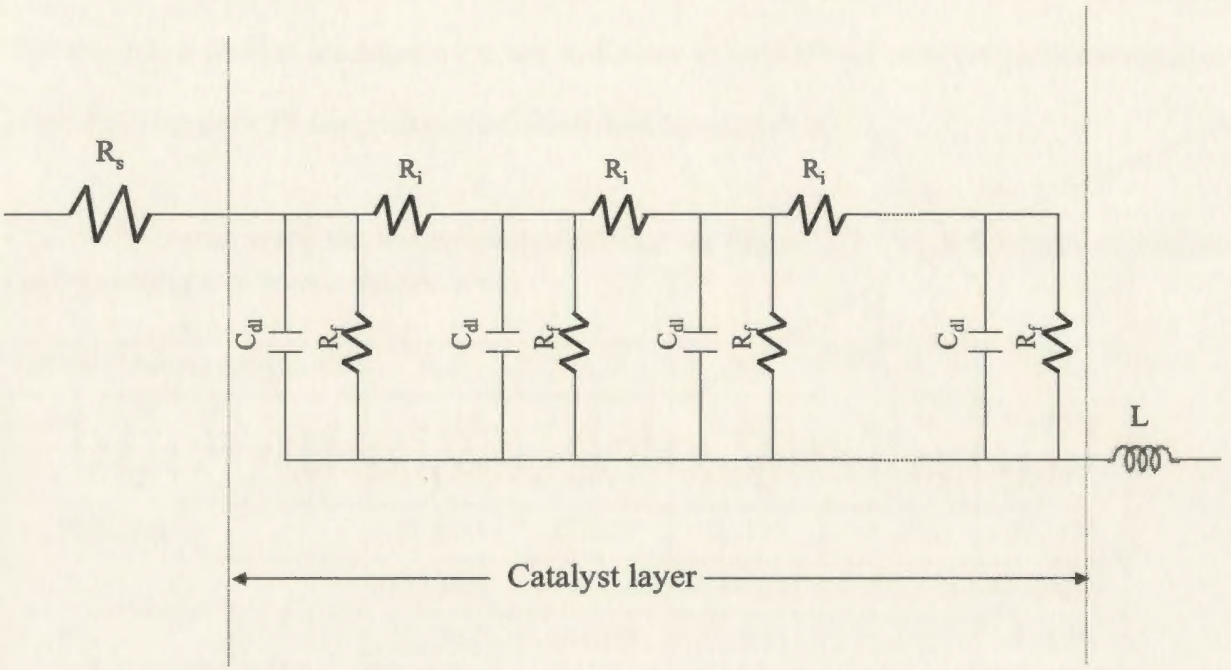

Figure 3.12. Finite transmission-line equivalent circuit describing cathode impedances.

The proposed equivalent circuit shown in Figure 3.11 was also used to explain the cathode impedance behaviour under a nitrogen atmosphere by setting R_C as infinite. The extracted parameters are listed in Table 3.5. Except for low Nafion loading cathodes (0.3 mg/cm^2 and 0.6 mg/cm^2) in the low frequency region, the fit between the experimental data and simulation data is quite good as shown in Figure 3.13. The poor fit for the low Nafion loading cathodes in the low frequency region is presumably due to the inhomogeneity of the cathode catalyst layer. A possible reason for the inhomogeneity is that these low Nafion loadings were not sufficient to bind all the catalyst particles together. Note that this poor fit can make simulation data less reliable.

Table 3.5. Parameters for the equivalent circuit in Figure 3.11 as a function of Nafion loading under a nitrogen atmosphere

Nafion loading (mg/cm^2)	0. 3	0. 6	0.9	1.2	1.5
R_s (Ω cm^2)	0. 496	0. 411	0.320	0.374	0.354
$C_{dl,C}$ (F/cm^2)	0. 00099	0. 00241	0.00287	0.00385	0.00531
W_o-R (Ω cm^2)	0. 606	0. 667	0. 306	0. 201	0. 178
W_o-T	0. 0051	0. 00820	0. 00551	0. 00338	0. 00306
W_o-P	0. 387	0. 409	0. 446	0. 452	0. 459
R_C (Ω cm^2)	infinite	infinite	infinite	infinite	infinite

Interestingly, it was found that the extracted parameters for the nitrogen atmosphere were quite close to the extracted parameters for the oxygen atmosphere (Table 3.3). This indicates that the ionic conductivity profiles (Figure 3.7) extracted under the nitrogen atmosphere represent the values in operating cells. Furthermore, it was found that there were small increases in the membrane resistance and ionic resistance, and small decreases in capacitance for the nitrogen atmosphere. These changes are reasonable since there

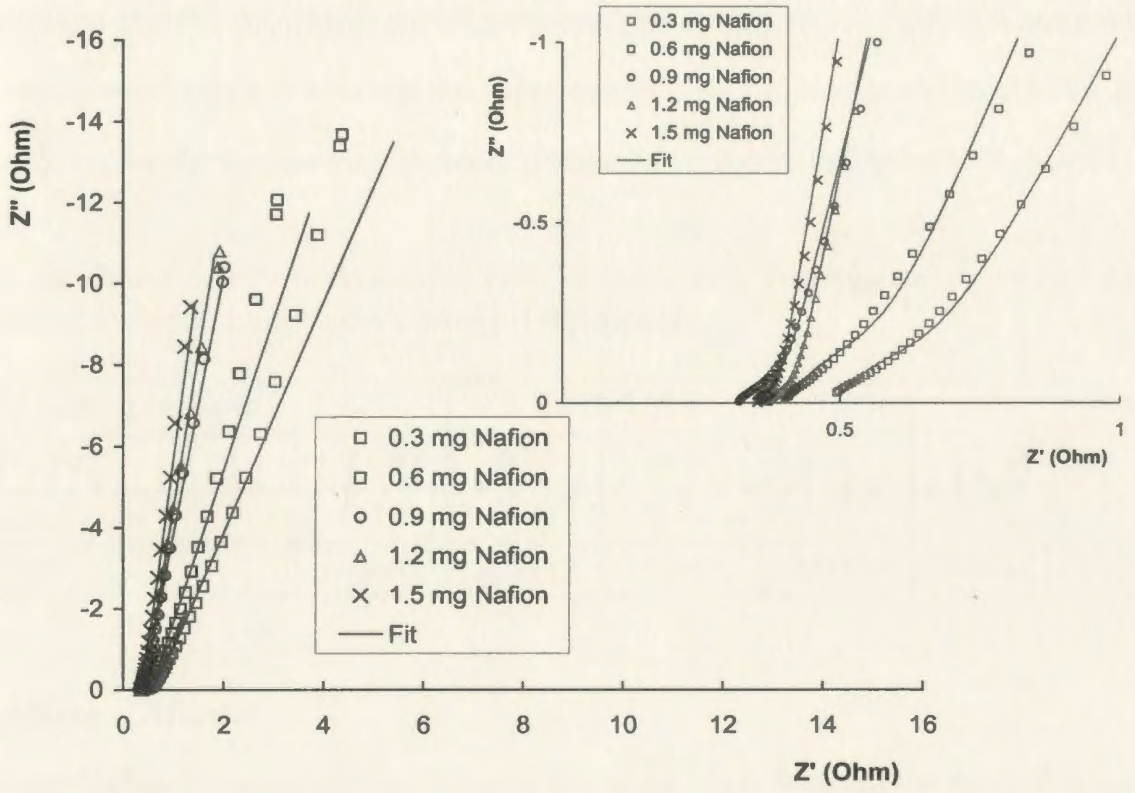

Figure 3.13. Complex plane impedance plots for nitrogen-bathed cathodes with various Nafion loadings. The inset shows an expansion of the high frequency region of the plots.

would have been a lower water content in the cathode catalyst layer under the nitrogen atmosphere.

Table 3.6 lists resistance values for the cathode catalyst layer under a nitrogen atmosphere. These values were extracted by using the finite transmission line equivalent circuit shown in Figure 3.12. It can be seen that these values are close to the resistance values extracted by using the proposed equivalent circuit shown in Figure 3.11. This again demonstrates that the equivalent circuit proposed here is reasonable. Note that there were also significant deviations between the experimental data and simulation data in the low frequency region for the low Nafion loading cathodes as shown in Figure 3.14.

Table 3.6. Resistance values for the finite transmission line equivalent circuit as a function of Nafion loading under a nitrogen atmosphere

Nafion loading (mg/cm^2)	0. 3	0. 6	0.9	1.2	1.5
R_{ionic} ($\Omega\ cm^2$)	0. 59	0. 46	0. 27	0. 17	0. 13
$R_{membrane}$ ($\Omega\ cm^2$)	0. 43	0. 35	0. 30	0. 36	0. 34
R_C ($\Omega\ cm^2$)	infinity	infinity	infinity	infinity	infinity

3.3.6 Bilayer Cathodes

Since Nafion is expensive, and balance has to be made between the ionic resistance and O_2 transport resistance in the cathode catalyst layer to ensure good cathode performance, knowledge of the effects of Nafion distribution on the cathode performance is of significant importance to optimise the performance and composition of the cathode. In order to investigate these effects, bilayer cathodes with two different Nafion gradients have been prepared. These bilayer cathodes were prepared by applying two layers of catalyst ink sequentially onto carbon fibre paper. Each layer contained 0.2 mg of Pt, and

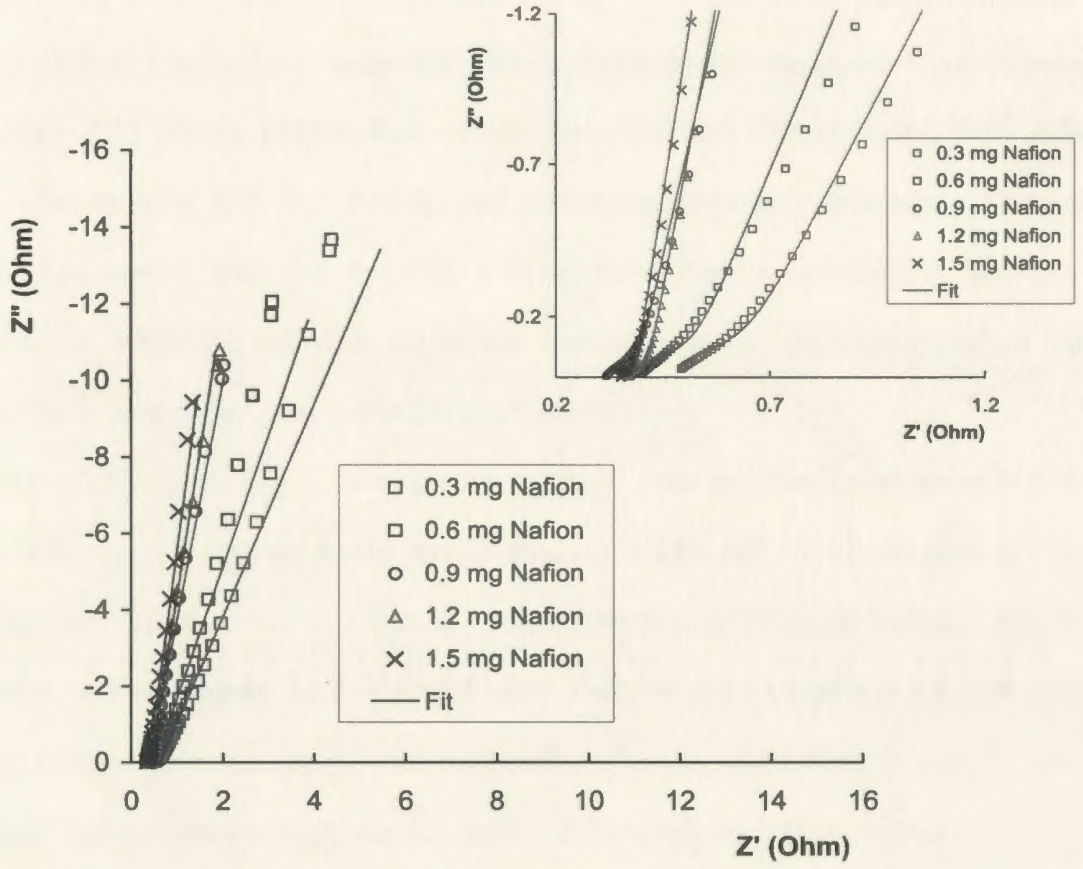

Figure 3.14. Complex plane impedance plots for nitrogen-bathed cathodes with various Nafion loadings. The inset shows an expansion of the high-frequency region of the plots. Simulation was based on the finite transmission line equivalent circuit shown in Figure 3.12.

so the total Pt loading was the same as that for the uniform layer cathodes. In one bilayer cathode, the layer adjacent to the membrane contained 0.6 mg/cm^2 of Nafion and the layer adjacent to the carbon paper contained 0.3 mg/cm^2 of Nafion. The total Nafion loading of the bilayer cathode was 0.9 mg/cm^2, the optimum value for the cathodes with uniform Nafion distributions. In another bilayer cathode, the two layers were reversed.

Figure 3.15 shows polarization curves for cells with the cathodes with different Nafion distributions. It is seen that the cell performance strongly depends on the cathode Nafion distribution, and that the cell with uniform Nafion distribution had the best performance, while the cell with the bilayer cathode that had the higher Nafion loading next to the carbon paper gave the worst performance.

Figure 3.16 shows impedance spectra for these cells at a fixed voltage of 0.8 V. The cells were operated with an anode feed of humidified H_2 and a cathode feed of O_2. It is seen that the cell with the cathode of uniform Nafion distribution had the lowest low frequency real resistance, while the cell with more Nafion adjacent to the carbon paper had the largest low frequency real resistance. This significant difference in the low frequency real resistances accounts for the big differences in cell performance.

Figure 3.17 shows ionic conductivity profiles for the cathodes with different Nafion distributions. It is seen that the bilayer cathode with more Nafion close to the membrane had the highest ionic conductivity in the region close to the membrane as expected, while the bilayer cathode with less Nafion close to the membrane exhibited the lowest conductivity and the conductivity decreased rapidly with the distance from the membrane. Theoretically, the bilayer cathode with less Nafion close to the membrane should exhibit higher conductivity in the region adjacent to the carbon paper since this region had more

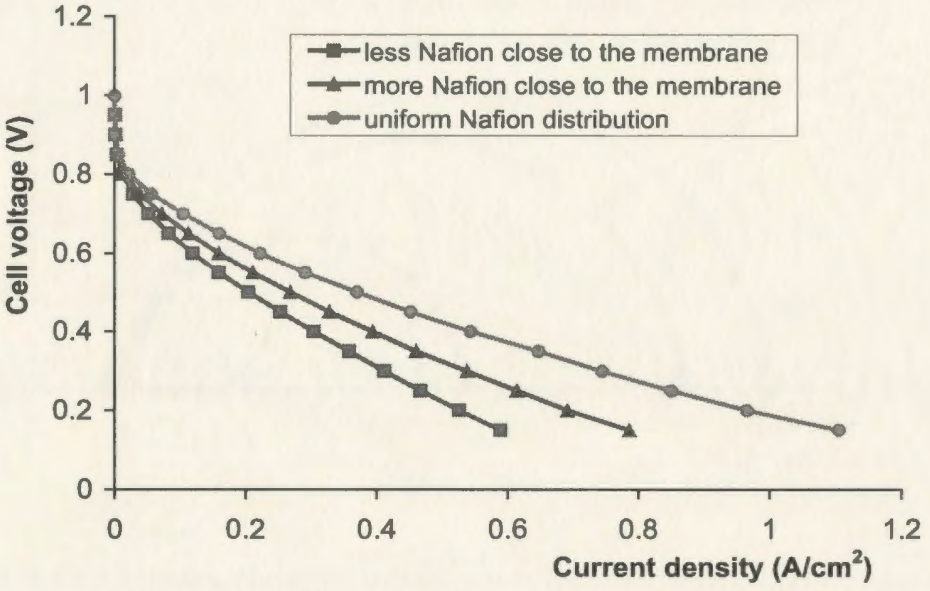

Figure 3.15. Polarization curves for cells with cathodes with different Nafion distributions. The cell was operated at ambient temperature and pressure with an anode feed of humidified H_2 and a cathode feed of O_2.

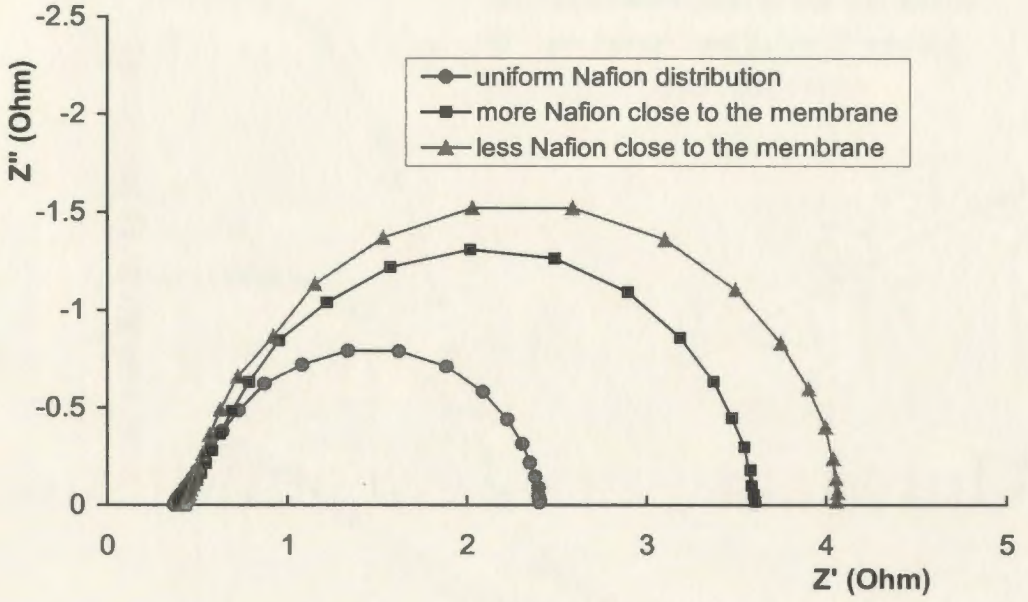

Figure 3.16. Complex plane impedance plots for cells with cathodes with different Nafion distributions at a cell voltage of 0.8 V. The cell was operated at ambient temperature and pressure with an anode feed of H_2 and a cathode feed of O_2.

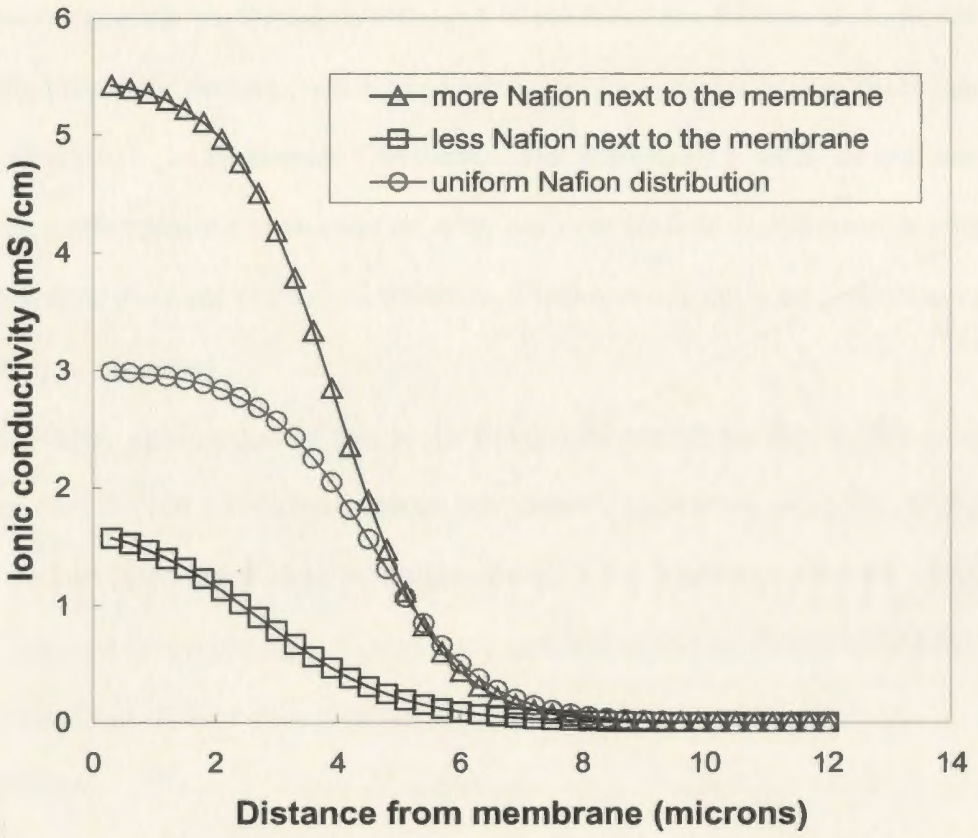

Figure 3.17. Conductivity profiles for the cathodes with different Nafion distributions. All of the electrodes contained 0.9 mg/cm^2 Nafion.

Nafion content. This discrepancy is presumably due to Nafion falling into the pores of the carbon paper.

Based on these observations, the cathode with more Nafion close to the carbon paper was not expected to give good performance. The polarization curve (Figure 3.15) supports this conclusion. However, the bilayer cathode with more Nafion close to the membrane did not show the highest performance although it exhibited the highest ionic conductivity. This suggests that other factors such as the O_2 transport resistance have a more significant influence on the cell performance. Obviously, this preliminary work is not enough to show that the performance of the cathode with uniform Nafion distribution is better than the cathode with a gradient Nafion distribution. Further work such as preparing cathodes with more layers is needed.

Recently (after publication of this work [26]), Liu and coworkers [27] reported that the optimum distribution of Nafion content is a linearly increasing function of coordinate x from the carbon fibre paper side to the membrane side. Their results were obtained by simulation. Obviously, preparing cathodes with multiple layers of different Nafion content is a good method to test their assertion.

3.4 Conclusions

The polarization measurements reported here clearly show that Nafion contents and distribution in the cathode catalyst layer have a strong influence on cell performance. It was also found that there is an optimum Nafion loading of 0.9 mg/cm^2 in the cathode catalyst layer for the best cell performance. A preliminary study also showed that a cathode with uniform Nafion distribution had better performance than cathodes with uneven Nafion distributions.

Impedance spectroscopy has been shown to be a powerful diagnostic tool to analyse

cell performance and it can provide valuable information for optimisation of cathode performance and composition. This technique unveiled that the optimum Nafion loading for the best cell performance is due to the fact that a balance has to be made between the ionic conductivity and O_2 transport resistance.

Finally, the excellent fit between the experimental data and the simulation shows that the finite transmission-line equivalent circuit and the proposed equivalent circuit are suitable to explain cathode impedance behaviour. The extracted conductivity profiles and resistance values are reasonable and they can provide insights into the understanding of cathode behaviour.

3.5 References

[1] L. Carrette, K.A. Friedrich, and U. Stimming, Chemphyschem. 1 (2000) 162.

[2] D. G. Lovering, J. Power Sources 86 (2000) 1.

[3] G. J. K. Acres, J. Power Sources 100 (2001) 60.

[4] J. A. Kerres, J. Membrane Sci. 185 (2001) 3.

[5] S. Y. Cha and W. M. Lee, J. Electrochem. Soc. 146 (1999) 4055.

[6] F. Lufrano, E. Passalacqua, G. Squadrito, A. Patti, and L. Giorgi, J. Appl. Electrochem. 29 (1999) 445.

[7] M. S. Wilson and S. Gottesfeld, J. Electrochem. Soc. 139 (1992) L28.

[8] F. Jaouen, G. Lindbergh, and G. Sundholm, J. Electrochem. Soc. 149 (2002) A437.

[9] J. Fleig and J. Maier, J. Electrochem. Soc. 144 (1997) L302.

[10] T. E. Springer, M. S. Wilson, and S. Gottesfeld, J. Electrochem. Soc. 140 (1993) 3513.

[11] V. A. Paganin, E. A. Ticianelli, and E. R. Gonzalez, J. Appl. Electrochem. 26 (1996) 297.

[12] O. Antoine, Y. Bultel, P. Ozil, and R. Durand, Electrochim. Acta 45 (2000) 4493.

[13] E. Passalacqua, F. Lufrano, G. Squadrito, A. Patti, and L. Giorgi, Electrochim. Acta 43 (1998) 3665.

[14] E. B. Easton, Z. Qi, A. Kaufman, and P. G. Pickup, Electrochem. Solid. State. Lett. 4 (2001) A59.

[15] I. D. Raistrick, in Diaphragms, Separators, and Ion Exchange Membranes, J. W. Van Zee, R. E. White, K. Kinoshita, and H. S. Burney, Eds., Electrochemical Society, Pennington, NJ, 1986, p172.

[16] S. J. Lee, S. Mukerjee, J. McBreen, Y. W. Rho, Y. T. Kho, and T. H. Lee, Electrochim. Acta 43 (1998) 3693.

[17] T. E. Springer, T. A. Zawodzinski, and S. Gottesfeld, J. Electrochem. Soc. 138 (1991) 2334.

[18] T. E. Springer and I. D. Raistrick, J. Electrochem. Soc. 136 (1989) 1594.

[19] E. Passalacqua, F. Lufrano, G. Squadrito, A. Patti, and L. Giorgi, Electrochim. Acta 46 (2001) 799.

[20] T. E. Springer, T. A. Zawodzinski, M. S. Wilson, and S. Gottesfeld, J. Electrochem. Soc. 143 (1996) 587.

[21] M. C. Lefebvre, R. B. Martin, and P. G. Pickup, Electrochem. Solid-State Lett. 2 (1999) 259.

[22] V. A. Paganin, C. L. F. Oliveira, E. A. Ticianelli, T. E. Springer, and E. R. Gonzalez, Electrochim. Acta 43 (1998) 3761.

[23] M. Ciureanu and R. Roberge, J. Phys. Chem. B. 105 (2001) 3531.

[24] A. J. Bard and L. R. Faulkner, Electrochemical Methods. Fundamentals and Applications, 2 nd ed. Wiley, New York, 2001.

[25] N. Jia, R. B. Martin, Z. Qi, M. C. Lefebvre, and P. G. Pickup, Electrochim. Acta 46 (2001) 2863.

[26] G. Li and P. G. Pickup, J. Electrochem. Soc.150 (2003) C745.

[27] D. Song, Q. Wang, Z. Liu, M. Eikerling, Z. Xie, T. Navessin, and S. Holdcroft, Electrochim. Acta 50 (2005) 3347.

[28] R. Makharia, M. F. Mathias, and D. R. Baker, J. Electrochem. Soc. 152 (2005) A970.

[29] Z. Poltarzewski, P. Staiti, V. Alderucci, W. Wieczorek, and N. Giordano, J. Electrochem. Soc. 139 (1992) 761.

[30] K. E. Swider and D. R. Rolison, J. Electrochem. Soc. 143 (1996) 813.

[31] A. Essalik, K. Amouzegar, and O. Savadogo, J. Appl. Electrochem. 25 (1995) 404.

[32] E. A. Ticianelli, C. R. Derouin, and S. Srinivasan, J. Electroanal. Chem. 251 (1988) 275.

[33] A. Pozio, M. De Francesco, A. Cemmi, F. Cardellini, and L. Giorgi, J. Power Sources 105 (2002) 13.

[34] J. Shan and P. G. Pickup, Electrochim. Acta 46 (2000) 119.

[35] M. Neergat and A. K. Shukla, J. Power Sources 104 (2002) 289.

[36] S. Srinivasan, D. J. Manko, H. Koch, M. A. Enayetullah, and A. J. Appleby, J. Power Sources 29 (1990) 367.

[37] Y. W. Rho, O. A. Velev, S. Srinivasan, and Y. T. Kho, J. Electrochem. Soc. 141 (1994) 2084.

[38] N. Wagner, in Impedance Spectroscopy, E. Barsoukov and J. R. Macdonald, Editors, 497-537, John Wiley & Sons, Inc. New Jersey, (2005).

Chapter 4 Development of Reference Electrodes for Thin Layer Polymer Electrolyte Fuel Cells

4.1 Introduction

Thin layer polymer electrolyte fuel cells, such as hydrogen fuel cells and direct methanol fuel cells, have been the focus of intensive study in recent years as promising alternative energy sources [1-2]. However, their performances are still far from ideal for commercialization. Knowledge of individual electrode behavior in an operating cell is crucial for improving cell performance, and this can only be acquired by using a reference electrode [3-4]. Commercial reference electrodes, such as SCE and Ag/AgCl reference electrodes, are obviously too big to be fitted into a thin layer cell. So a stable reference electrode that is suitable for electrochemical studies of thin layer cells is strongly needed.

The requirement for designing a reference electrode for a three-electrode cell configuration is that the cell geometry should ensure a uniform current density at the working electrode; otherwise, different regions of the working electrode will experience different potentials, and therefore, the measured data may be misleading [5]. The placement of a reference electrode in the thin layer cell strongly affects the results of electrochemical measurements. The reference electrode should be placed in the uniform potential region as shown in Figure 4.1. The distance between the reference electrode and the active electrodes of the cell should be at least three times the thickness of the polymer electrolyte layer in order to avoid potential gradients along the electrolyte surface and make the measurement insensitive to the exact location of the reference electrode [6]. The potential in the uniform potential region is a half of the potential drop between the active electrodes [6], and this means that the resistance between the active electrode and the

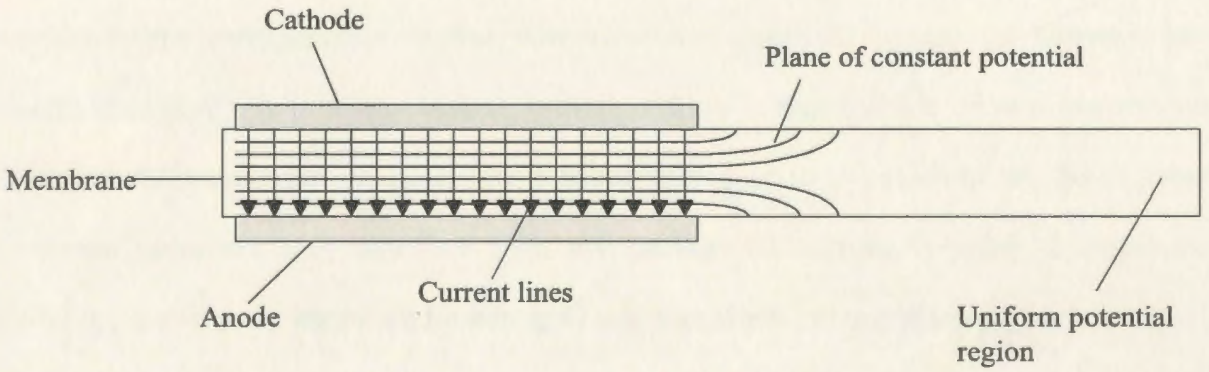

Figure 4.1. A schematic diagram of potential gradients in a thin layer polymer electrolyte cell.

reference electrode is a half of the resistance between the two active electrodes for the uniform electrolyte.

Another requirement for meaningful electrochemical measurements on thin layer cells is that the cathode and anode should be perfectly aligned with each other in a symmetric configuration to avoid uneven current distributions [5-6]. Even with perfect alignment, there will still be minor current dependent errors in the measured potentials due to differences in the potential dependencies of the electrode overpotentials [7].

Generally, two different reference electrode configurations have been used for the electrochemical study of thin layer cells: sandwich-type and edge-type. In the sandwich-type configuration, a fine wire reference electrode is inserted between two membranes [8-9]. A problem with this configuration is that the use of two membranes increases the membrane resistance by a factor of two or more. In addition, the inserted reference electrode may interfere with the passage of current between the working electrode and counter electrode, resulting in a non-uniform current distribution.

In the edge-type configuration, the reference electrode has normally been attached to an exposed strip of the polymer electrolyte [10-11]. For this configuration, special measures must be taken to maintain the hydration of the exposed polymer electrolyte, since the exposed electrolyte quickly becomes dehydrated. In addition, the cell can be custom designed to accommodate the reference electrode into the cell, and commercial versions are available.

The dynamic hydrogen electrode (DHE) has been shown to be suitable for use as a reference electrode [12]. In a DHE, hydrogen is produced at the working electrode of the DHE by a small cathodic current such that the coverage of hydrogen on the electrode can be considered constant, resulting in a stable potential. Advantages of the DHE include

minimal contamination of the measured system and no need for a salt bridge [10]. Kuver and coworkers [10] have used a DHE as a reference electrode to resolve the polarization of a direct methanol fuel cell into individual electrode polarization curves. In their configuration, the working electrode and counter electrode of the DHE were bonded onto each side of the exposed Nafion membrane and hydrogen was produced at the working electrode by a small cathodic current. A serious potential drift was observed for their DHE reference electrode at high current densities. This was explained by the authors as being due to an extreme change in proton activity in the vicinity of the reference electrode, caused by current density-dependent electro-osmotic drag of water across the membrane, which would promote dehydration of the exposed Nafion membrane.

In this chapter, a novel reference electrode configuration for the electrochemical study of thin layer polymer electrolyte fuel cells is presented. The validity of data obtained with the reference electrode has been confirmed by a variety of methods in hydrogen fuel cells and direct methanol fuel cells. It was found that the reference electrode was quite stable, and with its aid, the performances of operating fuel cells have been resolved into the individual electrode behaviors.

4.2 Experimental

4.2.1 Chemicals and Materials

Nafion 115 and 117 membranes were cleaned following the procedure described in section 2.1. Poly(vinyl chloride) (M_w ca. 60,000, Aldrich), 100 μm diameter Pt wire (Aldrich), and all other chemicals and materials were used as received.

4.2.2 Cells and Electrodes

A 1 cm^2 locally made fuel cell and a 5 cm^2 commercial cell (Fuel Cell Technology) were used as the hydrogen fuel cells. For the hydrogen fuel cell, both the anode and the

cathode (4 mg/cm^2 Pt black on carbon paper) were provided by Ballard Power Systems. The 5 cm^2 cell was also used as the direct methanol fuel cell. For the direct methanol fuel cell, the anode (4.5 mg/cm^2 Pt/Ru (1:1) on carbon paper) was provided by H Power Corp., while the cathode was the same as that used in the hydrogen fuel cell.

4.2.3 Preparation of MEAs

For the hydrogen fuel cell, membrane and electrode assemblies (MEAs) were prepared by hot pressing the cathode and the anode onto each side of a Nafion 115 membrane at a pressure of 200 kg/cm^2 at 135 °C for 90 s, while for the direct methanol fuel cell, a Nafion 117 membrane was used. In addition, two Nafion 115 membranes were used for experiments in the sandwich-type configuration. The electrodes and the membrane were fixed in a stainless steel die before being put into the press. This provides alignment between the cathode and the anode, with a variation of < 0.1 mm.

4.2.4 Electrochemistry

The voltage and impedance measurements of the fuel cell were made in a two-electrode (cathode *vs* anode) mode. For a H_2 cell in this mode, the anode serves as a pseudoreference electrode and counter electrode. Individual anode and cathode potentials and impedances were made in a three-electrode mode using a reference electrode. When the fuel cell anode was used as the working electrode, the cathode was used as the counter electrode, and vice versa.

Measurements were made with a Solartron 1286 electrochemical interface and 1250 frequency response analyzer. Impedance measurements were conducted with a perturbation amplitude of 5 mV over a frequency range of 65 KHz to 0.1 KHz for the constant applied potential mode, while for the constant applied current mode, a perturbation amplitude of 10 mA was used.

4.2.5 Configuration of the Reference Electrodes

Figure 4.2a shows a schematic diagram of a thin layer cell with a DHE reference electrode. The working electrode and counter electrode of the DHE were placed on the cathode side of an outer section of the Nafion membrane and sandwiched between the two halves of the body of the cell. The distance between the thin Pt wire (100 μm diameter) electrodes of the DHE and the edge of the active electrodes of the fuel cell was always much larger than three times the thickness of the membrane to avoid potential gradients. A small current of typically ca. 6×10^{-5} A was passed between the two Pt wires to maintain the hydrogen coverage on the cathode, which was used as the DHE. Except for the two ends, the fine Pt wires were insulated with a thin coating of poly(vinyl chloride) (coating was accomplished by dipping the Pt wire into the THF solution of poly(vinyl chloride)). The current to the DHE was supplied by a 9 V battery and controlled by adjusting the series resistance with a resistance box. Before measurements, the cell was fed with hydrogen on the anode and the potential of the reference electrode was set to zero with respect to the hydrogen anode by changing the series resistance.

In addition, a sandwich-type configuration was also investigated in which the reference electrode was sandwiched between two membranes as shown in Figure 4.2b. It was found that the membrane resistance of the sandwich-type cell was higher than two times the resistance of one membrane. This was presumably due to the interfacial resistance between the two membranes where they were hot-pressed together.

4.3 Results and Discussion

An ideal reference electrode should be reversible and obey the Nernst equation at zero current. It also should be stable with time and its potential should return to the

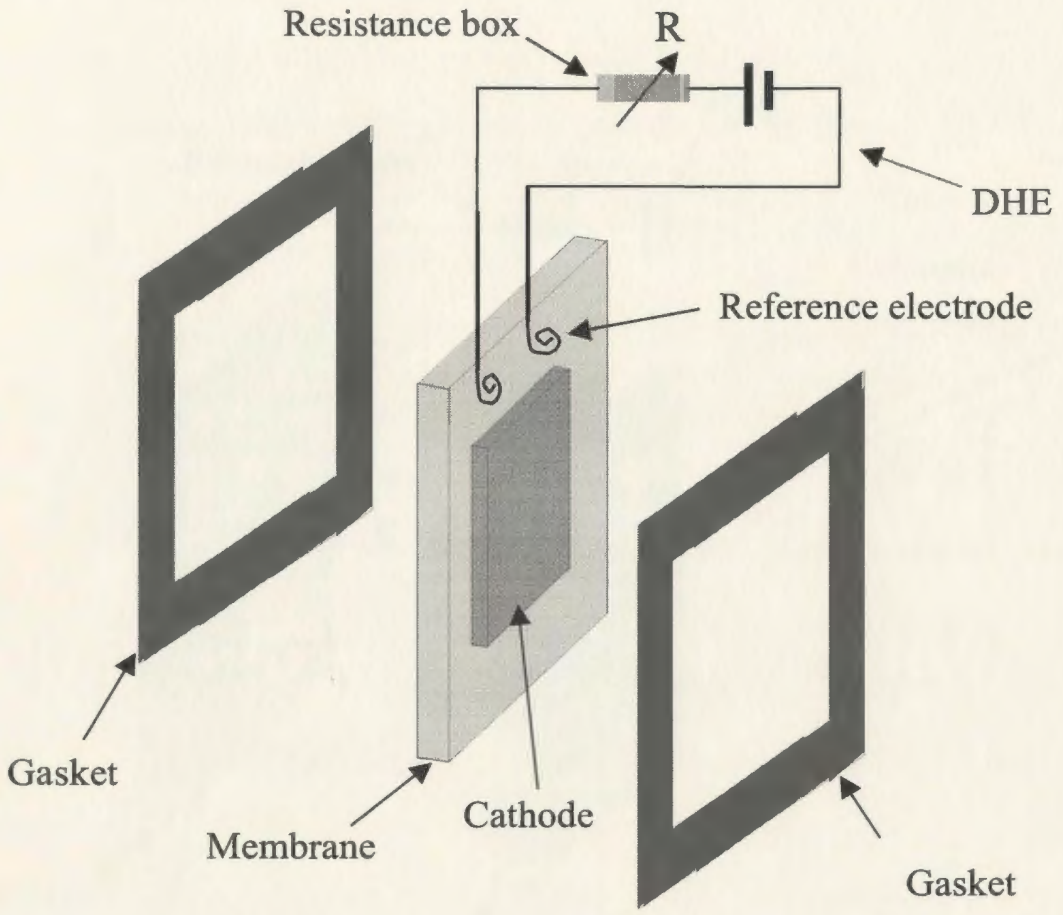

Figure 4.2a. Schematic diagram of a cell with an edge-type DHE reference electrode.

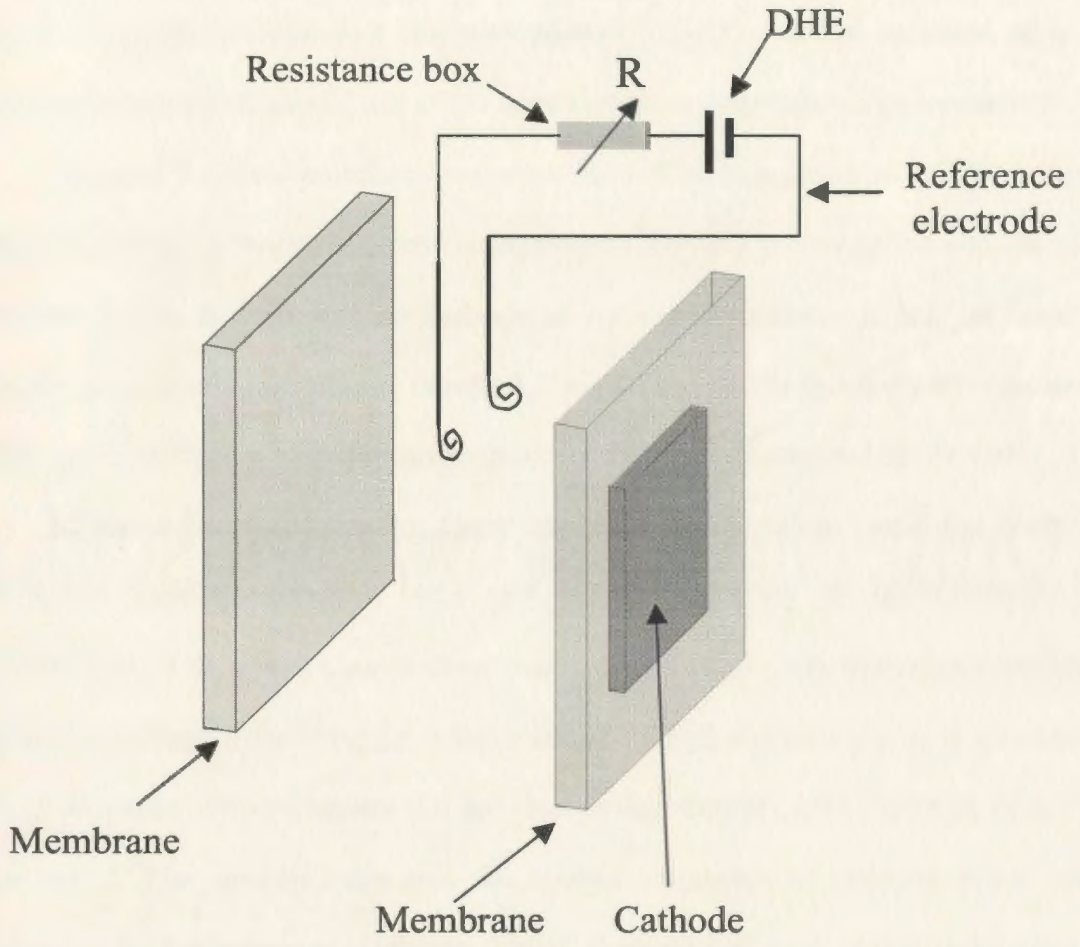

Figure 4.2b. Schematic diagram of a cell with a sandwich-type DHE reference electrode.

original value if perturbed by a current. In addition, it should be insensitive to a small change of temperature [13]. Based on these criteria, a variety of methods have been used to evaluate the DHE reference electrode used in this work.

4.3.1 Influence of the Reference Electrode on the Cell

Polarization measurements and impedance spectroscopy are the most widely used methods to characterize fuel cell performance [14-15]. Ideally, insertion of a reference electrode into a cell should not affect polarization or impedance measurements.

Figure 4.3 shows polarization curves for a 5 cm^2 commercial cell with and without insertion of the reference electrode (edge-type). The cell was supplied with humidified H_2 on the anode and air on the cathode at room temperature. It can be seen that two polarization curves are almost identical. This indicates that the cell performance does not change significantly with the insertion of the reference electrode into the cell.

Figure 4.4 shows complex plane impedance plots for a 5 cm^2 commercial cell at different applied potentials with and without insertion of the reference electrode (edge-type). The results clearly show that insertion of the reference electrode into the cell does not influence the impedance behavior of the cell significantly. It is also seen that the high frequency real resistance did not change significantly after insertion of the reference electrode. This demonstrates that the contact resistance of the cell is not affected by insertion of the reference electrode. The unchanged cell contact resistance after insertion of the reference electrode results from the fact that the fine Pt wire reference electrode was pressed into the soft Nafion membrane when the cell was assembled.

4.3.2 Reversibility of the Reference Electrodes

The reversibility of a reference electrode can be investigated by cyclic voltammetry. Figure 4.5a shows a cyclic voltammogram for a DHE reference electrode with respect to

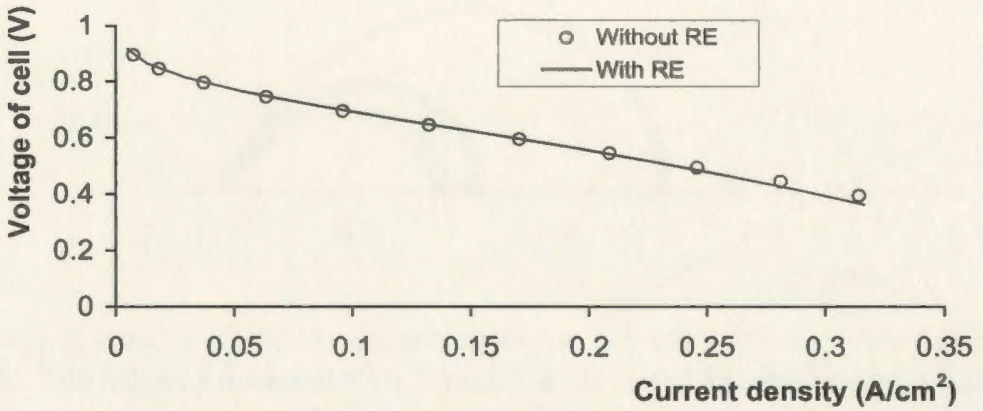

Figure 4.3. Polarization curves for a 5 cm^2 cell with and without insertion of a RE (edge-type). The cell was operated with humidified H_2 on the anode and air on the cathode at ambient temperature and pressure.

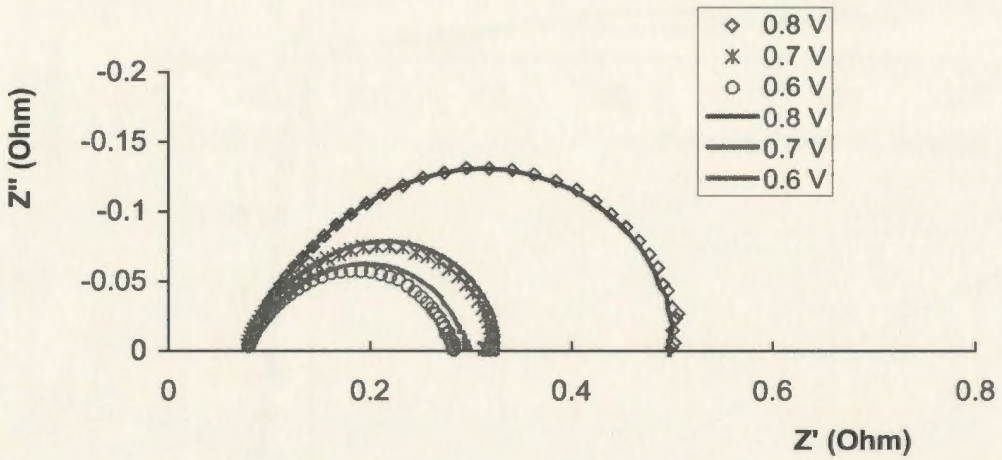

Figure 4.4. Complex plane impedance plots for a 5 cm^2 cell as a function of applied potential. The cell was operated with humidified H_2 on the anode and air on the cathode at ambient temperature. Symbols: without a RE; Solid line: with an RE (edge-type).

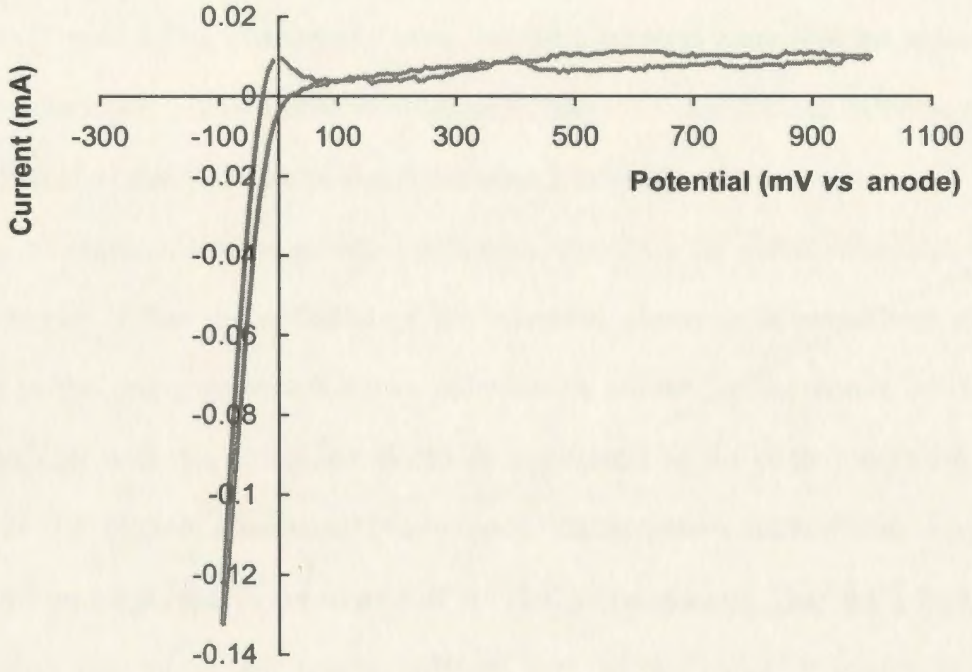

Figure 4.5a. A cyclic voltammogram for the DHE *vs* the fuel cell anode of a 5 cm^2 cell (edge-type). The cell was operated with humidified H_2 on the anode and N_2 on the cathode (counter electrode) at ambient temperature and pressure.

the hydrogen anode of a 5 cm^2 cell at open circuit (edge-type). The cell was operated with humidified hydrogen on the anode and nitrogen on the cathode at ambient temperature and pressure. It is seen that the cathodic current of the DHE reference electrode rises sharply with small changes of potential, approximating a non-polarized electrode. A similar voltammogram was also observed for the sandwich-type configuration reference electrode (Figure 4.5b). The steeply rising cathodic currents mean that the potential of the reference electrode will be stable to small perturbations of the applied cathodic current.

4.3.3 Effect of the Position of the Reference Electrode

One of requirements of an ideal reference electrode for electrochemical study of a thin layer cell is that the potential of the reference electrode is insensitive to its exact position in the cell. Figure 4.6 shows polarization curves for the anode (*vs* DHE) of a hydrogen cell with the reference electrode positioned at different places on the outer region of the Nafion membrane (edge-type). These places include the upper corner, middle of one edge, and lower corner of the Nafion membrane. The small changes in the polarization curves of the anode indicate that its measured potential is relatively insensitive to the position of the reference electrode.

Figure 4.7 shows the anode polarization curves for a hydrogen cell with a reference electrode positioned at different distances from the edge of the active electrodes of the cell. The distance between the reference electrode and the edge of the active electrodes of the cell was 0.2 and 1 cm, respectively, both of which are much larger than three times the thickness of the Nafion 115 membrane (ca. 0.1 mm). The similar anode performances demonstrate that the potential of the reference electrode and the anode overpotential are insensitive to this distance. The insensitivity of the measured anode potential to the distance between the reference electrode and the edge of active electrodes of the cell is

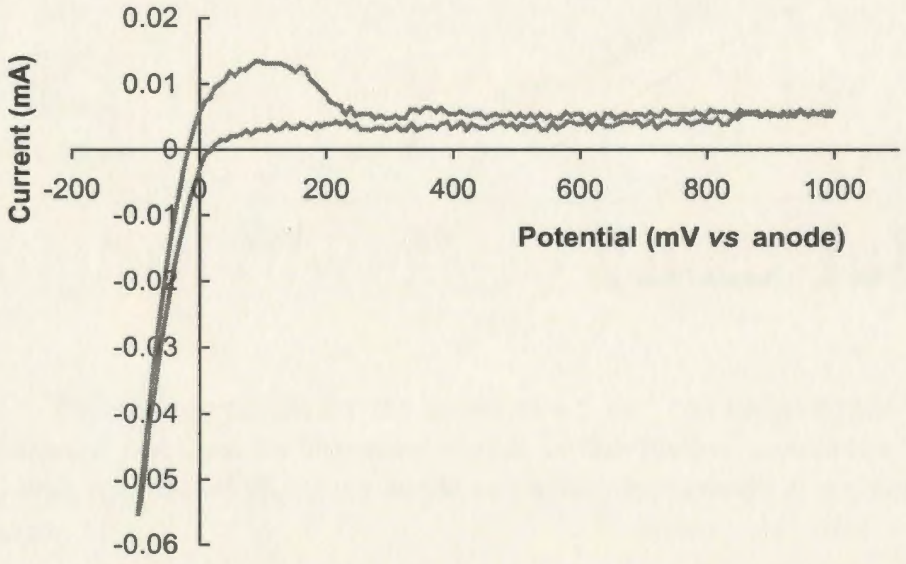

Figure 4.5b. A cyclic voltammogram for the DHE *vs* the fuel cell anode of a 5 cm^2 cell (sandwich-type). The cell was operated with humidified H_2 on the anode and N_2 on the cathode (counter electrode) at ambient temperature and pressure.

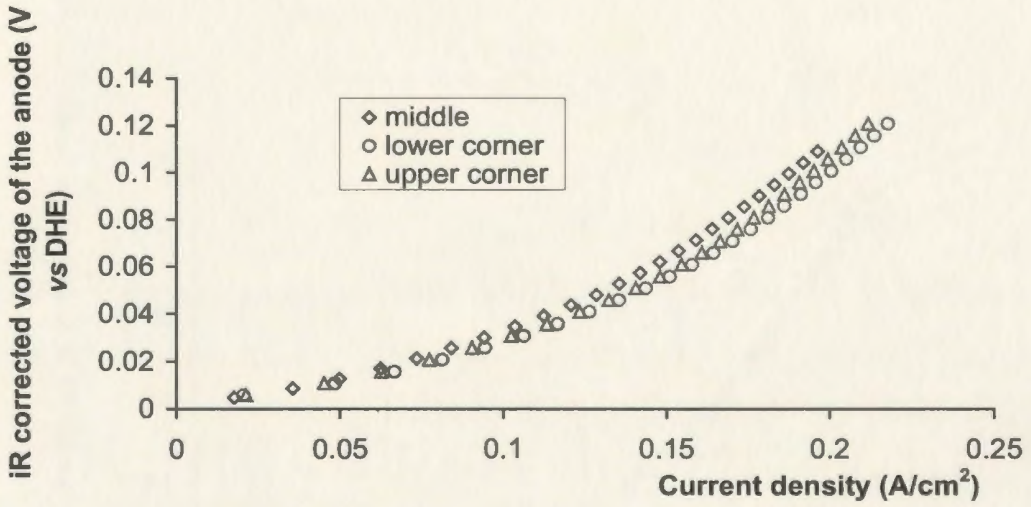

Figure 4.6. Polarization curves for the anode of a 5 cm^2 cell (edge-type). The DHE was put at different positions on the outer region of the Nafion membrane. The cell was operated with humidified H_2 on the anode and air on the cathode at ambient temperature and pressure.

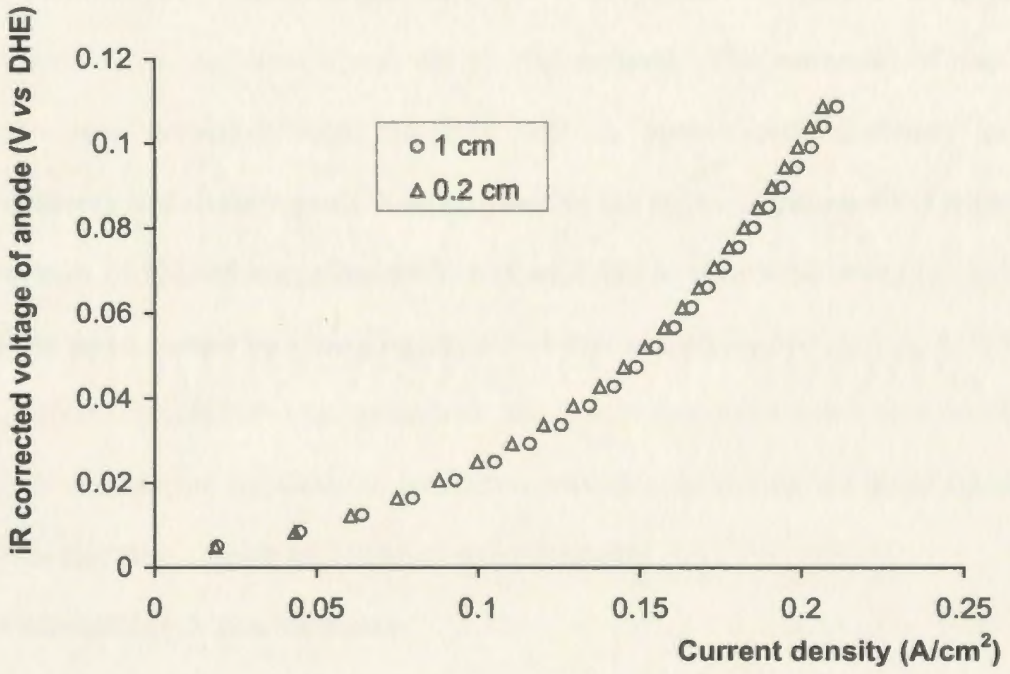

Figure 4.7. Polarization curves for the anode of a 5 cm^2 cell. The DHE was put at different positions from the edge of active electrodes of the cell. The cell was operated with humidified H_2 on the anode and air on the cathode at ambient temperature and pressure.

due to the uniform potential in this region of the membrane when this distance is much larger than three times the thickness of the membrane [6].

The insensitivity of the anode potential to the above positions also suggests good alignment of the cathode and anode in this MEA, since misalignment of the electrodes can lead to large variations in measured potentials with different positions [7].

4.3.4 Stability of the Reference Electrode

The potential of a DHE reference electrode with respect to the anode of a 5 cm^2 commercial cell during polarization measurements was monitored with a high impedance digital voltammeter. The hydrogen fuel cell was operated at ambient temperature with humidified H_2 on the anode and air on the cathode. The potential of the reference electrode was recorded with the fuel cell at open circuit between polarization measurements at decreasing cell voltages. Before the series of polarization measurements, the potential of the reference electrode was adjusted to zero with respect to the anode of the cell at open circuit by changing the series resistance (R). No drift of the potential of the reference electrode was observed for both the edge-type and sandwich-type configurations during polarization measurements, demonstrating the good stability of the reference electrode during polarization measurements.

4.3.5 Polarization Measurements

The validity of reference electrodes can be tested by polarization measurements. The polarization curve of a cell should equal the difference between the individual polarization curves of the cathode *vs* the reference electrode and anode *vs* the reference electrode. This will obviously be the case if the three potentials are measured simultaneously, but drifting of the reference potential could cause discrepancies, if the anode and cathode polarizations are measured at different times. Thus, in order to test the

stability of the reference electrode, the cell polarization and the anode potentials *vs* the reference electrode were measured simultaneously and then the cell polarization and the cathode potentials *vs* the reference electrode were measured simultaneously. As shown in Figure 4.8, the polarization curves of the cell for the two sets of measurements are almost identical and also close to the cathode potentials – the anode potentials (*vs* DHE). It can be concluded that the potential of the reference electrode is stable during individual electrode polarization measurements. In addition, for the sandwich-type configuration, the polarization of the cell, the anode *vs* the reference electrode, and the cathode *vs* the reference electrode were measured separately. As shown in Figure 4.9, the polarization curves of the cell are quite close to the difference between the polarization curves of the anode *vs* the reference electrode, and the cathode *vs* the reference electrode. This indicates the stability of the reference electrode.

The validity of the reference electrode can also be tested by comparing the potentials obtained with respect to different reference electrodes. Theoretically, after iR correction, the polarization curves of the anode of a direct methanol cell should be the same when measured with respect to the DHE reference electrode and the cathode when it is fed with H_2, respectively, assuming that the hydrogen fed cathode behaves as a reversible hydrogen electrode. iR correction is needed here since the Ohmic resistance between the anode and the DHE is much smaller than that between the anode and the cathode. The iR correction was accomplished by subtracting iR values from individual points on the polarization curve, where R is the membrane + cell contact resistance, which can be determined by impedance spectroscopy at high frequency [14].

Figure 4.10 shows polarization curves for the anode of a direct methanol fuel cell with respect to a DHE reference electrode and a hydrogen fed cathode, respectively. The

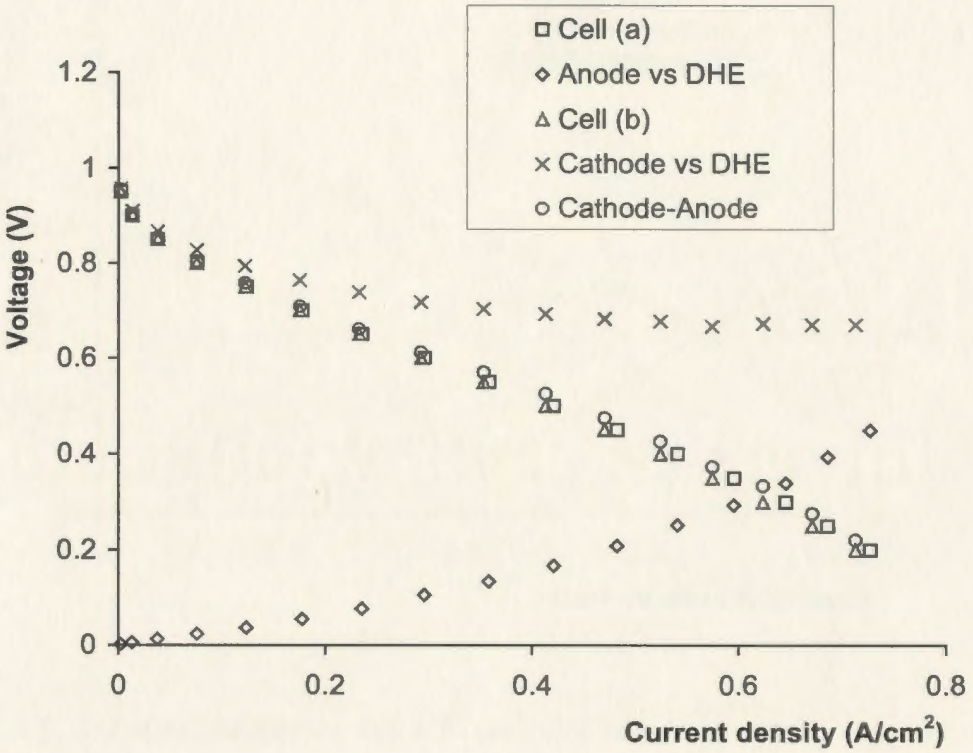

Figure 4.8. Polarization curves for a 1 cm^2 cell, together with anode potentials *vs* DHE and the cathode potentials *vs* DHE (edge-type). The cell was operated with an anode feed of H_2 humidified at 60 °C and a cathode feed of O_2 at ambient temperature and pressure.

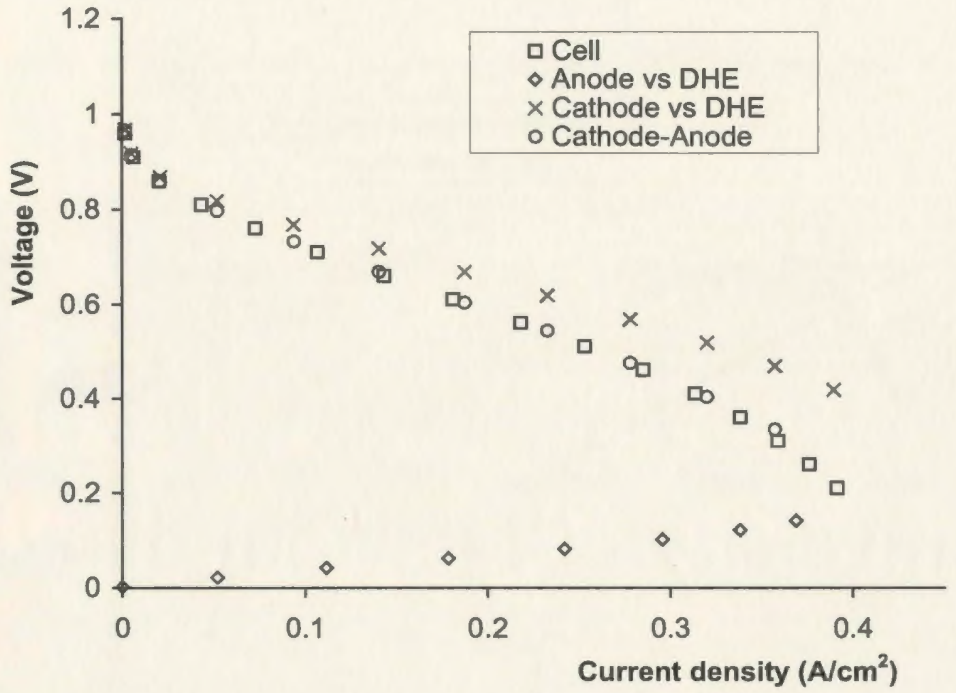

Figure 4.9. Polarization curves for a 5 cm^2 cell (sandwich-type), together with anode potentials *vs* DHE and cathode potentials *vs* DHE. The cell was operated with an anode feed of humidified H_2 and a cathode feed of O_2 at ambient temperature and pressure.

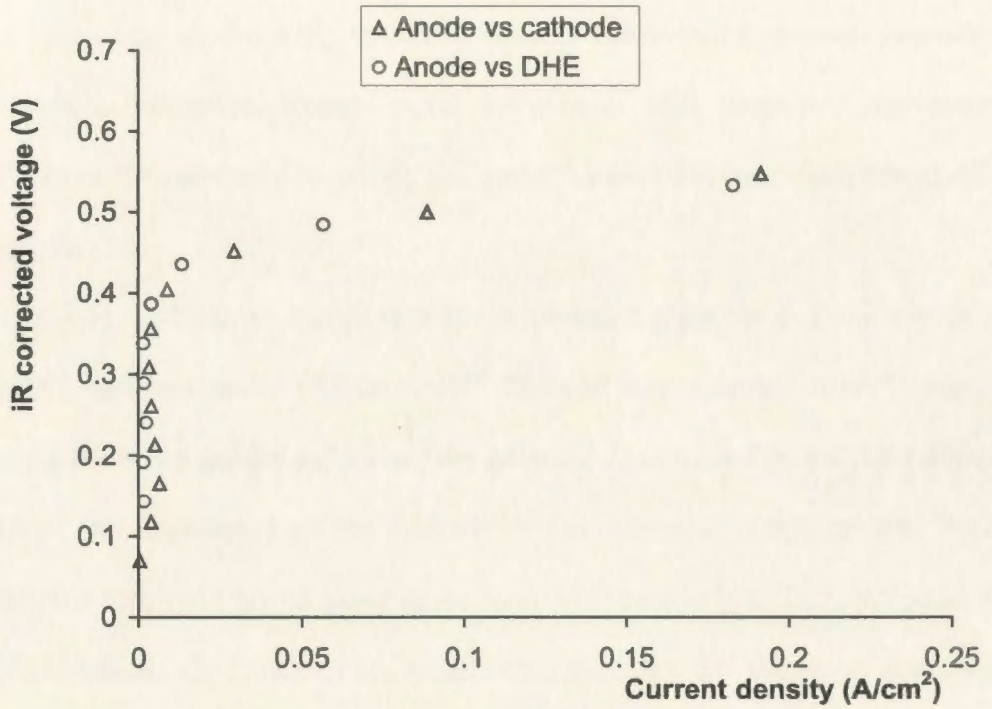

Figure 4.10. Polarization curves for the anode of a 5 cm^2 direct methanol fuel cell (edge-type) with respect to different reference electrodes. The cell was operated at 60 °C with an anode feed of 1 M methanol(aq) and a cathode feed of humidified H_2.

cell was operated with 1 M aqueous methanol on the anode and humidified H_2 on the cathode. The closeness of the two polarization curves after iR correction again illustrates the stability of the reference electrode.

4.3.6 Impedance Spectroscopy

If the reference electrode is stable, the impedance of a cell (cathode *vs* anode) should equal the sum of the impedance of the cathode *vs* the reference electrode and the anode *vs* the reference electrode at a constant current density [9]. Furthermore, the high frequency real resistance of the cell, which represents the sum of the cell contact and polymer electrolyte resistances, should equal the sum of high frequency real resistances of the cathode *vs* the reference electrode and anode *vs* the reference electrode at different current densities [11].

Figure 4.11 shows complex plane impedance plots for a 5 cm^2 direct methanol fuel cell at a current density of 0.04 A/cm^2. The cell was operated at 60 °C with 1 M aqueous methanol on the anode and air on the cathode. It is seen that the cell impedance and the sum of the impedance of the cathode *vs* the reference electrode and the anode *vs* the reference electrode are in good agreement with each other. This indicates the validity of the reference electrode. The small disagreement in the low frequency region is presumably due to the production of CO_2 bubbles within the anode, which creates turbulence in methanol transport to the anode catalyst.

Figure 4.12 shows complex plane impedance plots for a hydrogen fuel cell. It can be seen that the cell impedance matches quite well with the sum of the impedance of the cathode *vs* the reference electrode and the anode *vs* the reference electrode. This again demonstrates the validity of the reference.

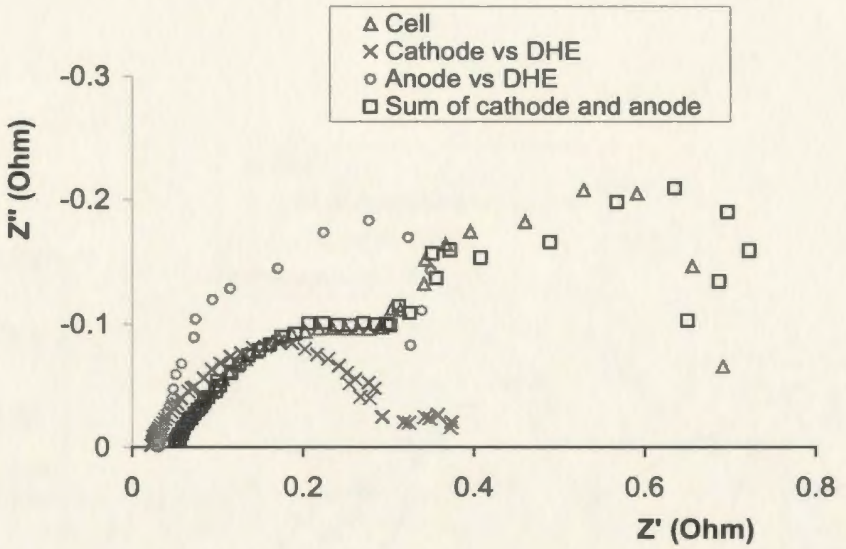

Figure 4.11. Complex plane impedance plot for a 5 cm^2 direct methanol fuel cell, together with anode and cathode complex plane impedance plots *vs* DHE at a current density of 0.04 A/cm^2. The cell was operated with 60 °C 1 M aqueous methanol on the anode and air on the cathode.

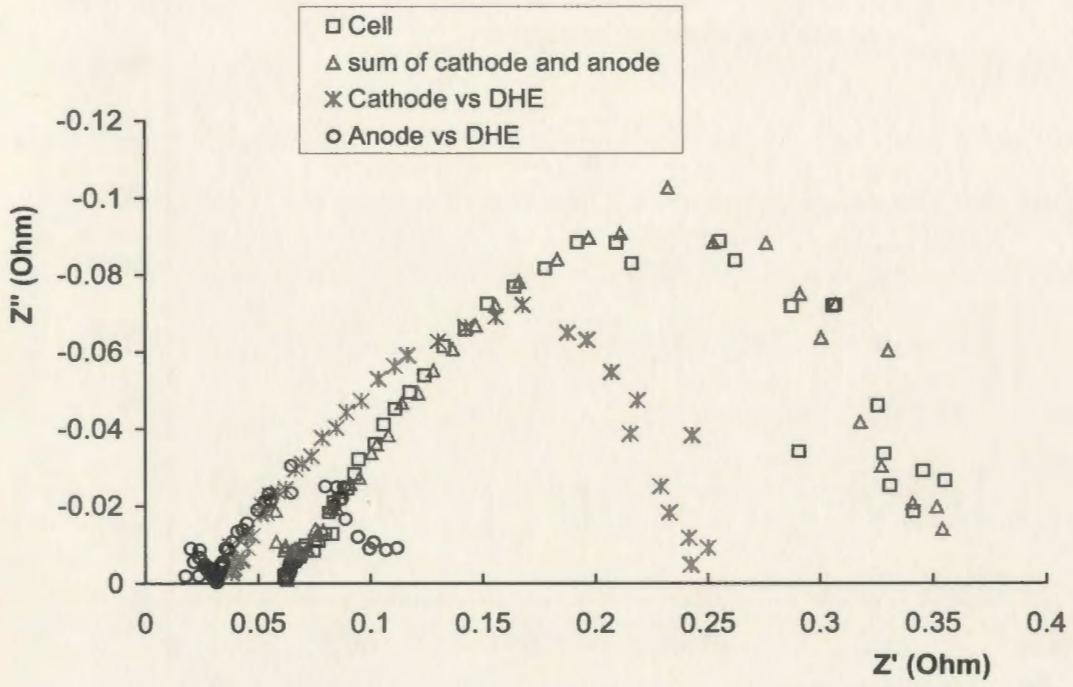

Figure 4.12. Complex plane impedance plot for a 5 cm^2 cell, together with cathode and anode complex plane impedance plots *vs* DHE at a current density of 0.2 A/cm^2. The cell was operated with humidified H_2 on the anode and air on the cathode at ambient temperature and pressure.

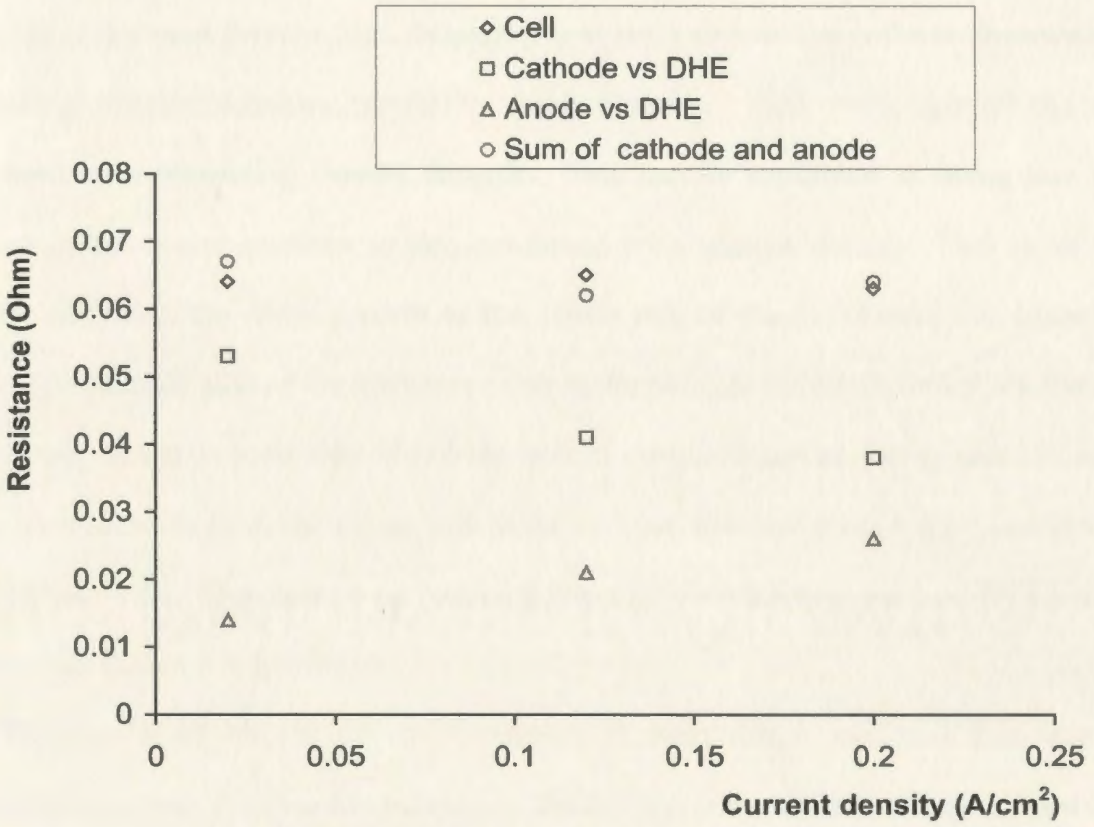

Figure 4.13. High frequency resistances of a 5 cm^2 cell, together with cathode and anode high frequency resistances *vs* DHE at different current densities. The cell was operated with humidified H_2 on the anode and air on the cathode at ambient temperature and pressure.

Figure 4.13 shows the high frequency real resistances of a cell at different current densities, together with that of the cathode *vs* the reference electrode and that of the anode *vs* the reference. It is seen that the high frequency real cell resistance is quite close to the sum of high frequency real resistances of the cathode *vs* the reference electrode and the anode *vs* the reference electrode. This indicates the validity of the reference electrode. In addition, it is found that the high frequency real resistance of the cathode decreased with increasing current densities, while the high frequency real resistance of the anode increased with increasing current densities. This can be explained as being due to the change of the water gradient in the membrane with current density. That is, at lower current densities, the water content in the anode side of the membrane was higher than that in the cathode side of the membrane due to the passage of humidified H_2 on the anode and dry air on the cathode side. However, at high current densities, more water is dragged by electro-osmosis from the anode side to the cathode side and more water is produced in the cathode side. This makes the water content in the cathode side of the membrane higher than that in the anode side.

The results of impedance measurements in both direct methanol fuel cells and hydrogen fuel cells confirm the validity of the DHE reference electrode developed in this work. They also demonstrate the value of using a reference electrode to analyze cell performance.

4.4 Conclusions

Both polarization measurements and electrochemical impedance spectroscopy have demonstrated that the edge-type reference electrode configuration is quite suitable for electrochemical study of an operating thin layer fuel cell. The main advantages of this novel reference electrode configuration are that it can be conveniently fitted into a

commercial fuel cell without any modification of the cell and that it does not need a special MEA. In addition, it has a very stable potential due to the use of a DHE.

This work also shows that with the aid of the reference electrode, one can resolve cell performance into the individual electrode behaviors, and therefore obtain valuable information for improving the cell performance and optimizing its operation conditions.

Furthermore, the concept of the reference electrode configuration used in this work should be instructive for designing reference electrodes for other kinds of thin layer solid electrolyte cells.

4.5 References

[1] L. Carrette, K. A. Friedrich, and U. Stimming, Chemphyschem 1 (2000) 162.

[2] P. Sridhar, R. Perumal, N. Rajalakshmi, M. Raja, and K. S. Dhathathreyan, J. Power sources 101 (2001) 72.

[3] N. Wagner, J. Appli. Electrochem. 32 (2002) 859.

[4] B. Andreaus, A. J. McEvoy, and G. G. Scherer, Electrochim. Acta 47 (2002) 2223.

[5] J. Winkler, P. V. Hendriksen, N. Bonanos, and M. Mogensen, J. Electrochem. Soc. 145 (1998) 1184.

[6] S. B. Adler, B. T. Henderson, M. A. Wilson, D. M. Taylor, and R. E. Richards, Solid State Ionics 134 (2000) 35.

[7] W. He and T. V. Nguyan, J. Electrochem. Soc. 151 (2004) A185.

[8] M. Dolle, F. Orsini, A. S. Gozdz, and J. M. Tarascon, J. Electrochem. Soc. 148 (2001) A851

[9] F. N. Buchi and G. G. Scherer, J. Electrochem. Soc. 148 (2001) A183.

[10] A. Kuver, I. Vogel, and W. Vielstich, J. Power Sources 52 (1994) 77.

[11] X. Ren, T. E. Springer, and S. Gottesfeld, J. Electrochem. Soc. 147 (2000) 92.

[12] J. Giner, J. Electrochem. Soc. 111 (1964) 376.

[13] D. A. Skoog, F. J. Holler, and T. A. Nieman, Principles of Instrumental Analysis, 5th Ed, Sauders College Publishing, 1998, p591.

[14] T. E. Springer, T. A. Zawodzinski, M. S. Wilson, and S. Gottesfeld, J. Electrochem. Soc. 143 (1996) 587.

[15] C. Mariana and R. Raymond, J. Phys. Chem. B 105 (2001) 3531.

Chapter 5 Analysis of Hydrogen Fuel Cell Performance with the Aid of a Reference Electrode

5.1 Introduction

Hydrogen fuel cells have attracted huge interest in recent years due to their promising high energy efficiency and the great potential of hydrogen as an alternative energy source for fossil fuels [1-2]. High-energy efficiency requires high performance cells. However, many factors such as slow oxygen reduction kinetics, membrane resistance, and mass transport resistances limit the performance of a cell. Among these limiting factors, the sluggish oxygen reduction on the cathode is considered to be the main contributor to cell performance losses. Therefore, a great deal of effort has been devoted to improve the performance of fuel cell cathodes [3-4]. Much less attention has been paid to anode performance and it is generally assumed that the hydrogen anode is reversible and that performance losses at the anode are negligible compared with the cathode performance loss.

However, recently, Andreaus and coworkers [5] found that at high current densities, the overpotential for hydrogen oxidation on the anode became significant due to the dehydration of the anode catalyst layer caused by electro-osmotic drag of water from the anode to the cathode. These authors also showed that the dehydration of the anode catalyst layer at high current densities couldn't be compensated even with 100% relative humidity hydrogen gas. These conclusions were based on impedance measurements on cells with membranes of different thickness, different ionic density, and different humidification conditions. However, due to the lack of a reference electrode, they did not

provide direct evidence such as anode polarization curves and anode impedance spectra to support their arguments.

In addition, membrane resistances also play an important part in cell performance. Obviously, low resistance membranes are preferred for high cell performance. Currently, Nafion membranes are the most widely used membrane in hydrogen fuel cells.

Although the performance of a cell mainly depends on the catalysts, it is also strongly influenced by the water distribution in the cell. On one hand, high performance requires high water content in the anode and in the membrane. For the membrane, full hydration is pursued to ensure a low membrane resistance. On the other hand, too much water in the cathode can cause flooding, resulting in an increase in oxygen transport resistance and lower cathode performance.

In an operating cell, water is transported from the anode to the cathode due to electro-osmotic drag caused by the movement of hydrogen ions from the anode to the cathode. This results in dehydration of the anode catalyst layer and the anode side of the membrane. Moreover, the dehydration increases with increasing current density [6]. Another mechanism for movement of water is back transport of water from the cathode side to the anode side due to diffusion. It was found that the back transport of water could only partially compensate for the dehydration of the anode catalyst layer and the anode side of the membrane [5,6]. Because the rate of water production and transport increases with increasing current density, at high current densities, water transport has a more significant influence on cell performance.

There is disagreement in the literature regarding performance losses due to changes in the membrane resistance with current density. Springer and coworkers [4] found that

membrane resistances increased with increasing current density. In contrast, Watanabe and coworkers [7] found that membrane resistances decreased with increasing current density.

In order to optimize the performance of a cell and its operating conditions, complete information on polarization of the cathode, the anode, and the membrane is greatly desired. Generally, cell polarization information can be conveniently obtained by polarization measurements, and membrane resistance polarization information can also be easily determined by impedance spectroscopy at high frequency. Polarization information on the individual electrode can only be obtained with the aid of a reference electrode, and generally, a specially designed reference electrode is needed.

Knowledge of the individual electrode performance losses and the membrane performance loss of an operating cell is prerequisite to improvement of the performance of a cell. The objectives of the work in this chapter are to resolve the performance losses of a hydrogen cell into anode performance losses, cathode performance losses, and the membrane performance losses with the aid of a reference electrode. The performance losses of the cell, the anode, the cathode, and the membrane were analyzed with both polarization measurements and electrochemical impedance spectroscopy.

5.2 Experimental

Experimental procedures are described in Section 4.2.

5.3 Results and Discussion

5.3.1 Analysis of Anode Performance Losses

5.3.1.1 Polarization Measurements

Figure 5.1 shows polarization curves for the anode of a 5 cm^2 cell operated at two

different temperatures with anode feeds of H_2 humidified at the cell's operating temperature. It is seen that in the low current density region (< 0.1 A/cm^2), the anode overpotential was close to zero, as expected for the reversible H_2 oxidation reaction. In the high current density region, the anode overpotential increased rapidly with increasing current density, especially at room temperature. Large anode overpotentials at high current densities were also observed with a 1 cm^2 locally made cell (Figure 5.2). Steep increases in electrode overpotentials at high current densities are normally due to concentration polarization. However, for hydrogen oxidation on fuel cell anodes, it is also found that a significant increase of overpotential at high current densities can be due to an increase of activation overpotentials caused by a decrease in the number of active sites on the anode [5]. The decrease in number of active sites was attributed to dehydration of the anode catalyst layer at high current densities [5]. In addition, a significant increase of overpotential at high current densities can also be partially due to an increase in the membrane resistances with increasing current density (see below).

Figure 5.3 shows the high frequency resistance of the anode as a function of current density at room temperature (RT) and 60 °C. The high frequency resistance consists of the anode contact resistances, plus the portion of the membrane resistance between the anode and the reference electrode. It can be seen that, at RT, the high frequency resistance increased rapidly with increasing current density, especially in the high current density region. This would have caused the overpotential to increase super-linearly in polarization experiments. However, this increase cannot fully account for the steep increase of the anode overpotential observed with increasing current density at RT (Figure 5.1). For example, when the current density increased from 0.33 A/cm^2 to 0.35 A/cm^2, the high

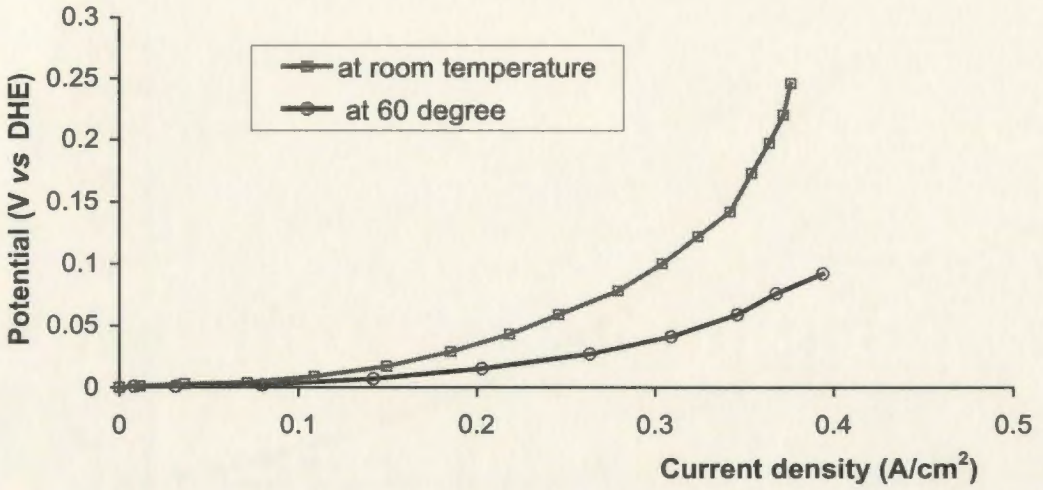

Figure 5.1. Polarization curves for the anode of a 5 cm^2 cell with an anode feed of H_2 humidified at the cell's operating temperature and a cathode feed of dry air. The cell was operated at room temperature and 60 °C.

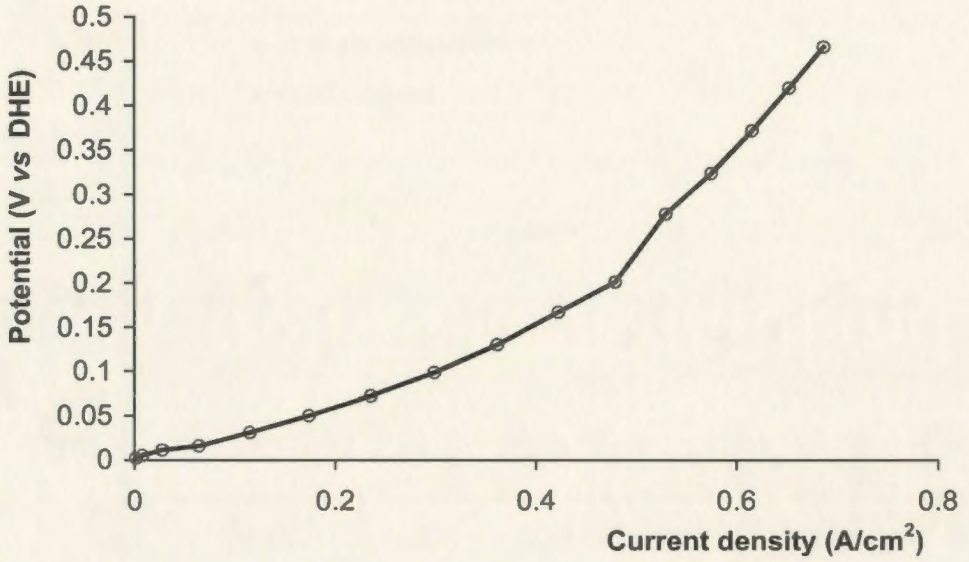

Figure 5.2. A polarization curve for the anode of a 1 cm^2 cell with an anode feed of humidified H_2 and a cathode feed of dry O_2. The cell was operated at room temperature.

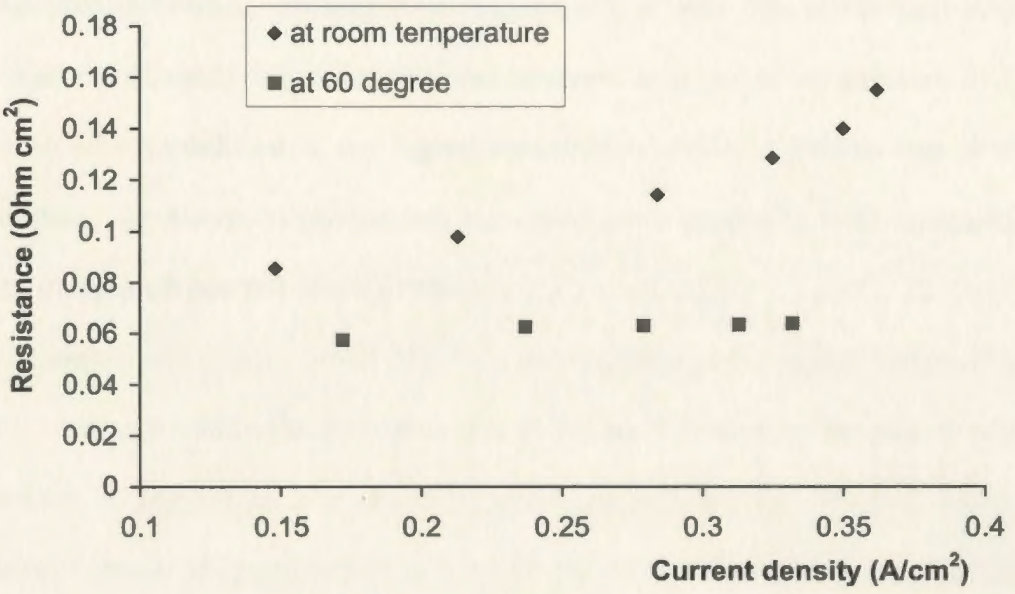

Figure 5.3. High frequency anode resistances for a 5 cm^2 cell as a function of current density. The cell was operated at RT and 60 °C with anode feeds of H_2 humidified at the cell's operating temperature and a cathode feed of dry air.

frequency resistance increased from 0.13 Ω cm^2 to 0.14 Ω cm^2. The overpotentials due to the high frequency anode resistance at these two current densities would have been 43 mV and 46 mV, respectively. However, the total anode overpotential (Figure 5.1) increased from 120 mV to 160 mV. This indicates that the increase of the high frequency resistance with current density was not the main reason for the steep increase of the anode overpotential at high current densities.

Another interesting finding from Figure 5.1 is that the anode performance was improved significantly when the cell was operated at a higher temperature of 60 °C and hydrogen was humidified at the higher temperature. Also, it is seen that at the higher temperature, the anode overpotentials increased more gradually with increasing current density in the high current density region.

The significant improvement of anode performance at the higher temperature seen in Figure 5.1 was partially due to a decrease in the high frequency resistance at the higher temperature (Figure 5.3). For example, when the temperature was increased, the high frequency resistance decreased from 0.13 Ω cm^2 to 0.065 Ω cm^2 at a current density of 0.34 A/cm^2. This amounts to a decrease in overpotential of ca. 22mV, while the total decrease in anode overpotential was ca. 70 mV at this current density. This again indicates that the significantly lower overpotential at the higher temperature was largely due to some other factors, presumably a decrease of the activation overpotential and/or decrease of the H_2 transport resistance.

The higher temperature used for humidification of the H_2 is definitely significant in this context, since at the higher temperature, the water content of the anode would be increased significantly, resulting in an increase in the number of active sites on the anode

catalyst. The effects of the higher humidification temperature on the H_2 transport resistance are more difficult to assess. On one hand, when hydrogen was humidified at the higher temperature with the same flow rate and pressure as at room temperature, the concentration of hydrogen would have decreased relative to that at room temperature due to the higher water content. This would result in an increase in the H_2 transport resistance. On the other hand, the H_2 diffusion rate increases with increasing temperature, resulting in a decrease in the H_2 transport resistance. Thus, further experiments are needed to determine which one of these effects is more significant.

In conclusion, the anode performance was improved significantly at the higher temperature. The improvement was due to decreases in high frequency resistance and activation overpotential attributed to the increased water content of H_2 humidified at the higher temperature.

5.3.1.2 Impedance Spectroscopy

Figure 5.4 shows complex plane impedance plots for the anode of a 5 cm^2 cell as a function of anode potential *vs* DHE. It is seen that the typical feature of the spectra is that they consist of two arcs: a small arc at high frequencies and a large arc at medium and low frequencies. It was also found that the large arc increased rapidly with increasing potential. This indicates that the anode performance decreased significantly at high current densities (high anode potentials). This conclusion is consistent with the anode polarization curves (Figure 5.1).

The anode impedance behavior can be explained by using a simplified equivalent circuit as shown in Figure 5.5a, where C_g represents the geometric capacitance associated with the leads, and it is reflected by the small arc at high frequencies; Z_A represents the

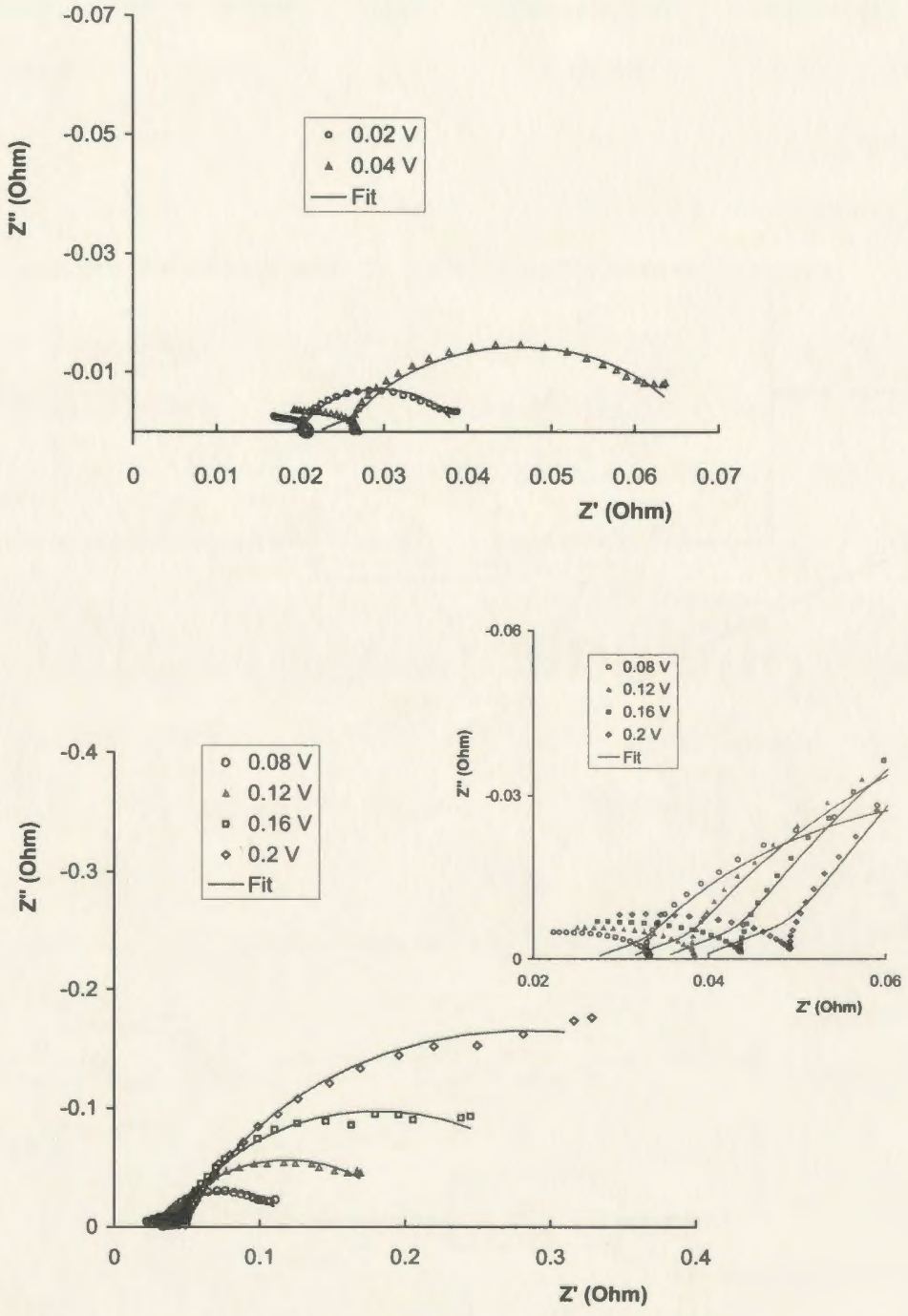

Figure 5.4 Complex plane impedance plots for the anode of a 5 cm^2 cell as a function of anode potential (*vs* DHE). The cell was operated with humidified H_2 on the anode and dry air on the cathode at room temperature. Inset shows an expansion of the high frequency part.

(a)

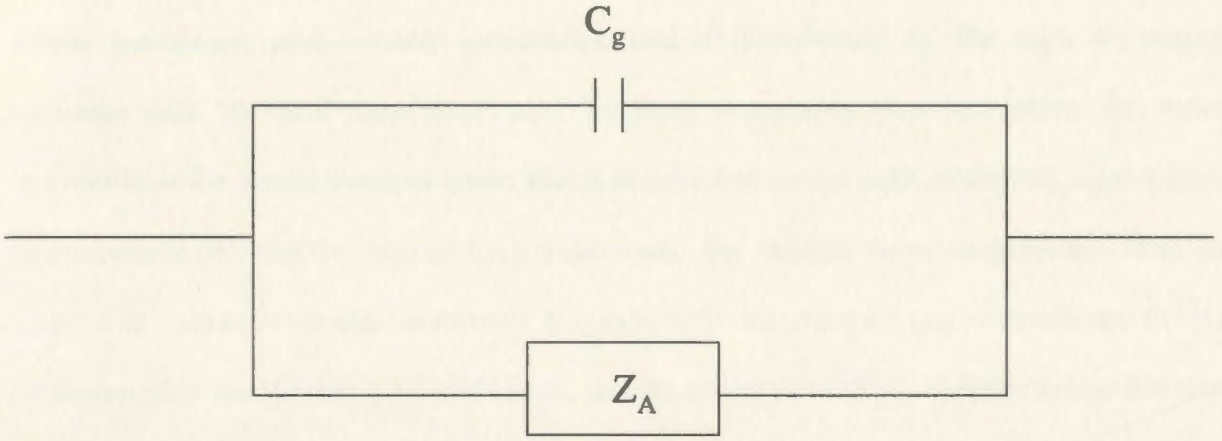

(b)

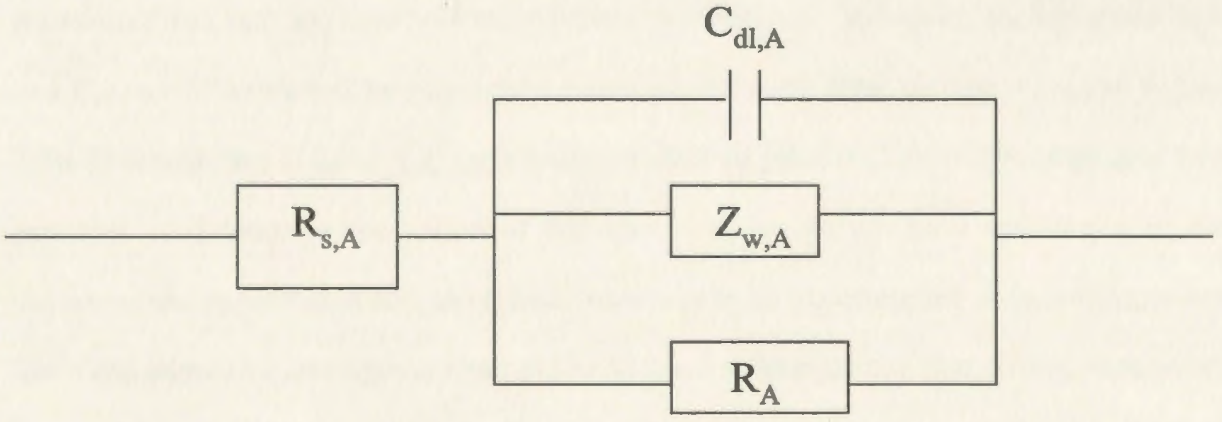

Figure 5.5. Equivalent circuits describing impedance behavior of a fuel cell anode. The equivalent circuit in Figure b represents Z_A in Figure a.

anode impedance, and it is mainly reflected by the large arc at medium and low frequencies. Z_A can be approximately represented by a simplified equivalent circuit as shown in Figure 5.5b. In this equivalent circuit, $R_{s,A}$ represents the anode side resistance of the membrane plus contact resistances, and it is reflected by the high frequency intercept with the real axis; $Z_{w,A}$ is a Warburg impedance that represents the ionic resistance in the anode catalyst layer, and it is reflected in the high frequency region by a characteristic 45 degree slope; $C_{dl,A}$ represents the double layer capacitance due to catalyst in contact with the membrane; R_A represents the charge transfer resistance for H_2 oxidation plus the H_2 transport resistance, and the magnitude of R_A is reflected by the size of the large arc.

It is seen that the anode impedances (Z_A) were complicated by the geometric impedance as shown in the inset of Figure 5.4. For example, no Warburg impedance (45 degree slope at high frequencies) was observed. This means that $R_{s,A}$, R_A, and ionic resistances can not be directly obtained from the large arc. However, the values of $R_{s,A}$ and R_A can be extracted by simulation based on the equivalent circuit shown in Figure 5.5b. It is seen that (Figure 5.4) the simulation data fit most regions of the large arc. This provides confidence in the values of R_A. However, we do not have confidence in the values of the capacitance and ionic resistance, since no experimental data that represent ionic resistances in the catalyst layer are available for fitting. Note that during simulation, an open terminus finite length Warburg model was used to represent $Z_{w,A}$, and W_o-R denotes the resistance of $Z_{w,A}$.

The extracted parameters for the equivalent circuit shown in Figure 5.5b are listed in Table 5.1. It is seen that R_A increased rapidly with increasing potential, especially at high

potentials, and the change of R_A with potential totally matches the change of the size of the large arc with potential.

Normally, charge transfer resistances decrease with increasing potential, and therefore, at high overpotentials, R_A in the medium and low frequency region mainly reflects mass transport resistances. However, for H_2 oxidation on anodes, there can be a significant activation overpotential at high overpotentials due to dehydration of the anode catalyst layer [5]. Therefore, it is difficult to tell whether the rapid increase of R_A at high overpotentials was mainly due to the charge transfer resistance and/or due to the mass transport resistance.

Table 5.1. Parameters for the equivalent circuit in Figure 5.5b as a function of anode potential

Potential (V)	0. 02	0. 04	0.08	0.12	0.16	0.2
$R_{s,A}$ (Ω cm^2)	0. 0945	0. 112	0.134	0.156	0.175	0.196
$C_{dl,A}$(mF /cm^2)	7. 46	3. 10	2.00	1.84	1.45	1.33
W_o-R (Ω cm^2)	0. 0200	0. 0570	0. 0815	0. 0895	0. 116	0. 145
W_o-T	0. 0217	0. 0267	0. 0253	0. 0226	0. 0264	0. 0346
W_o-P	0. 415	0. 386	0. 380	0. 381	0. 391	0. 382
R_A (Ω cm^2)	0. 100	0. 223	0. 471	0. 855	1. 42	2. 41

Although we do not have confidence in values of W_o-R, interestingly, it was found that W_o-R increased significantly with increasing potential, indicating that the ionic resistance of the anode catalyst layer increased with increasing anode potential. This is in good agreement with the results reported by Andreaus and coworkers [5]. This maybe suggests that the model proposed here (shown in Figure 5.5b) can predict, at least, the

trend in ionic resistances with potential.

Table 5.2 lists parameters for the equivalent circuit as a function of potential at 60 °C. It can be seen that R_A increased rapidly with increasing potential. However, the values of R_A at 60 °C are much smaller than at room temperature. This means that anode performance was improved greatly at the higher temperature, and is consistent with the results shown in Figure 5.1.

From Table 5.2 it can also be seen that at the higher temperature, the predicted values of W_o-R also increased markedly with increasing potential. However, the values of W_o-R at the higher temperature are significantly smaller than at room temperature. This indicates that the dehydration of the anode catalyst layer would have been greatly compensated at the higher temperature humidification of H_2. This again suggests that the proposed model can predict the trend in ionic resistance with humidification temperature.

Table 5.2. Parameters for the equivalent circuit in Figure 5.5b as a function of anode potential at 60 °C

Potential (V)	0. 01	0. 02	0.03	0.04	0.05
$R_{s,A}$ (Ω cm^2)	0. 0620	0. 0670	0.0665	0.0685	0.0700
$C_{dl,A}$(mF /cm^2)	100	6. 56	4.42	3.62	3.34
W_o-R (Ω cm^2)	0. 0002	0. 0265	0. 0379	0. 0490	0. 0555
W_o-T	0. 000128	0. 0170	0. 0140	0. 0186	0. 0207
W_o-P	0. 300	0. 276	0. 303	0. 315	0. 329
R_A (Ω cm^2)	0. 0274	0. 0915	0. 152	0. 212	0. 295

5.3.2 Analysis of Cathode Performance Losses

5.3.2.1 Polarization Measurements

Figure 5.6 shows polarization curves for the cathode of a 5 cm^2 cell operated at two different temperatures with anode feeds of H_2 humidified at the cell's operating temperature and a cathode feed of dry air. It is seen that in the low current density region, the potential of the cathode decreased rapidly with increasing current density. This reflects the slow kinetics of oxygen reduction. In the medium current density region, the potential of the cathode decreased almost linearly with increasing current density, indicating that the polarization curves are governed by Ohm's law in this region. In the high current density region, the potential of the cathode decreased rapidly with increasing current density, especially at room temperature. The rapid decrease of cathode performance at high current densities is generally attributed to an increase of O_2 mass transport resistance caused by cathode flooding [4,9].

Another interesting finding is that cathode performance was improved significantly in the medium and high current density regions at the higher temperature. The significant improvement of cathode performance at the higher temperature in the high current density region can be attributed to a rapid decrease in the resistance to O_2 transport [4,9]. It was reported that water evaporated faster at higher temperatures, leading to less cathode flooding and therefore a decreased O_2 transport resistance [9-12].

Surprisingly, in the low current density region, the cathode performance was not improved at the higher temperature as expected, since at the higher temperature, the rate of oxygen reduction should be faster. This is presumably due to the increase of ionic resistance in the cathode catalyst layer (see below).

5.3.2.2 Impedance Spectroscopy

Figures 5.7 shows complex plane impedance plots for the cathode of a 5 cm^2 cell as a

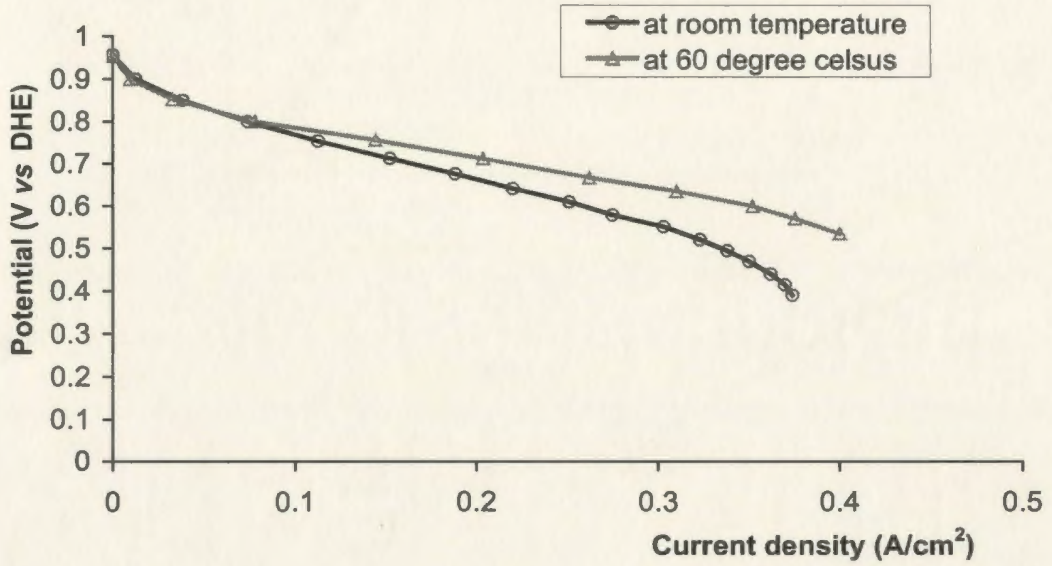

Figure 5.6. Polarization curves for the cathode of a 5 cm^2 cell with anode feeds of H_2 humidified at the cell's operating temperature and a cathode feed of dry air. The cell was operated at room temperature and 60 °C, respectively.

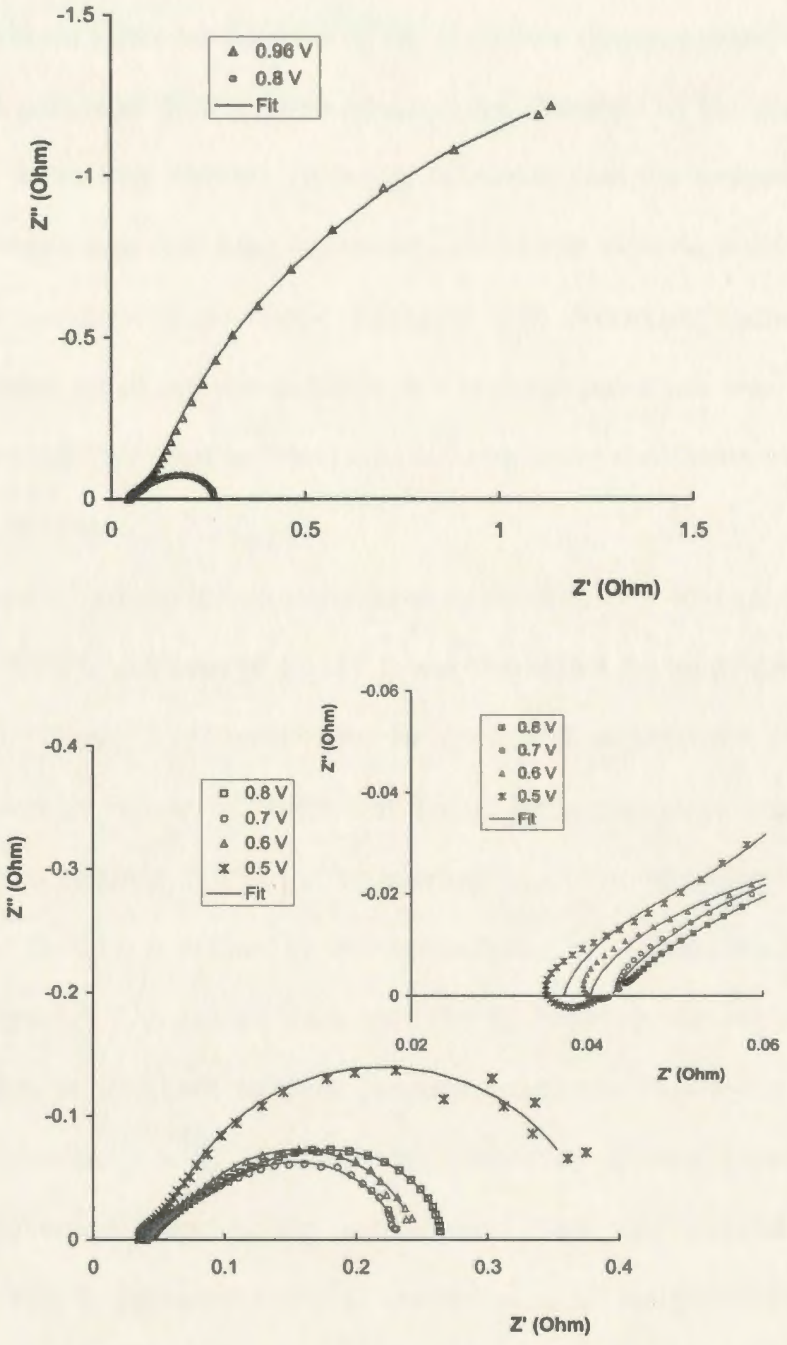

Figure 5.7. Complex plane impedance plots for the cathode of a 5 cm^2 cell as a function of cathode potential (*vs* DHE). The cell was operated at room temperature with an anode feed of H_2 humidified at room temperature and a cathode feed of dry air. Inset shows an expansion of the high frequency part.

function of cathode potential (*vs* DHE). These plots consist of a single distorted semicircle. It is seen that the diameter of the semicircle changed greatly with potential. At high cathode potentials (low current density), the diameter of the semicircle decreased rapidly with decreasing cathode potential, indicating that the oxygen reduction charge transfer resistance was dominant in this region. At low cathode potentials (high current density), the diameter of semicircle increased with decreasing cathode potential, and finally, the diameter of the semicircle at low cathode potentials was larger than that at high cathode potentials. This indicates that mass transport resistances became dominant at high current densities.

A number of equivalent circuits have been proposed to explain the impedance behavior of PEMFC cathodes [9,11,13]. It was found that the equivalent circuit proposed in Chapter 3 (Figure 3.11) could also be applied to explain the cathode impedance behavior shown in Figure 5.7. Note that during simulation, $C_{dl,C}$ was substituted by a constant phase element (CPE) to compensate for non-homogeneity in the porous electrode, and the CPE is defined by two parameters: CPE-T and CPE-P [14].

From Figure 5.7 it can be seen that the fit between the experimental data and simulation data is excellent in most frequency regions. This again suggests that the proposed equivalent circuit is reasonable. However, it was found that there was significant deviation between the experimental data and simulation data at high frequencies. This is presumably due to the influence of the geometric capacitance and wire induction which leads to extension of the spectrum into the forth quadrant at high frequencies as seen in the inset of Figure 5.7 [13]. For simplicity, the proposed simplified equivalent circuit does not include these impedances.

Table 5.3. Parameters for the equivalent circuit in Figure 3.11 as a function of cathode potential

Potential (V)	0. 96	0. 8	0.7	0.6	0.5
$R_{s,C}$ (Ω cm^2)	0. 209	0. 217	0.214	0.202	0.185
CPE-T	0. 136	0. 229	0.119	0.098	0.170
CPE-P	0. 755	0. 729	0.883	1	1
W_o-R (Ω cm^2)	1. 10	1. 55	1. 02	0. 645	0. 530
W_o-T	0. 0905	0. 0590	0. 0713	0. 0814	0. 0730
W_o-P	0. 425	0. 450	0. 429	0. 420	0. 446
R_C (Ω cm^2)	18. 2	1. 13	0. 950	1. 03	1. 73

Table 5.3 lists parameters for the equivalent circuit as a function of cathode potential. It is seen that R_C changed greatly with changing cathode potential. At a potential of 0.96 V, close to OCP of the cathode, the value of R_C is much larger than at other potentials. This reflects the charge transfer resistance of O_2 reduction, since the O_2 transport resistance is insignificant at this potential (very low current density). In the high potential region (low current density), it can be seen that R_C dropped rapidly with decreasing cathode potential (increase of overpotential). This indicates that R_C mainly reflects the charge transfer resistance for O_2 reduction in this region. In the low potential region (high current density), it was found that R_C increased with decreasing cathode potential. This indicates that the O_2 transport resistance became dominant in this region. In conclusion, the change of R_C with changing potential is in good agreement with the change of the diameter of the semicircle with changing potential. This again demonstrates the validity of the proposed equivalent circuit.

It was also found that W_o-R changed significantly with changing cathode potential. The values of W_o-R at low potentials (high current density) were significantly smaller than those at high potentials. This is reasonable, since at high potentials, the cathode catalyst layer would have been dried by the passage of dry air, resulting in an increased ionic resistance, while at low potentials, the water content at the cathode catalyst layer would have increased due to production of water by O_2 reduction. This results in a decreased ionic resistance.

Another finding is that at low current densities, W_o-R at the higher temperature (Table 5.4) was significantly higher than at room temperature. This is presumably due to the fact that water evaporated much faster at the higher temperature, leading to more dehydration of the cathode catalyst layer, and consequently a higher ionic resistance. The higher ionic resistance explains why in the low current density region, the cathode performance at the higher temperature was not better than at room temperature.

In addition, it is seen that in the high current density region, R_C at the higher temperature was significantly smaller than at room temperature. This suggests that in the high current density region, the cathode has much better performance at the higher temperature. Cathode polarization curves (Figure 5.6) support this assertion.

Table 5.4. Resistance values as a function of cathode potential at 60 °C

Potential (V)	$R_{s,C}$ (Ω cm^2)	W_o-R (Ω cm^2)	R_C (Ω cm^2)
0.91	0.18	5.0	15
0.8	0.20	2.8	1.0
0.7	0.20	0.70	0.60
0.6	0.16	0.60	0.75

Surprisingly, at the higher temperature, $R_{s,C}$ did not decrease greatly as observed with $R_{s,A}$. This is presumably due to the faster evaporation of water at the cathode at the higher temperature.

5.3.3 Analysis of Cell Performance Losses

5.3.3.1 Polarization Measurements

Figure 5.8 shows a polarization curve for a 5 cm^2 cell operated at room temperature with an anode feed of H_2 humidified at room temperature and a cathode feed of dry air, together with anode potentials *vs* DHE, and cathode potentials *vs* DHE. It can be seen that in the low current density region, the cell voltage dropped rapidly with increasing current density. In addition, the polarization curve of the cell is quite close to the cathode polarization curve in this region, indicating that the cell performance loss in the low current density region is mainly due to the cathode performance loss, which was caused by the slow kinetics of oxygen reduction. In the medium current density region, the cell voltage decreased almost linearly with increasing current density, indicating that the polarization curve in this region was mainly governed by Ohm's law. In the high current density region, the cell voltage also dropped rapidly with increasing current density, and the polarization curve of the cell was significantly different from the cathode polarization curve. This indicates that the anode polarization became significant at high current densities. The rapid increase of the anode potential at high current densities confirms this assertion. As discussed before, the rapid increase of anode potential at high current densities was mainly due to an increase of the activation overpotential and/or H_2 transport resistance, rather than due to an increase of the anode side resistance of the membrane.

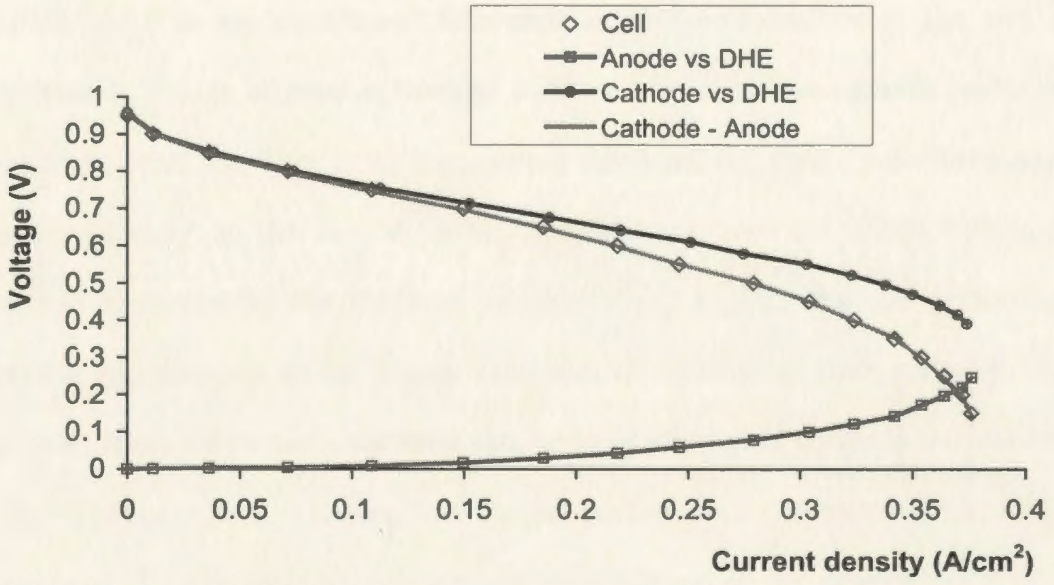

Figure 5.8. A polarization curve for a 5 cm^2 cell, together with cathode potentials *vs* DHE, and anode potentials *vs* DHE. The cell was operated at room temperature with an anode feed of H_2 humidified at room temperature and a cathode feed of dry air.

From Figure 5.8 it can also be seen that the cathode potential *vs* DHE minus the anode potential *vs* DHE is almost identical to the polarization curve of the cell. This demonstrates that with the aid of a reference electrode, cell performance losses can be resolved into the cathode performance loss and the anode performance loss.

Figure 5.9 compares cell performances at two different operating temperatures (note that H_2 was humidified at the cell's operating temperature). It is seen that at low current densities, there is no significant difference in cell performance at the two different temperatures. This is in good agreement with the anode and the cathode performances at low current densities. That is, at low current densities, the cathode performance did not change markedly at the two different temperatures and the anode behaved like a reversible electrode. In the medium current density region, the cell performance was improved significantly at the higher temperature. This is at least partially due to the significant decrease of the membrane resistance at the higher temperature (see below). In the high current region, it is seen that the cell performance was much better at the higher temperature. This better performance can be attributed to the improvement of both the cathode performance and the anode performance at the higher temperature.

5.3.3.2 Impedance Spectroscopy

Figures 5.10a and 5.10b show complex plane impedance plots for a 5 cm^2 cell as a function of cell voltage. The cell was operated at room temperature with an anode feed of H_2 humidified at room temperature and a cathode feed of dry air. It is seen that the typical feature of the plot is that it consists of one distorted semicircle, and the diameter of the semicircle changed greatly with changing cell voltage. In the low current density region

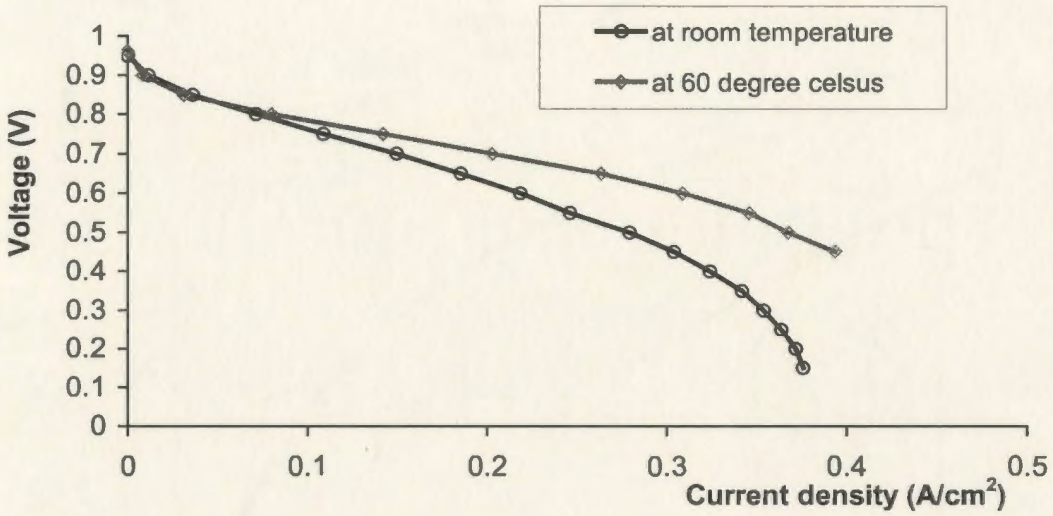

Figure 5.9. Polarization curves for a 5 cm^2 cell operated at two different temperatures with anode feeds of H_2 humidified at the cell's operating temperature and a cathode feed of dry air.

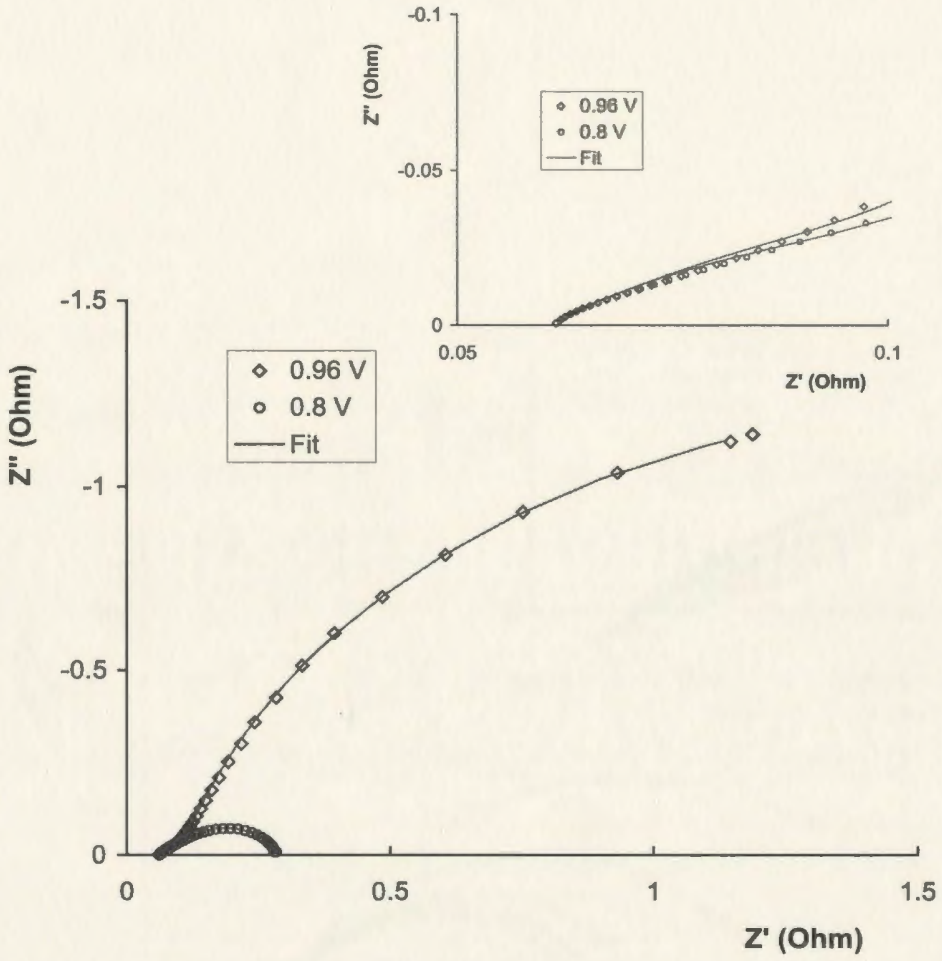

Figure 5.10a. Complex plane impedance plots for a 5 cm^2 cell as a function of cell voltage (at high cell voltages). The cell was operated at room temperature with an anode feed of H_2 humidified at room temperature and a cathode feed of dry air. Inset shows an expansion of the high frequency part.

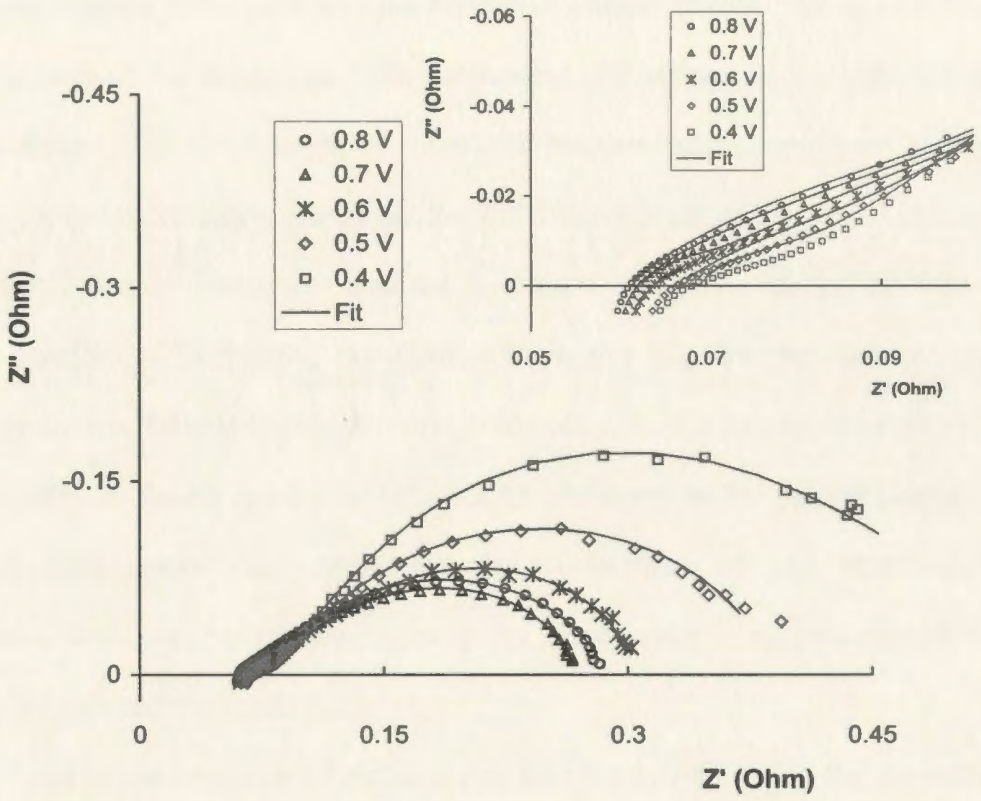

Figure 5.10b. Complex plane impedance plots for a 5 cm^2 cell as a function of cell voltage. The cell was operated at room temperature with an anode feed of H_2 humidified at room temperature and a cathode feed of dry air. Inset shows an expansion of the high frequency part.

(cell voltages between 0.96 V and 0.7 V), the diameter of the semicircle decreased with decreasing cell voltage. While in the high current density region (cell voltages between 0.6 V and 0.4 V), the diameter of the semicircle increased with decreasing cell voltage. The decrease of the diameter of the semicircle with decreasing cell voltage in the low current density region (high cell voltage) indicates that charge transfer resistances dominated in this region. Since the oxygen reduction charge transfer resistance was dominant in the low current density region, the semicircle in the low current density region must mainly reflect the oxygen reduction charge transfer resistance. The increase of the diameter of the semicircle with decreasing cell voltage in the high current density region indicates that other kinds of resistance became more significant at high current densities (low cell voltage). Based on the previous discussion, at high current densities, the oxygen transport resistance and the hydrogen reduction charge transfer resistance became significant. Therefore, the semicircle in the high current density region must mainly represents these resistances. Also, it is seen that at high frequencies, the spectrum extended into the fourth quadrant. This can be attributed to the lead induction [13]. Cell geometric impedances can complicate the explanation of cell impedance at high frequencies, and can be reduced greatly by appropriate arrangements of connection between the cell and the leads [13].

The impedance behavior of the cell can be modeled by using the equivalent circuit shown in Figure 5.11. Actually, this circuit is just a series combination of the equivalent circuits for the cathode and the anode. Here, R_s represents the cell membrane resistance plus contact resistances.

During simulation, R_A was fixed at the value obtained from the anode impedance

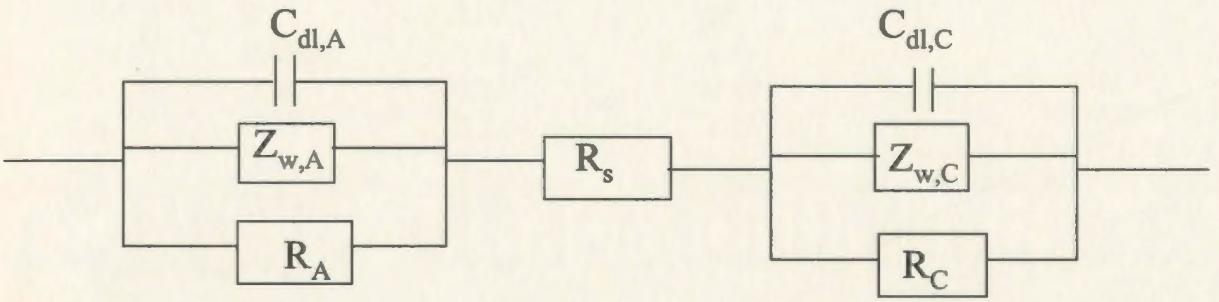

Figure 5.11. An equivalent circuit describing the impedance of a PEMFC.

simulation data (Table 5.1). Other resistance values obtained by simulation are listed in Table 5.5. It was found that the fit between experimental data and the simulation was quite good in most frequency regions as seen in Figures 5.10a and 5.10b. This suggests that the proposed equivalent circuit is reasonable.

Table 5.5. Resistance values as a function of cell voltage at room temperature

Voltage (V)	R_A (Ω cm^2)	R_s (Ω cm^2)	R_C (Ω cm^2)	R_{total}^* (Ω cm^2)
0.96	0	0.36	16	16
0.8	0.005	0.35	1.1	1.1
0.7	0.08	0.31	0.93	1.0
0.6	0.21	0.32	1.1	1.3
0.5	0.46	0.33	1.2	1.7
0.4	0.80	0.34	1.7	2.5

* $R_{total} = R_A + R_C$.

From Table 5.5 it is seen that R_{total} (R_A + R_C) changed greatly with changing cell voltage. At high cell voltages, R_{total} decreased with decreasing cell voltage (increase of overpotential). At low cell voltage, R_{total} increased with decreasing cell voltage (increase of current density). It was found that the change of R_{total} with cell voltage totally matches the change of the diameter of the semicircle with cell voltage. This again supports the validity of the proposed equivalent circuit, since the diameter of the semicircle mainly represents R_{total}.

Interestingly, as listed in Table 5.6, at the same cathode potential, the values of R_C obtained by cell simulation were quite close to the R_C values obtained by cathode simulation. This further supports the validity of the proposed equivalent circuit.

Table 5.6. R_C as a function of cathode potential at room temperature

Potential$^{\$}$ (V)	$R_C^{\$}$ (Ω cm^2)	Potential$^{\#}$ (V)	$R_C^{\#}$ (Ω cm^2)
0.96	18	0.96	16
0.8	1.2	0.8	1.1
0.7	0.95	0.72	0.93
0.6	1.1	0.65	1.1
0.5	1.7	0.58	1.2
		0.52	1.7

$: values obtained by cathode impedance simulation: #: values obtained by cell impedance simulation.

Table 5.7 lists resistance values at the higher temperature of 60 °C. It was found that at the higher temperature, R_s decreased significantly compared with that at room temperature. As discussed before, at the higher temperature, $R_{s,A}$ dropped significantly, while $R_{s,C}$ dropped a little bit, thus the significant drop of the cell membrane resistance at the higher temperature must be mainly due to the marked drop of the anode side resistance of the membrane.

Table 5.7. Resistance values as a function of cell voltage at 60 °C

Voltage (V)	R_A (Ω cm^2)	R_s (Ω cm^2)	R_C (Ω cm^2)	R_{total}^{*} (Ω cm^2)
0.96	0	0.20	1.8	2.0
0.8	0.01	0.22	0.84	0.85
0.7	0.14	0.21	0.54	0.68
0.6	0.19	0.21	0.90	1.1
0.5	0.27	0.22	1.1	1.4

* $R_{total} = R_A + R_C$.

It was also found that in the high current density region, R_{total} dropped significantly at the higher temperature. This is due to the fact that both R_A and R_C dropped rapidly at the higher temperature. This also suggests that at the higher temperature, the cell performance would become better. This is consistent with the results observed from polarization curves (Figure 5.9).

Figure 5.12a shows impedance spectra for a 5 cm^2 cell at a current density of 0.02 A/cm^2, together with cathode impedance *vs* DHE, and anode impedance *vs* DHE. It is seen that in the medium and low frequency region, the cell impedance is quite close to the cathode impedance *vs* DHE. This again indicates that at low current densities, cell performance is mainly determined by cathode performance. In other words, anode polarization is negligible at low current densities.

Figure 5.12b shows impedance spectra for a 5 cm^2 cell at a current density of 0.2 A/cm^2, together with cathode impedance *vs* DHE, and anode impedance *vs* DHE. It can be seen that the cell impedance is significantly different from the cathode impedance *vs* DHE. This indicates that at high current densities, the anode impedance became significant. This is consistent with the fact that at high current densities, anode impedance increased rapidly with increasing current density. From Figure 5.12b it is seen that in the low frequency region, the impedance of the anode *vs* DHE accounts for ca. 30% of the cell impedance. This indicates that at high current densities, anode impedance cannot be taken as negligible.

Another finding from Figure 5.12b is that the cell impedance is quite close to the sum of the cathode impedance *vs* DHE and the anode impedance *vs* DHE. This again demonstrates that cell performance losses can be separated into cathode performance

(a)

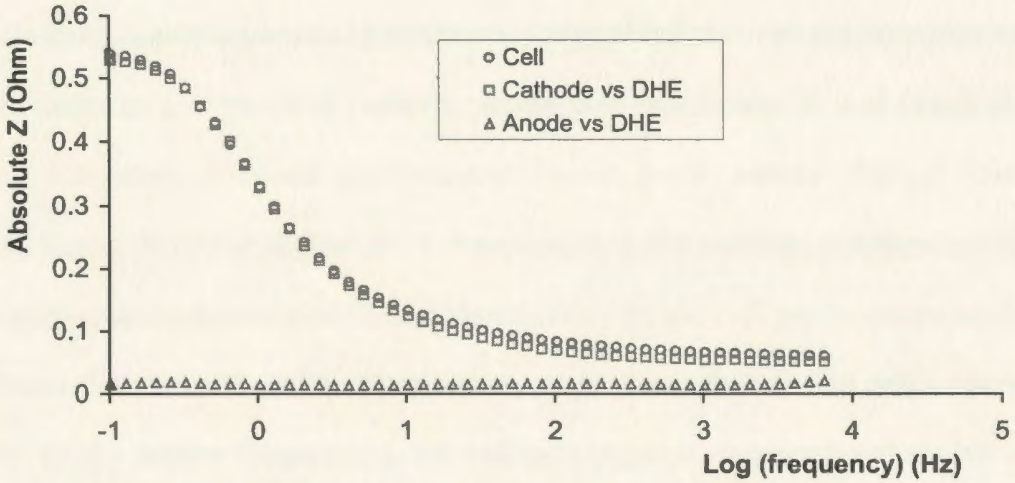

(b)

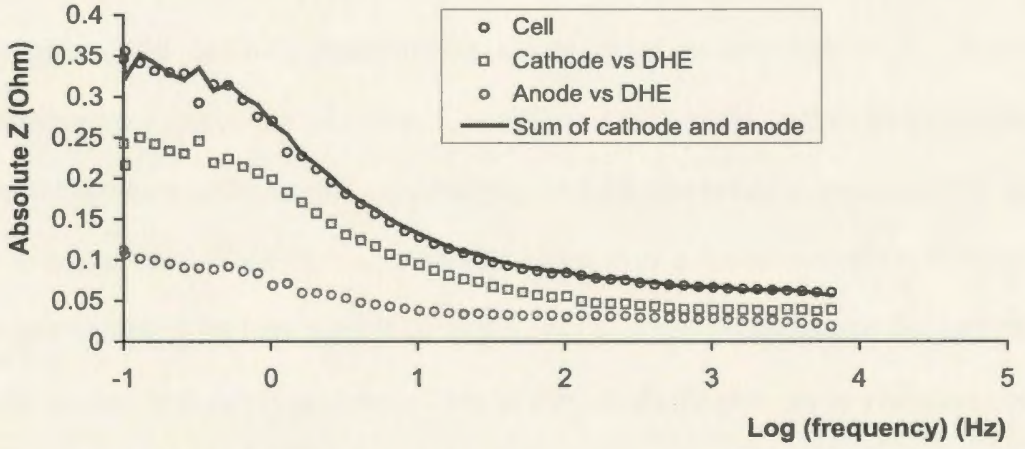

Figure 5.12. Impedance spectra for a 5 cm^2 cell at two different current densities: (a) 0.02 A/cm^2; (b) 0.2 A/cm^2. The cell was operated at room temperature with an anode feed of H_2 humidified at room temperature and a cathode feed of dry air.

losses and anode performance losses.

5.4 Conclusions

The polarization and impedance spectroscopy data show that cell performance losses were due to performance losses of cathode, anode, and membrane. It was found that at low current densities, the cell performance losses were mainly due to cathode performance losses. While at high current densities, both the cathode performance losses and anode performance losses contributed significantly to the cell performance losses. It was also found that the cell performance was strongly dependent on the cell's operating temperature. At the higher temperature, the cell performance was improved significantly at high current densities, and this improvement was mainly due to performance improvements for both the cathode and the anode.

For the cathode, it was found that the potential dropped significantly both at low current densities and at high current densities. At low current densities, the cathode performance losses were mainly due to the slow kinetics of O_2 reduction, while at high current densities, the cathode performance losses were mainly due to an increasing oxygen transport resistance. In addition, it was found that at the higher temperature, the cathode performance was improved significantly at high current densities, and this can be attributed to a decrease of the O_2 transport resistance plus a faster rate of O_2 reduction at the higher temperature. At low current densities, the cathode performance did not change significantly at the higher temperature. This is due to the higher ionic resistance at the cathode catalyst layer at the higher temperature caused by the dehydration of the catalyst layer.

For the anode, it was found that at low current densities, anode overpotentials were

close to zero, indicating that anode polarization at low current densities is negligible. At high current densities, the anode overpotential increased rapidly, especially at room temperature. This can be attributed to increased activation overpotentials for H_2 oxidation caused by dehydration of the anode catalyst layer, an increased anode side resistance of the membrane. It was also found that at high current densities, anode performance was improved significantly at the higher temperature. This suggests that high temperature humidification of H_2 is needed to compensate the dehydration of the anode.

For the membrane, it was found that the membrane performance was strongly dependent on the temperature of H_2 humidification. The membrane resistance was significantly decreased at the higher temperature, and this decrease was mainly due to a marked decrease of the anode side resistance of the membrane at the higher temperature humidification of H_2.

5.5 References

[1] A. J. Appleby, A. C. Lloyd, and C. K. Dyer, Scientific American 7 (1999) 72.

[2] L. Gubler, G. G. Scherer, and A. Wokaun, Chem. Eng. Technol. 24 (2001) 1.

[3] T. E. Springer, T. A. Zawodzinski, and S. Gottesfeld, J. Electrochem. Soc. 138 (1991) 2334.

[4] T. E. Springer, M. S. Wilson, and S. Gottesfeld, J. Electrochem. Soc. 140 (1993) 3513.

[5] B. Andreaus, A. J. McEvoy, and G. G. Scherer, Electrochimica Acta 47 (2002) 2223.

[6] F. N. Buchi and G. G. Scherer, J. Electrochem. Soc. 148 (2001) A183.

[7] M. Watanabe, H. Igarashi, H. Uchida, and F. Hirasawa, J. Electroanal. Chem. 399 (1995) 239.

[8] N. Wagner, in Impedance Spectroscopy, E. Barsoukov and J. R. Macdonald, Editors, 497-537, John Wiley & Sons, Inc. New Jersey, (2005).

[9] C. Mariana and R. Raymond, J. Phys. Chem. B 105 (2001) 3531.

[10] X. Wang, I. M. Hsing, Y. J. Leng, and P. L. Yue, Electrochemica Acta 46 (2001) 4397.

[11] N. Wagner, J. Appli. Electrochem. 32 (2002) 859.

[12] X. Ren, T. E. Springer, and S. Gottesfeld, J. Electrochem. Soc. 147 (2000) 92.

[13] R. Makharia, M. F. Mathias, and D. R. Baker, J. Electrochem. Soc. 152 (2005) A970.

[14] Circuit modeling fitting and simulation (Tutor # 3) in Zview, Scribner Associates, Inc. Southern Pines, NC 1997.

Chapter 6 Analysis of Performance Losses of Direct Methanol Fuel Cells with the Aid of a Reference Electrode

6.1 Introduction

Direct methanol fuel cells (DMFCs) have been the focus of intensive study in recently years, because they have many advantages over hydrogen fuel cells. These advantages include high energy densities, ease of transport and distribution of fuel, and simple operation systems [1-3]. However, the performance of DMFCs is much inferior to that of hydrogen fuel cells due to the slow kinetics of methanol oxidation on state of the art catalysts, and methanol crossover. Methanol crossover not only wastes fuel but also causes depolarization of the cathode, resulting in low cell performance [4].

Obviously, the development of high performance DMFCs depends on better catalysts to facilitate the slow kinetics of electro-oxidation of methanol and better membranes to suppress methanol crossover. In addition, optimization of all of the components of a DMFC and its operating conditions are also important for achieving high performance [3, 5]. It was reported that methanol crossover could be reduced significantly by optimizing electrode structure and operating conditions [5].

Optimization of DMFC performance and operating conditions is greatly simplified by the availability of detailed information on individual potential losses at the anode and cathode, and this information can only be acquired by using a reference electrode. Kuver and coworkers [6] have demonstrated that the polarization of a DMFC can be resolved into anode polarization and cathode polarization curves by using a DHE reference electrode. By using the same configuration reference electrode as that used by Kuver and

coworkers, Ren and coworkers [7] further analyzed the performance of DMFCs using two types of Nafion membranes. They found that there was a noticeable methanol concentration polarization at the anode at high current densities when the concentration of methanol(aq) was below 1 M. They also found that the performance of the cathode was strongly influenced by the concentration of methanol.

Instead of using a DHE reference electrode to measure anode polarization curves, the cathode of the fuel cell can be supplied with H_2 and used as both a reference electrode and a counter electrode to determine the polarization curve of a methanol-fed anode [5]. However, this method does not provide anode polarization information on an operating DMFC, and so the results may be misleading.

Impedance studies of DMFCs have drawn increasing attention in recent years [8-10]. In previous work, anode impedances were determined by two approaches. One used a hydrogen-fed cathode as a reference electrode to determine the impedance of the methanol-fed anode [11-12]. The problem with this method is that it does not provide the anode impedance of an operating DMFC. The other method involved using a Pt wire in the methanol solution as a reference electrode [10]. However, data obtained at high frequencies were very noisy, and this was explained as being due to the placement of the reference electrode in a low conductivity medium [10].

In the work presented in this chapter, the performance losses of DMFCs have been separated into the performance loss at the anode and the cathode with the aid of a DHE reference electrode. Polarization measurements and impedance spectroscopy were used to analyze performance losses. The information obtained sheds light on how the performance and operating conditions of a DMFC can be optimized.

6.2 Experimental

Experimental details are described in Chapter four.

6.3 Results and Discussion

6.3.1 Analysis of Anode Performance Losses

6.3.1.1 Polarization Measurements

Figure 6.1 shows polarization curves for the anode of a DMFC operated with two different methanol concentrations. It is seen that in the low current density region, the anode potential increased dramatically with increasing current density. This reflects the slow kinetics of electro-oxidation of methanol on the anode. In the high current density region, the anode potential did not increase sharply with increasing current density, indicating the absence of concentration polarization.

Another interesting finding is that, in the low current density region, the performance of the anode with 1 M methanol(aq) was better than with 2 M methanol, while in the high current density region, the performance of the anode with 2 M methanol was better than with 1 M methanol. Unfortunately, the current density of the anode with 2 M methanol could not go as high as that with 1 M methanol due to the worse performance of the cathode when 2 M methanol was used (see below). Ren and coworkers [7] also found that in the high current density region, the performance of an anode with 2 M methanol was better than with 1 M methanol.

The anode performance differences with different methanol concentrations can be explained as follows. In the low current density region (low overpotentials), more methanol was absorbed on the anode when the methanol concentration was higher. The adsorbed methanol can inhibit formation of oxygenated species which are involved in

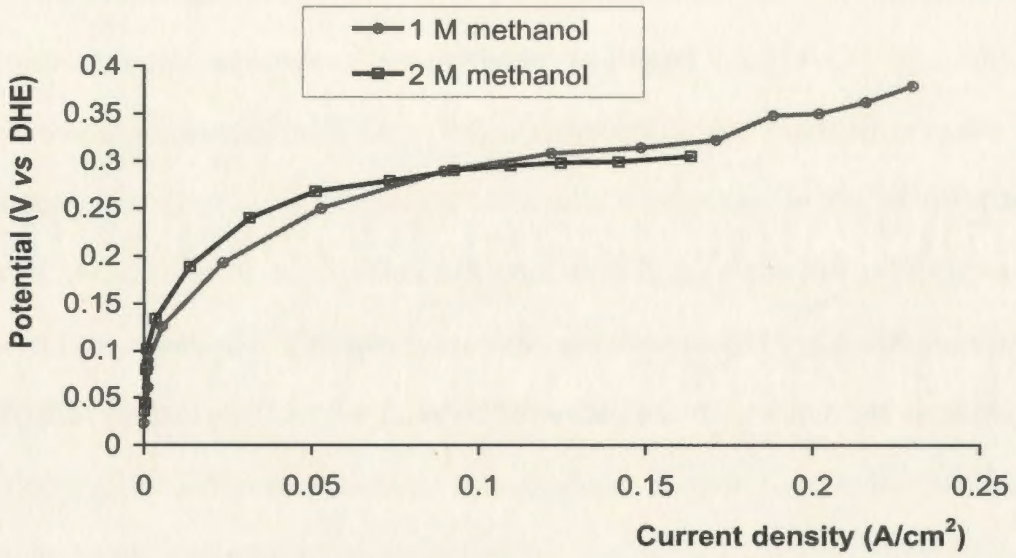

Figure 6.1. Anode polarization curves for a 5 cm^2 DMFC fed with 60 °C methanol(aq) of different concentrations at the anode and air at the cathode with Nafion 117 as the membrane. The cell was operated at 60 °C.

the oxidation of adsorbed CO [13]. In the high current density region (high overpotentials), the adsorbed CO was oxidized and the problem with CO adsorption became insignificant. At the same time, other factors such as the methanol transport resistance may become marked. The better performance of the anode with 2M methanol was likely due to a lower methanol transport resistance.

6.3.1.2 Impedance Spectroscopy

The impedance behavior of a porous electrode can be modeled by the finite transmission line equivalent circuit shown in Figure 6.2 [14-17]. The circuit consists of two parallel resistance rails. One (R_{ionic}) represents ionic conduction in the catalyst layer, and the other ($R_{electronic}$) represents electronic conduction in the catalyst layer. $R_{electronic}$ can be assumed to be negligible compared with R_{ionic}, since Pt/Ru black was used here as an electron conductor. The resistance rails are connected by a distributed impedance ($Z = \sum Z_i$) that represents both the faradaic impedance and double layer capacitance. Z_i can be represented by different equivalent circuits depending on the conditions of the experiment (e.g. potential, presence of electroactive species, mass transport conditions).

For a methanol-fed anode at low overpotentials, Z_i can be approximately represented by the equivalent circuit shown in Figure 6.3 (a) [15]. Here, $C_{dl,A}$ is the double layer capacitance, $R_{ct,A}$ is the charge transfer resistance for methanol oxidation, Z_{ad} is the impedance due to CO adsorption, and $Z_{w,A}$ is a Warburg impedance that represents the mass transport resistance. At high overpotentials, the adsorbed CO begins to be oxidized, and Z_{ad} becomes insignificant. Eventually, the oxidation of adsorbed CO leads to inductive behavior. Therefore, we use an inductor (L) to replace Z_{ad} as shown in Figure 6.3 (b) [18-19].

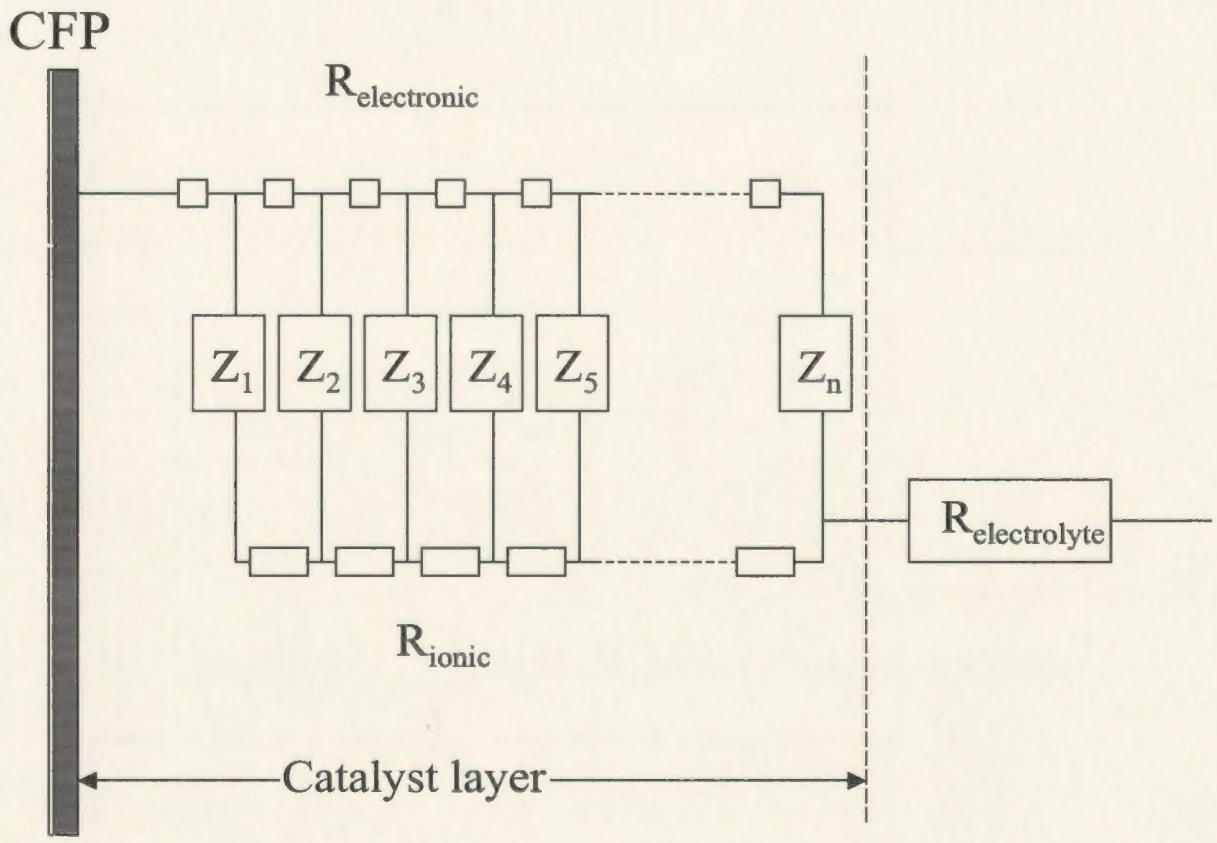

Figure 6.2. Finite transmission line equivalent circuit describing the impedance behavior of a porous fuel cell electrode.

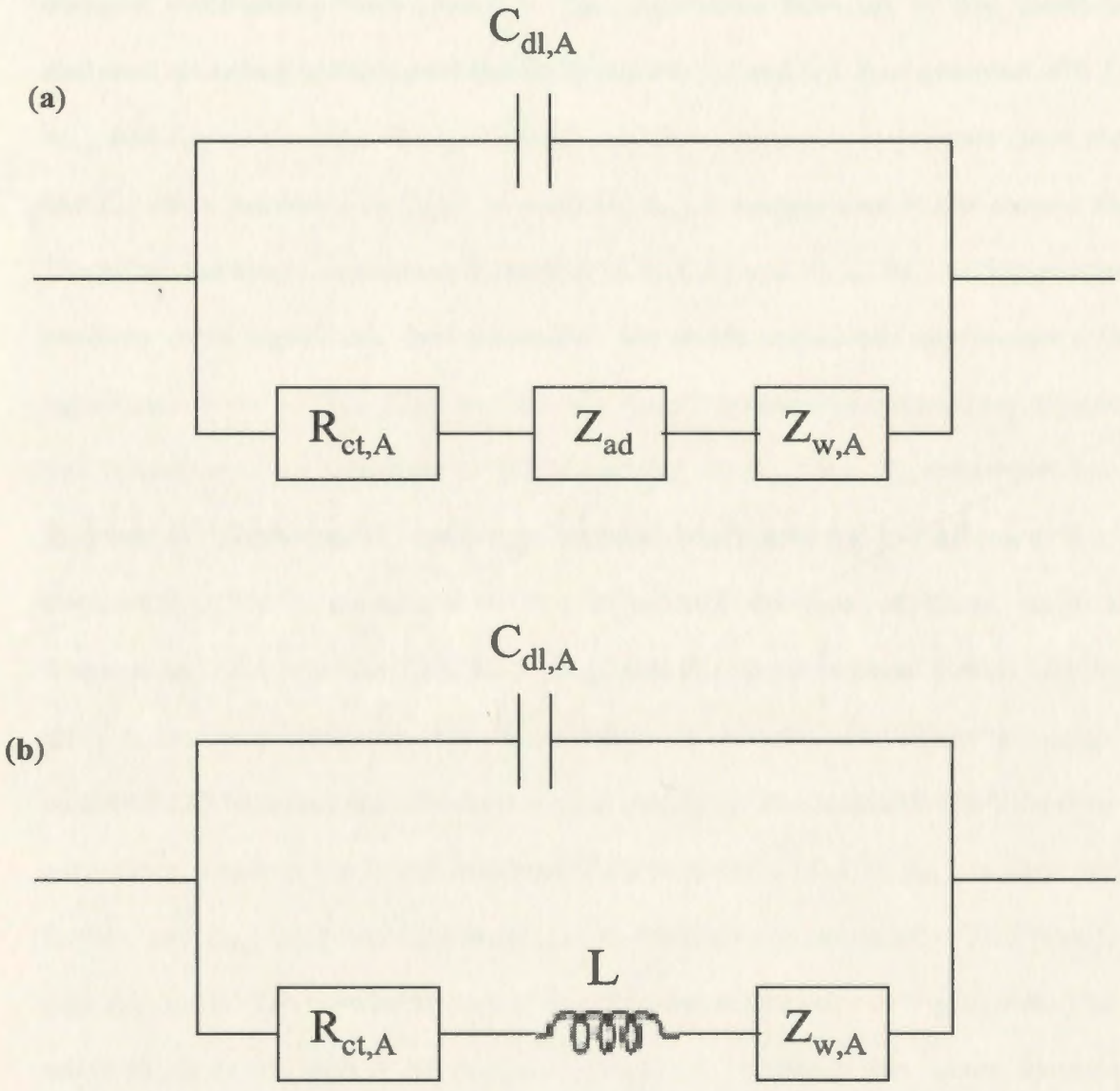

Figure 6.3. Equivalent circuits for Z_i at low overpotentials (**a**) and at high overpotentials (**b**).

Figure 6.4 shows experimental complex plane impedance plots for the anode of a DMFC as a function of anode potential. It is seen that the impedance of the anode changed significantly with potential. The impedance behavior of the anode can be analyzed according to the model shown in Figures 6.2 and 6.3. At a potential of 0.1 V, the $R_{ct,A}$ and Z_{ad} are too large to significantly influence the anode impedance (note that $R_{ct,A}$ and Z_{ad} are in parallel with $C_{dl,A}$). In addition, $Z_{w,A}$ is insignificant at low current densities. Therefore, the anode impedance is dominated by $C_{dl,A}$ and R_{ionic}. At low frequencies, $C_{dl,A}$ becomes more significant, and eventually, the anode impedance approaches a limiting capacitance equal to $C_{dl.A}$. This explains the sharp increase of the imaginary impedance at low frequencies. At potentials of 0.2 V and 0.3 V, $R_{ct,A}$ and Z_{ad} are lower due to the increase of overpotential, and they become small enough to influence the anode impedance. This is evidenced by the significant decrease of phase angle at low frequencies. At a potential of 0.35 V, $R_{ct,A}$ and Z_{ad} are decreased further. At the same time, L becomes dominant due to oxidation of adsorbed CO. That is, oxidation of adsorbed CO becomes the rate-determining step [20]. This explains the extension of the impedance plot into the fourth quadrant. At a potential of 0.4 V, $R_{ct,A}$ is decreased even further, and $Z_{w,A}$ becomes significant due to the high current density. This results in the new feature in the impedance plot at low frequencies as seen in Figure 6.4. The anode polarization curve with 1 M methanol (Figure 6.1) shows that anode overpotentials increased significantly at high current densities, indicating an increase in mass transport resistance. This supports the assertion that $Z_{w,A}$ becomes significant at high current densities.

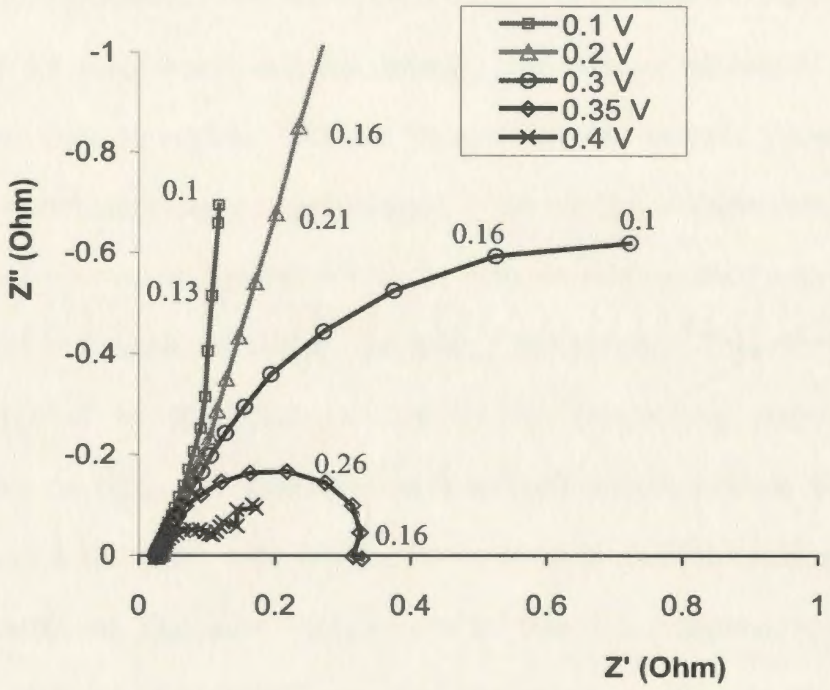

Figure 6.4. Complex plane impedance plots for the anode of a 5 cm^2 DMFC as a function of anode potential (*vs* DHE). The cell was operated at 60 °C with an anode feed of 60 °C 1 M methanol(aq) and a cathode feed of dry air. Nafion 117 was used as the membrane. The marked numbers are frequencies in Hz.

6.3.2 Analysis of Cathode Performance Losses

6.3.2.1 Polarization Measurements

Figure 6.5 shows cathode polarization curves for a DMFC with two different methanol feed concentrations. It can be seen that the open circuit potential (OCP) of the cathode decreased significantly with increasing methanol concentration. This can be attributed to depolarization of the cathode caused by methanol crossover [4].

Figure 6.5 also shows that the cathode performance decreased significantly in the high current density region. This can be attributed to cathode flooding at high current densities, which can cause a rapid increase in the oxygen transport resistance [7].

Another interesting finding is that the cathode performance with an anode feed of 2 M methanol was much worse than that with 1 M methanol. This is in agreement with the results reported by Ren and coworkers [7]. The strong dependence of cathode performance on methanol concentration is unlikely due to cathode flooding, since at the same current density, the water content in the cathode could not vary greatly between 1 M and 2 M methanol. The more likely reason for this strong dependence is due to methanol crossover, because at a higher methanol concentration, the rate of methanol crossover would be twice as high.

Figure 6.6 compares cathode performances for anodes fed with humidified hydrogen and 1 M methanol. It is seen that the OCP of the cathode with hydrogen was significantly higher than that with methanol. In addition, the cathode performance with hydrogen was much better than that with methanol. This further demonstrates the negative influence of methanol crossover on cathode performance.

Also, it can be seen that in the high current density region, the cathode potential

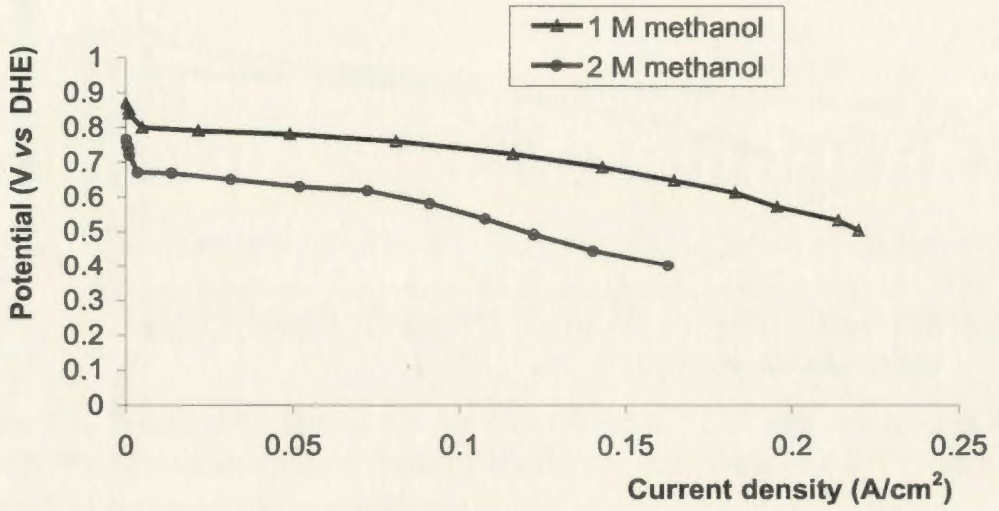

Figure 6.5. Cathode Polarization curves for a 5 cm^2 DMFC operated at 60 °C with a cathode feed of air and anode feeds of different concentrations of methanol(aq) at 60 °C. Nafion 117 was used as the membrane.

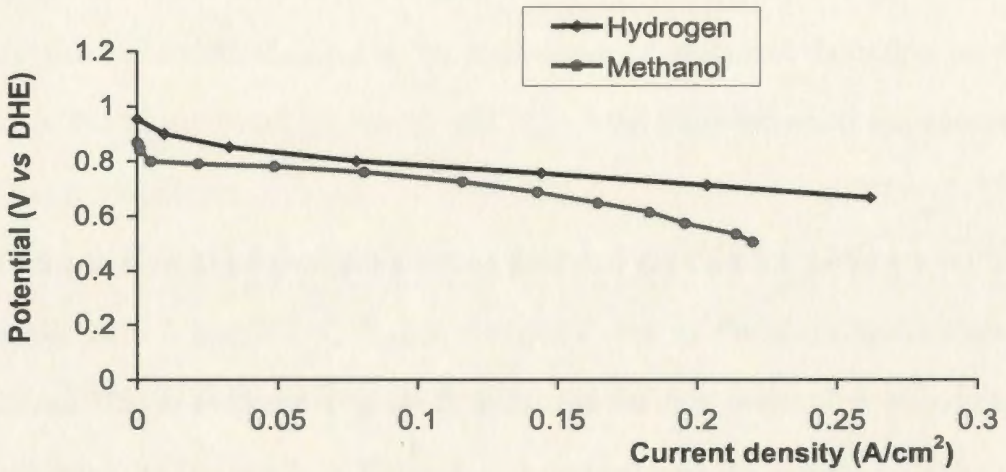

Figure 6.6. Polarization curves for the cathode of a 5 cm^2 cell operated at 60 °C with a cathode feed of air and anode feeds of humidified hydrogen or 60 °C 1 M methanol(aq). Nafion 117 was used as the membrane.

dropped much more rapidly with methanol than that with hydrogen. This is presumably due to cathode flooding since the water content in the cathode fed with aqueous methanol would have been much higher than that fed with humidified H_2.

6.3.2.2 Impedance Spectroscopy

The cathode impedance behavior of a fuel cell can also be modeled by the finite transmission line equivalent circuit shown in Figure 6.2 [16]. Here, Z_i is represented by an equivalent circuit as shown in Figure 6.7. Where $R_{ct,C}$ is the charge transfer resistance for oxygen reduction, $Z_{methanol}$ is the impedance of methanol oxidation on the cathode, which is due to methanol crossover, and $Z_{w,C}$ is the mass transport impedance associated with oxygen transport.

Cathode impedances exhibit a strong potential dependence as shown in Figure 6.8. At potentials of 0.8 and 0.7 V, $R_{ct,C}$ is dominant due to the sluggish kinetics of oxygen reduction. This is evidenced by the fact that the cathode potential dropped rapidly at low current densities (Figure 6.5). Since $R_{ct,C}$ decreases with decreasing potential (increase of overpotential), the cathode impedance at 0.7 V is smaller than that at 0.8 V as seen in Figure 6.8. At potentials of 0.6 V and below, $R_{ct,C}$ would have decreased further with decreasing potential. At the same time, $Z_{w,C}$ increases with increasing current density, and becomes significant and finally dominates the cathode impedance. The rapid drop of cathode potential at high current densities (Figure 6.5) indicates that $Z_{w,C}$ increased significantly at high current densities. The dominance of $Z_{w,C}$ results in an increase of impedance with decreasing potential. This is evidenced by the fact that the cathode impedance at 0.5 V was the largest.

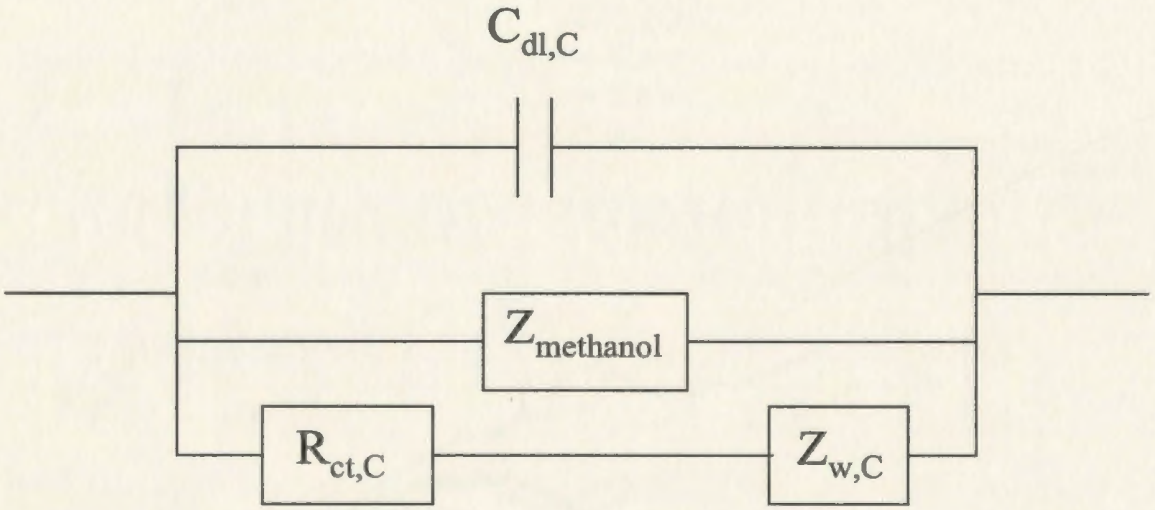

Figure 6.7. An equivalent circuit representing Z_i in Figure 6.2 for impedance of a fuel cell cathode.

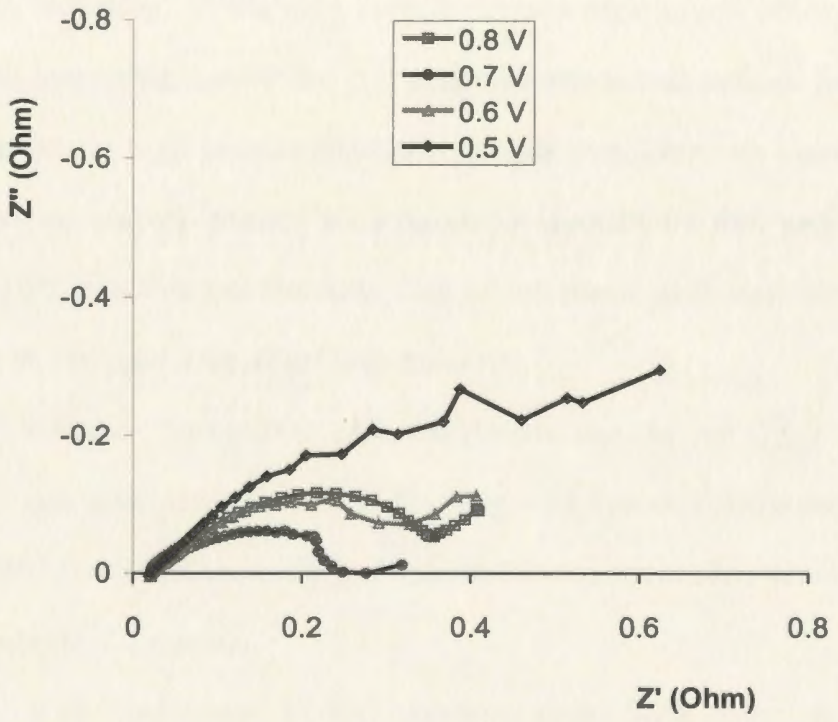

Figure 6.8. Complex plane impedance plots for the cathode of a 5 cm^2 DMFC as a function of cathode potential (*vs* DHE). The cell was operated at 60 °C with an anode feed of 60 °C 1 M methanol(aq) and a cathode feed of air.

6.3.3 Analysis of Cell Performance Losses

6.3.3.1 Polarization Measurements

Figure 6.9 shows polarization curves for a DMFC, together with cathode potentials *vs* DHE and anode potentials *vs* DHE. The cell was operated with two different methanol concentrations. It can be seen that cell performance losses come from both anode performance losses and cathode performance losses. In the low current density region, cell potentials dropped very fast, reflecting the slow kinetics of both methanol oxidation and oxygen reduction. In the high current density region, cell potentials also dropped rapidly with increasing current density. From the anode and cathode polarization curves, we can see that at high current densities, cathode overpotentials increased much faster with increasing current density than anode overpotentials did, especially with 2 M methanol. This indicates that the rapid drop of cell potential at high current densities was mainly due to the rapid drop of cathode potential.

Figure 6.9 also shows that cell polarization curves are quite close to cathode potentials-anode potentials (*vs* DHE). This suggests that cell performance losses can be separated into individual electrode performance losses reasonably accurately with the aid of a DHE reference electrode.

Figure 6.10 compares DMFC performances with two different methanol concentrations. It is seen that cell performance became much worse with the higher methanol concentration. This must be due to the rapid decrease of cathode performance with the higher methanol concentration, since anode performance improved with the higher methanol concentration.

(a)

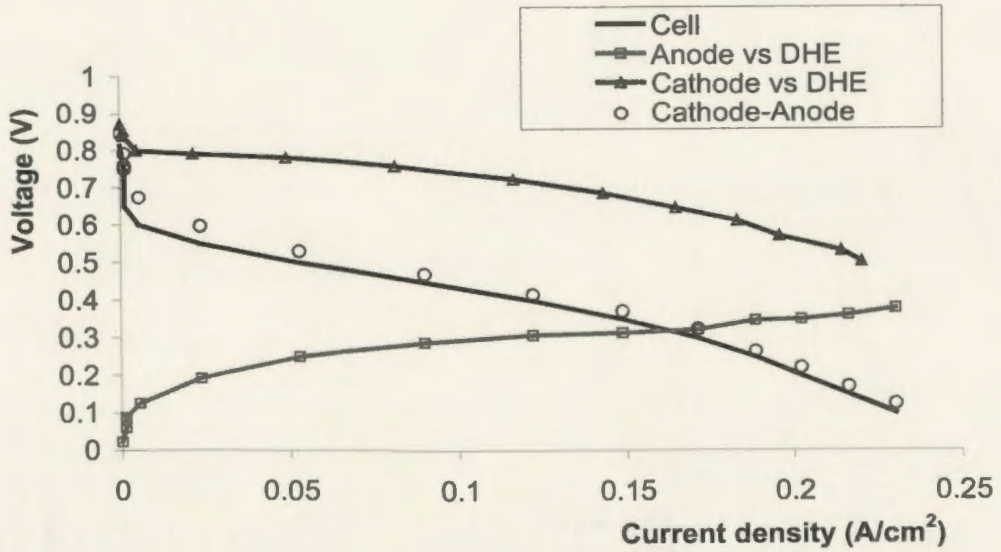

(b)

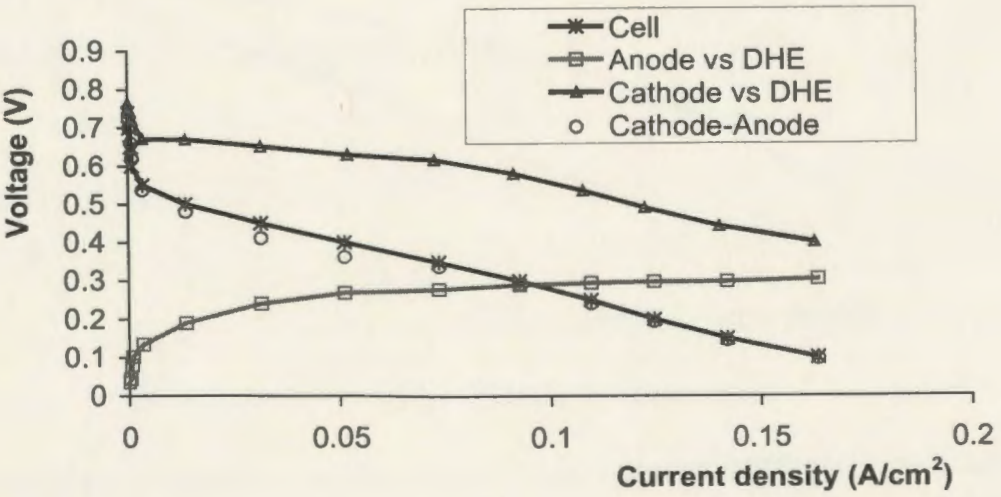

Figure 6.9. Polarization curves for a 5 cm^2 DMFC, together with cathode and anode potentials *vs* DHE. The cell was operated at 60 °C with a cathode feed of air and anode feeds of 60 °C 1 M methanol(aq) (**a**) and 2 M methanol (**b**), respectively.

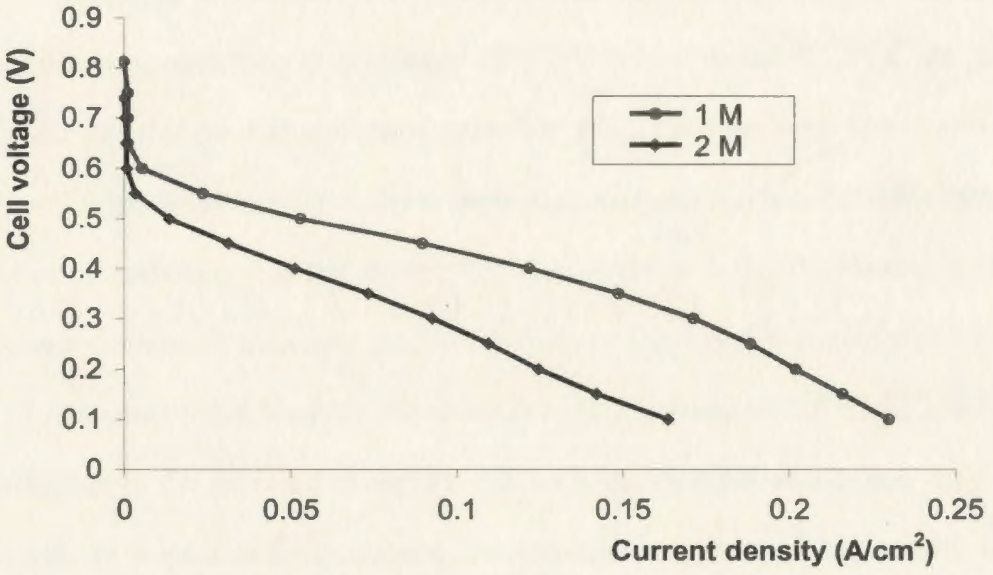

Figure 6.10. Polarization curves for a 5 cm^2 DMFC operated at 60 °C with a cathode feed of air and anode feeds of 60 °C methanol(aq) of different concentrations. Nafion 117 was used as the membrane.

In addition, the OCP of the cell with 2 M methanol was significantly lower than that with 1 M methanol. This is mainly due to a lower OCP of the cathode at the higher methanol concentration, which is caused by methanol crossover. This suggests that the magnitude of the OCP of a DMFC can be used as a measure of methanol crossover [21].

6.3.3.2 Impedance Spectroscopy

The impedance behavior of a DMFC can be modeled by equivalent circuits as shown in Figure 6.11. Essentially, these equivalent circuits are series combinations of the equivalent circuits for the cathode and anode.

Figure 6.12 shows that DMFC impedance spectra are strongly dependent on the cell voltage. It is seen that at a voltage of 0.7 V (close to the OCP of the cell), the charge transfer resistances for methanol oxidation ($R_{ct,A}$) are so large (see section 6.3.1.2) that the cell impedance mainly reflects oxygen reduction ($R_{ct,C}$), the double layer capacitances, and ionic resistances of the electrodes. At low frequencies, the double layer capacitances become dominant, and lead to the sharp rise of imaginary impedance as seen in Figure 6.12 (approaching a limiting capacitance). At a voltage of 0.6 V, $R_{ct,A}$ and $R_{ct,C}$ are both lower due to the increase of anodic and cathodic overpotentials, and they becomes small enough to significantly influence the impedance spectra. This results in a significant decrease of the phase angle at low frequencies as seen in Figure 6.12. At cell voltages of 0.5 V and 0.4 V, $R_{ct,A}$ and $R_{ct,C}$ decrease further and the inductance (L) becomes dominant due to oxidation of adsorbed CO. This results in the extension of impedance spectrum into the fourth quadrant. At cell voltages of 0.3 V and lower, with the increase of overpotentials, $R_{ct,A}$ and $R_{ct,C}$ decreased greatly and become relatively insignificant. At the same time, mass transport resistances ($Z_{w,A}$ and $Z_{w,C}$) become significant and they

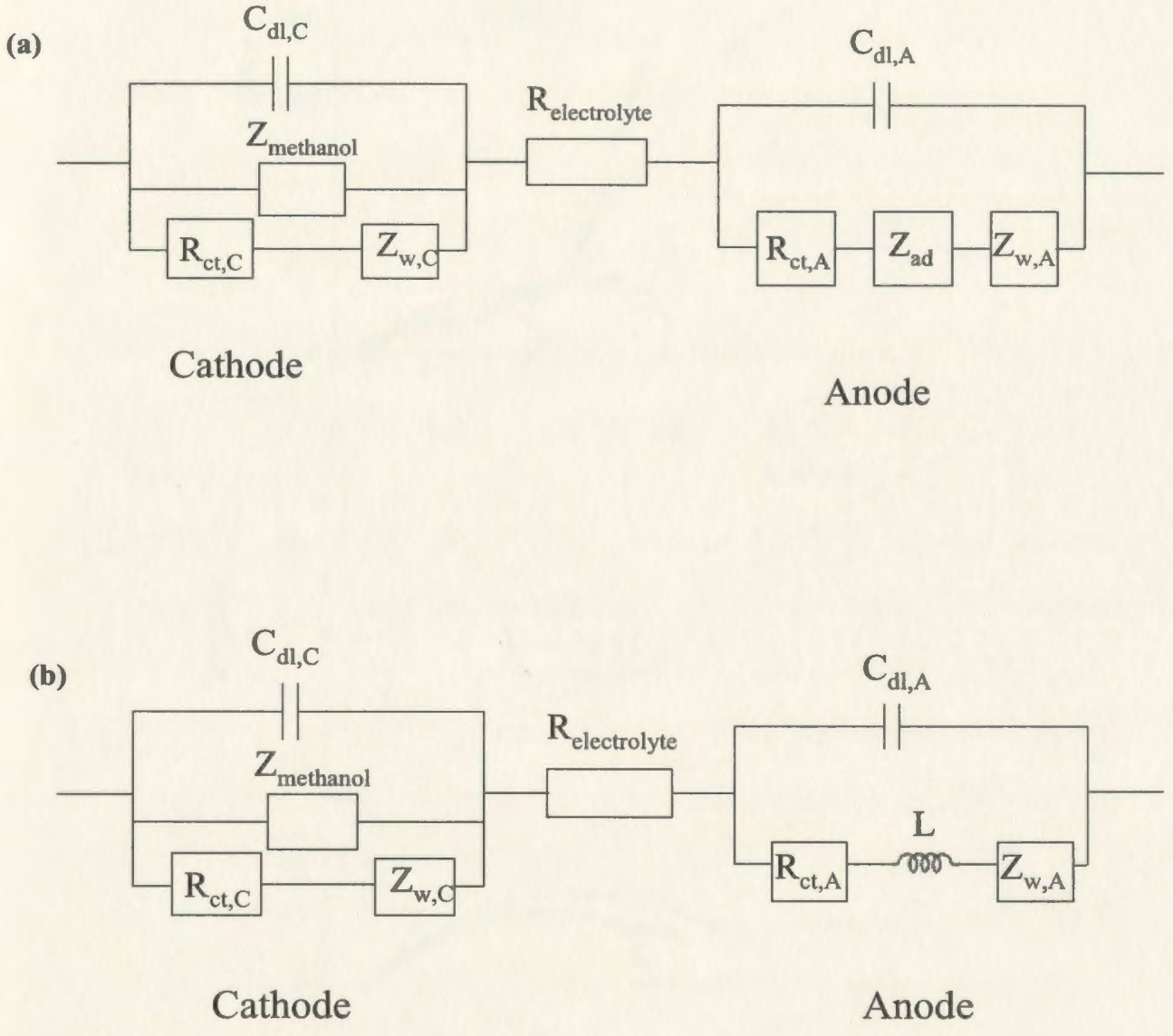

Figure 6.11. Equivalent circuits for a DMFC at high cell voltages (a) and at low cell voltages (b).

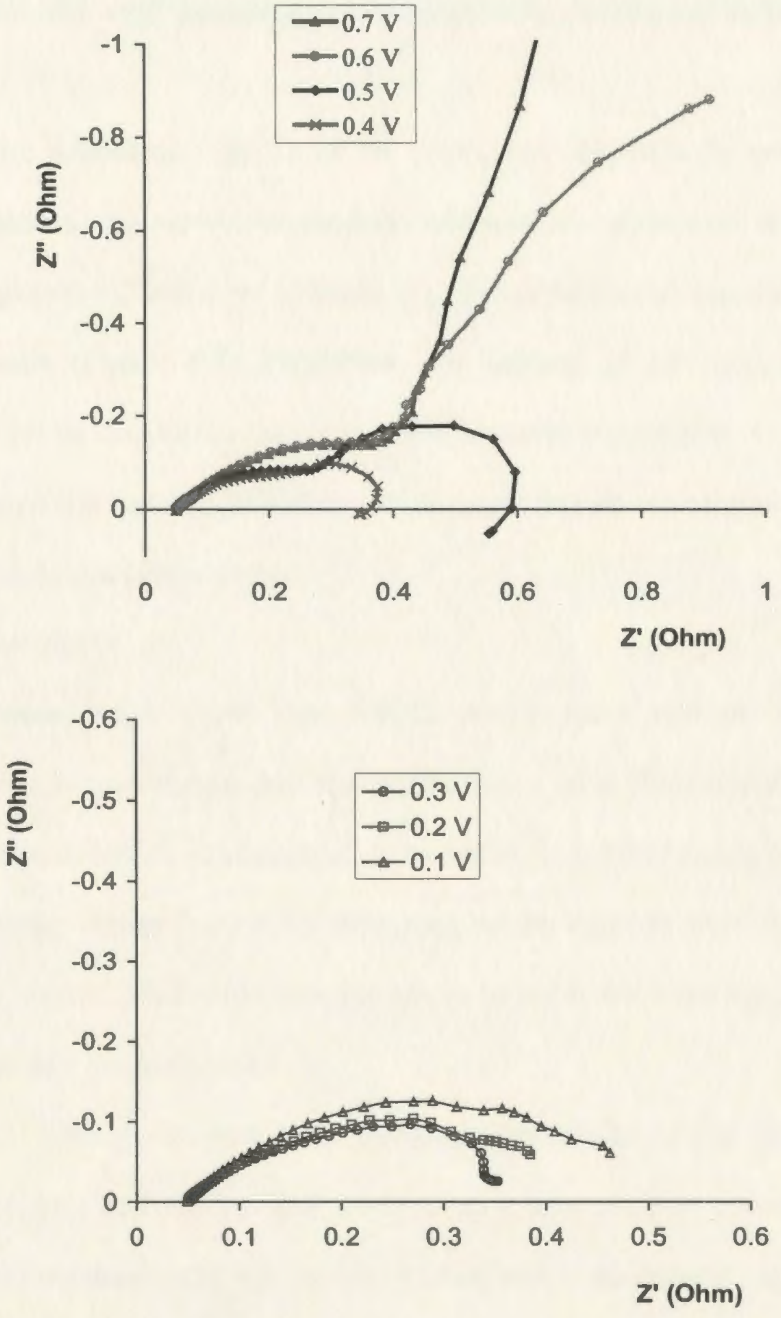

Figure 6.12. Complex plane impedance plots for a 5 cm^2 DMFC as a function of cell voltage. The cell was operated at 60 °C with an anode feed of 60 °C 1 M methanol(aq) and a cathode feed of air.

increase with decreasing cell potential (increasing current density). This is evidenced by the fact that the cell impedance increased with decreasing cell voltage at low cell voltages.

From the impedance spectra of the anode and the cathode, we can see that at high current densities, the anode impedance continuously decreased with increasing current density (Figure 6.4), while the cathode impedance increased significantly with increasing current density (Figure 6.8). Therefore, the increase of cell impedance at high current densities must be due to the increase of the cathode impedance. As we discussed before, the increase of the cathode impedance at high current densities was due to the increase of the oxygen transport resistance.

6.4 Conclusions

The present work shows that DMFC performance strongly depends on methanol concentration. It was found that the performance of a DMFC with 1 M methanol was much better than with 2 M methanol. It was also found that anode performance improved with the higher concentration of methanol, while cathode performance decreased to a much larger extent. Therefore, balance has to be made between the cathode and the anode for optimum cell performance.

Another finding is that cell performance losses come from both the anode performance loss and the cathode performance loss. At low current densities, both the cathode performance and the anode performance decreased rapidly with increasing current density. However, at high current densities, the cathode performance loss is much more significant, and this results in a rapid drop of cell potential at high current densities.

This work also shows that methanol crossover can result in a significant decrease of cathode performance. Therefore, better membranes with low methanol permeability and methanol tolerant cathode catalysts are greatly needed to improve cathode performance.

6.5 References

[1] L. Carrette, K. A. Friedrich, and U. Stimming, ChemPhysChem 1 (2000) 162.

[2] C. Lamy, A Lima, V. LeRhun, F. Delime, C. Coutanceau, and J. M. Leger, J. Power Sources 105 (2002) 283.

[3] S. C. Thomas, X. Ren, S. Gottesfeld, and P. Zelenay, Electrochim. Acta 47 (2002) 3741.

[4] X. Ren, T. E. Springer, T. A. Zawodzinski, and S. Gottesfeld, J. Electrochem. Soc. 147 (2000) 466.

[5] V. Gogel, T. Frey, Z. Y. Sheng, K. A. Friedrich, L. Jorissen, and J. Garche, J. Power Sources 127 (2004) 172.

[6] A. Kuver, I. Vogel, and W. Vielstich, J. Power Sources 52 (1994) 77.

[7] X. Ren, T. E. Springer, and S. Gottesfeld, J. Electrochem. Soc. 147 (2000) 92.

[8] K. Furukawa, K. Okajima, and M. Sudoh, J. Power Sources 139 (2005) 9.

[9] A. Havranek and K Wippermannk, J. Electroanal. Chem. 567 (2004) 305.

[10] J. P. Diard, N. Glandut, P. Landaud, B. L. Gorrec, and C. Montella, Electrochim. Acta 48 (2003) 555.

[11] J. T. Mueller, and P. M. Urban, J. Power Sources 75 (1998) 139.

[12] J. C. Amphlett, B. A. Peppley, E. Halliop, A. Sadiq, J. Power Sources 96 (2001) 204.

[13] A. O. Neto, M. J. Giz, J. Perez, E. A. Ticianelli, and E. R. Gonzalez, J. Electrochem. Soc. 149 (2002) A272.

[14] J. Bisquert, G. Garcia-Belmonte, F. Fabregat-Santiago, N. S. Ferriols, P. Bogdanoff, and E. C. Pereira, J. Phys. Chem. B 104 (2000) 2287.

[15] X. Zhao, X. Fan, S. Wang. S. Yang. B. Yi, Q. Xin, and G. Sun, International J. Hydrogen Energy 30 (2005) 1003.

[16] N. Wagner, in Impedance Spectroscopy, E. Barsoukov and J. R. Macdonald, Editors, 497-537, John Wiley & Sons, Inc. New Jersey, (2005).

[17] E. B. Easton and P.G. Pickup, Electrochim. Acta 50 (2005) 2469.

[18] J. T. Muller, P. M. Urban, and W. F. Holderich, J. Power Sources 84 (1999) 157.

[19] I. M. Hsing, X. Wang, and Y. J. Leng, J. Electrochem. Soc. 149 (2002) A615.

[20] M. Ciureanu and H. Wang, J. Electrochem. Soc. 146 (1999) 4031.

[21] V. M. Barragan and A. Heinzel, J. Power Sources 104 (2002) 66.

Chapter 7 Preparation and Characterization of Carbon Supported Pt/Sn Catalysts for Electro-Oxidation of Ethanol

7.1 Introduction

Direct methanol fuel cells have been studied intensively in recent years due to the advantages of methanol as a fuel. As a liquid fuel at ambient temperature, methanol has many advantages such as high energy density and ease of storage and transportation over hydrogen [1-2]. However, methanol is toxic, therefore, it can pose environmental problems such as air and water contamination if it is widely used [3]. In contrast, ethanol is relatively non-toxic and has many attractive advantages [2,4]. For example, ethanol is a renewable fuel, since it can be easily produced from agricultural products and biomass in large quantities. Also, ethanol can be termed as a green fuel, because the carbon dioxide produced by ethanol fuel cells is consumed by biomass growth. Finally, the theoretical energy density of ethanol oxidation is ca. 8.0 kWh/kg, comparable to that of gasoline. Surprisingly, in spite of these fascinating advantages, research on direct ethanol fuel cells is insignificant compared with that on direct methanol fuel cells. To date, only a few papers have been published on direct ethanol fuel cells.

Although the thermodynamic equilibrium potential of ethanol oxidation is only 0.084 V *vs* SHE [2], electro-oxidation of ethanol is much slower than that of hydrogen and involves multiple pathways. Side products such as acetaldehyde and acetic acid have been found during electro-oxidation of ethanol [5-6]. In addition, electro-oxidation of ethanol is more difficult than that of methanol, since complete oxidation of ethanol to CO_2 involves breaking a C-C bond. Finding active catalysts to break the C-C bond is one of

the challenges of developing direct ethanol fuel cells.

Pt has been shown to be the only active and stable single metal catalyst for electro-oxidation of ethanol in acid media [7]. However, Pt is readily poisoned by reaction intermediates such as CO and becomes inactive for ethanol oxidation in the potential region of fuel cell interest. Fortunately, a number of Pt based binary catalysts such as Pt/Ru [6,8-9], Pt/Sn [7,9-10], and Pt/Mo[6] have been found to be more active for ethanol oxidation than Pt alone. Pt/Sn binary catalysts have been shown to be more active for ethanol oxidation than Pt/Ru binary catalysts [10]. The promoting effect of the second metal to the Pt catalyst has been explained by a bi-functional mechanism and electronic (ligand) effects [3,11]. In the bi-functional mechanism, the second metal activates water at lower potentials than Pt and the activated water can oxidize the adsorbed CO and therefore liberate Pt active sites. The promoting effect of the second metal can also result, in part, from changes of the electronic properties of the Pt.

A variety of methods have been used to prepare Pt/Sn catalysts, including chemical reduction [9-10], mechanical ball milling [12], electrochemical reduction [7,13], and microfabrication techniques [14]. It has been found that the catalytic activity of Pt/Sn catalysts strongly depends on the preparation method [15-16]. For example, Gotz and coworker [17] reported that addition of Sn to Pt catalysts exhibited inhibitory effects on methanol oxidation, while other researchers [12] demonstrated that addition of Sn to Pt catalysts had pronounced promoting effects on methanol oxidation.

In the work described in this chapter, a number of carbon supported Pt/Sn catalysts were prepared and their catalytic activities for electro-oxidation of ethanol were characterized. The catalysts were prepared by co-impregnating Pt and Sn on a C support

or by successively impregnating Pt and Sn on the C support. Another aim of this work was to try to increase Pt utilization by decorating Sn with Pt, since Pt is a precious metal and its resource is very limited [18]. Theoretically, decorating Sn with Pt not only can guarantee a bi-functional mechanism but also can prevent the blockage of Pt active sites by Sn.

7.2 Experimental

7.2.1 Preparation of Catalysts

Carbon supported Pt/Sn catalysts were prepared by four different methods as follows:

7.2.1.1 Co-impregnation - Method A

40 mg of Vulcan carbon (XC-72R, E-Tek) was dispersed in 30 ml of DI water by stirring, followed by dropwise addition of 50 ml of metal precursor solution(aq) containing 21.3 mg K_2PtCl_4 (PMO Ltd) (giving a nominal 20% Pt on C) and an appropriate amount of $SnCl_4$ (Aldrich). The suspension was then stirred for 0.5 h, followed by dropwise addition of a 2 times excess of $NaBH_4$ (BDH Inc.) in 40 ml of DI water and further stirring for 0.5 h. The product was collected by filtration and washed well with copious amounts of DI water, then dried at room temperature in a vacuum oven.

7.2.1.2 Successive Impregnation - Method B

For successive impregnation, one metal was deposited on C support first, followed by impregnation of the second metal. The details were as follows:

40 mg of Vulcan carbon (XC-72R, E-Tek) was dispersed in 30 ml of DI water by stirring, followed by dropwise addition of 50 ml of metal precursor solution(aq)

containing K_2PtCl_4 or $SnCl_2 \cdot 2H_2O$ (Anachemia) and stirring for 0.5 h. A 2 times excess of $NaBH_4$ in 40 ml of DI water was then added with further stirring for 0.5 h. The product was collected by filtration and washed well with copious amounts of DI water, then dried at room temperature in a fume hood. The product was then re-dispersed in 30 ml of DI water by stirring, followed by dropwise addition of 50 ml solution(aq) of the second metal and stirring for 0.5 h. A 2 times excess of $NaBH_4$ in 40 ml of DI water was then added with further stirring for 0.5 h. The product was collected by filtration and washed well with copious amounts of DI water, then dried at room temperature in a vacuum oven.

7.2.1.3 Decoration of a Commercial Pt Catalyst - Method C

50 mg of 20% Pt on C (E-Tek) was dispersed in 30 ml of DI water by stirring. An appropriate amount of $SnCl_2 \cdot 2H_2O$ dissolved in 30 ml of DI water was then added dropwise and stirred for 0.5 h, followed by dropwise addition of a 2 times excess of $NaBH_4$ dissolved in 40 ml of DI water with further stirring for 0.5 h. The product was collected by filtration and washed well with copious amounts of DI water, then dried at room temperature in a vacuum oven.

7.2.1.4 Decoration of a Commercial Pt Catalyst - Method D

50 mg of 20% Pt on C (E-Tek) was dispersed in 30 ml of DI water by stirring. An appropriate amount of $SnCl_2 \cdot 2H_2O$ dissolved in 30 ml of DI water was then added dropwise and stirred for 1 h. The product was collected by filtration and washed well with copious amounts of DI water, then dried at room temperature in a vacuum oven.

7.2.2 Characterization of Catalysts

7.2.2.1 X-ray Photoelectron Spectroscopy (XPS)

XPS analysis of the catalysts was performed at Ecole Polytechnique de Montreal.

7.2.2.2 X-ray Diffraction (XRD)

XRD patterns of the catalysts were obtained on a X-ray diffracometer (Rigaku D/Max-2200V-PC) using a Cu K_α source ($\lambda = 1.5418\ \Delta$) at a scan rate of 1.5 degrees per minute. The scan range was from 20 degrees to 120 degrees. Samples were ground in a mortar before measurements.

7.2.2.3 Transmission Electron Microscopy (TEM)

TEM images of the catalysts were acquired with a Zeiss 109 high resolution TEM at 70 keV. Samples for TEM measurements were prepared as follows: 2 mg of the catalyst was dispersed in 500 μl of ethanol by sonication for 30 minutes. A drop of the resulting ink was then deposited onto a carbon coated copper grid and dried at room temperature.

7.2.2.4 Energy Dispersive X-ray Microanalysis (EDX)

EDX analyses of the catalysts were conducted on a Tracor Northern 5500 energy dispersive X-ray analyzer. X-ray data were analyzed with Tracor Northern's Software (SQ) for standardless analysis.

7.2.3 Electrochemistry

7.2.3.1 Preparation of Electrodes

2 mg of the catalyst was dispersed in 500 μl of 5% Nafion solution (DuPont) by sonication for 50 minutes. 2 μl of the resulting ink was then deposited onto a 0.071 cm^2 glassy carbon electrode with a micropipet and dried at room temperature, giving a catalyst loading of ca. 0.11 mg/cm^2. The glassy carbon electrode was polished with 0.3 μm alumina before deposition. For long term electrolysis, the electrode was prepared as follows: 5 mg of the catalyst was mixed with 20 mg of 5% Teflon suspension by

sonication for 30 minutes. The resulting paste was then applied onto 1 cm^2 of carbon fiber paper (CFP) and dried at room temperature.

7.2.3.2 Electrochemical Measurements

Electrochemical measurements were carried out in a conventional three-compartment cell at room temperature with an EG&G PAR 273A potentiostat/galvanostat or a Solartron 1286 electrochemical interface. A Pt wire was used as the counter electrode. The reference electrode was a SCE (0.24 V *vs* SHE). However, all potentials are reported with respect to the SHE. Before measurements the electrolyte solution was purged with pure N_2 to expel oxygen, and then protected with N_2 during measurements.

7.3 Results and Discussion

7.3.1 XPS

Figure 7.1 shows a XPS survey spectrum of a carbon supported Pt/Sn (4:1) catalyst prepared by method C. It can be seen that the catalyst contained C, Pt, and Sn as expected. It also contained oxygen, indicating that some elements were in an oxide form. The atomic % of O in the catalyst was 10.5 as listed in Table 7.1. It was also found that the atomic ratio of Pt to Sn was ca. 2:1, much lower than the nominal ratio of 4:1. This is in good agreement with the results reported by Crabb and coworkers [16] who also found that experimental surface atomic ratios of Pt/Sn determined with XPS were ca. half of nominal atomic ratios for their Pt/Sn catalysts prepared from organometallic precursors using surface organometallic chemistry. The surface enrichment of Sn can be explained as being due to the nature of catalyst preparation methods and XPS analysis, since XPS only reflects surface information [16].

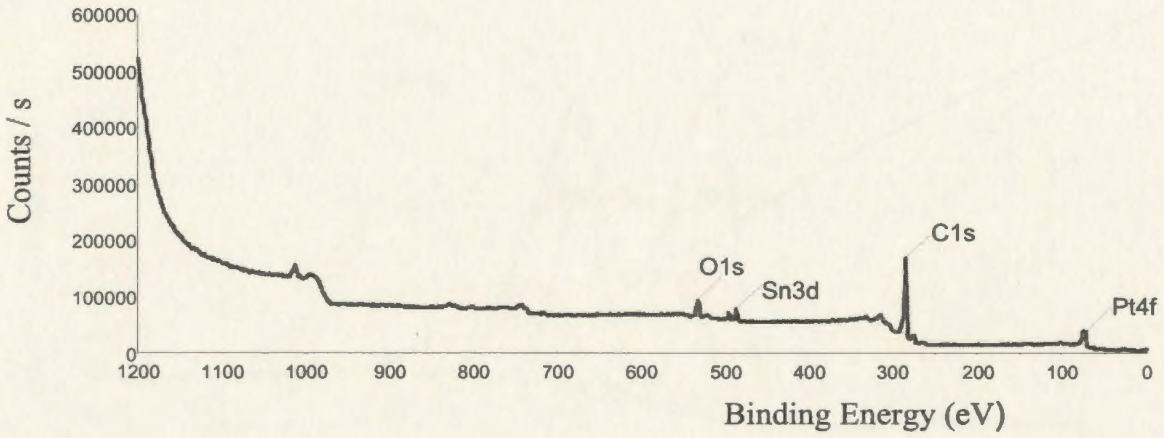

Figure 7.1. A XPS survey spectrum of a carbon supported Pt/Sn (4:1) catalyst prepared by method C.

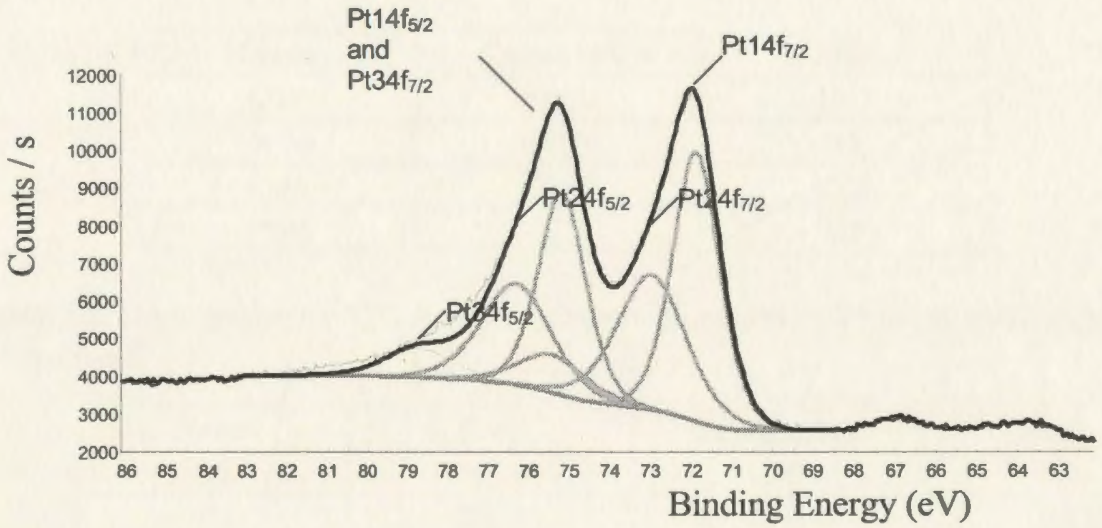

Figure 7.2. A high resolution XPS spectrum of the Pt region of Figure 1.

Figure 7.2 shows a high resolution XPS spectrum of Pt in the catalyst. It can be seen that there are three different oxidation states for Pt. They are Pt (0), Pt (II), and Pt (IV). The atomic % of Pt (0)/Pt (II)/Pt (IV) was 1.8/1.3/0.4 (Table 7.2), indicating that only ca. 50% of the Pt was in the metallic state on the catalyst surface, although the catalyst has been reduced with $NaBH_4$. The higher oxidation states of Pt are assumed to be due to the formation of $Pt\text{-}O_{ads}$ and surface PtO and PtO_2 [19].

Table 7.1. XPS survey data for a carbon supported Pt/Sn (4:1) catalyst prepared by method C

Element	Center (eV)	% atomic
O1s	533.0	10.5
Sn 3d	487.0	0.7
C 1s	285.0	97.3
Pt 4f	72.0	1.5

Table 7.2. High resolution XPS data for a carbon supported Pt/Sn (4 :1) catalyst prepared by method C

Name	B.E. (eV)	Identification	% atomic
C1	285.0	C-C	51.4
C2	286.3	C-O	15.7
C3	287.7	C=O	7.1
C4	289.1	O-C=O	5.9
C5	291.2	Shake-up π- π^*	3.6
O1	531.3	O-metal	2.6
O2	532.7	C=O	3.3
O3	534.0	C-O	3.3
O4	535.3	?	1.2
O5	536.7	?	0.5
Pt1	71.9-75.2	Pt° and Pt-Sn	1.8
Pt2	73.0-76.3	Pt (II)	1.3
Pt3	75.4-78.7	Pt(IV)	0.4
Sn1	487.4-495.9	Sn(II) and Sn(IV)	2.0

Figure 7.3 shows a high resolution XPS spectrum of Sn in the catalyst. As shown in the figure, there are two peaks corresponding to Sn (II) and/or Sn (IV). No peaks for metallic Sn were found. This indicates that Sn existed in the oxide forms on the catalyst surface, although $NaBH_4$ was added as the reducing agent. Other researchers also found that most tin atoms existed as oxides in Pt/Sn catalysts prepared with different methods [16,19-20]. In addition, it is impossible to distinguish between Sn (II) and Sn (IV) by XPS, since their binding energies are quite close [19-20].

In conclusion, only ca. 50% of the Pt was in the metallic state on the catalyst surface and no evidence of metallic Sn was found on the catalyst surface. This means that no Pt and Sn alloys were formed on the catalyst surface.

7.3.2 XRD

Figure 7.4 presents XRD patterns of different carbon supported Pt/Sn catalysts, together with that of 20% Pt on C from E-Tek. The diffraction peak at ca. 25° is due to the C (002) plane, while the peaks at ca. 40°, 46°, 67.5°, and 81.5° represent the Pt (111), Pt (200), Pt (220), and Pt (311) planes, respectively. No peaks for Sn or Pt/Sn alloys were observed, suggesting that Sn was either highly dispersed or in an amorphous state [16]. XPS data clearly show that Sn was in an oxidized state in one sample, at least. Therefore, Sn was more likely in an amorphous state in the Pt/Sn catalysts.

Figure 7.5 compares XRD patterns of homemade 20% Pt on C and commercial 20% Pt on C catalysts. It can be seen that XRD patterns for the two catalysts are quite similar and that the commercial catalyst has wider peaks. This indicates that they have similar crystal structures and the particle size of the commercial catalyst was smaller than that of the homemade catalyst.

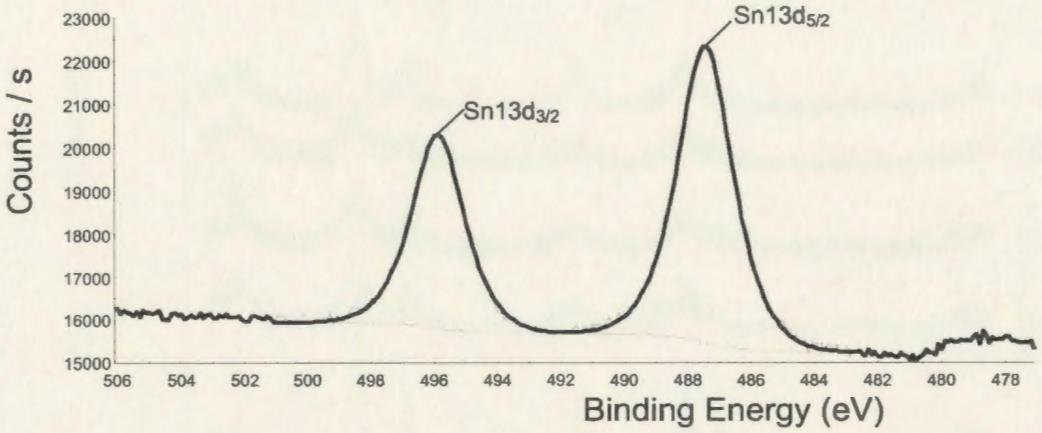

Figure 7.3. A high resolution XPS spectrum of the Sn region of Figure 1.

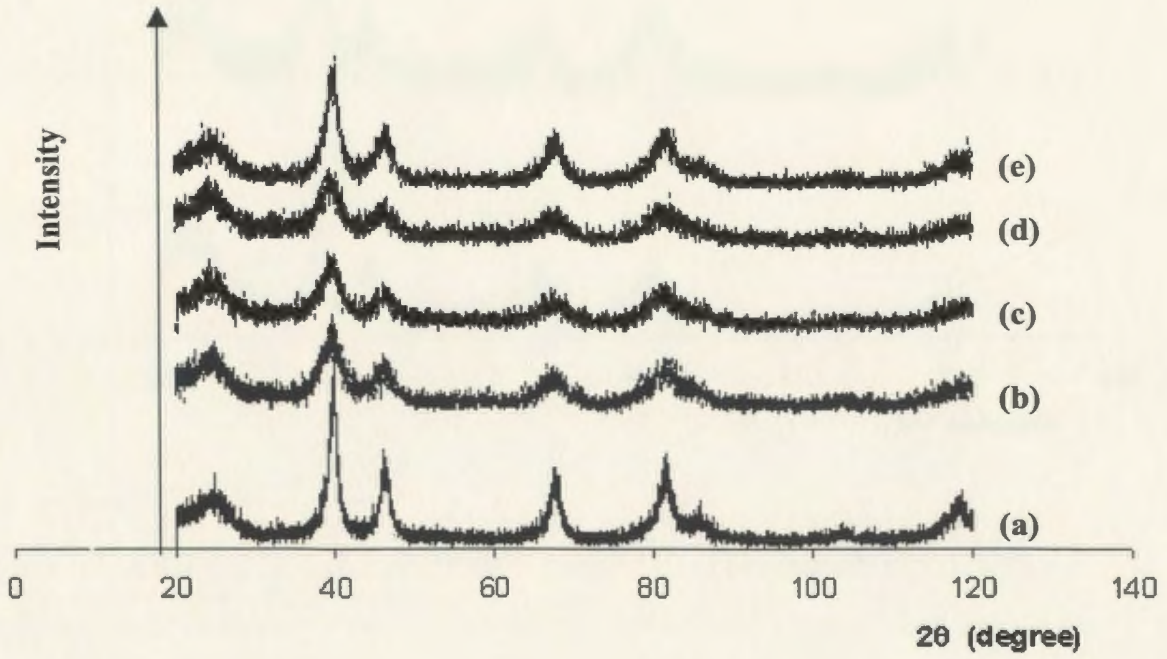

Figure 7.4. XRD patterns for carbon supported Pt/Sn catalysts. (a) Pt/Sn (5:1) from method A; (b) 20% Pt on C (E-Tek); (c) Pt/Sn (4:1) from method C; (d) Pt/Sn (4:1) from method D; (e) Pt/Sn from method B.

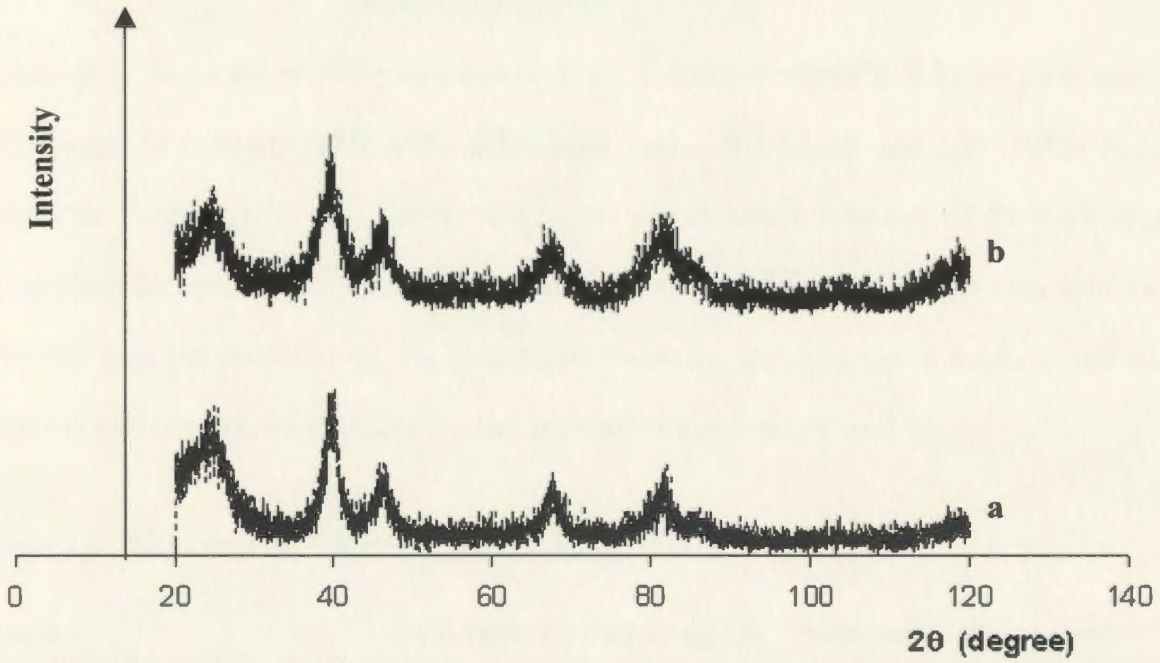

Figure 7.5. XRD patterns of 20% Pt on C catalysts. (a) Homemade; (b) E-Tek.

The mean particle sizes were estimated from the (111) peak width according to the Scherrer equation [9, 21]:

$$D = 0.9\lambda/(B \cos \theta) \qquad (7.1)$$

where D is the mean particle diameter, λ is the X-ray wavelength, B is the peak width at half height in radians, and θ is the diffraction angle. The results and other XRD data are listed in Table 7.3. It was found that there was a small increase of Pt particle size following decoration with Sn, as observed by other researchers [16]. It was also found that the catalyst prepared by the co-impregnation method (A) had a much larger mean particle size than those prepared by the decoration methods (C and D).

Table 7.3. XRD data of different catalysts based on the111 plane

Name	2θ (degree)	d-spacing (Å)	mean particle size (nm)	
20% Pt on C (E-Tek)	39.80	2.2630	2.5	5*
20% Pt on C (homemade)	39.99	2.2522	4.2	7.5
Pt/Sn (5:1) from method A	39.66	2.2707	5.4	6
Pt/Sn (4:1) from method B	39.76	2.2651	4.2	7.6
Pt/Sn (4:1) from method C	39.17	2.2980	2.8	5
Pt/Sn (4:1) from method D	39.15	2.2989	2.8	5

* The particle sizes in this column were estimated from TEM.

7.3.3 TEM

The morphology and particle size distribution of the catalysts were observed by TEM. Figures 7.6a and 7.6b show TEM micrographs of carbon supported Pt/Sn catalysts prepared by different methods. It is seen that the Pt/Sn particles were evenly distributed on the carbon support. It was found that the particle sizes of the catalysts prepared by

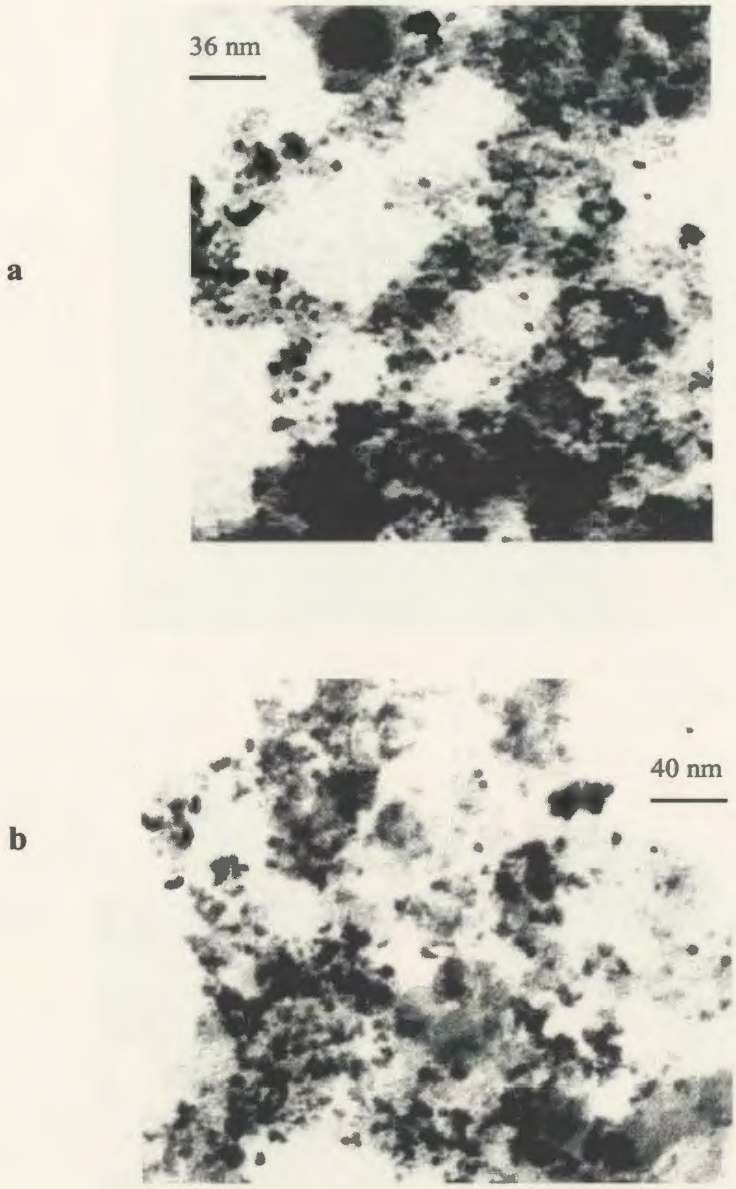

Figure 7.6a. TEM micrographs of carbon support Pt/Sn catalysts. (a) Pt/Sn (5:1) from method A; (b) Pt/Sn (4:1) from method B.

c

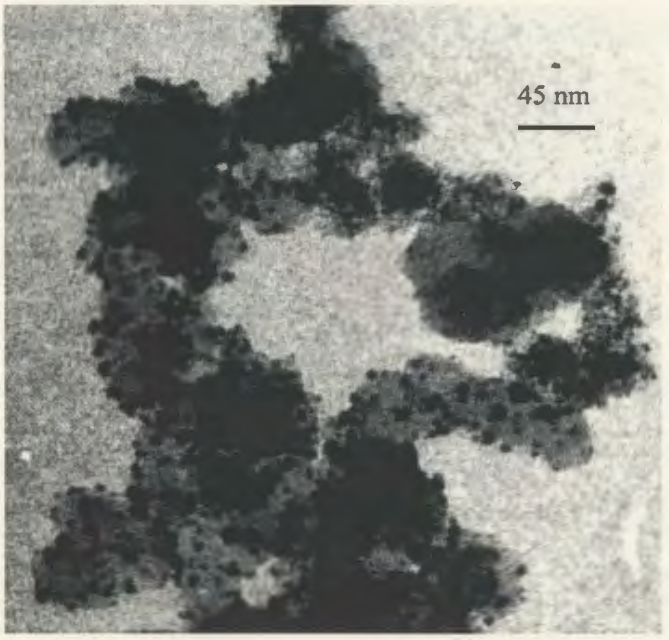

d

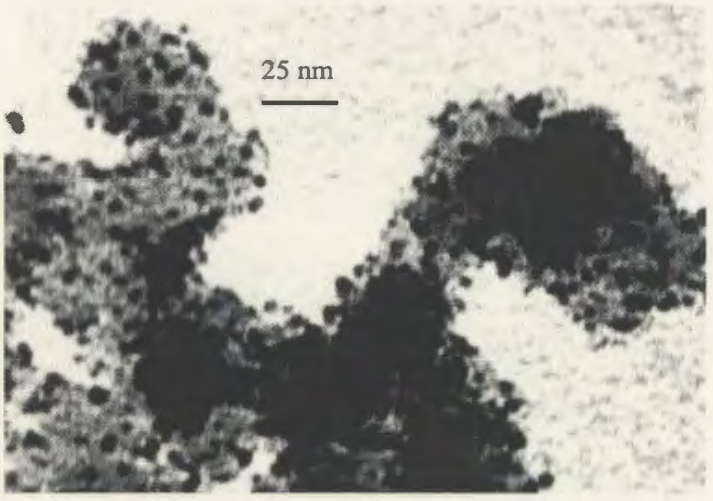

Figure 7.6b. TEM micrographs of carbon supported Pt/Sn catalysts. (c) Pt/Sn (4:1) from method C; (d) Pt/Sn (4:1) from method D.

methods A and B were bigger than those prepared by methods C and D. This indicates that the catalysts prepared by methods C and D had larger active surface areas than the catalysts prepared by methods A and B. It was also found that the particle sizes estimated from TEM were larger than those estimated from XRD (Table 3). This is probably due to the difference of two techniques [16], since larger particles are more easily observed in TEM micrographs, and the larger particles may consist of several crystallites.

Figure 7.6c compares TEM micrographs of the commercial 20% Pt on C catalyst with that of the homemade 20 % Pt on C catalyst. It can be seen that the Pt particles were evenly distributed on the carbon support for both catalysts. In addition, the commercial catalyst had smaller particle sizes than the homemade catalyst. This is consistent with the results estimated from XRD.

7.3.4 EDX

Figure 7.7 presents an EDX spectrum of a carbon supported Pt/Sn (4:1) catalyst prepared by method C. It clearly shows that Sn had been incorporated into the Pt catalyst. The atomic ratio of Pt to Sn determined from EDX was 6:1, much higher than the nominal value of 4:1. Interestingly, the atomic ratio of Pt to Sn determined by XPS was 2:1, half of the nominal value. These differences are acceptable given the semiquantitative nature of EDX, and the surface selectivity of XPS.

7.3.5 Cyclic Voltammetry (CV)

The electrochemically active areas of the catalysts were determined by CV in 1 M H_2SO_4(aq). Figure 7.8 compares a CV of an E-Tek 20% Pt on C catalyst with that of a carbon supported Pt/Sn (4:1) catalyst prepared by method C. It is seen that the hydrogen adsorption waves on the Pt/Sn catalyst were smaller than those for the Pt catalyst,

a

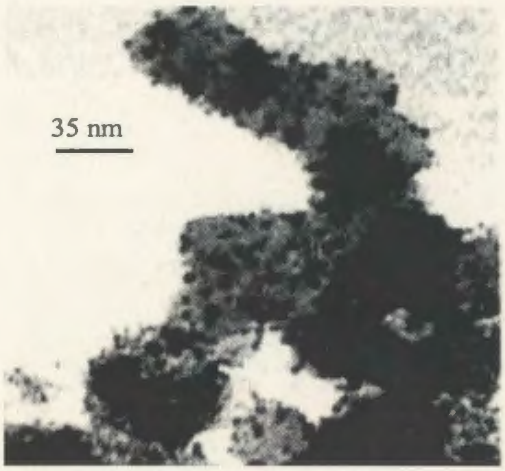

b

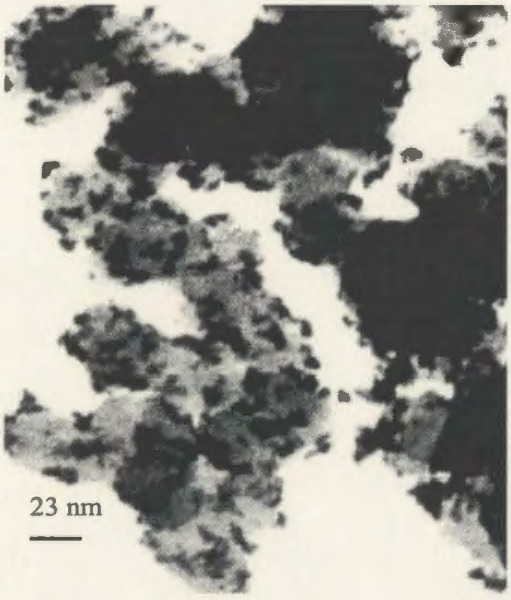

Figure 7.6c. TEM micrographs of 20% Pt on C catalysts. (a) E-Tek; (b) Homemade.

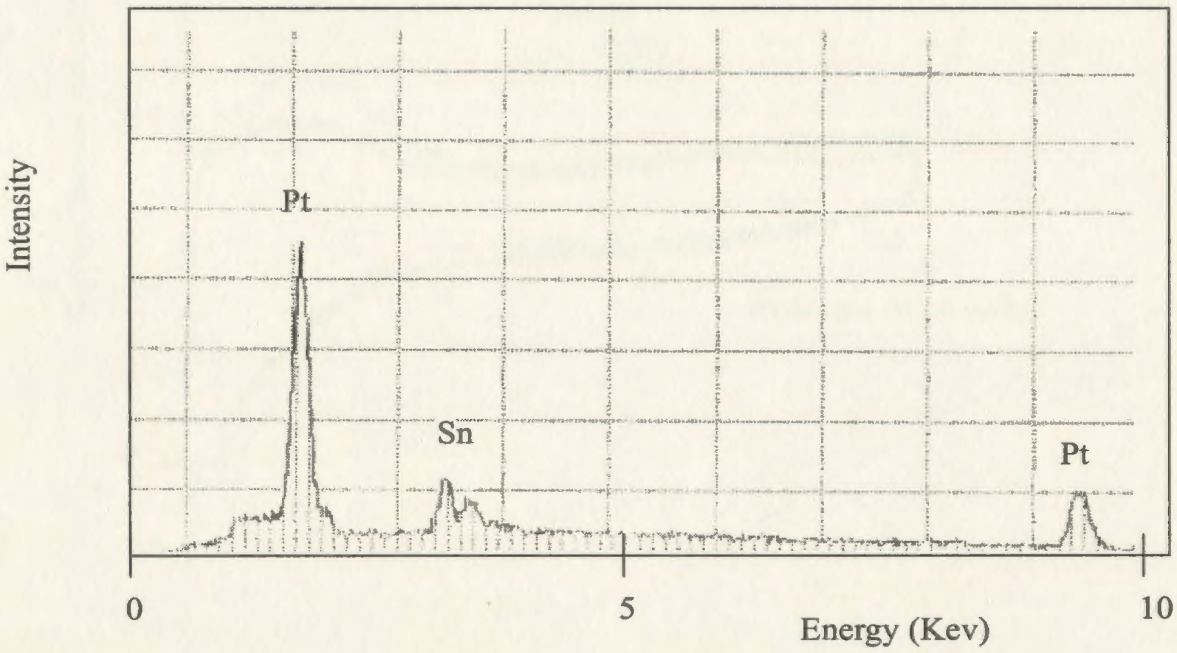

Figure 7.7 An EDX spectrum of a carbon supported Pt/Sn (4:1) catalyst prepared by method C.

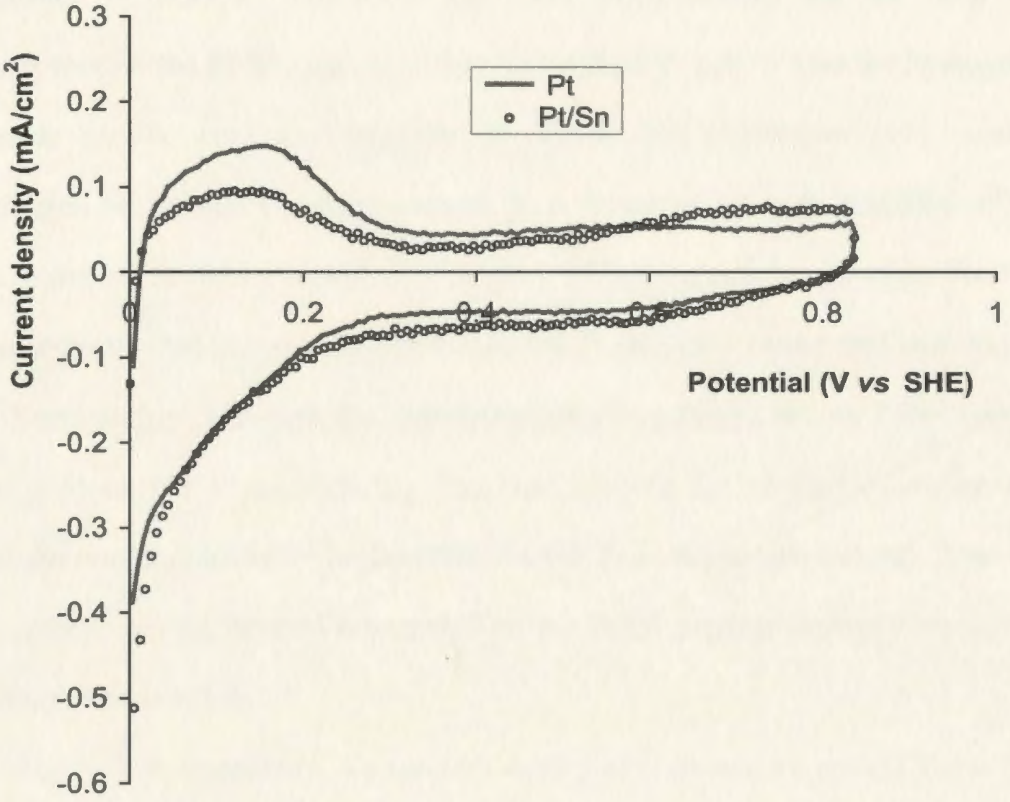

Figure 7.8. Cyclic voltammetry in 1 M H_2SO_4(aq) of an E-Tek 20% Pt on C catalyst and a carbon supported Pt/Sn (4:1) catalyst prepared by method C. Scan rate: 10 mV/s.

indicating that some of the Pt active sites for hydrogen adsorption were blocked by Sn or the electronic properties of Pt changed significantly by addition of Sn. Frelink and coworkers [22] reported that Sn was preferentially deposited onto Pt active sites for hydrogen adsorption. Therefore, the more likely reason for the drop of hydrogen adsorption on the Pt/Sn catalyst is that Sn blocked Pt active sites for hydrogen adsorption. Similar results were also reported by Crabb and coworkers [16], who found that hydrogen adsorption on Pt decreased by a factor of 30 with addition of 1 monolayer equivalent of Sn to a Pt catalyst. The drop of hydrogen adsorption on the Pt/Sn catalyst also suggests that Sn was deposited onto the Pt particles, rather that onto the C support.

Surprisingly, although the chemisorption of hydrogen on the Pt/Sn catalyst was less than that on the Pt catalyst, the catalytic activity for ethanol oxidation on the Pt/Sn catalyst was significantly higher than on the Pt catalyst (see below). This suggests that the active sites for ethanol adsorption on the Pt/Sn catalyst were different from those for hydrogen adsorption.

Figure 7.9 compares CVs (second cycle) of a carbon supported Pt/Sn (4:1) catalyst prepared by method C in 1 M H_2SO_4(aq) before and after electrolysis of 1 M ethanol(aq) for one hour at a potential of 0.5 V *vs* SHE. It is seen that the hydrogen adsorption peaks did not change significantly. This suggests that dissolution of Sn into the acidic ethanol aqueous solution was insignificant. Otherwise, the hydrogen adsorption peaks on the catalyst should increase significantly after long term electrolysis.

Figure 7.10 shows CVs of different 20% Pt on C catalysts in 1 M H_2SO_4(aq). It is seen that hydrogen adsorption waves on the E-Tek catalyst were significantly larger than those on the homemade catalyst, indicating that the E-Tek catalyst had a larger

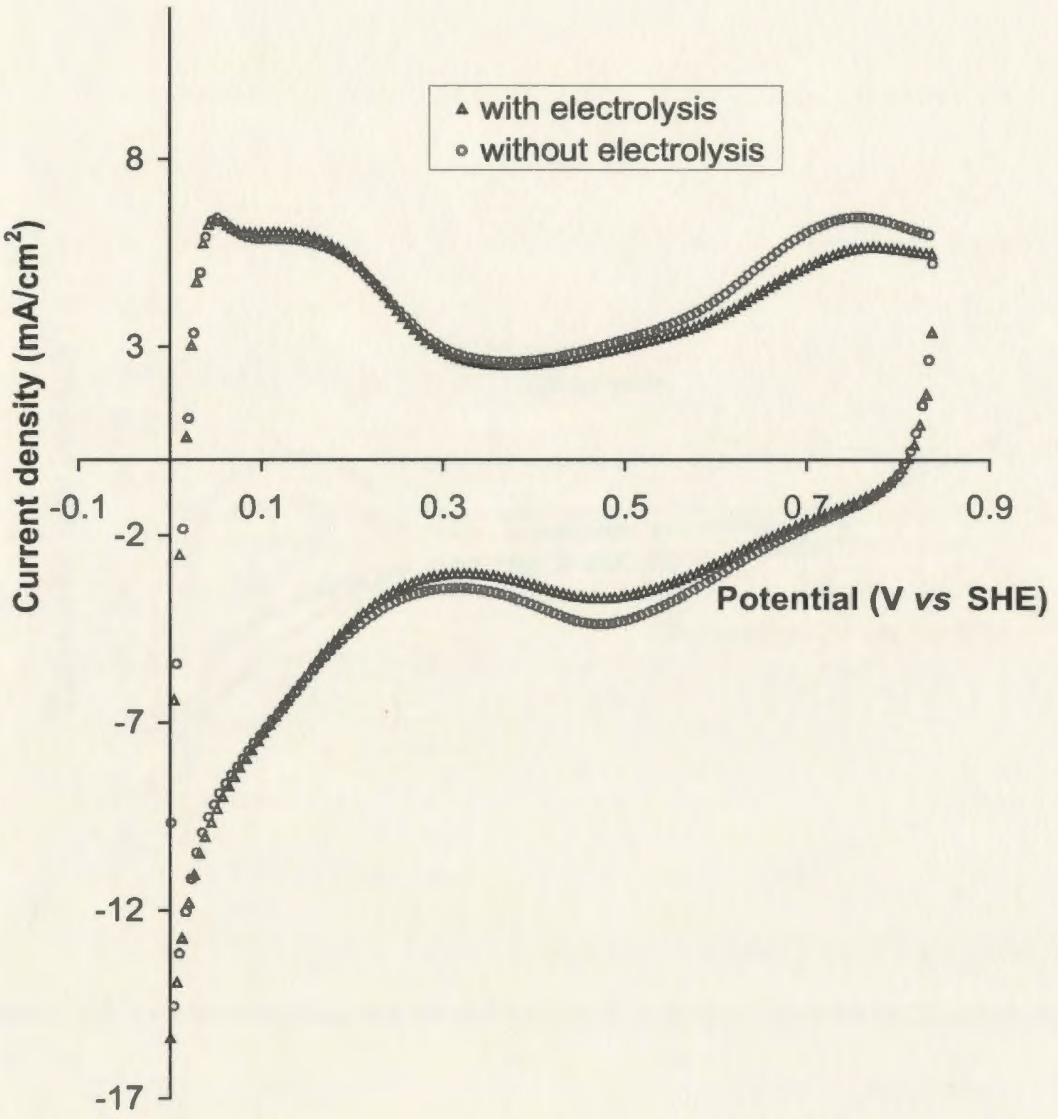

Figure 7.9. Cyclic voltammetry in 1 M H_2SO_4(aq) of a carbon supported Pt/Sn (4:1) catalyst prepared by method C before and after electrolysis of 1 M ethanol(aq) for one hour at 0.5 V *vs* SHE. Scan rate: 10 mV/s.

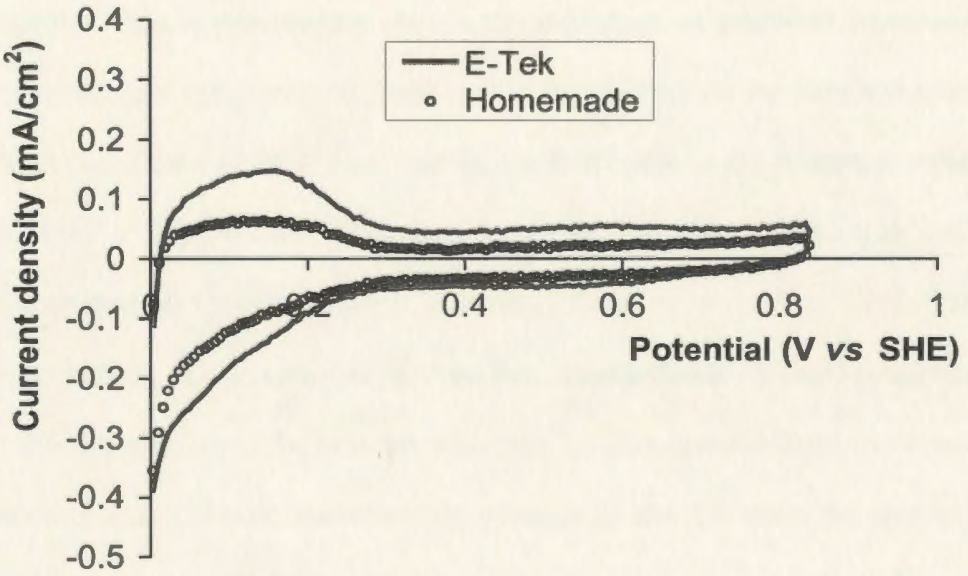

Figure 7.10. Cyclic voltammetry of 20% Pt on C catalysts in 1 M H_2SO_4(aq). Scan rate: 10 mV/s.

electrochemically active area. In other words, the E-Tek catalyst had a smaller Pt particle size than the homemade catalyst. This is consistent with the results estimated from XRD and TEM (Table 3).

Figure 7.11 presents typical CVs of a carbon supported Pt/Sn catalysts in 1 M ethanol(aq). One feature of the CVs is that the current on the reverse scan was bigger than that on the forward scan in the potential region of ca. 0.43 V to 0.78 V *vs* SHE for the first cycle and in the potential region of ca. 0.4 V to 0.84 V *vs* SHE for the 10th cycle, respectively. This is presumably due to the oxidation of adsorbed intermediates at high potential. Another interesting finding is that the current on the forward scan on the 10th cycle was significant smaller than that on the first cycle in the potential region of ca. 0.15 V to 0.65 V *vs* SHE, while the current on the reverse scan on the 10th cycle was much bigger than that on the first cycle at potentials above ca. 0.48 V *vs* SHE. This is possibly due to poisoning of the catalyst by reaction intermediates during continuous cycling or due to the dissolution of Sn into the solution. As discussed before, the dissolution of the catalyst was insignificant, therefore, the change in the CV must be due to poisoning of the catalysts by adsorbed intermediates. The significant increase of the current on the reverse scan on the 10th cycle than the first cycle suggests that more intermediates were adsorbed on the catalyst in the 10th cycle than that in the first cycle. An increased amount of poisonous species with increasing cycle number was also reported by other researchers [5-6].

7.3.6 Catalytic Activities

The catalytic activities of different catalysts for electro-oxidation of ethanol were investigated by linear sweep voltammetry (LSV) and chronoamperometry (CA). It was

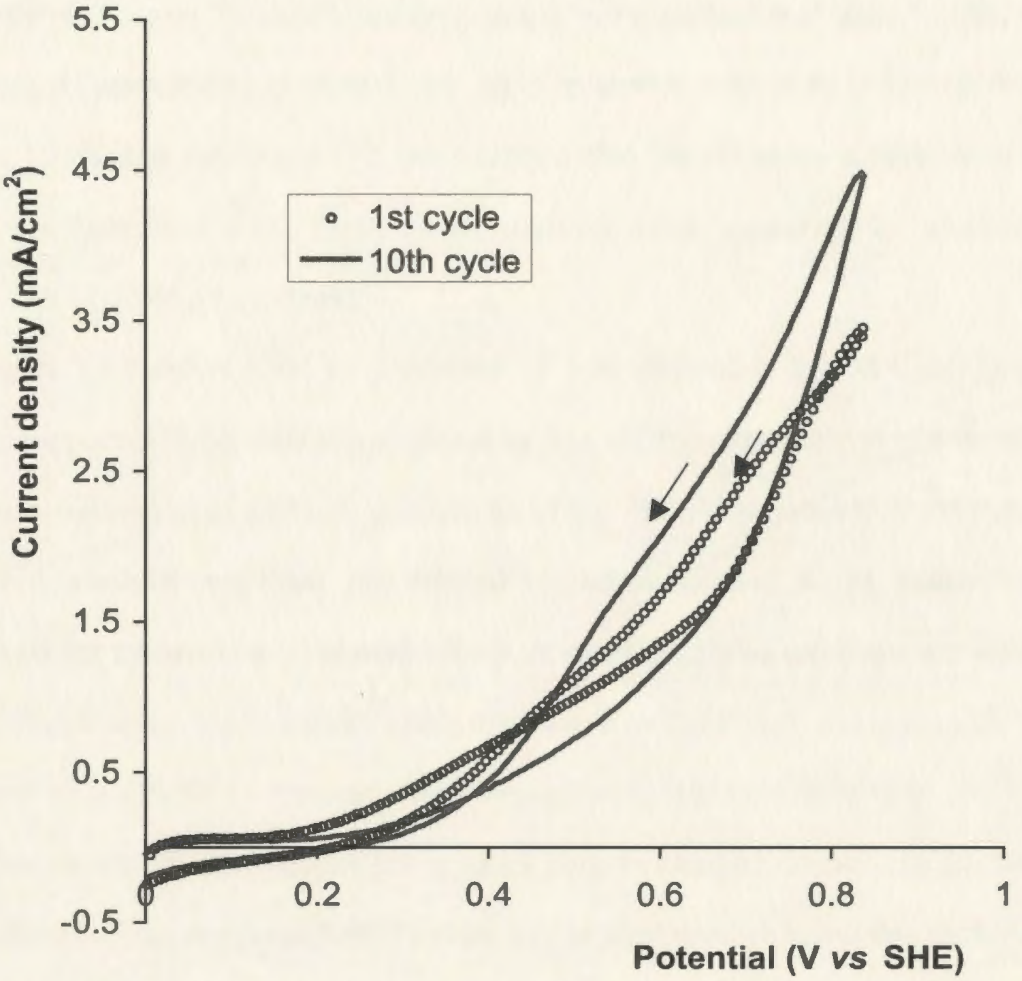

Figure 7.11. Cyclic voltammetry in 1 M ethanol(aq) containing 0.1 M H_2SO_4 of a carbon supported Pt/Sn (4:1) catalyst prepared by method C. Scan rate: 10 mV/s.

found that there was an optimum Pt to Sn ratio for the best performance of the catalyst for ethanol oxidation. Addition of too much Sn resulted in a decrease in catalytic activity, since too much Sn can block Pt active sites for ethanol adsorption. The optimum atomic ratio of Pt to Sn was 5:1 for the catalysts prepared by method A (Figure 7.12b), while for the catalysts prepared by method C, the optimum atomic ratio of Pt to Sn was 4:1 (Figure 7.12a). Lamy and coworkers [7] also reported that the optimum atomic ratio for their Pt/Sn catalysts was 4:1. Their Pt/Sn catalysts were prepared by electrochemical deposition of Sn on Pt electrodes.

Figure 7.13 shows LSV for oxidation of 1 M ethanol in 0.1 M H_2SO_4(aq) on the carbon supported Pt/Sn catalysts prepared by four different methods. It is seen that, in the low potential region of fuel cell interest, all of the Pt/Sn catalysts exhibited significantly enhanced catalytic activities for ethanol oxidation relative to Pt alone. The onset potentials for oxidation of 1 M ethanol(aq) on all of the Pt/Sn catalysts was significantly lower than that on the E-Tek Pt catalyst as listed in Table 7.4. For example, the onset potential of the Pt/Sn catalyst prepared by method C was 0.15 V *vs* SHE, 0.11 V lower than that on the Pt catalyst. The lower onset potential and enhanced catalytic activity of the Pt/Sn catalysts compared with Pt alone can be explained as being due to the oxidation of the poisonous adsorbed intermediates by tin oxides [7,16].

Table 7.4. Onset potentials for oxidation of 1 M ethanol on different catalysts

	Pt/Sn (A*)	Pt/Sn (B)	Pt/Sn (C)	Pt/Sn (D)	Pt (E-Tek)
(V *vs* SHE)	0.2	0.14	0.15	019	0.26

* A means that the catalyst was prepared by method A.

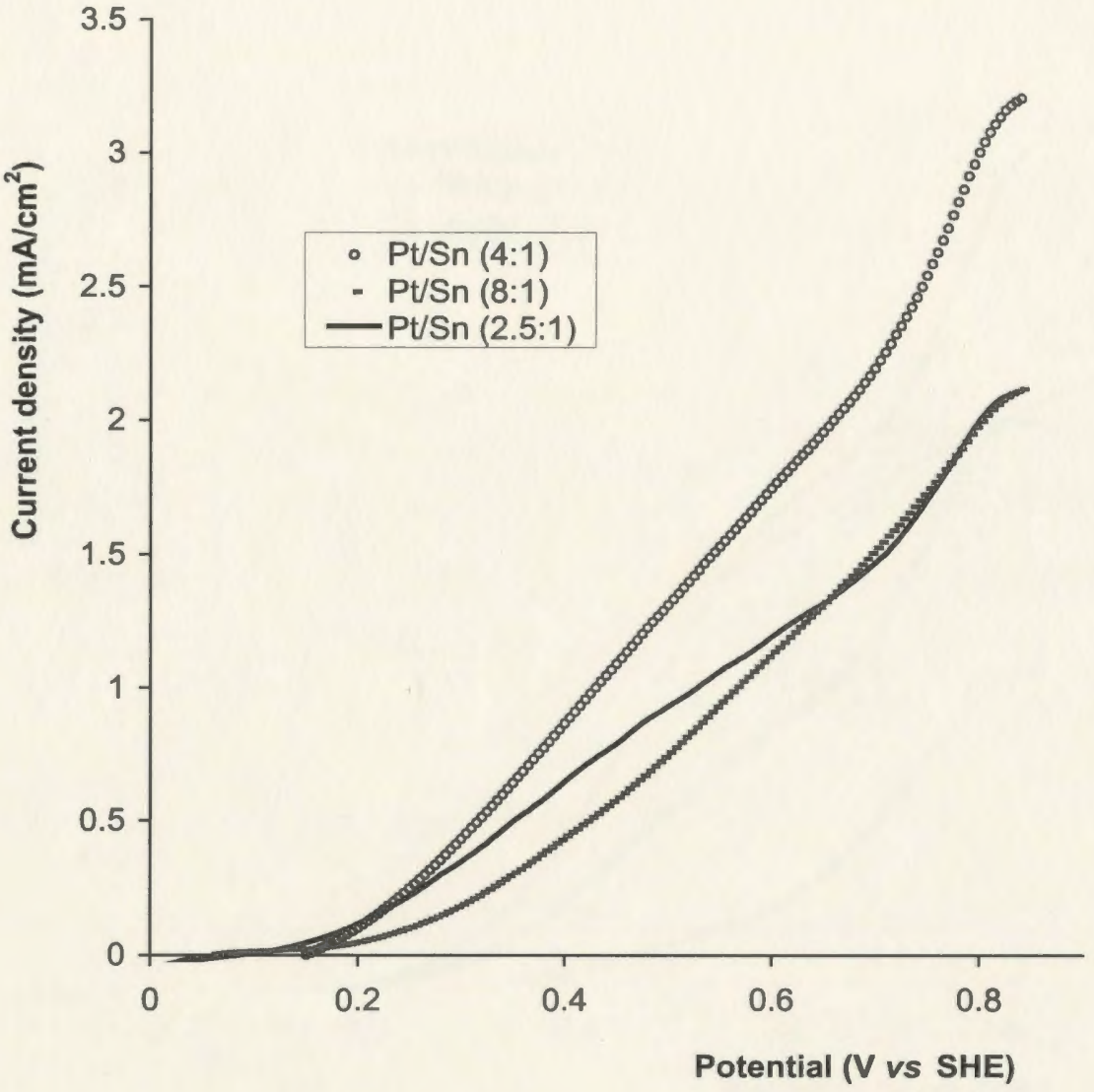

Figure 7.12a. Linear sweep voltammograms for oxidation of 1 M ethanol in 0.1 M H_2SO_4(aq) on different Pt/Sn catalysts prepared by method C. Scan rate: 10 mV/s.

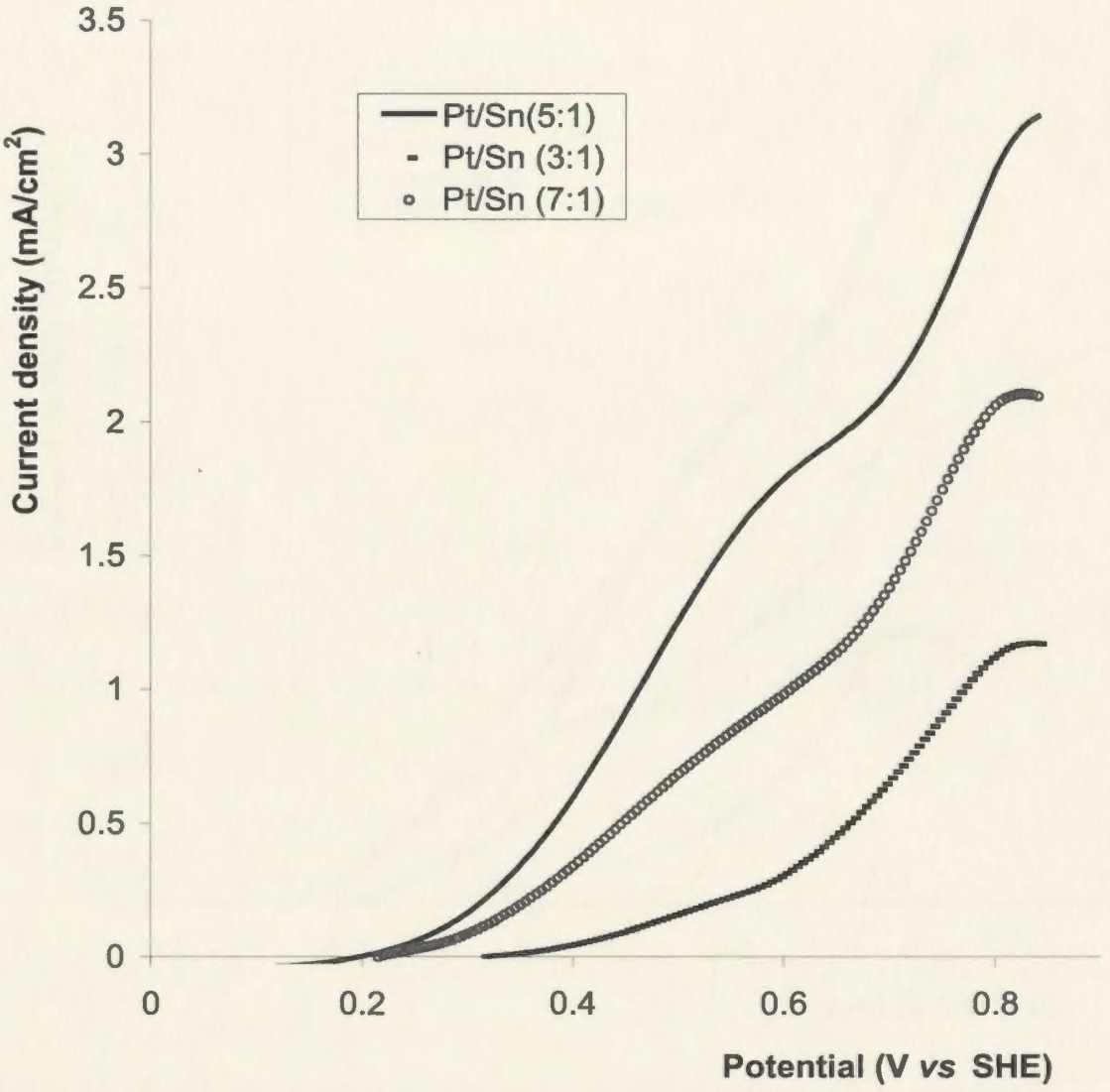

Figure 7.12b. Linear sweep voltammograms for oxidation of 1 M ethanol in 0.1 M H_2SO_4(aq) on different Pt/Sn catalysts prepared by method A. Scan rate: 10 mV/s.

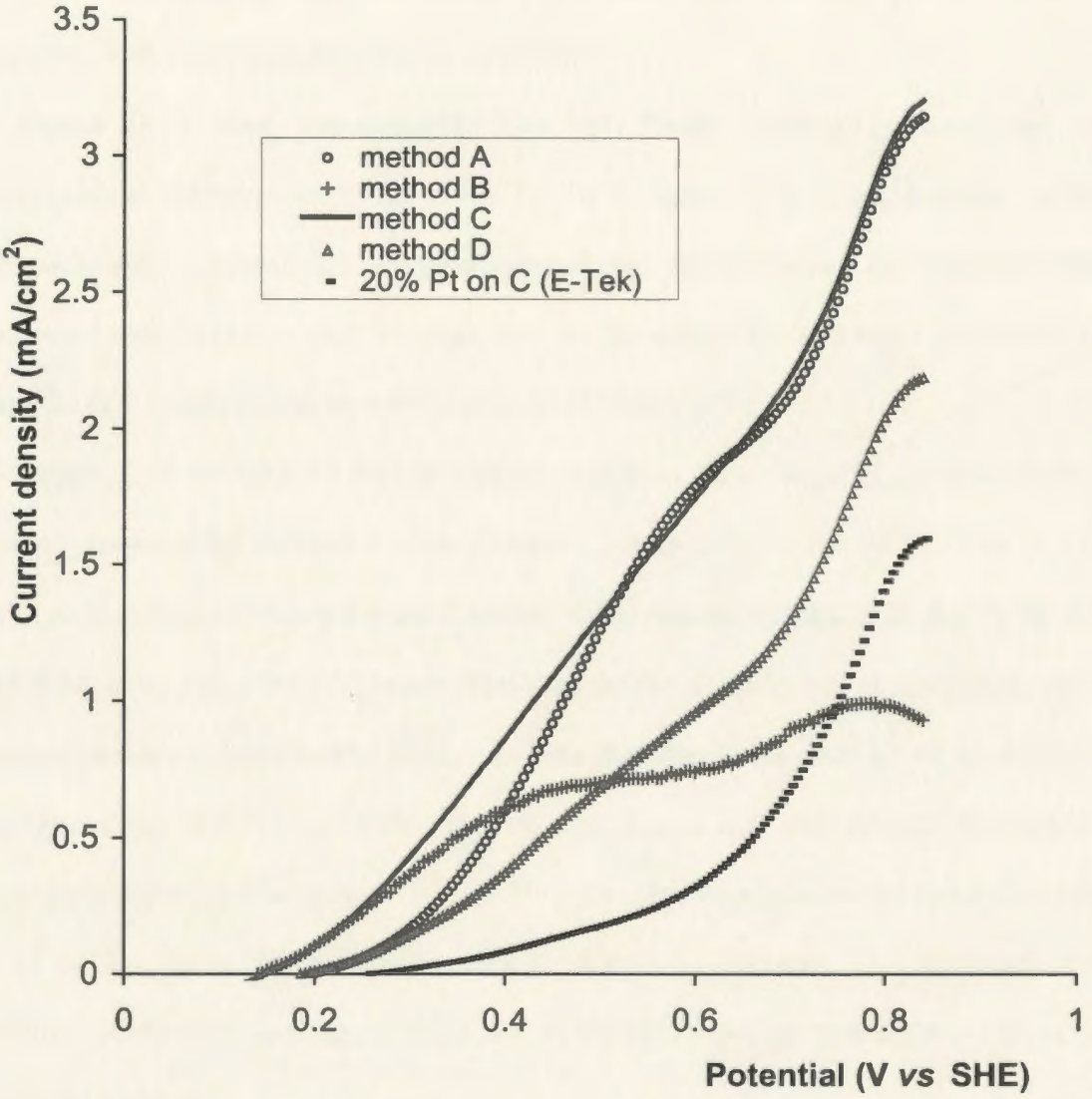

Figure 7.13. Linear sweep voltammograms for oxidation of 1 M ethanol in 0.1 M H_2SO_4(aq) on carbon supported Pt/Sn catalysts, together with that on a E-Tek 20% Pt on C catalyst. Scan rate: 10 mV/s.

Another finding from Figure 7.13 is that the carbon supported Pt/Sn (4:1) catalyst prepared by method C gave the highest current densities in the potential region of fuel cell interest, indicating that this method is the best method among the four methods for preparing Pt/Sn catalysts for ethanol oxidation.

Figure 7.13 also demonstrates that the Pt/Sn catalyst prepared by simply impregnating commercial E-Tek 20% Pt on C with $SnCl_2 \cdot 2H_2O$ solution without a reduction step (method D) exhibited significant enhancement for ethanol oxidation compared with Pt alone. This indicates that Sn (II) and/or Sn (IV) had a promoting effect, since Sn (II) solutions can be oxidized to Sn (IV) in air [23].

Figure 7.14 compares LSV of ethanol oxidation on a carbon supported Pt/Sn (4:1) catalyst prepared by method C with that on a commercial E-Tek 20% Pt/Ru (1:1) on C catalyst. It can be seen that the onset potential for ethanol oxidation on the Pt/Ru catalyst was 0.14 V *vs* SHE, 0.01 V lower than that on the Pt/Sn catalyst. However, the Pt/Sn catalyst provided significantly larger currents than the Pt/Ru catalyst when the potential was above ca. 0.25 V *vs* SHE. It was also found that the current decreased with increasing potential above ca. 0.7 V *vs* SHE for ethanol oxidation on the Pt/Ru catalyst, while on the Pt/Sn catalyst the current continued to increase. This indicates that the reaction mechanism for ethanol oxidation on the Pt/Sn catalyst was different from that on the Pt/Ru catalyst.

For comparison, oxidation of methanol on these two catalysts was also investigated. As shown in the Figure 7.14, the Pt/Sn catalyst was much more active for ethanol oxidation than for methanol oxidation in the potential region of fuel cell interest, while the Pt/Ru was more active for ethanol oxidation than for methanol oxidation at potentials

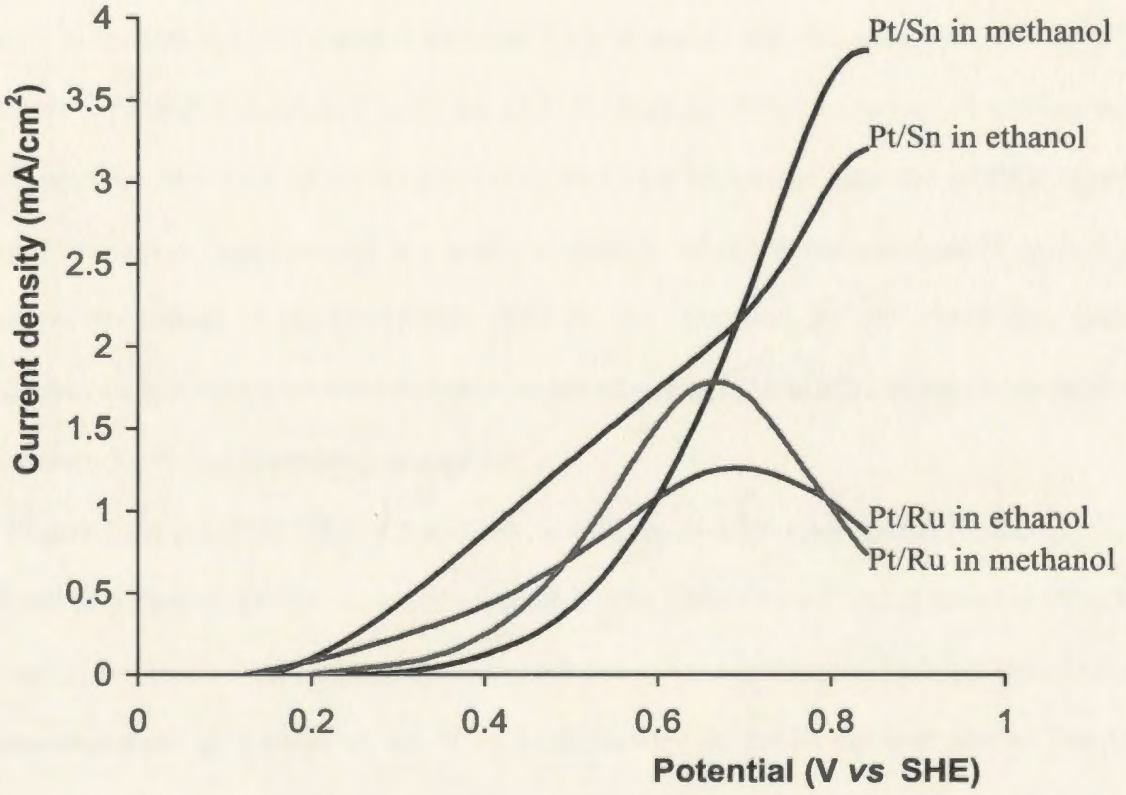

Figure 7.14. Linear sweep voltammograms for oxidation of 1 M ethanol in 0.1 M H_2SO_4(aq) on a carbon supported Pt/Sn (4:1) catalyst prepared by method C and on an E-Tek 20% Pt/Ru (1:1) on C catalyst, together with oxidation of 1 M methanol in 0.1 M H_2SO_4(aq) on these catalysts. Scan rate: 10 mV/s.

below ca. 0.5 V *vs* SHE, but more active for methanol oxidation at higher potentials.

Figure 7.15 compares LSV for ethanol oxidation on a homemade 20% Pt on C catalyst with that on the commercial E-Tek 20% Pt on C catalyst. It is seen that the onset potential for ethanol oxidation on both the catalysts was ca. 0.26 V *vs* SHE. However, the homemade catalyst provided much larger currents than the commercial catalyst. XRD data and TEM micrographs clearly show that the homemade catalyst had a much larger particle size than the commercial catalyst. This suggests that the catalytic activity of Pt catalysts for ethanol oxidation does not simply increase with increasing Pt surface area. The electronic structure of the catalyst may be more important than the particle size for ethanol oxidation. Surprisingly, the catalytic activity of the Pt/Sn catalysts (Figure 7.13) based on decoration of the homemade 20% Pt on C (method B) was lower than that of the Pt/Sn catalyst based on decoration of the commercial E-tek 20% Pt on C (method C). The reason for this discrepancy is unclear.

Figure 7.16 presents CA for oxidation of ethanol on different carbon supported Pt/Sn catalysts together with that on a commercial E-Tek 20% Pt on C catalyst. It is seen that all four of the Pt/Sn catalysts exhibited significant enhancements in catalytic activities for electro-oxidation of ethanol at 0.5 V *vs* SHE relative to the Pt catalyst alone. The best catalyst for electro-oxidation of ethanol at 0.5 V *vs* SHE was carbon supported Pt/Sn (4:1) prepared by method C. This is consistent with the LSV results. The catalytic activity of this catalyst was ca. 23 fold higher than that of the Pt catalyst at 0.5 V *vs* SHE, when the current attained a relatively steady state. It was also found that for all of the four catalysts the current dropped quickly at first, then dropped slowly and finally became relatively stable after ca. 500 s. The large currents at the beginning are presumably due to the

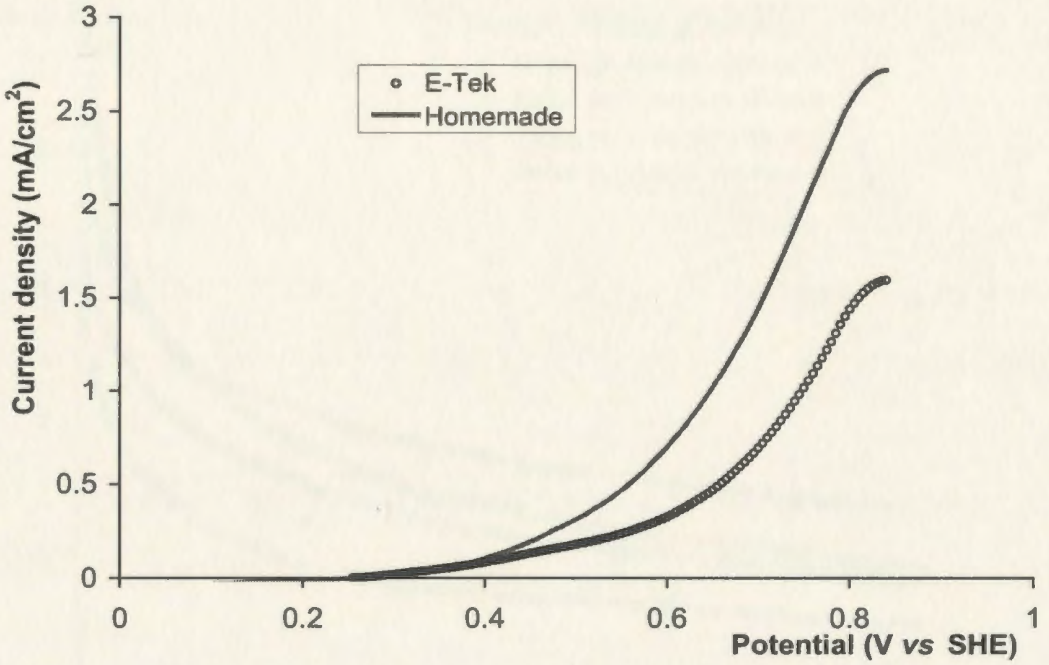

Figure 7.15. Linear sweep voltammograms for oxidation of 1 M ethanol in 0.1 M H_2SO_4(aq) with different 20% Pt on C catalysts. Scan rate: 10 mV/s.

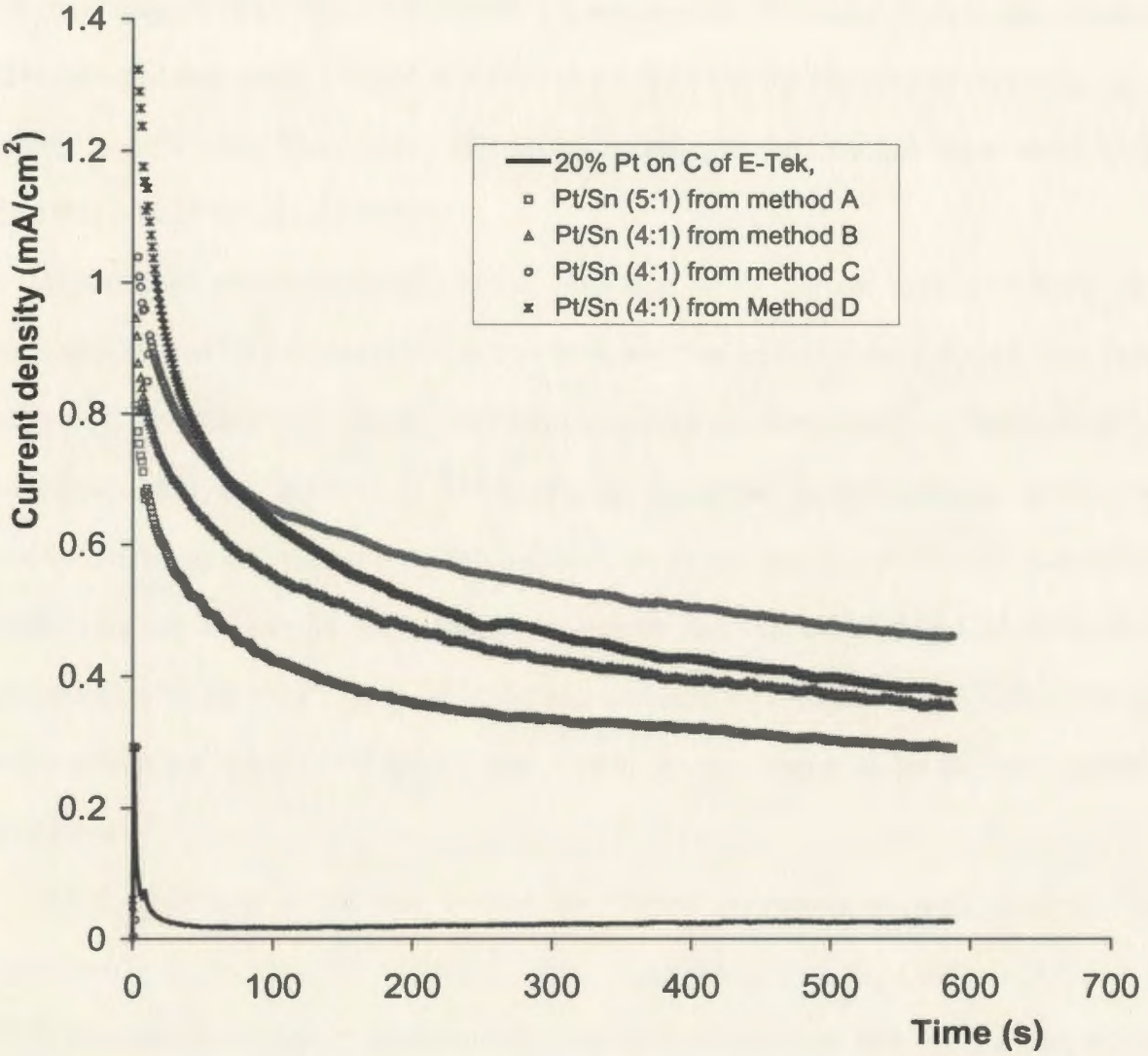

Figure 7.16. Chronoamperometry for oxidation of 1M ethanol in 0.1 M H_2SO_4(aq) at 0.5 V *vs* SHE on different catalysts.

charging current, while the drop of current at later times is due to poisoning of the catalyst by adsorbed intermediates, due to the dissolution of Sn into acidic solution, or due to both. Previously, we have shown that dissolution of Sn into solution was not significant. Therefore, the more probable reason for the drop of current at later times is the poisoning of the catalyst by adsorbed intermediates. However, Wendt and coworker [24] reported that using a single electrode and CA to test the stability of catalysts was of limited significance. They found that stability data obtained by CA were much lower than that gained in fuel cell testing.

Figure 7.17 presents CA for ethanol oxidation on the carbon supported Pt/Sn (4:1) catalyst prepared by method C at 0.5 V *vs* SHE and that on commercial E-Tek 20% Pt/Ru (1:1) on C, together with CA for methanol oxidation on these catalysts. Interestingly, it was found that the homemade Pt/Sn catalyst exhibited higher catalytic activity for electro-oxidation of ethanol than the commercial Pt/Ru catalyst, while the commercial Pt/Ru catalyst shows the better catalytic activity for methanol oxidation. This is in agreement with results reported by Zhou and coworkers [10], who found that Pt/Sn was more active for ethanol oxidation than Pt/Ru, while inferior to Pt/Ru for methanol oxidation.

Another finding is that the current for ethanol oxidation on both catalysts was significantly higher than the current for methanol oxidation on the catalysts at 0.5 V *vs* SHE. Obviously, further investigation is needed to see whether this will be true in fuel cells.

Figure 7.18 shows CA of ethanol oxidation on the carbon supported Pt/Sn (4:1) catalyst prepared by method C at different potentials. It is seen that the current increased

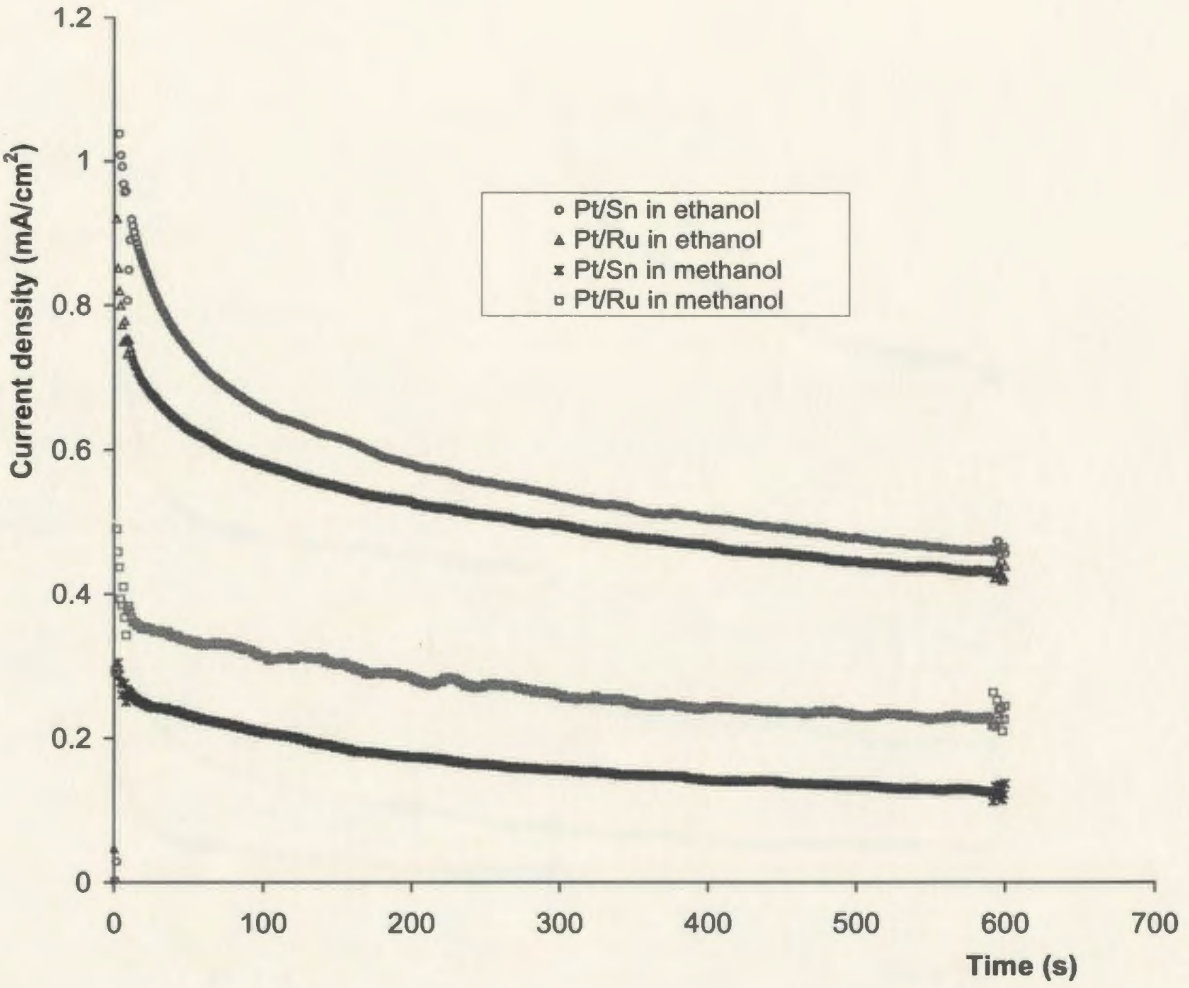

Figure 7.17. Chronoamperometry for oxidation of 1 M ethanol in 0.1 M H_2SO_4(aq) at 0.5 V *vs* SHE on a carbon supported Pt/Sn (4:1) catalyst prepared by method C and on an E-Tek 20% Pt/Ru (1:1) on C catalyst, together with that for oxidation of 1 M methanol in 0.1 M H_2SO_4(aq) on these catalysts.

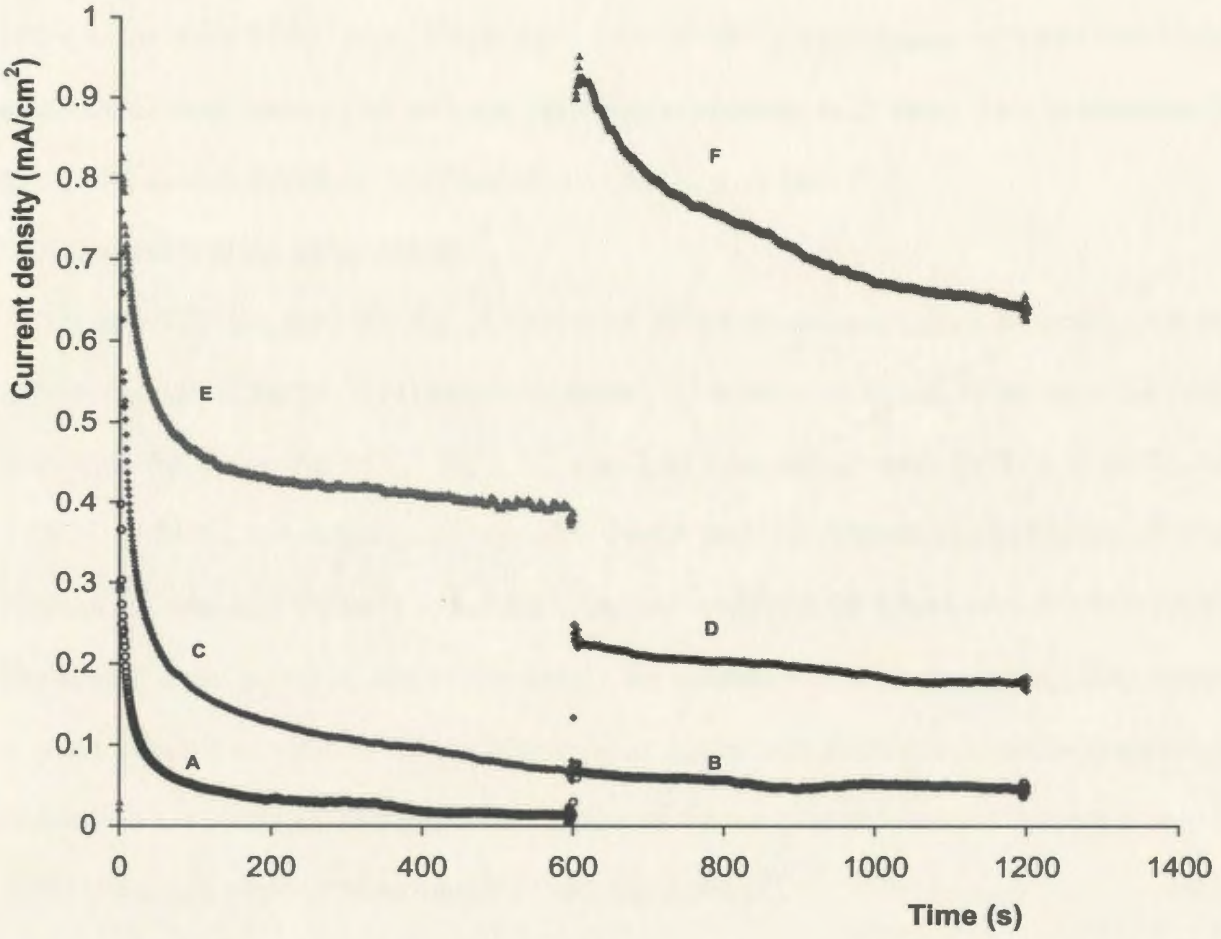

Figure 7.18. Chronoamperometry for oxidation of 1M ethanol in 0.1 M H_2SO_4(aq) on a carbon supported Pt/Sn (4:1) catalyst prepared by method C as a function of potential *vs* SHE. A: 0.25 V; B: 0.3 V; C: 0.35 V; D: 0.4 V; E: 0.5 V; F: 0.6 V. Note: during measurements, two different potentials were set at each run.

significantly with increasing potential as expected. This is consistent with the results of LSV.

Figure 7.19 presents Tafel plots for oxidation of ethanol on the carbon supported Pt/Sn (4:1) catalyst prepared by method C (data were taken from Figure 7.18). It is found that the slopes of the Tafel plots decreased from ca. 0.22 V/dec at an electrolysis time of 180 s to ca. 0.18 V/dec at an electrolysis time of 480 s. The change of Tafel slope with electrolysis time means that reaction mechanism changes with time. This is presumably due to the accumulation of adsorbed intermediates with time [26].

7.3.7 Concentration Dependence

Figure 7.20 shows LSV for oxidation of different concentrations of ethanol on the carbon supported Pt/Sn (4:1) catalyst prepared by method C. It was found that the onset potentials for oxidation of 0.5 M, 1 M, and 2 M ethanol(aq) were 0.09 V, 0.13 V, and 0.13 V *vs* SHE, respectively. It was also found that the current for oxidation of 2 M ethanol(aq) was significantly lower than that for oxidation of 0.5 M or 1 M ethanol(aq). The higher onset potential and lower current for oxidation of 2 M ethanol(aq) may be due to more ethanol adsorption on the electrode at higher concentration, since adsorption of ethanol on the electrode can inhibit formation of the oxygenated species that are involved in the oxidation of poisonous adsorbed intermediates [5].

Figure 7.21 presents CA for oxidation of different concentrations of ethanol on the carbon supported Pt/Sn (4:1) catalyst prepared by method C. It is seen that when the electrolysis time was less than ca. 150 s, the current for oxidation of 2 M ethanol(aq) was smaller than that for oxidation of 0.5 M or 1 M ethanol(aq). However, at later times, the

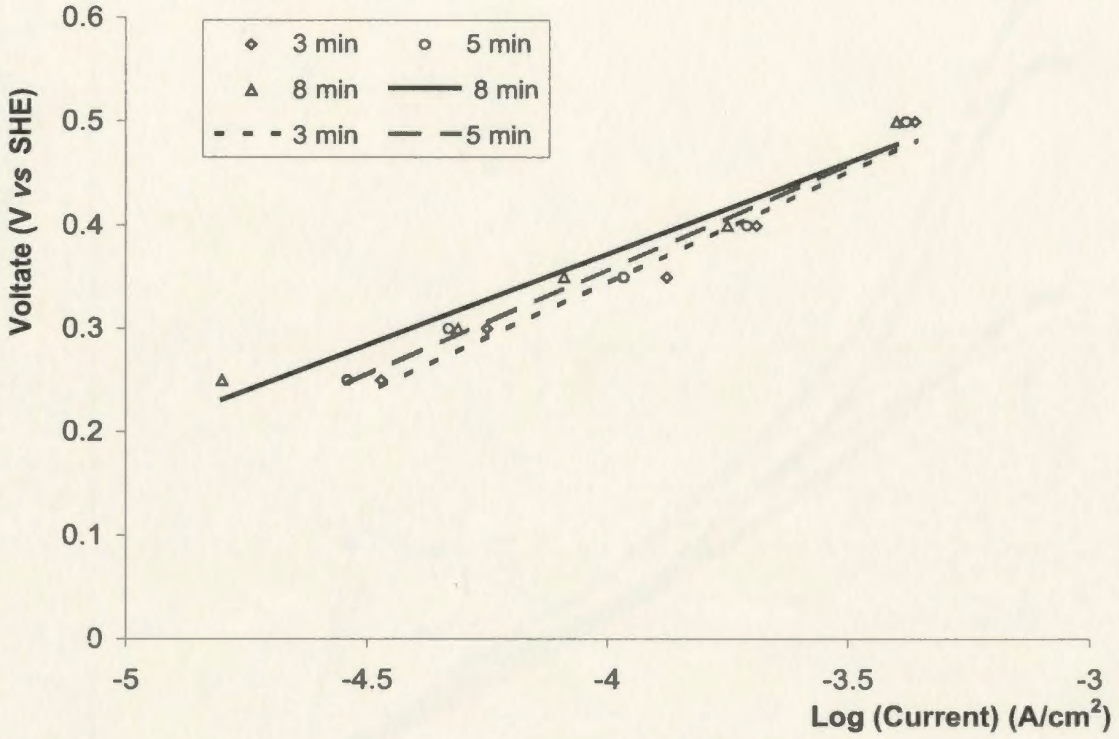

Figure 7.19. Tafel plots for oxidation of 1 M ethanol in 0.1 M H_2SO_4(aq) on a carbon supported Pt/Sn (4:1) catalyst prepared by method C at different times of electrolysis. Data were taken from Figure 7.18.

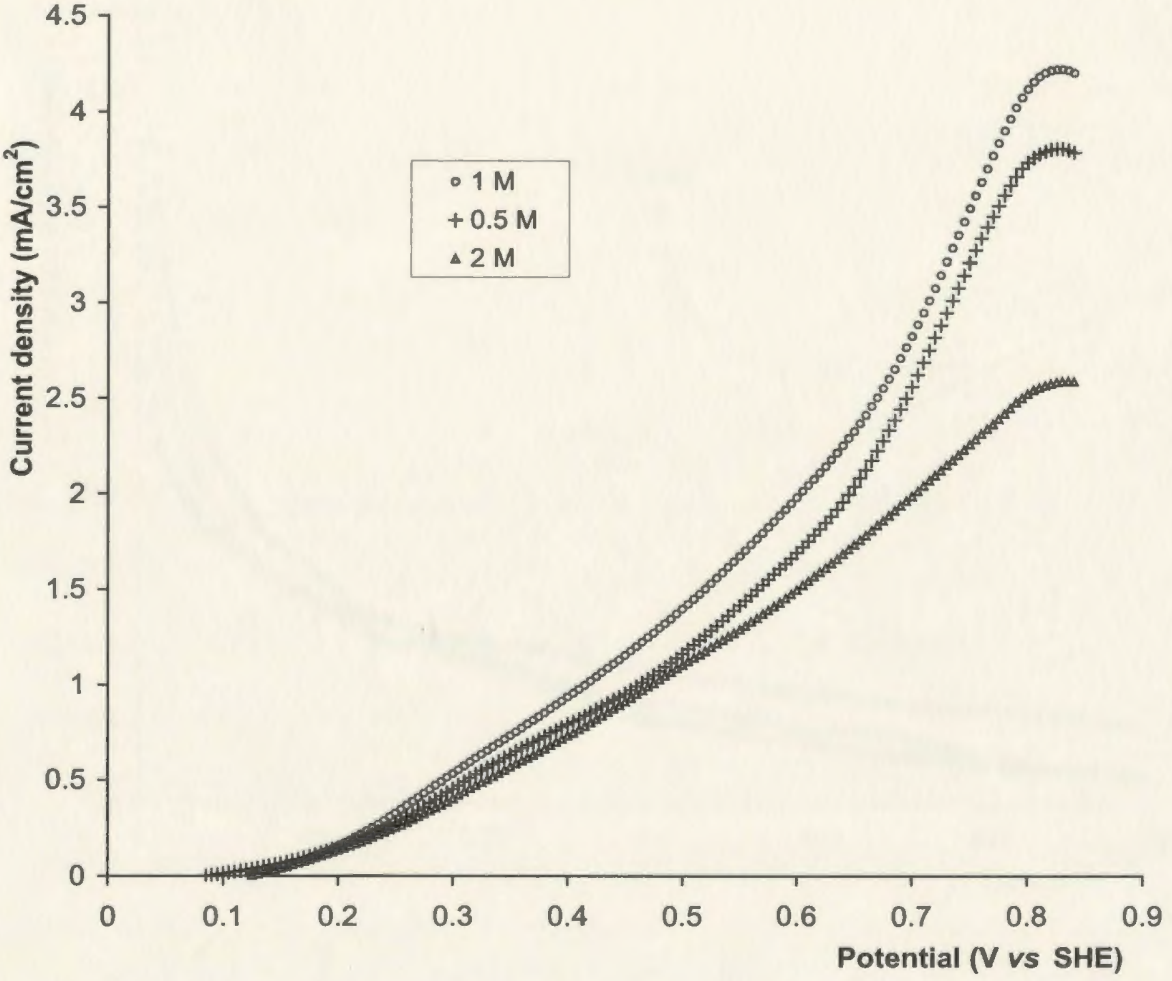

Figure 7.20. Linear sweep voltammograms for oxidation of different concentrations of ethanol in 0.1 M H_2SO_4(aq) on a carbon supported Pt/Sn (4:1) catalyst prepared by method C. Scan rate: 10 mV/s.

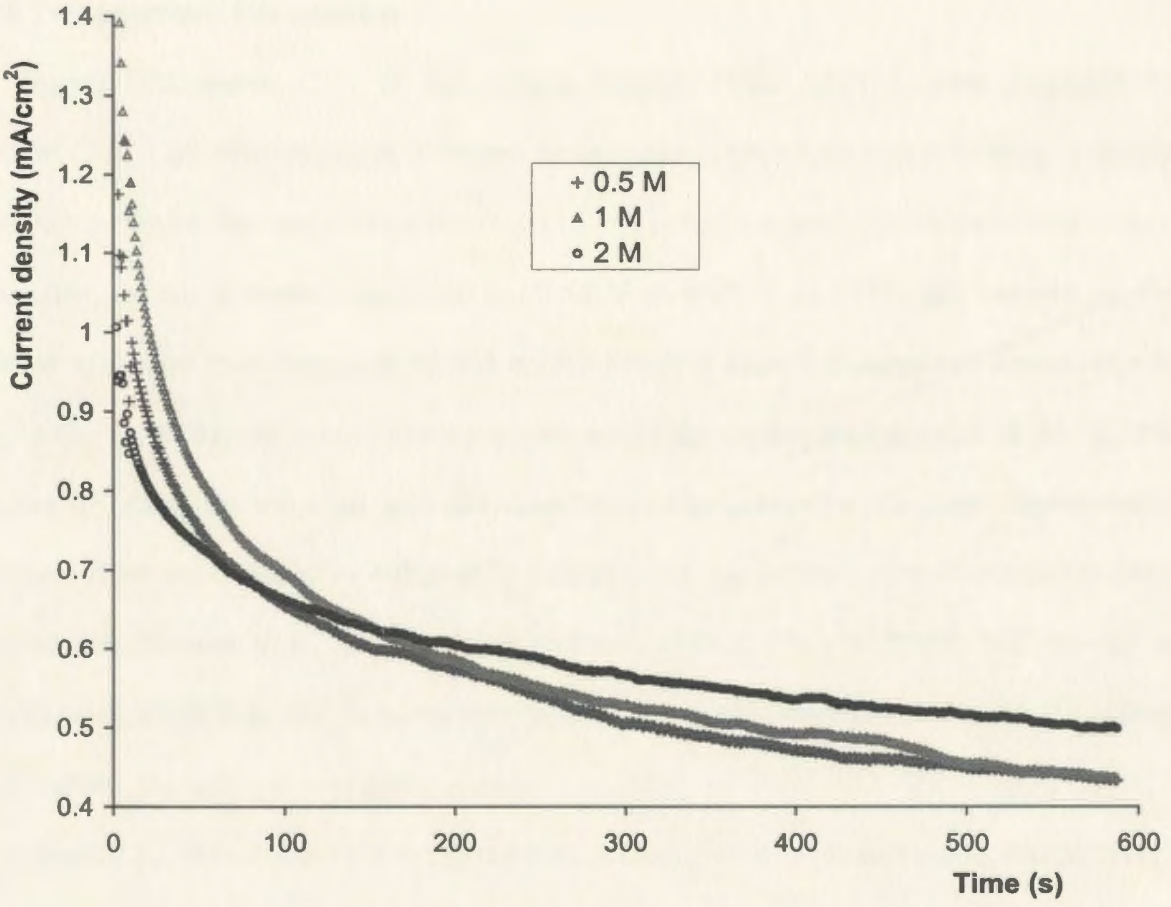

Figure 7.21. Chronoamperometry for oxidation of different concentrations of ethanol in 0.1 M H_2SO_4(aq) on a carbon supported Pt/Sn (4:1) catalyst prepared by method C at 0.5 V *vs* SHE.

current for oxidation of 2 M ethanol(aq) became larger than that for oxidation of 0.5 M or 1 M ethanol(aq). This can be explained by the depletion of ethanol in the diffusion layer, which will decrease ethanol adsorption in the 2 M solution and lead to larger mass transport current losses for the more dilute solutions.

7.3.8 Temperature Dependence

Figure 7.22 shows CVs of the carbon support Pt/Sn (4:1) catalyst prepared by method C in 1 M ethanol(aq) at different temperatures. One interesting finding is that at room temperature, the currents on the forward and reverse scans were close to each other. Moreover, in the potential region of ca. 0.55 V to 0.75 V *vs* SHE, the current on the reverse scan was even bigger than that on the forward scan. As discussed above, this is due to the oxidation of adsorbed intermediates. At the higher temperature of 47 °C, the current on the forward scan and the current on the reverse scan were significantly different from each other. In addition, the current on the reverse scan was smaller than that on the forward scan in the whole potential region. This indicates that at higher temperature, there was less intermediate adsorption on the electrode. Thus, at the higher temperature, the catalyst was more active.

Figure 7.22 also shows that the current increased greatly with increasing temperature, especially at higher potentials. Another interesting finding is that the onset potential for ethanol oxidation on the catalyst decreased from 0.15 V to 0.10 V *vs* SHE when the temperature was increased from room temperature to 47 °C. This again indicates that the catalyst was more active for ethanol oxidation at the higher temperature. Honma and coworker [12] also found that the onset potential for methanol oxidation on an unsupported Pt/Sn alloy catalyst decreased significantly with increasing temperature.

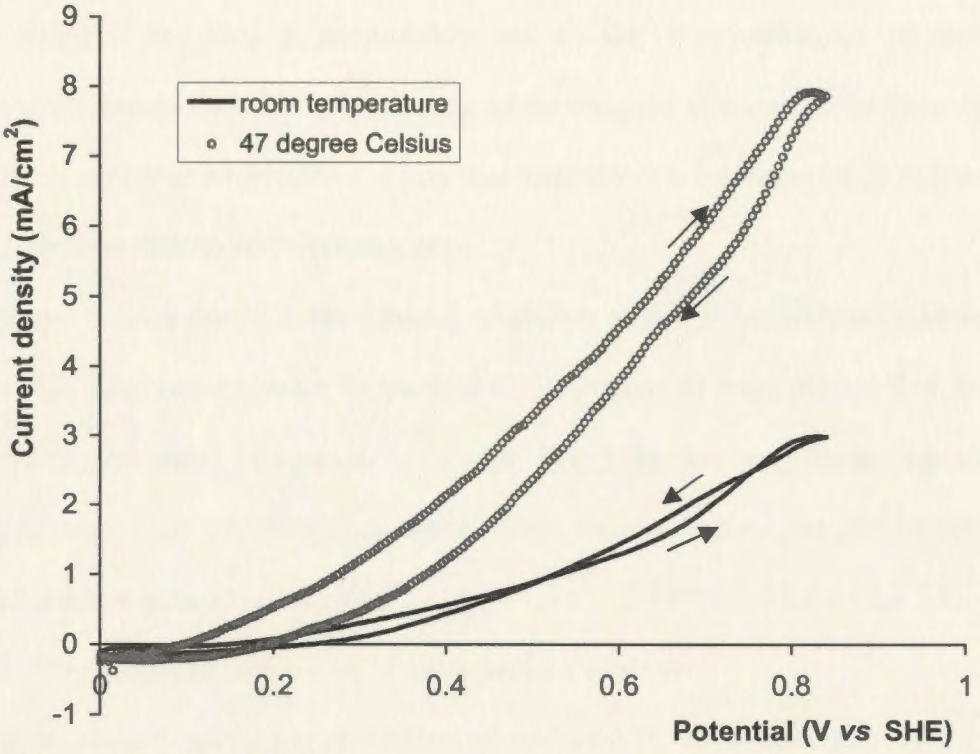

Figure 7.22. Cyclic voltammetry of 1 M ethanol in 0.1 M H_2SO_4(aq) on a carbon supported Pt/Sn (4:1) catalyst prepared by method C at different temperatures. Scan rate: 10 mV/s.

Figure 7.23 shows CA for oxidation of ethanol on the carbon supported Pt/Sn (4:1) catalyst at 0.5 V *vs* SHE at different temperatures. It can be seen that currents were significantly higher at the higher temperature. For example, after five minutes of electrolysis, the current at 47 °C was ca. four times greater than that at room temperature. It was also found that the current dropped more quickly at the higher temperature than at room temperature. This is presumably due to the evaporation of ethanol at higher temperature, rather than due to poisoning of the catalyst, since the poisonous intermediate adsorption at higher temperature is less than that at room temperature as discussed before.

7.3.9 Reproducibility of Experiments

Figure 7.24 shows CA for ethanol oxidation at 0.5 V *vs* SHE on carbon supported Pt/Sn (4:1) catalysts prepared by method C. The catalysts were prepared at four different times with the same procedure. It is seen that there are only small variations in the catalytic activities for these catalysts. This indicates that the preparation and test procedures are quite reproducible.

7.3.10 Preparation of Sn on C Based Sn/Pt Catalysts

In order to increase the utilization of precious Pt, some catalysts were prepared by decoration of carbon supported Sn with Pt, rather than by decoration of Pt with Sn. The obvious benefit of this approach is that precious Pt atoms are on the surface of the catalyst, not covered by Sn atoms. Therefore, the utilization of Pt should be greatly increased. However, it was found that it was very difficult to filter high loading Sn on C products prepared by using $NaBH_4$ as the reducing agent, and even difficult with 10% Sn on C. Using formaldehyde as the reducing agent, 20% Sn on C was successfully prepared. However, LSV showed that Sn/Pt catalysts based on this 20% Sn on C exhibited no

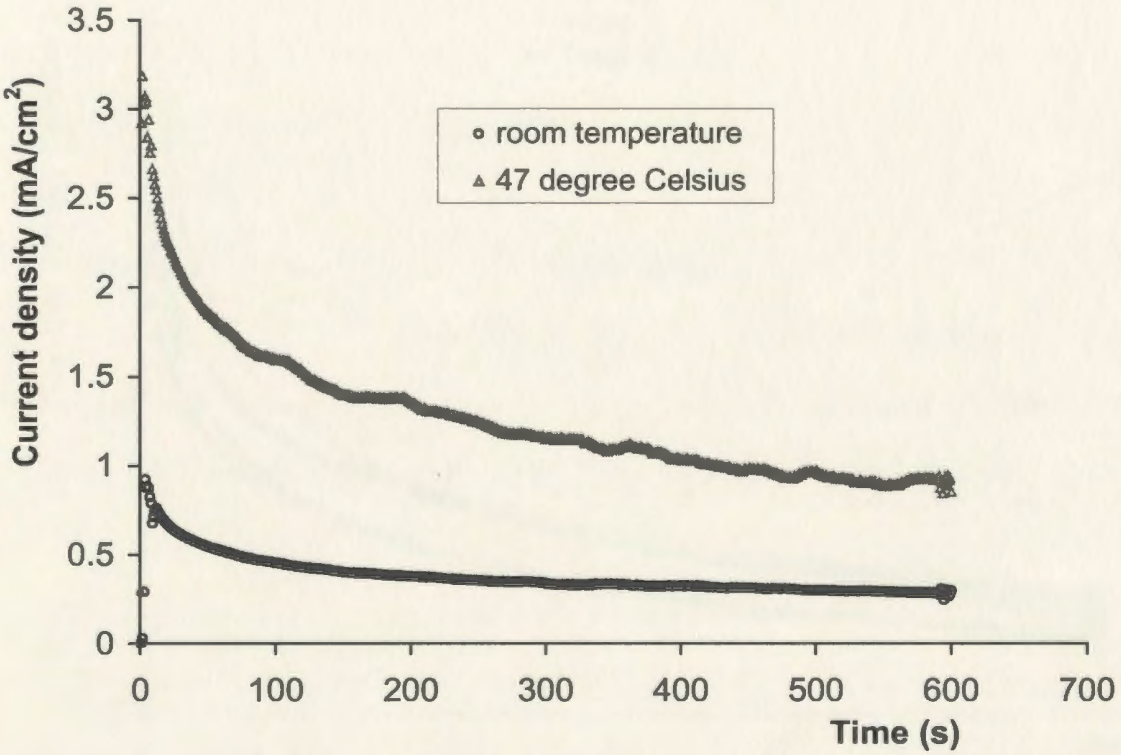

Figure 7.23. Chronoamperometry for oxidation of 1 M ethanol in 0.1 M H_2SO_4(aq) at 0.5 V *vs* SHE on a carbon supported Pt/Sn (4:1) catalyst prepared by method C at different temperatures.

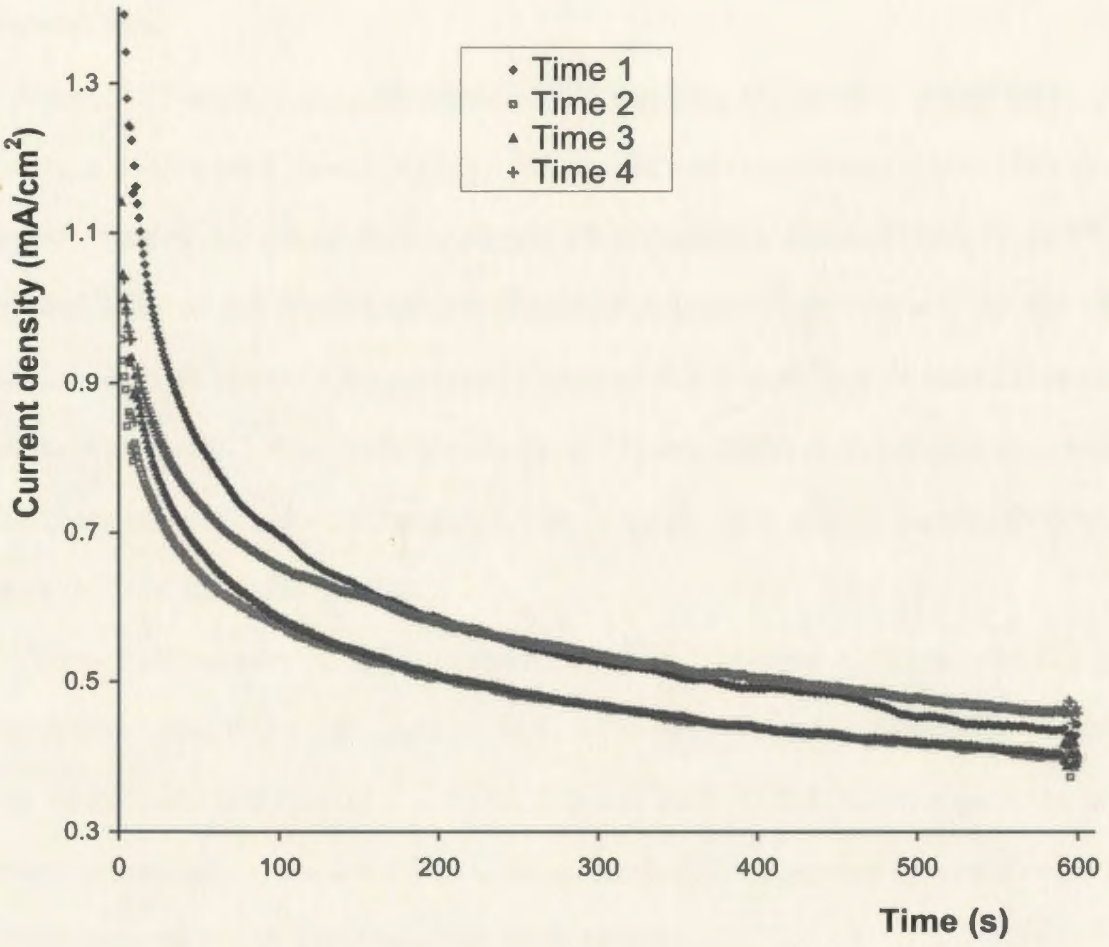

Figure 7.24. Chronoamperometry for oxidation of 1M ethanol in 0.1 M H_2SO_4(aq) at 0.5 V *vs* SHE on 20% Pt on C based Pt/Sn (4:1) catalysts prepared by method C. The catalysts were prepared at four different times with the same procedure.

catalytic activity for ethanol oxidation. A possible reason for this is that Sn existed as oxides on the carbon support, resulting in very low electronic conductivity to the Pt sites.

Some low loading Sn on C based Sn/Pt catalysts were also prepared by using $NaBH_4$ as the reducing agent and these catalysts exhibited enhanced catalytic activity for ethanol oxidation in the potential region of fuel cell interest. The preliminary results are presented here.

Figure 7.25 shows LSVs for ethanol oxidation on a 2% Sn on C based Sn/Pt (1:7.5) catalyst, a 5% Sn on C based Sn/Pt (1:3) catalyst, and commercial E-Tek 20% Pt on C catalyst, respectively (these three catalysts all contained a nominal 20% Pt on C). It is seen that both of the Sn/Pt catalysts exhibited enhanced catalytic activity for ethanol oxidation over Pt alone in the potential region of 0.3 V to 0.72 V *vs* SHE. However, at potentials above 0.72 V *vs* SHE, the 5% Sn on C based Sn/Pt (1:3) catalyst showed lower activity for ethanol oxidation compared with Pt alone. This may be due to low electronic conductivity of the Sn/Pt catalyst.

Figure 7.26 compares CA for oxidation of ethanol on these three catalysts at 0.5 V *vs* SHE. It was found that the currents on both Sn/Pt catalysts were significantly higher than those on Pt alone and that the 2% Sn on C based Sn/Pt (1:7.5) catalyst gave the highest currents. Furthermore, the 2% Sn on C based Sn/Pt (1:7.5) catalyst provided more stable currents than the 5% Sn on C based Sn/Pt (1:3) catalyst.

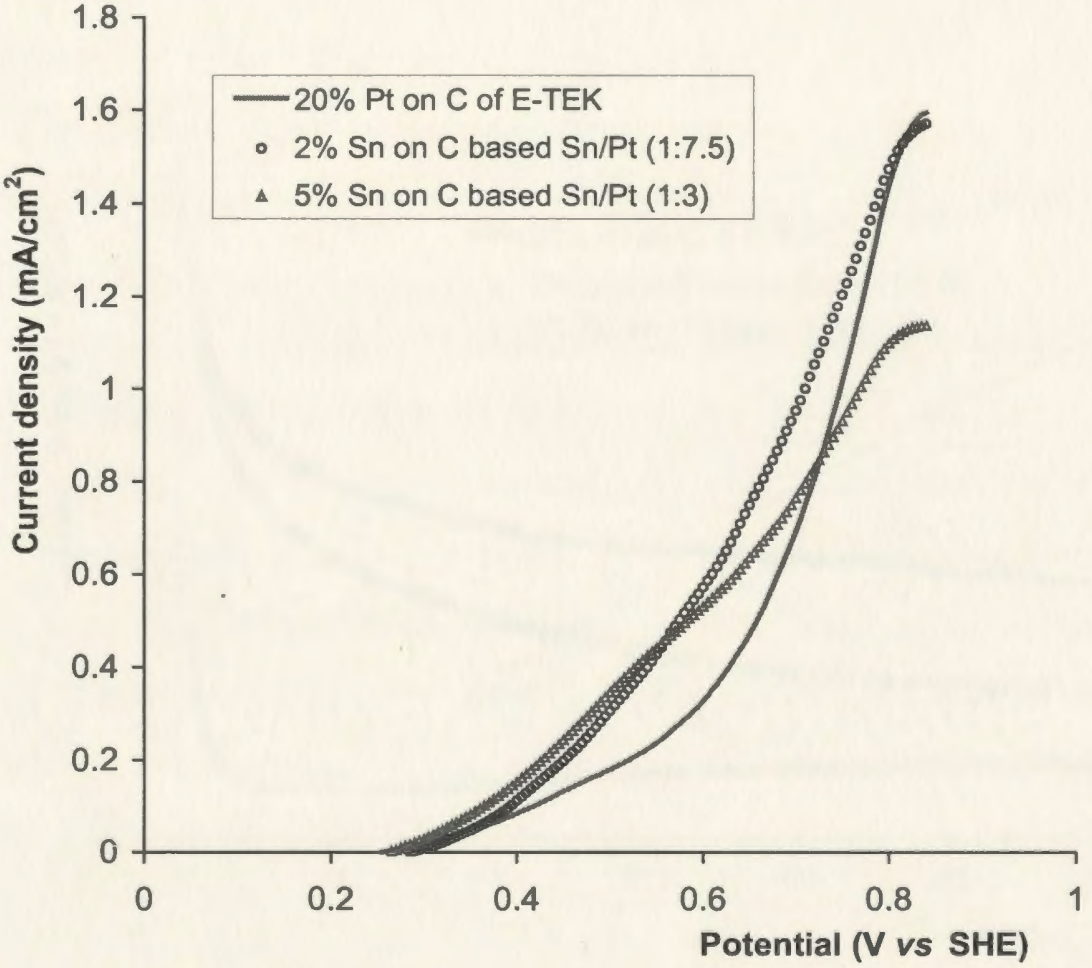

Figure 7.25. Linear sweep voltammograms for oxidation of 1 M ethanol in 0.1 M H_2SO_4(aq) on Sn on C based Sn/Pt catalysts, together with that on an E-Tek 20% Pt on C catalyst. Scan rate: 10 mV/s.

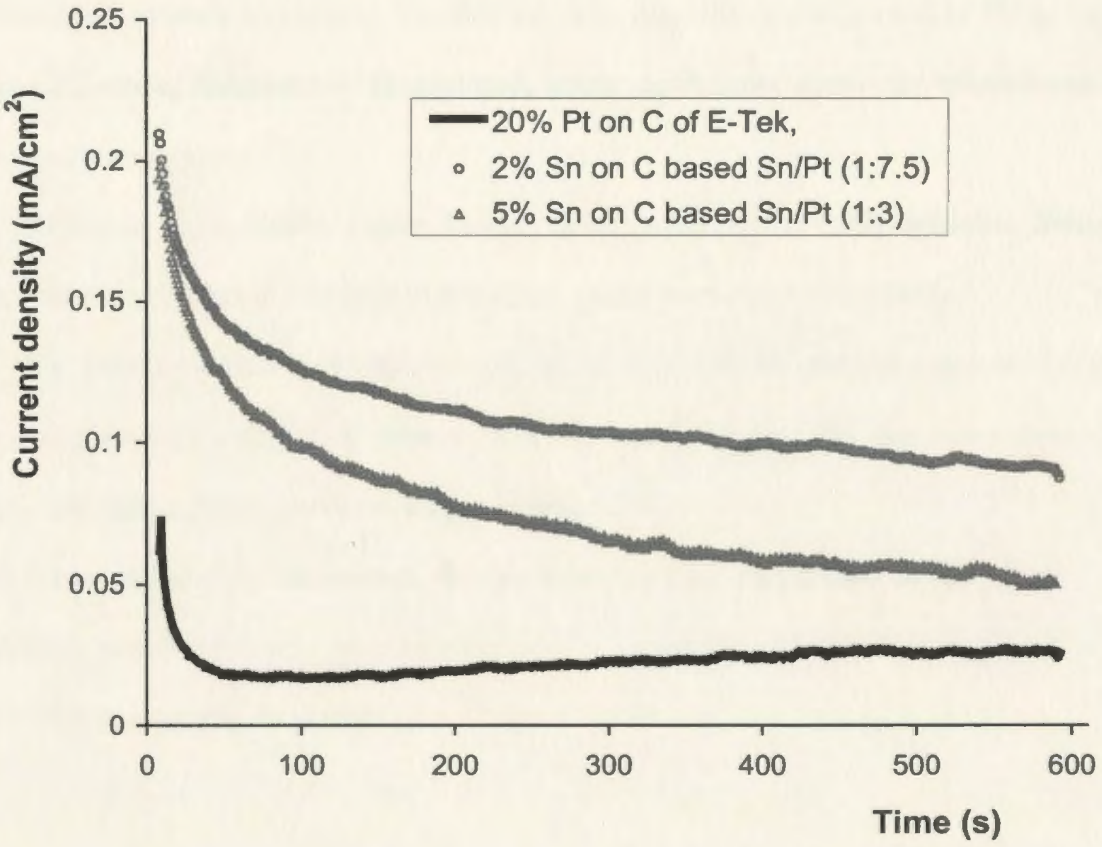

Figure 7.26. Chronoamperometry for oxidation of 1M ethanol in 0.1 M H_2SO_4(aq) at 0.5 V *vs* SHE on Sn on C based Sn/Pt catalysts, together with that on an E-Tek 20% Pt on C catalyst.

7.4 Conclusions

A number of carbon supported Pt/Sn catalysts have been prepared and all exhibited significantly enhanced catalytic activity for ethanol oxidation compared with Pt alone. Among these catalysts, the carbon supported Pt/Sn (4:1) catalyst prepared by reductive decoration of a commercial Pt on C catalyst (method C) showed the highest catalytic activity for ethanol oxidation. In addition, the catalytic activity of this Pt/Sn catalyst showed a strong temperature dependence, being much more active for ethanol oxidation at higher temperature.

XPS data show that tin atoms existed as tin oxides in the Pt/Sn catalysts. Therefore, the promoting effect is due to the tin oxides, rather than due to tin metal.

CV data show that hydrogen chemisorption on the Pt/Sn catalyst was lower than that on the parent Pt catalyst. It appears that Sn was preferentially deposited onto the Pt particles, rather than onto the carbon support.

Preliminary data show that the methodology of decoration of Sn with Pt was effective and this strategy may be extended to decoration of other metals with Pt so that Pt utilization can be increased.

7.5 References

[1] Y. H. Chu, Y. G. Shul, W. C. Choi, S. I. Woo, and H. S. Han, J. Power Sources 118 (2003) 334.

[2] C. Lamy, E. M. Belgsir, and J. M. Leger, J. Appl. Electrochem. 31 (2001) 799.

[3] F. Vigier, C. Coutanceau, F. Hahn, E. M. Belgsir, C. Lamy, J. Electroanal. Chem. 563 (2004) 81.

[4] V. Klouz, V. Firro, P. Denton, H. Katz, J. P. Lisse, S. Bouvot-Mauduit, and C. Mirodatos, J. Power Sources 105 (2002) 26.

[5] A. O. Neto, M. J. Giz, J. Perez, E. A. Ticianelli, and E. R. Gonzalez, J. Electrochem. Soc. 149 (2002) A272.

[6] N. Fujiwara, K. A. Friedrich, and U. Stimming, J. Electroanal. Chem. 472 (1999) 120.

[7] F. Delime, J. M. Leger, C. Lamy, J. Appl. Electrochem. 29 (1999) 1249.

[8] A. O. Neto, E. G. Franco, E. Arico, M. Linardi, and E. R. Gonzalez, J. European Ceramic Soc. 23 (2003) 2987.

[9] W. J. Zhou, Z. H. Zhou, S. Q. Song, W. Z. Li, G. Q. Sun, Q. P. Tsiakaras, S. Xin, Appl. Catal. B 46 (2003) 273.

[10] W. J. Zhou, B. Zhou, W. Z. Li, Z. H. Zhou, S. Q. Song, G. Q. Sun, Q. Xin, S. Douvartzides, M. Goula, P. Tsiakaras, J. Power Sources 126 (2004) 16.

[11] K. W. Park, J. H. Choi, B. K. Kwon, S. A. Lee, Y. E. Sung, H. Y. Ha, S. A. Hong, H. Kim, A. Wieckowski, J. Phy. Chem. B 106 (2002) 1869.

[12] I. Honma and T. Toda, J. Electrochem. Soc. 150 (2003) A1689.

[13] M. A. A. Rahim, M. W. Khalil, and H. B. Hassan, J. Appl. Electrochem. 30 (2000) 1151.

[14] M. J. Gonzalez, C. H. Peters, and M. S. Wrighton, J. Phys. Chem. B 105 (2001) 5470.

[15] W. H. Lizcano-Valbuena, V. A. Paganin, C. A. P. Leite, F. Galembeck, and E. R. Gonzalez, Electrochim. Acta 48 (2003) 3869.

[16] E. M. Crabb, R. Marshall, and D. Thompsett, J. Electrochem. Soc. 147 (2000) 4440.

[17] M. Gotz and H. Wendt, Electrochim. Acta 43 (1998) 3637.

[18] F. Jaouen, S. Marcotte, J. P. Dodelet, and G. Lindbergh, J. Phys. Chem. B 107 (2003) 1376.

[19] G. Neri, C. Milone, S. Galvagno, A. P. J. Pijpers, and J. Schwank, Appl. Catal. A 227 (2002) 105.

[20] S. R. D. Miguel, M. C. Roman-Martinez, E. L. Jablonski, J. L. G. Fierro, D. Cazorla-Amoros, and O. A. Scelza, J. Catal. 184 (1999) 514.

[21] C. He, H. R. Kunz, and J. M. Fenton, J. Electrochem. Soc. 150 (2003) A1017.

[22] T. Frelink, W. Visscher, and J. A. R. van Veen, Electrochim. Acta 39 (1994) 1871.

[23] H. Massong, H. Wang, G. Samjeske, and H. Baltruschat, Electrochim. Acta 46 (2000) 701.

[24] M. Goetz and H. Wendt, J. Appl. Electrochem. 31 (2001) 811.

[25] N. M. Markovic, A. Widelov, P. N. Ross, O. R. Monteiro, and I. G. Brown, Catal. Lett. 43 (1997) 161.

[26] M. Zhao, C. Rice, R. I. Masel, P. Waszczuk, and A. Wieckowski, J. Electrochem. Soc. 151 (2004) A131.

Chapter 8 Preparation and Characterization of Other Pt Based Catalysts for Electro-Oxidation of Ethanol

8.1 Introduction

In recent years, development of catalysts for electro-oxidation of ethanol has been the subject of increasing research [1]. In addition to Pt/Sn catalysts (see Chapter 7), several Pt based binary and ternary catalysts have been found to be more active than Pt for electro-oxidation of ethanol. These catalysts include Pt/Ru [2-4], Pt/Mo [2], Pt/W [5], Pt/Rh [6], Pt/Pd [7], Pt/Ru/W, Pt/Ru/Sn, and Pt/Ru/Mo [7]. For the binary catalysts, it was found that the catalytic activity for electro-oxidation of ethanol increased in the following order: Pt < Pt/Pd (1:1) < Pt/W (1:1) < Pt/Ru (1:1) < Pt/Sn (1:1). It was also reported that the catalytic activity of Pt/Ru catalysts for electro-oxidation of ethanol was increased by addition of a third metal such as W or Mo [7].

However, these catalysts are far from satisfactory to be used in DEFCs, especially at low temperatures. Also, the reaction mechanism for ethanol oxidation on these catalysts is not clear yet [1,8]. Therefore, further studies are greatly needed to resolve these issues.

In the work presented in this chapter, a number of Pt based binary and ternary catalysts were prepared, and their catalytic activity for electro-oxidation of ethanol was characterized by cyclic voltammetry and chronoamperommetry. It was found that carbon supported Pt/Ru, Pt/Mo, and Pt/Pb binary catalysts and carbon supported Pt/Ru/Mo, Pt/Ru/Pb, and Pt/Ru/W ternary catalysts exhibited a significantly enhanced catalytic activity for electro-oxidation of ethanol relative to Pt alone.

8.2 Experimental

8.2.1 Preparation of Catalysts

Carbon supported Pt based binary catalysts were prepared by decoration of a commercial 20% Pt on C catalyst with other metals as follows:

50 mg of 20% Pt on C (E-Tek) was dispersed in 30 ml of DI water by stirring. An appropriate amount of the second metal precursor (the metal precursors used were $RuCl_3$ hydrate (Aldrich), $Pb(NO_3)_2$ (Fisher), $MoCl_5$ (Aldrich), and $RhCl_3$ hydrate (Aldrich)) dissolved in 30 ml of DI water was then added dropwise and stirred for 0.5 h, followed by dropwise addition of a 2 times excess of $NaBH_4$ (BDH Inc.) dissolved in 40 ml of DI water with further stirring for 0.5 h. The product was collected by filtration and washed well with copious amounts of DI water, then dried at room temperature in a vacuum oven.

Carbon supported Ru based Ru/Pt catalysts were prepared by two steps as follows:

40 mg of Vulcan carbon (XC-72R, E-Tek) was dispersed in 30 ml of DI water by stirring, followed by dropwise addition of 50 ml of metal precursor solution(aq) containing an appropriate amount of $RuCl_3$ hydrate and stirring for 0.5 h. A 2 times excess of $NaBH_4$ in 40 ml of DI water was then added with further stirring for 0.5 h. The product was collected by filtration and washed well with copious DI water, then dried at room temperature in a fume hood. The product was then re-dispersed in 30 ml of DI water by stirring, followed by dropwise addition of a 50 ml solution(aq) containing an appropriate amount of K_2PtCl_4 (PMO Ltd) and stirring for 0.5 h. A 2 times excess of $NaBH_4$ in 40 ml of DI water was then added with further stirring for 0.5 h. The product was collected by filtration and washed well with copious amounts of DI water, then dried

at room temperature in a vacuum oven.

Carbon supported Pt based ternary catalysts were prepared by decoration of a commercial 20% Pt/Ru (1:1) on C catalyst with a third metal as follows:

30 mg of 20% Pt/Ru (1:1) on C (E-Tek) was dispersed in 30 ml of DI water by stirring. An appropriate amount of a third metal precursor (the metal precursors used were $Pb(NO_3)_2$ (Fisher), $MoCl_5$ (Aldrich), and WCl_4 (Aldrich)) dissolved in 30 ml of DI water was then added dropwise and stirred for 0.5 h, followed by dropwise addition of a 2 times excess of $NaBH_4$ dissolved in 40 ml of DI water with further stirring for 0.5 h. The product was collected by filtration and washed well with copious amounts of DI water, then dried at room temperature in a vacuum oven.

8.2.2 Characterization of Catalysts and Electrochemistry

The experimental characterization and electrochemistry procedures were the same as those described in Section two of Chapter 7.

8.3 Results and Discussion

8.3.1 Binary Catalysts

8.3.1.1 EDX

Figure 8.1 presents EDX spectra of the binary catalysts. It is seen that the peaks for Pb, Rh, and Ru were well separated from the peaks for Pt, while the peak for Mo was quite close to one peak for Pt. The spectra indicate that Mo, Pb, Rh, and Ru have been incorporated into the parent Pt catalyst.

8.3.1.2 XRD

Figure 8.2 presents XRD patterns of an E-Tek 20% Pt on C catalyst and Pt based Pt/Mo, Pt/Pb , Pt/Rh, and Pt/Ru binary catalysts. The diffraction peak at ca. 25° is due to

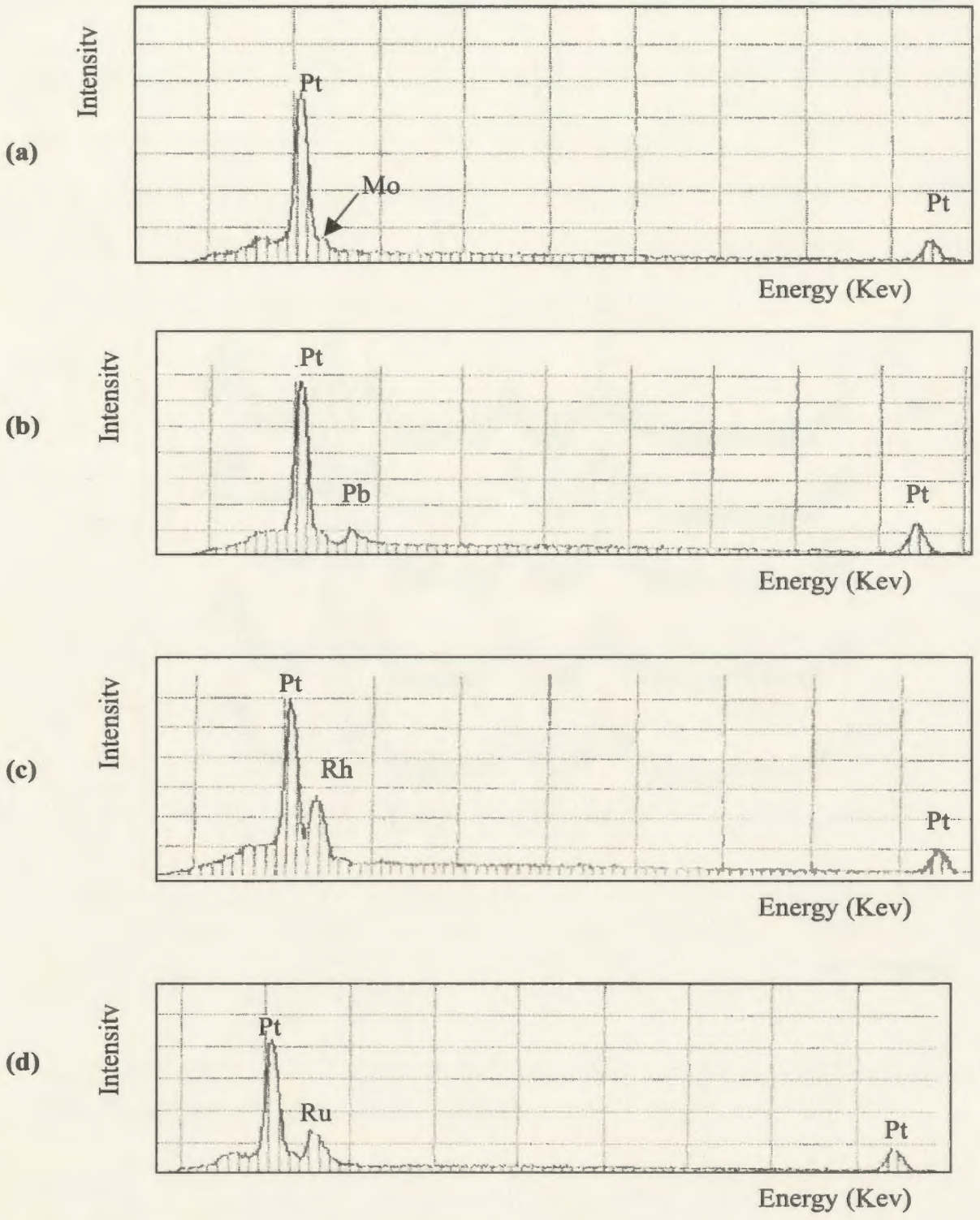

Figure 8.1. EDX spectra of 20% Pt on C based binary catalysts: (a) Pt/Mo (5:2); (b) Pt/Pb (4:1); (c) Pt/Rh (9:2); (d) Pt/Ru (7:2).

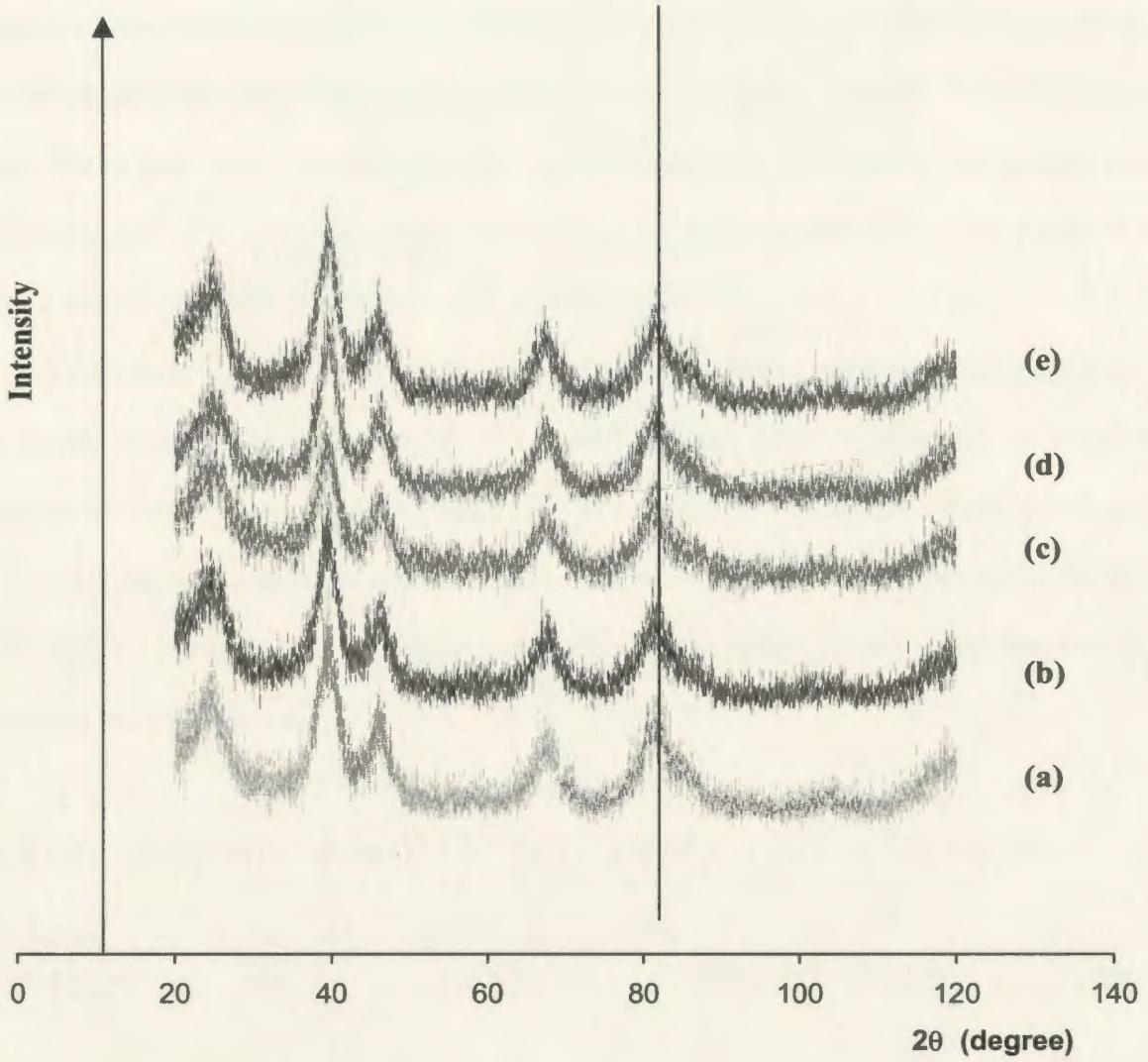

Figure 8.2. XRD patterns of 20% Pt on C and binary catalysts prepared from it: (a) E-Tek 20% Pt on C; (b) Pt/Mo (5:2); (c) Pt/Pb (4:1); (d) Pt/Ru (7:2); (e) Pt/Rh (9:2).

the reflection of the C (002) plane, while the peaks at ca. 40°, 46°, 67.5°, and 81.5° represent the reflection of Pt (111), Pt (200), Pt (220), and Pt (311) planes, respectively. It can be seen that the XRD patterns only show characteristic peaks for Pt and C. Also, no significant peak shift was observed for the Pt peaks after addition of the second metal. This suggests that the other metals were either highly dispersed or in amorphous states, since formation of alloys should result in peak shifts [7.9].

The mean particle sizes of the binary catalysts were estimated according to the Scherrer equation (based on the Pt (311) peak), and are listed in Table 8.1. It is seen that the mean particle sizes of Pt/Ru and Pt/Rh were a little bit larger than those of the parent Pt, while the mean particle sizes of Pt/Mo and Pt/Pb were the same as those of the parent Pt. This indicates that no significant differences in the mean particle sizes between the Pt and the binary catalysts.

Table 8.1. Mean particle sizes of 20% Pt on C and binary catalysts derived from it

Sample	Pt/Mo (5:2)	Pt/Pb (4:1)	Pt/Ru (7:2)	Pt/Rh (9:2)	Pt
Particle size	2.5 nm	2.5 nm	2.8 nm	2.8 nm	2.5 nm

8.3.1.3 TEM

Figures 8.3a and 8.3b show TEM micrographs of the binary catalysts. It was found that the metal particles were evenly distributed on the C support.

8.3.1.4 Catalytic Activities

The catalytic activity of the binary catalysts was tested by linear sweep voltammetry (LSV) and chronoamperommtry (CA). It was found that there was an optimum atomic

(a)

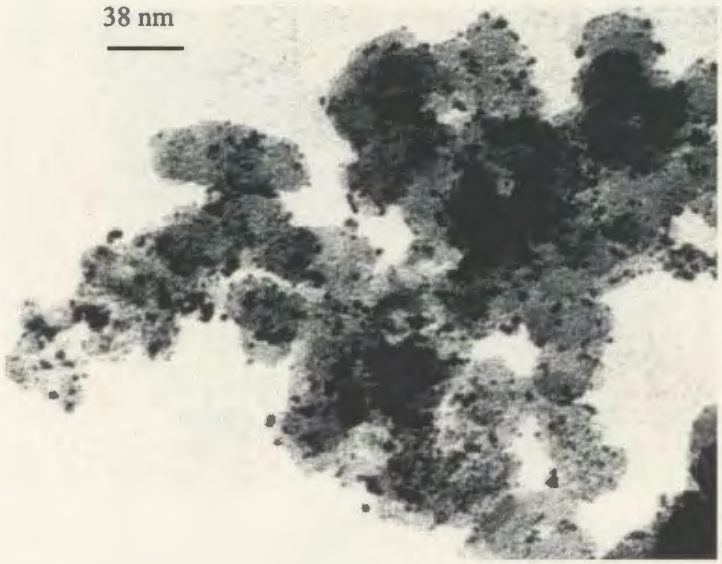

(b)

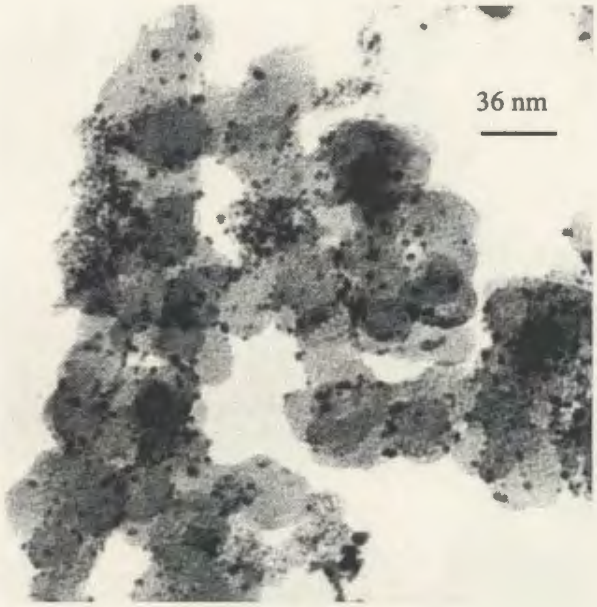

Figure 8.3a. TEM micrographs of 20% Pt on C based binary catalysts: (a) Pt/Mo (5:2), (b) Pt/Pb (4:1).

(c)

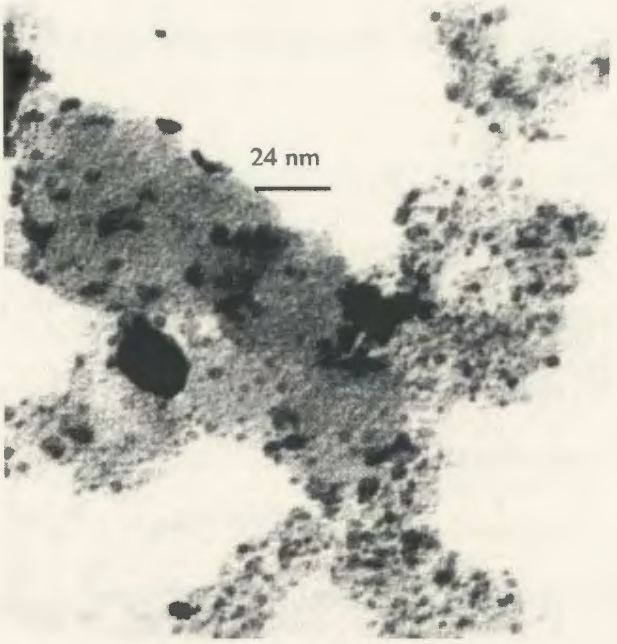

(d)

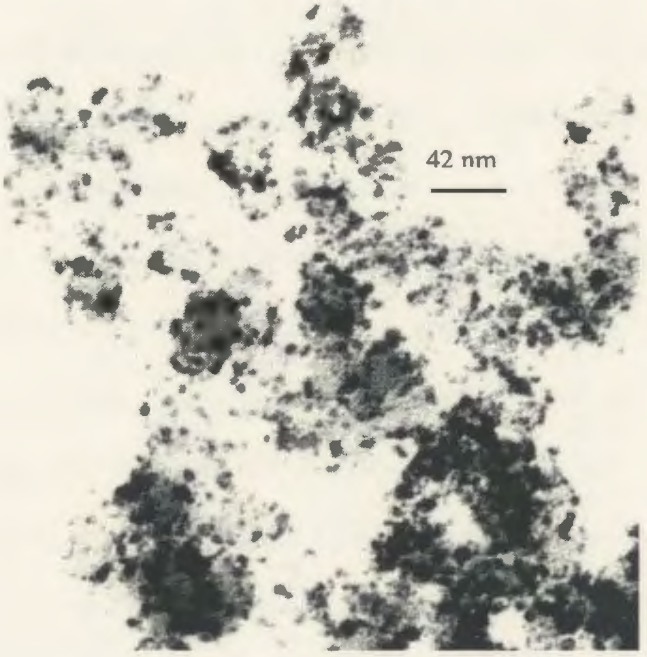

Figure 8.3b. TEM micrographs of 20% Pt on C based binary catalysts: (c) Pt/Rh (9:2), (d) Pt/Ru (7:2).

ratio between Pt and the second metal for the best performance. The results presented here are for the optimum ratios.

Figure 8.4a and 8.4b show LSV for oxidation of 1 M ethanol in 0.1 M H_2SO_4(aq) on the catalysts. It is seen that in the low potential region of fuel cell interest, Pt/Mo (5:2), Pt/Pb (4:1), and Pt/Ru (7:2) catalysts exhibited significant enhancements in catalytic activity for ethanol oxidation relative to the parent Pt catalyst. For comparison, Figure 8.4a and 8.4b also show LSV for oxidation of ethanol on a Pt/Sn (4:1) catalyst. It can be seen that, in the low potential region, the Pt/Sn catalyst exhibited the highest catalytic activity. In the high potential region, the catalytic activity of the Pt/Pb catalyst increased greatly, and the Pt/Pb catalyst became the best catalyst for ethanol oxidation. Among the five Pt based binary catalysts, only Pt/Rh did not exhibit enhanced catalytic activity in the high potential region relative to the parent Pt catalyst. However, the onset potential for ethanol oxidation on the Pt/Rh catalyst was the lowest.

Figure 8.5 presents CA for oxidation of ethanol on the binary catalysts, together with that on a commercial E-Tek 20% Pt on C catalyst. It is seen that at a potential of 0.5 V *vs* SHE, all of the catalysts tested exhibited significantly enhanced catalytic activities for electro-oxidation of ethanol relative to the Pt catalyst. Among these four catalysts, the Pt/Ru (7:2) catalyst was the best. However, it is significantly inferior to the Pt/Sn (4:1) catalyst reported in Chapter 7. Zhou and coworkers also reported that Pt/Sn catalysts were better than Pt/Ru catalysts for electro-oxidation of ethanol and worse than Pt/Ru catalysts for methanol oxidation. Their catalysts were prepared by a co-impregnation method [5].

It was found that there was some discrepancy between the results of CA and LSV. Based on LSV, at the potential of 0.5 V *vs* SHE, the Pt/Pb was better than the Pt/Ru

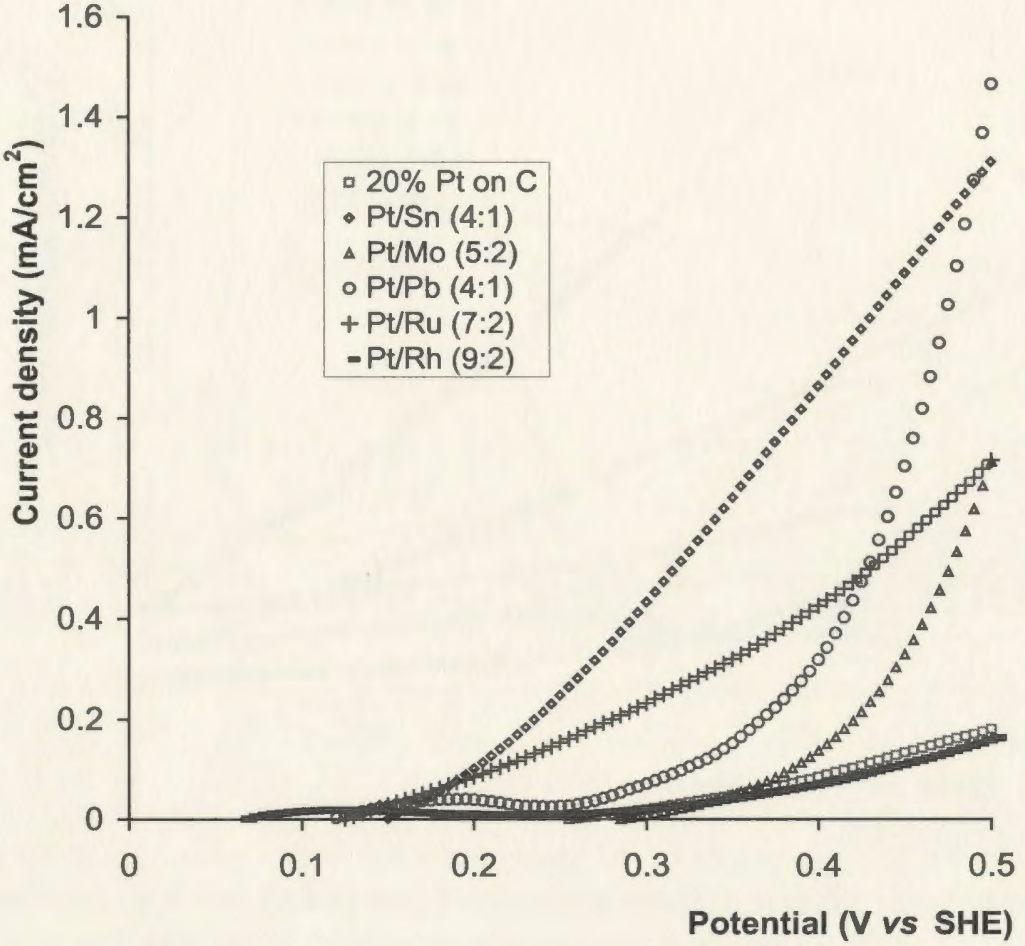

Figure 8.4a. Linear sweep voltammograms for oxidation of 1 M ethanol in 0.1 M H_2SO_4(aq) on E-Tek 20% Pt on C based binary catalysts, together with that on an E-Tek 20% Pt on C catalyst (in the low potential region). Scan rate: 10 mV/s.

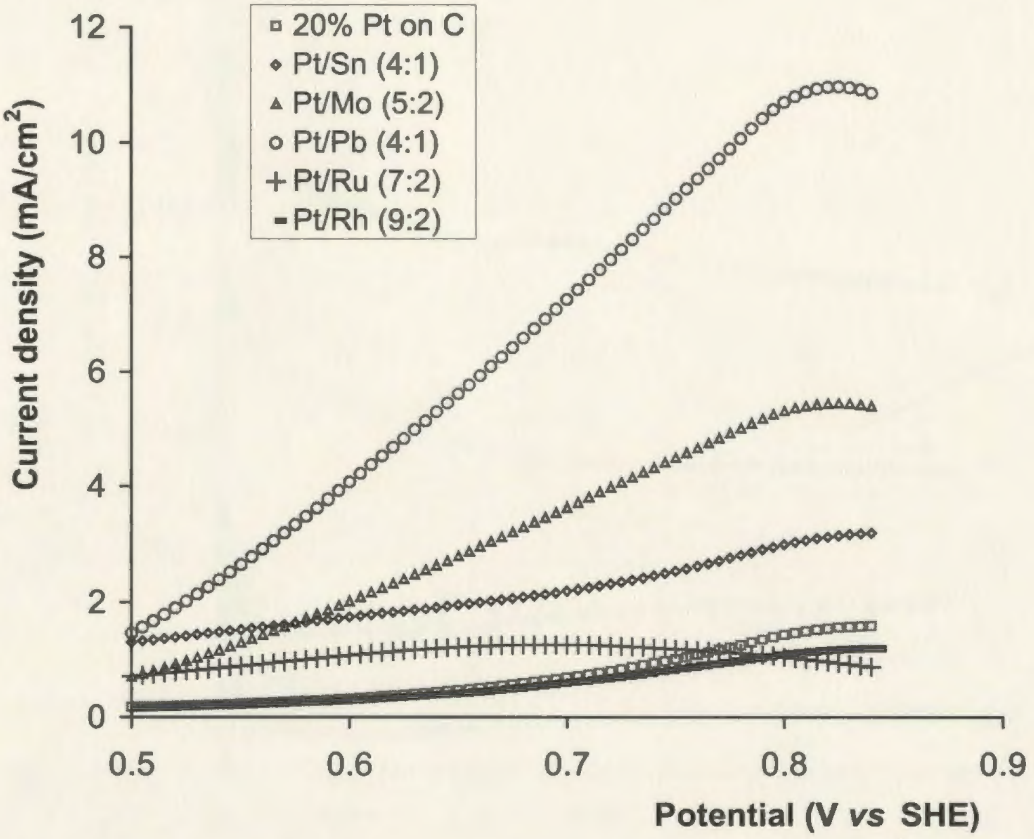

Figure 8.4b. Linear sweep voltammograms for oxidation of 1 M ethanol in 0.1 M H_2SO_4(aq) on E-Tek 20% Pt on C based binary catalysts, together with that on an E-Tek 20% Pt on C catalyst (in the high potential region). Scan rate: 10 mV/s.

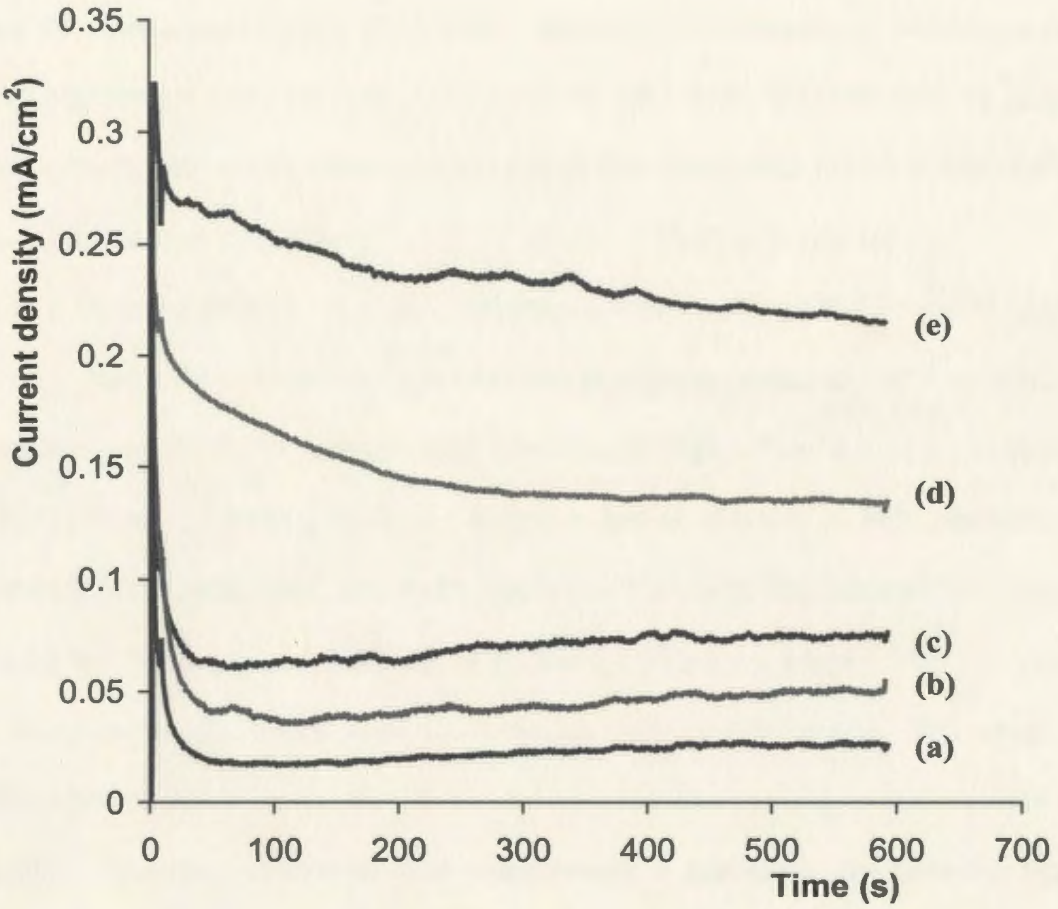

Figure 8.5. Chronoamperometry for oxidation of 1 M ethanol in 0.1 M H_2SO_4 on different catalysts at 0.5 V *vs* SHE: (a) E-Tek 20% Pt on C; (b) Pt/Rh (9:2); (c) Pt/Mo (5:2); (d) Pt/Pb (4:1); (e) Pt/Ru (7:2).

catalyst and the Pt/Rh was a little worse than the Pt catalyst. However, the results of CA were reversed. This is in part due to differences in the charging currents at the different catalysts. This is also possibly due to differences in the stability of the catalysts.

8.3.2 Ru Based Ru/Pt Catalysts

Since the resource of Pt is quite limited, research on increasing Pt utilization is of significant importance [10]. In order to increase Pt utilization, we have tried to prepare binary catalysts by decorating other metals with Pt and found that Ru on C based Ru/Pt catalysts exhibited high catalytic activities for electro-oxidation of ethanol.

Figure 8.6a and 8.6b show CA for oxidation of 1 M ethanol in 0.1 M H_2SO_4(aq) on 50% Ru on C based Ru/Pt catalysts. It is seen that at a low potential of 0.3 V *vs* SHE, the catalytic activity of the Ru/Pt catalysts was significantly higher than that of a commercial 20% Pt/Ru (1:1) on C catalyst, while at a higher potential of 0.6 V *vs* SHE, initially, the Pt/Ru catalyst was better than the Ru/Pt catalysts. However, the currents for ethanol oxidation on the Pt/Ru catalyst decreased significantly with time, whereas the currents for ethanol oxidation on the Ru/Pt catalysts were relatively stable, and at later times the current for ethanol oxidation on the Ru/Pt (6.3:1) catalyst were bigger than that on the Pt/Ru catalyst. The clear conclusion from these results is that in the low potential region of fuel cell interest, the 50% Ru on C based Ru/Pt (6.3:1) catalyst is much better than the commercial 20% Pt/Ru (1:1) on C catalyst for electro-oxidation of ethanol. In addition, it was found that 50% Ru on C catalysts exhibited no catalytic activities for ethanol oxidation. However, they became active after addition of Pt, and the catalytic activity increased significantly with increasing Pt loading as seen in Figure 8.6a and 8.6b.

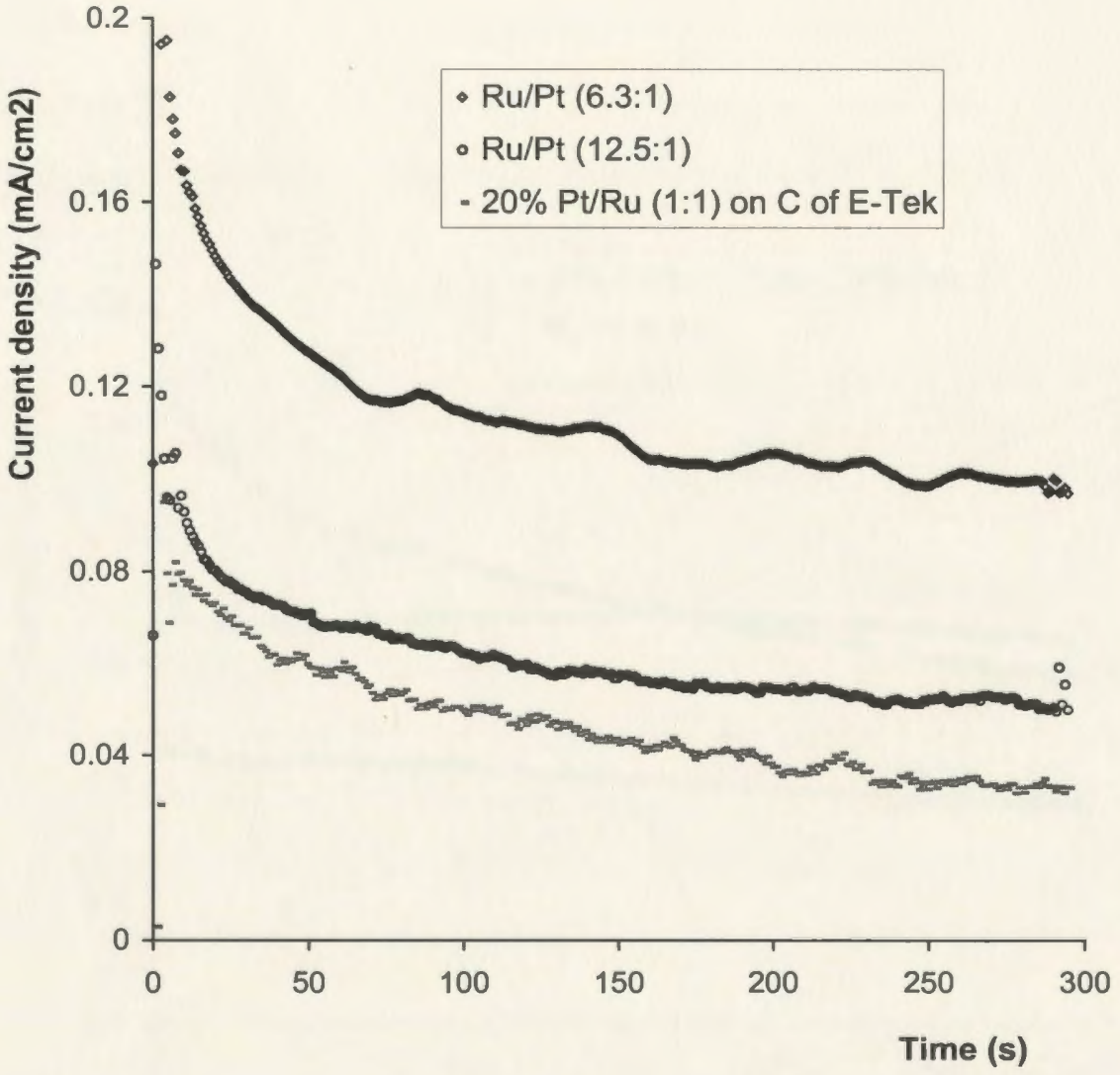

Figure 8.6a. Chronoamperometry for oxidation of 1M ethanol in 0.1 M H_2SO_4(aq) on different 50% Ru on C based Ru/Pt catalysts, together with that on a commercial 20% Pt/Ru (1:1) on C catalyst at 0.3 V *vs* SHE.

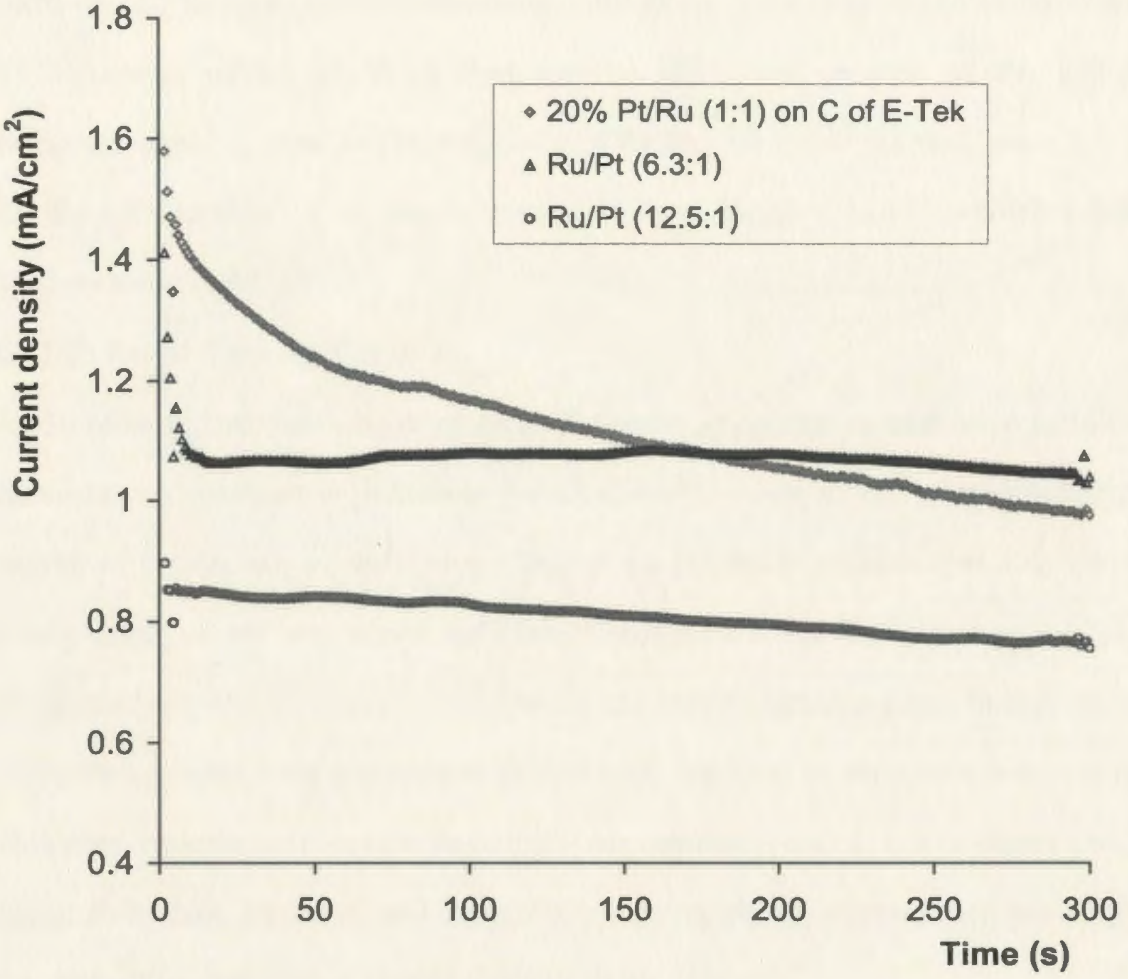

Figure 8.6b. Chronoamperometry for oxidation of 1M ethanol in 0.1 M H_2SO_4(aq) on different 50% Ru on C based Ru/Pt catalysts, together with that on a commercial 20% Pt/Ru (1:1) on C catalyst at 0.6 V *vs* SHE.

Considering the fact that 100 mg of the 20% Pt/Ru (1:1) on C catalyst contains ca. 13 mg of Pt and 100 mg of the 50% Ru on C based Ru/Pt (6.3:1) catalyst contains ca. 11 mg Pt, Pt utilization really is increased significantly with the 50% Ru on C based Ru/Pt catalysts if based on the same catalytic activity at 0.3 V *vs* SHE.

Figure 8.7 presents XRD patterns of a 50% Ru on C catalyst, a 50% Ru on C based Ru/Pt (6.3:1) catalyst, and a commercial 20% Pt on C catalyst. It can be seen that the XRD patterns of the Ru/Pt catalyst showed diffraction patterns of Ru without Pt diffraction patterns. This maybe suggests that Ru/Pt alloys were formed, since it is found that for a Pt/Ru alloy, if the atomic percent of Ru is bigger than 62%, it will exhibit the XRD patterns of Ru [11].

8.3.3 Pt Based Ternary Catalysts

In order to find more active catalysts for electro-oxidation of ethanol, a number of Pt based ternary catalysts have been prepared. Initially, it was thought that different metals maybe add their unique promoting effect to the parent Pt catalyst. For example, Pt/Sn binary catalysts are very active for ethanol oxidation in the low potential region while Pt/Pb catalysts exhibit superior activities in the high potential region. Therefore, ternary Pt/Sn/Pb catalysts were expected to exhibit high activities in the whole potential region. However, experimental results denied this expectation. Finally, it was found that Pt/Ru based Pt/Ru/Mo, Pt/Ru/W, and Pt/Ru/Pb ternary catalysts exhibited enhanced activities for ethanol oxidation relative to the parent Pt/Ru catalysts.

8.3.3.1 EDX

Figure 8.8 shows EDX spectra of ternary catalysts of Pt/Ru/Mo, Pt/Ru/W, and Pt/Ru/Pb. The spectra clearly show that Mo, W, and Pb have been incorporated into the

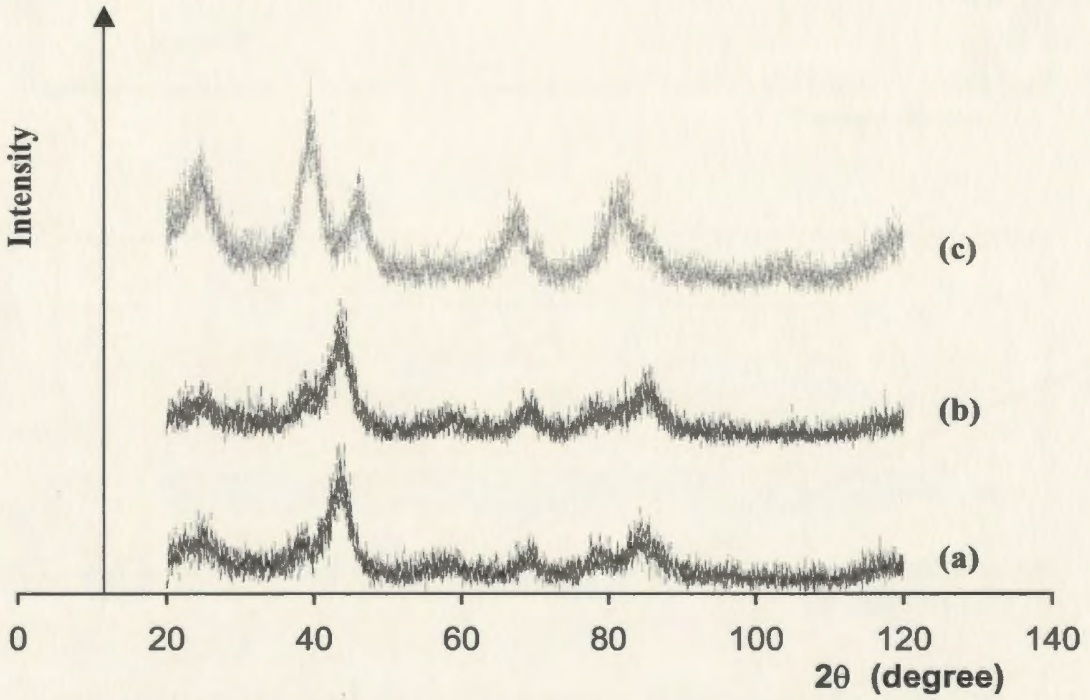

Figure 8.7. XRD patterns of different catalysts: (a) a 50% Ru on C; (b) a 50% Ru on C based Ru/Pt (6:3:1); (c) an E-Tek 20% Pt on C.

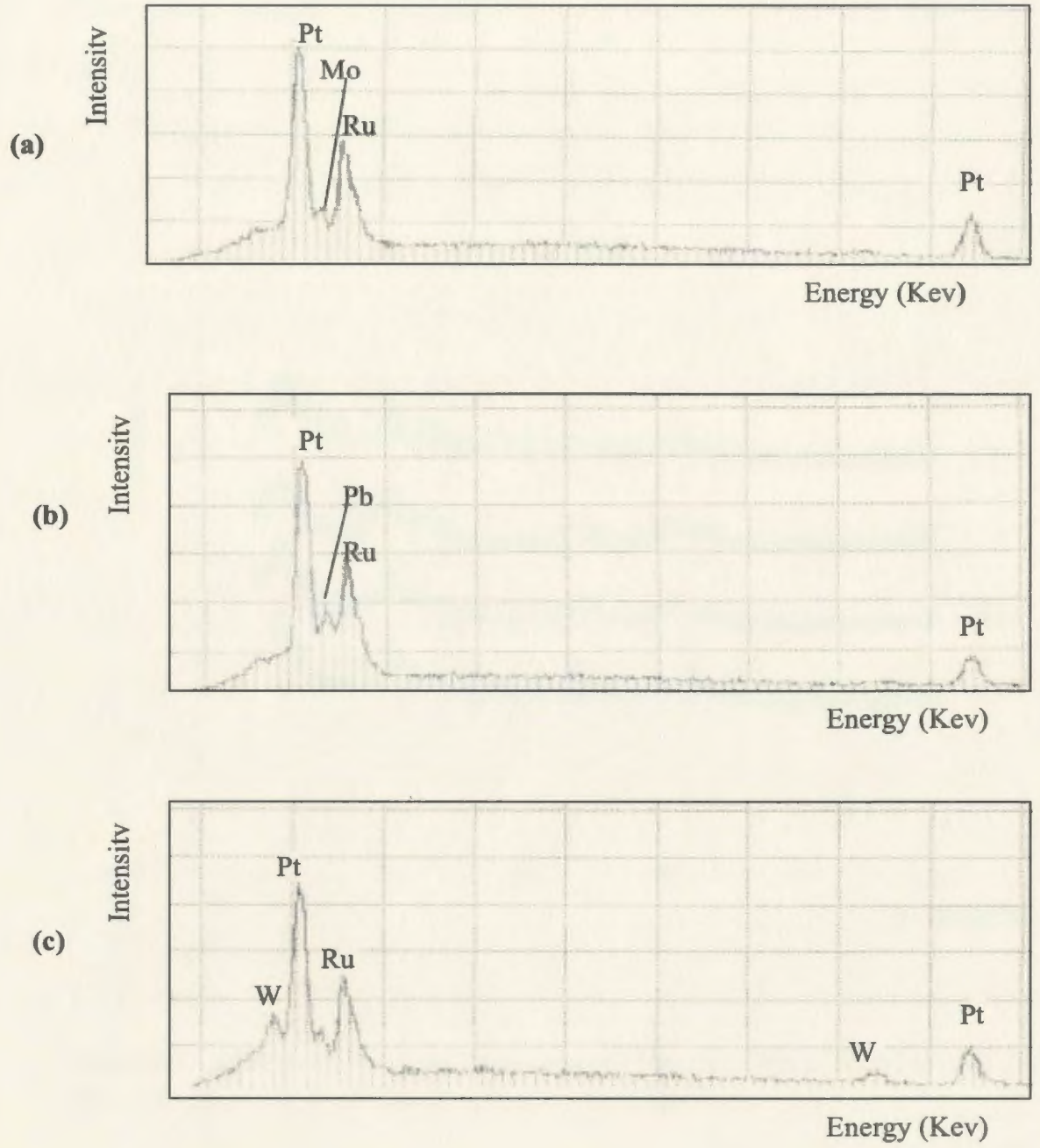

Figure 8.8. EDX spectra of 20% Pt/Ru (1:1) on C based ternary catalysts: (a) Pt/Ru/Mo (1:1:0.4); (b) Pt/Ru/Pb (1:1:0.3); (c) Pt/Ru/W (1:1:0.3).

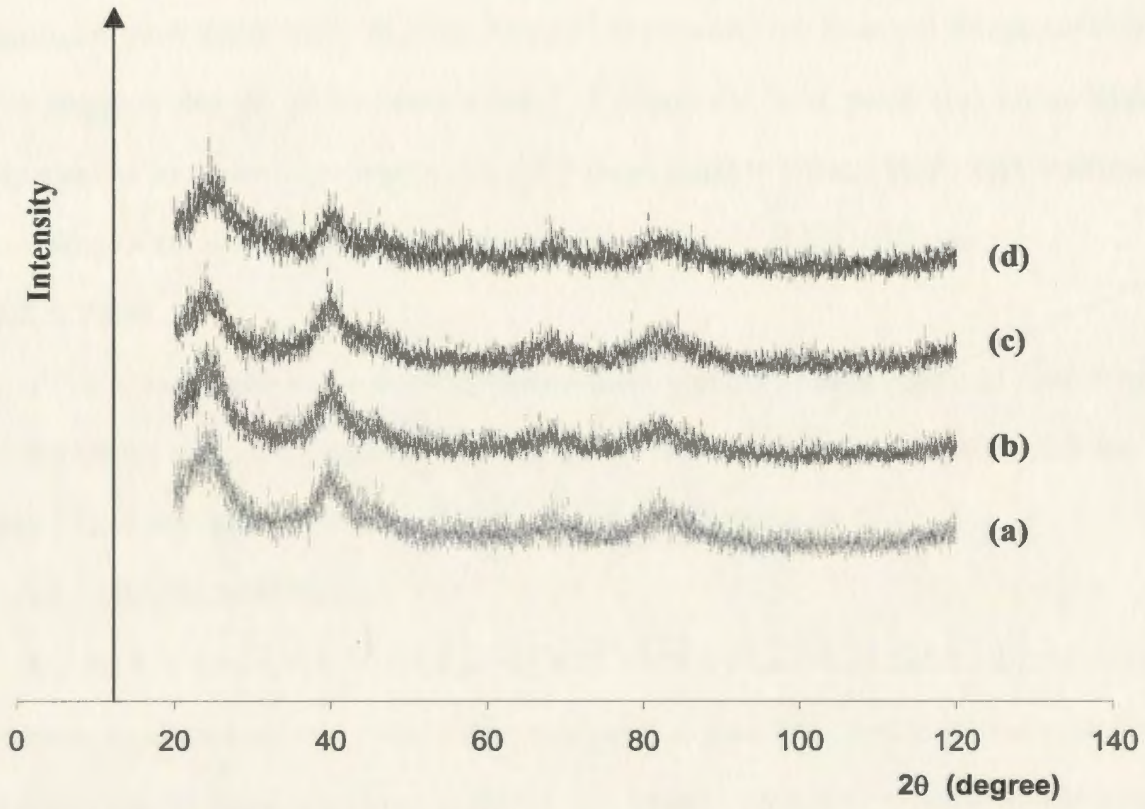

Figure 8.9. XRD patterns of different catalysts: (a) 20% Pt/Ru (1:1) on C of E-Tek; (b) Pt/Ru/Mo (1:1:0.4); (c) Pt/Ru/W (1:1:0.3); (d) Pt/Ru/Pb (1:1:0.3).

parent Pt/Ru catalyst.

8.3.3.2. XRD

Figure 8.9 presents XRD patterns of the ternary catalysts. It can be seen that the XRD patterns of the ternary catalysts are similar to that of the parent Pt/Ru catalyst. Also, no significant peak shifts were observed between the ternary catalysts and the parent Pt/Ru. This suggests that no alloys were formed, and that the third metal was either highly dispersed or in amorphous states [11]. The mean particle sizes, which were calculated according to the Scherrer equation, were ca. 1.3 nm for all of the catalysts.

8.3.3.3. TEM

TEM micrographs show that the metal particles of the ternary catalysts were evenly distributed on the carbon support and that the average particle sizes were ca. 2.5 nm. A typical TEM micrograph of the catalysts is shown in Figure 8.10.

8.3.3.4 Catalytic Activities

Figure 8.11 shows LSV for oxidation of 1 M ethanol in 0.1 M H_2SO_4 on the ternary catalysts, together with that on the Pt/Ru catalyst. It is seen that all of the ternary catalysts exhibited significantly enhanced activities for ethanol oxidation relative to the parent Pt/Ru catalyst. At potentials below ca. 0.26 V *vs* SHE, the Pt/Ru/Mo (1:1:0.4) catalyst exhibited the highest activity. In the high potential region, the Pt/Ru/Pb (1:1:0.3) catalyst was the best. It was also found that there was an optimum atomic ratio between the parent Pt/Ru metals and the third metal for the best performance (the atomic ratio used here is the optimum ratio). Obviously, too much of the third metal can result in blockage of the active sites of the parent Pt/Ru catalyst.

Figure 8.12 shows CA for oxidation of 1 M ethanol in 0.1 M H_2SO_4 on the ternary

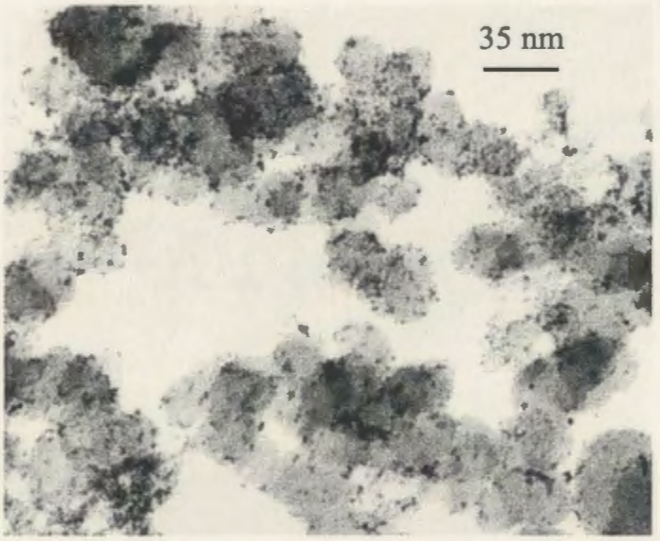

Figure 8.10. A TEM micrograph of a Pt/Ru/Mo (1:1:0.4) catalyst.

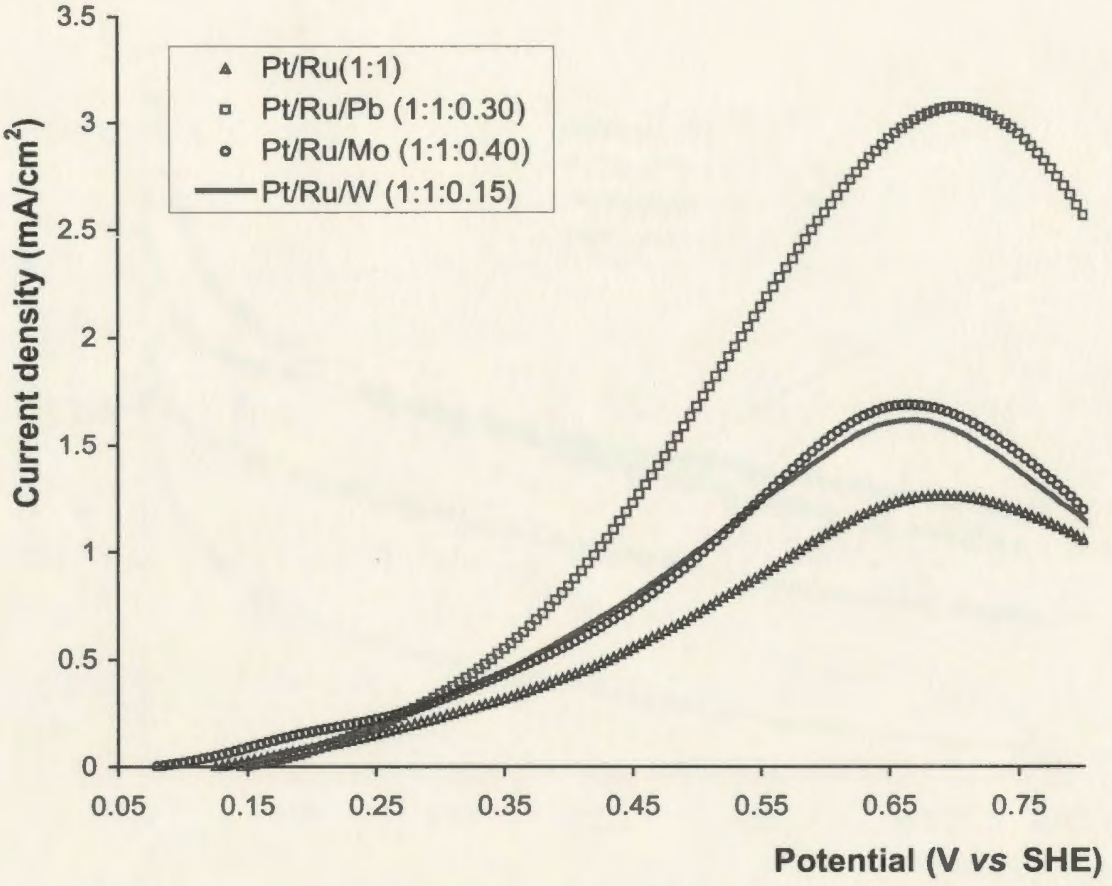

Figure 8.11. Linear sweep voltammograms for oxidation of 1 M ethanol in 0.1 M H_2SO_4 on different 20% Pt/Ru (1:1) on C based ternary catalysts, together with that on a commercial 20% Pt/Ru (1:1) on C catalyst. Scan rate: 10 mV/s.

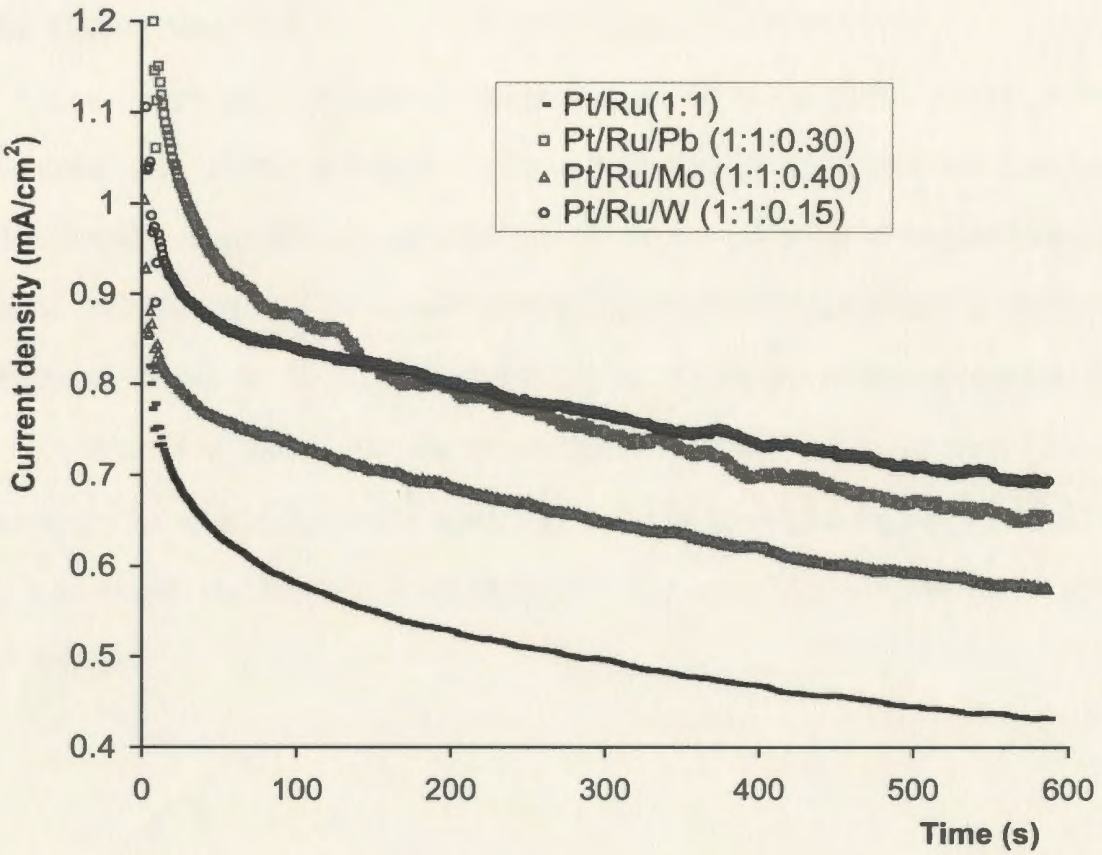

Figure 8.12. Chronoamperometry for oxidation of 1 M ethanol in 0.1 M H_2SO_4 on different 20% Pt/Ru (1:1) on C (E-Tek) based ternary catalysts at 0.5 V *vs* SHE, together with that on a commercial 20% Pt/Ru (1:1) catalyst.

catalysts at 0.5 V *vs* SHE. It can be seen that all of the ternary catalysts were much more active than the parent Pt/Ru catalyst for ethanol oxidation. This is consistent with the results of LSV. It was also found that initially, the Pt/Ru/Pb (1:1:0.3) was the best. However, after electrolysis for ca. 200 s, the Pt/Ru/W (1:1:0.15) catalyst became the best. This indicates that the Pt/Ru/W (1:1:0.15) catalyst was more stable than the Pt/Ru/Pb (1:1:0.3) catalyst.

8.4 Conclusions

The results of LSV and CA show that the Pt based Pt/Ru, Pt/Mo, Pt/Pb binary catalysts and Pt/Ru based Pt/Ru/Mo, Pt/Ru/Pb, Pt/Ru/W ternary catalysts have significantly enhanced catalytic activities for electro-oxidation of ethanol relative to their parent Pt catalysts. For the binary catalysts, the Pt/Ru (7:2) catalyst was the best and for the ternary catalysts, the Pt/Ru/W (1:1:0.15) had the highest sustained catalytic activity.

It was also found that Ru based Ru/Pt catalysts exhibited promising catalytic activities for ethanol oxidation, especially in the low potential region of fuel cell interest. It was found that deposition of Pt on Ru was an effective approach to increase Pt utilization.

8.5 References

[1] C. Lamy, A. Lima, V. LeRhun, F. Delime, C. Coutanceau, and J. M. Leger, J. Power Sources 105 (2002) 283.

[2] A. O. Neto, M. G. Giz, J. Perez, E. A. Ticianelli, and E. R. Gonzalez, J. Electrochem. Soc. 149 (2002) A272.

[3] E. V. Spinace, A. O. Neto, and M. Linardi, J. Power Sources 124 (2003) 426.

[4] N. Fujiwara, K. A. Friedrich, and U. Stimming, J. Electroanal. Chem. 472 (1999) 120.

[5] W. J. Zhou, Z. H. Zhou, S. Q. Song, W. Z. Li, G. Q. Sun, Q. P. Tsiakaras, and Q. Xin, Appl. Catal. B 46 (2003) 273.

[6] J. P. I. de Souza, S. L. Queiroz, K. Bergamaski, E. R. Gonzalez, and F. C. Nart, J. Phys. Chem. B 106 (2002) 9825.

[7] W. J. Zhou, W. Z. Li, Q. Song, Z. H. Zhou, L. H. Jiang, G. Q. Sun, Q. Xin, K. Poulianitis, S. Kontou, and P. Tsiakaras, J. Power Sources 131 (2004) 217.

[8] F. Vigier, C. Coutanceau, F. Hahn, E. M. Belgsir, C. Lamy, J. Electroanal. Chem. 563 (2004) 81.

[9] E. M. Crabb, R. Marshall, and D. Thompsett, J. Electrochem. Soc. 147 (2000) 4440.

[10] E. V. Spinace, A. O. Neto, and M. Linardi, J. Power Sources 129 (2004) 121.

[11] C. He, H. R. Kunz, and J. M. Fenton, J. Electrochem. Soc. 150 (2003) A1017.

Chapter 9 Performance of Pt Based Catalysts in Direct Ethanol Fuel Cells

9.1 Introduction

Development of Pt based catalysts for electro-oxidation of ethanol has drawn increasing attention in recent years due to the potential of ethanol as a fuel for fuel cells. However, only a few papers have been published regarding the performance of direct ethanol fuel cells (DEFCs) [1-2].

Previous research has shown that the performance of DEFCs is quite promising. For example, Wang and coworkers [3] reported that at a high temperature of 170 °C, the performance of a DEFC was close to that of a DMFC when Pt/Ru was used as the anode catalyst. Arico and coworkers [4] found that with Pt/Ru as the anode catalyst, a maximum power density of 110 mW/cm^2 could be obtained for a DEFC at 145 °C. Recently, it was reported that with Pt/Sn as the anode catalyst, a DEFC could provide a maximum power density of 52 mW/cm^2 at 90 °C [5].

Theoretically, a DEFC can provide much larger current than a DMFC if ethanol can be oxidized completely to CO_2. However, complete oxidation of ethanol is a major challenge at low temperatures. It has been found that electro-oxidation of ethanol on Pt based catalysts is quite complicated and involves many pathways. Many products such as acetic acid, acetaldehyde, and CO_2 have been detected [6-7]. Generally, the products of ethanol oxidation have been analyzed with IR, DEMS, and chromatographic methods.

In chapters 7 and 8, it has been shown that a number of Pt based catalysts have much higher catalytic activities for electro-oxidation of ethanol than the parent Pt catalyst. In

the work presented in this chapter, the catalytic activity of these catalysts was tested in DEFCs. In addition, the performance losses of DEFCs were resolved into cathode performance losses and anode performance losses with the aid of a DHE reference electrode. Furthermore, the products of ethanol oxidation were analyzed by titration.

9.2. Experimental

9.2.1 Preparation of Catalysts

The details of preparation of catalysts are described in chapters 7 and 8.

9.2.2 Preparation of Anodes

An appropriate amount of catalyst was mixed with 200 mg of 5 % Nafion solution by sonication for 30 min. The resulting paste was then applied onto a 5 cm^2 CFP and dried at ambient temperature in a fume hood (giving a Pt loading of 2 mg/cm^2).

9.2.3 Preparation of MEAs

Membrane and electrode assemblies (MEAs) were prepared by pressing an anode and a cathode (Pt black, 4 mg /cm^2 on carbon paper, donated by Ballard Power Systems) onto each side of a Nafion 117 membrane at a pressure of 200 kg /cm^2 at 135 °C for 180 s.

9.2.4 Product Analysis

Procedures for product analysis are described in section 10 of chapter 2.

9.2.5 Fuel Cell Measurements

A 5 cm^2 commercial cell (ElectroChem) were used to perform fuel cell tests. The cell was operated with an anode feed of aqueous ethanol solution at a fixed flow rate of 5 ml/min and a cathode feed of dry air at a fixed flow rate of 60 ml/min. For product analysis, the cell was operated with an anode feed of 1 M ethanol(aq) at a fixed flow rate of 0.30 ml/min and a cathode feed of dry air at a fixed flow rate of 30 ml/min.

Electrochemical measurements were made with a Solartron 1286 electrochemical interface coupled with a 1250 frequency response analyser or an EG&G PAR 273A potentiostat/galvanostat.

9.3 Results and Discussion

9.3.1 Performances of Catalysts

The results of CA and LSV (Chapters 7 and 8) show that Pt based Pt/Sn (4:1) and Pt/Ru/Pb (1:1:0.3) catalysts have high catalytic activities for electro-oxidation of ethanol. Here, the catalytic activity of these catalysts was tested in DEFCs. As shown in Figure 9.1, the performance of a cell with Pt/Sn or Pt/Ru/Pb as the anode catalyst was much better than that of a cell with Pt as the anode catalyst. Also, the OCP of the cells with the Pt/Sn and the Pt/Ru/Pb catalysts were much higher than that of the cell with the Pt catalyst. These results confirm the conclusions from CA and LSV that Pt/Sn and Pt/Ru/Pb catalysts have higher catalytic activities for ethanol oxidation than the parent Pt catalyst. The high activities can be attributed to the promoting effect of Sn, Ru, and Pb.

Another finding is that the Pt/Sn catalyst had the best performance among the four catalysts. It is believed that addition of Sn is conductive to cleavage of C-C bonds [6]. However, the Pt/Ru/Pb catalyst did not exhibit as significant enhancements in activity relative to the parent Pt/Ru catalyst as that demonstrated by CA and LSV. The reason for this is not quite clear. It is possibly due to electrochemical dissolution of Pb into the ethanol solution.

Figure 9.2 shows polarization curves for a DEFC with anode feeds of ethanol(aq) of different concentrations. It is seen that at current densities below ca. 0.11 A/cm^2, the performance of the cell with 0.4 M ethanol was significantly better than with 1 M or 2 M

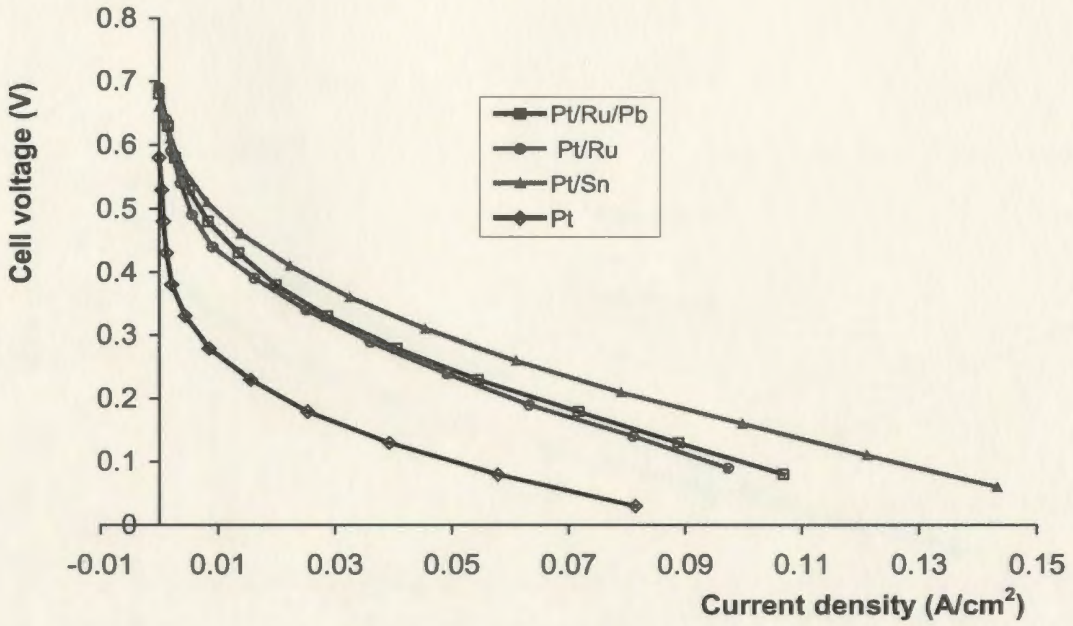

Figure 9.1. Polarization curves for a DEFC with different anode catalysts. The catalysts include 20% Pt on C from E-Tek, 20% Pt/Ru (1:1) on C from E-Tek, 20% Pt on C based Pt/Sn (4:1), and 20% Pt/Ru (1:1) on C based Pt/Ru/Pb (1:1:0.3). The cell was operated at 80 °C with an anode feed of 1 M ethanol(aq) and a cathode feed of dry air.

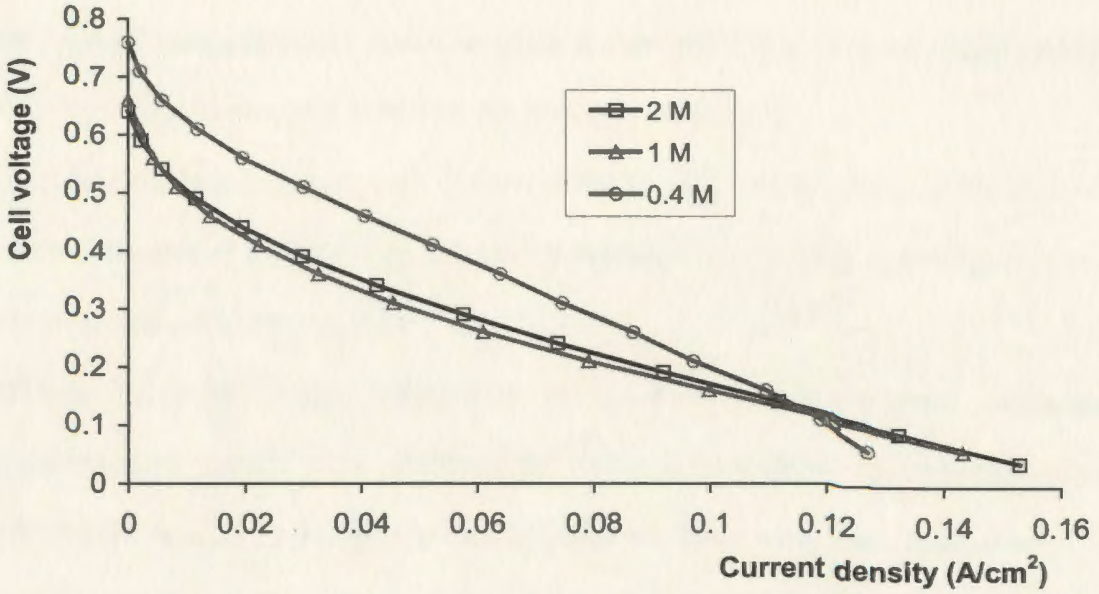

Figure 9.2. Polarization curves for a DEFC. The cell was operated at 80 °C with anode feeds of ethanol(aq) of different concentrations and a cathode feed of dry air. The anode catalyst was 20% Pt on C based Pt/Sn (4:1).

ethanol. Interestingly, at current densities higher than ca. 0.12 A/cm^2, the performance of the cell with higher ethanol concentration became much better. It is seen that the performance of the cell with 2 M ethanol was a little better than with 1 M ethanol.

We can also see that the OCP of the cell dropped significantly at the higher ethanol concentrations. Noticeably, the OCP of the cell with 0.4 M ethanol was much higher than with the higher ethanol concentrations. This is presumably due to ethanol crossover, since higher ethanol concentrations result in more severe ethanol crossover. Consequently, the OCP of the cathode dropped at higher ethanol concentrations.

Another finding is that at high current densities, the performance of the cell with 0.4 M ethanol decreased rapidly with increasing current density. This is mainly due to anode concentration polarization (see below).

Figure 9.3 shows anode polarization curves with different ethanol concentrations. The polarization curves were obtained by using a humidified H_2 fed cathode as the reference and counter electrodes. It can be seen that the anode with 2 M ethanol has the best performance, while the anode with 0.4 M ethanol exhibited significant concentration polarization at high current densities. Therefore, it can be concluded that the rapid drop of cell potential at high current densities with 0.4 M ethanol is mainly due to concentration polarization at the anode.

However, the different anode performances with different ethanol concentrations cannot fully explain the differences in cell performances with the changes of ethanol concentration. For example, based on the anode performance, a cell with 2 M ethanol should have the best performance, while a cell with 0.4 M ethanol should have the worst performance. In fact, the cell with 0.4 M ethanol had the best performance at low current

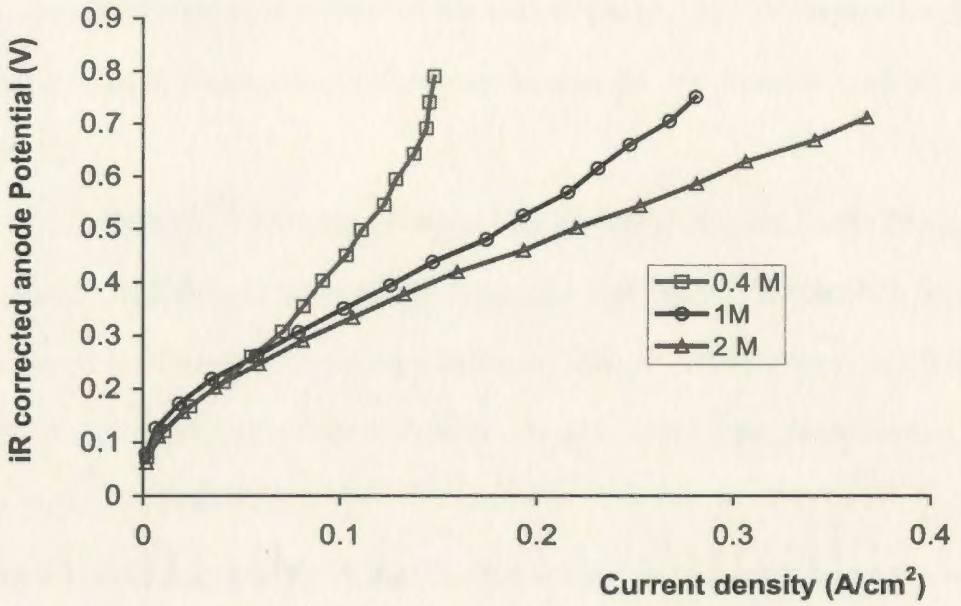

Figure 9.3. Anode polarization curves for a DEFC with anode feeds of ethanol(aq) of different concentrations and a cathode feed of humidified H_2. The cell was operated at 80 °C. The anode catalyst was 20% Pt on C based Pt/Sn (4:1).

densities. This contradiction suggests that the performance of the cathode must also be affected differently with different ethanol concentrations. Actually, the performance of the cathode decreased with increasing ethanol concentration (see below).

Figure 9.4 shows performances of a DEFC at different operating temperatures. It is seen that the cell performance was improved greatly with increasing temperature. However, the operating temperature of the cell is limited by the Nafion electrolyte used here, since it is well known that Nafion membranes do not perform well at temperatures above 100 °C.

Figure 9.5 shows CVs for the anodes with Pt and Pt/Sn catalysts. The cathode was fed with humidified H_2 and used as the reference and counter electrodes. It can be seen that currents on the forward scan on the Pt/Sn catalyst were significantly larger than those on the Pt catalyst, indicating that the Pt/Sn catalyst was much more active for ethanol oxidation than the Pt catalyst.

Another interesting finding is that for the Pt/Sn catalyst, the currents on the forward scan were always larger than the currents on the reverse scan, while for the Pt catalyst, in the potential region of ca. 0.4 V to ca. 0.68 V, the currents on the forward scan were smaller than the currents on the reverse scan. This suggests that there were more intermediates adsorbed on the Pt catalyst than on the Pt/Sn catalyst, and that addition of Sn was conductive to oxidation of the adsorbed intermediates on the Pt catalyst.

9.3.2 Analysis of Cell Performance Losses

Figure 9.6 shows polarization curves for a DEFC with different ethanol concentrations, together with anode potentials *vs* DHE and cathode potentials *vs* DHE. It is seen that the cell polarization curves were quite close to the cathode potential-anode

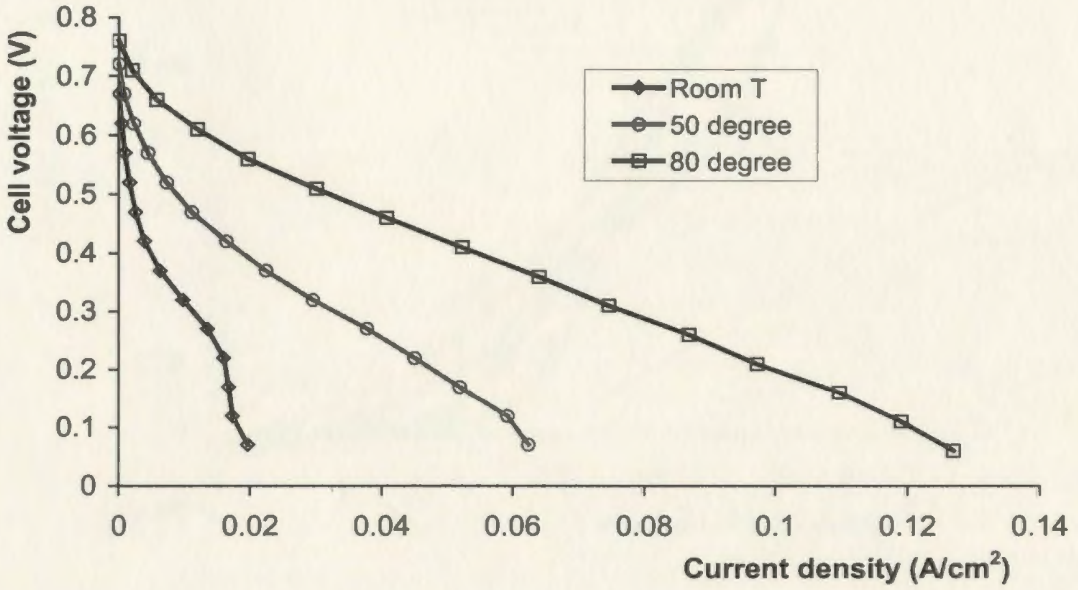

Figure 9.4. Polarization curves for a DEFC with an anode feed of 0.4 M ethanol(aq) and a cathode feed of dry air at different operating temperatures (Celsius). Anode catalyst: 20% Pt on C based Pt/Sn (4:1).

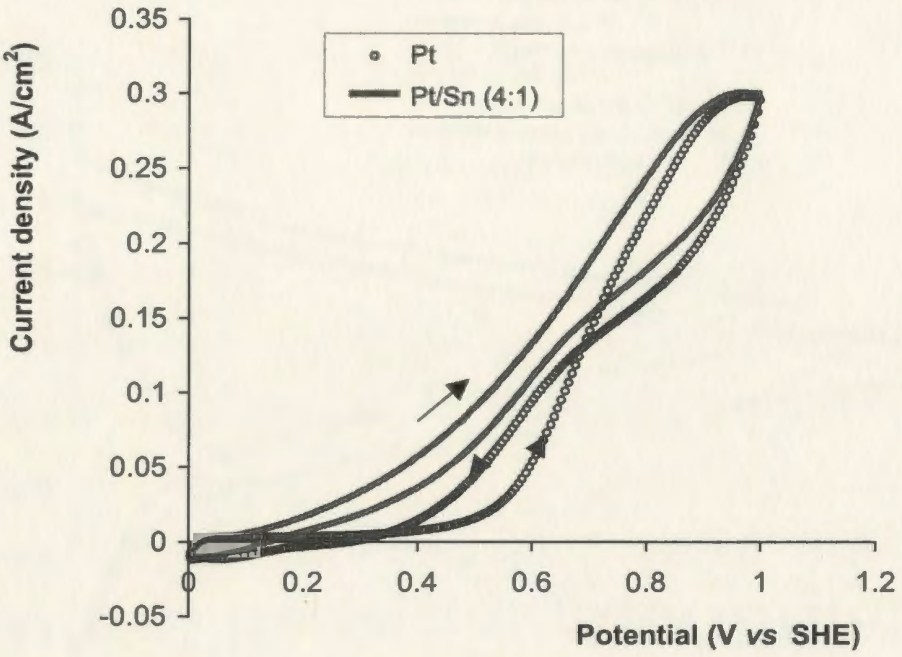

Figure 9.5. CVs for the anode of a 5 cm^2 DEFC with different anode catalysts: 20% Pt on C and 20% Pt on C based Pt/Sn (4:1). The cell was operated at 80 °C with an anode feed of 1 M ethanol(aq) and a cathode feed of humidified H_2. Scan rate: 10 mV/s.

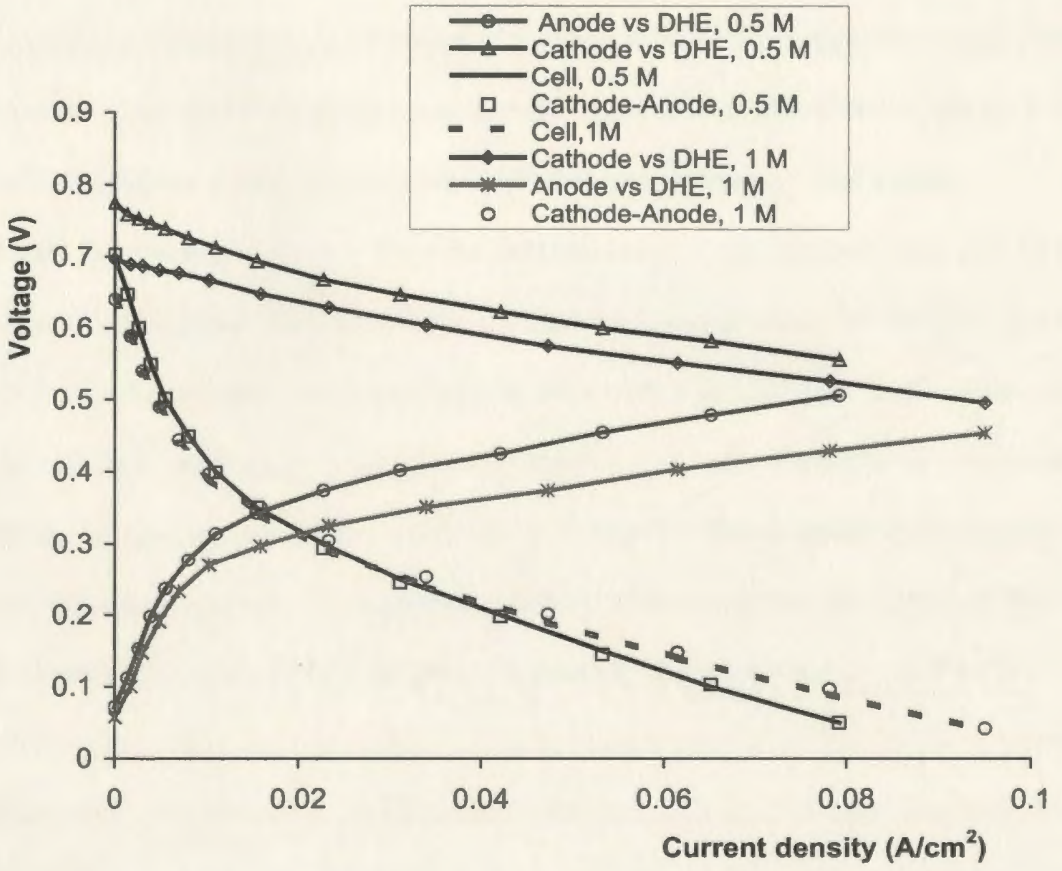

Figure 9.6. Polarization curves for a DEFC at 80 °C with anode feeds of ethanol(aq) of different concentrations and a cathode feed of dry air, together with anode potentials *vs* DHE and cathode potentials *vs* DHE. Anode catalyst: Pt/Ru (1:1, 5.47 mg/cm^2), donated by H Power Co.

potential (*vs* DHE) for both 0.5 M and 1 M ethanol. This indicates that cell performance losses can be resolved into cathode performance losses and anode performance losses with the aid of a DHE reference electrode. Also, we can see that at low current densities, the performance of the cell with 0.5 M ethanol was better than with 1 M ethanol. While at high current densities, the performance of the cell with 1 M ethanol was much better than with 0.5 M ethanol. These differences can be attributed to the different performances of the cathode and the anode with different ethanol concentrations (see below).

From Figure 9.6 it is seen that the performance of the cathode with 0.5 M ethanol was significantly better than that with 1 M ethanol. In addition, the OCP of the cathode with 0.5 M ethanol was much higher than that with 1 M ethanol. These differences are due to ethanol crossover [12], since ethanol crossover increased significantly with increasing ethanol concentration as shown in Table 9.1. These results also suggest that for the cathode performance, the lower the ethanol concentration, the better is the cathode performance. However, for the anode performance, things are reversed. It was found that the performance of the anode with 1 M ethanol was much better than with 0.5 M ethanol.

The clear conclusion from the above discussion is that balance between the anode performance and cathode performance has to be made for the best cell performance.

Table 9.1. Ethanol crossover currents at 80 °C

Ethanol(aq)	Crossover current (A/cm^2)	
	Nafion 115	Nafion 117
0.5 M	0.05	0.027
1 M	0.086	0.048
2 M	0.13	0.065

Figure 9.7 shows polarization curves for a DEFC at different operating temperatures, together with cathode potentials *vs* DHE and anode potentials *vs* DHE. It was seen that the cell performance was improved significantly with increasing temperature. It is also found that the anode performance was improved markedly with increasing temperature as expected, since increasing temperature can facilitate ethanol oxidation and increase mass transport rate. Surprisingly, it was found that the cathode performance decreased markedly with increasing temperature. This is presumably due to the increased ethanol crossover at higher temperatures. It is also possible that the depolarization effect of ethanol on the cathode becomes more significant at higher temperatures. Table 9.2 shows that ethanol crossover currents increased dramatically with increasing temperature. For example, when the temperature was increased from room temperature to 80 °C, the crossover current increased from 0.006 A/cm^2 to 0.048 A/cm^2; an eight-fold increase.

In conclusion, the improvement of cell performance at higher temperatures was due to the significant improvement of anode performance at higher temperatures.

Table 9.2. Ethanol crossover currents (1 M ethanol) at different temperatures

Temperature	23 °C	50 °C	80 °C
Crossover current (A/cm^2)	0.006	0.015	0.048

Figure 9.8 shows polarization curves for a DEFC with different anode catalysts of Pt and Pt/Ru, together with cathode potentials *vs* DHE and anode potentials *vs* DHE. It can be seen that the performance of the cell with Pt/Ru was much better than that with Pt. The much better performance of the cell with Pt/Ru is mainly due to the much better anode

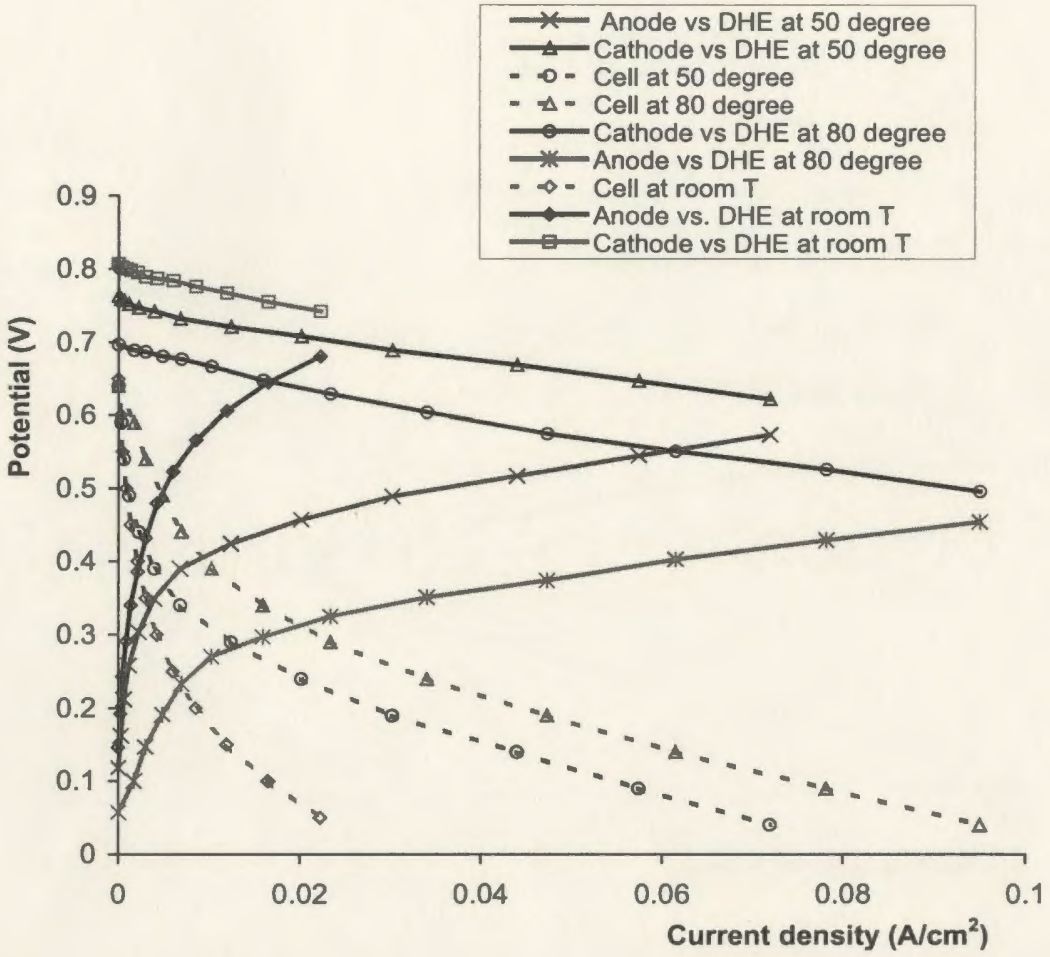

Figure 9.7. Polarization curves for a DEFC at different cell operating temperatures (Celsius) with an anode feed of 1 M ethanol(aq) and a cathode feed of dry air, together with cathode potentials *vs* DHE and anode potentials *vs* DHE. Anode catalyst: 5.47 mg/cm^2 Pt/Ru (1:1), donated by H Power Co.

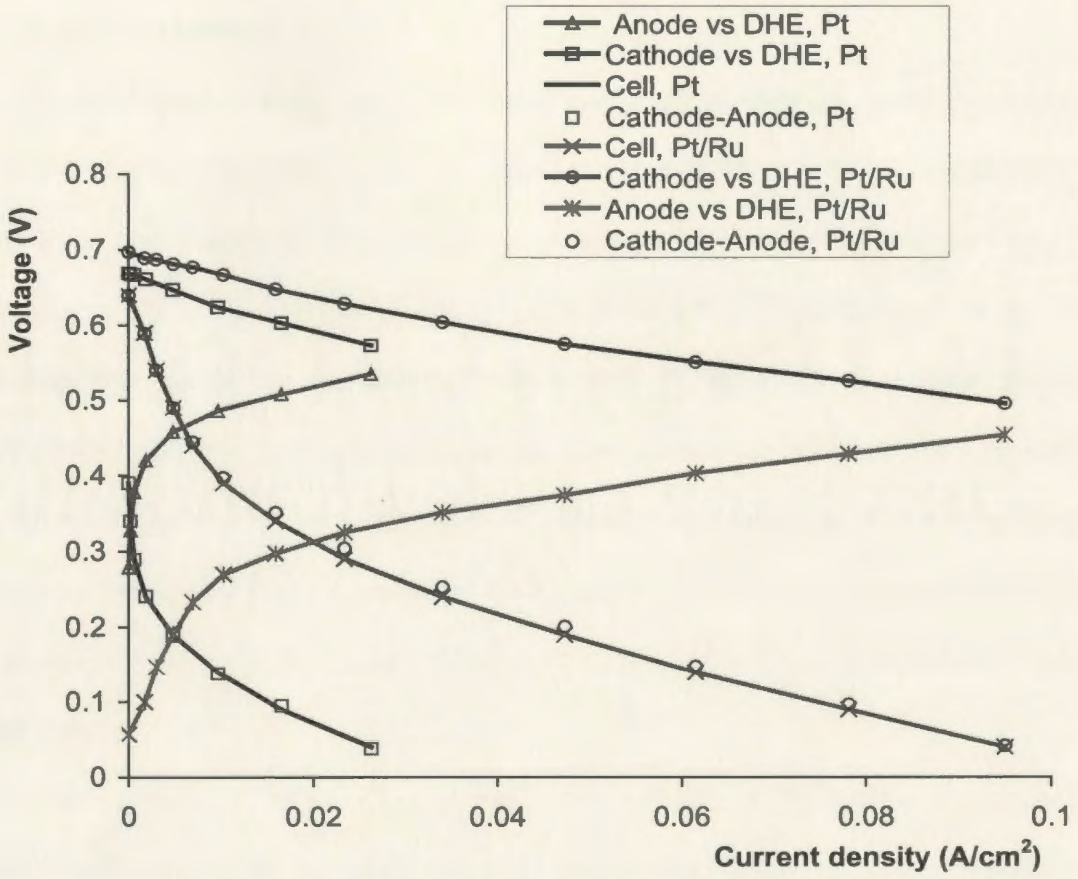

Figure 9.8. Polarization curves for a DEFC with different anode catalysts of Pt and Pt/Ru, together with cathode potentials *vs* DHE and anode potentials *vs* DHE. The cell was operated at 80 °C with an anode feed of 1 M ethanol(aq) and a cathode feed of dry air.

performance with Pt/Ru, since we can see that the performance of the anode with Pt/Ru was much better than that with Pt, demonstrating the promoting effect of Ru for ethanol oxidation on Pt. It was also found that the performance of the cathode with Pt/Ru as the anode catalyst was also significantly better than that of the cathode with Pt as the anode catalyst, although the cathodes consist of the same kind Pt catalysts. A possible reason for this is that different cathodes may have different performances.

9.3.3 Product Analysis

The products of ethanol oxidation were analyzed by titration methods and the results are listed in Table 9.3. The 5 cm^2 cell was operated at 80 °C with an anode feed of 1 M ethanol(aq) and a cathode feed of dry air. It is seen that at the higher current density of 0.06 A/cm^2, the yields of CO_2 were ca. 9.4 % for the Pt/Sn catalyst and ca. 6.2 % for the Pt/Ru catalyst. At the lower current density of 0.02 A/cm^2, the yield of CO_2 was ca. 9.0 % for the Pt/Sn catalyst. The clear conclusion from these data is that under these operation conditions, CO_2 is not the main product of ethanol oxidation, and the yield of CO_2 did not change significantly with cell voltage. Wang and coworkers [3] reported that CO_2 was not the main product in their DEFC. Their cell was operated at 180 °C with Pt/Ru as the anode catalyst.

In addition, it can be seen that for the Pt/Sn catalyst, at the higher current density, the yield of acid was ca. 48 %, while at the lower current density, the yield of acids was ca. 94 %. This indicates that the yield of acids varied greatly with cell voltage, and at a current density of 0.02 A/cm^2 (cell voltage of ca. 380 mV), the major products of ethanol oxidation are acids. It is noted that at a current of 0.02 A/cm^2, the sum of the yield of CO_2 and the yield of the acids was a little over 100%. One possible reason for this is that acids

produced at the cathode side can crossover through the membrane to the anode side, resulting in higher yields of the acids. For the Pt/Ru catalyst, the yield of acids also increased from ca. 60% to ca 77% when the current density was decreased from 0.06 A/cm^2 to 0.03 A/cm^2.

Table 9.3. Product analysis for ethanol oxidation on a 20% Pt on C based Pt/Sn (4:1) catalyst and a Pt/Ru (1:1) catalyst at constant current for one hour

	Pt/Sn					Pt/Ru		
Current (A)	0.3	0.3	0.1	0.1	0.1	0.3	0.3	0.15
Cell voltage#	121	139	356	378	402	137	176	281
CO_2%	8.39	10.4	8.39	10.1	8.40	6.71	5.60	6.72
Acid%*	45.2	50.7	98.0	93.6	94.4	55.6	64.8	76.8

There was a small variation in the cell voltage during constant current operation, generally within ca. $\pm$ 10 mV.
* Based on acetic acid.

In order to check the validity of the analysis method, we also performed product analysis on a DMFC. It was found that at a current density of 0.1 A/cm^2 (cell voltage of ca. 282 mV), the yield of CO_2 was ca. 82% and the yield of (formic) acid was ca. 5.8%. This demonstrates that the method used here is relatively reliable.

9.4 Conclusions

The performance of DEFCs confirmed that the carbon supported Pt based Pt/Sn (4:1) catalyst and Pt/Ru (1:1) catalyst have much higher catalytic activities than the parent Pt catalyst, and the Pt/Sn (4:1) catalyst exhibited the highest activity for ethanol oxidation. This is consistent with the results of LSV and CA.

The performance analysis illustrated that the anode performance was improved with

increasing temperature and ethanol concentration, while the cathode performance decreased with increasing temperature and ethanol concentration due to ethanol crossover. Therefore, balance between the anode and the cathode has to be made for the best cell performance.

The product analysis demonstrated that CO_2 was not the main product of ethanol oxidation under the conditions used here. In addition, the yield of CO_2 did not change significantly with cell voltage, while the yield of acids changed significantly with cell voltage.

9.5 References

[1] C. Lamy, A. Lima, V. LeRhun, F. Delime, C. Coutanceau, and J. M. Leger, J. Power Sources 105 (2002) 283.

[2] W. J. Zhou, B. Zhou, W. Z. Li, Z. H. Zhou, S. Q. Song, G. Q. Sun, Q. Xin, S. Douvartzides, M. Goula, and P. Tsiakaras, J. Power Sources 126 (2004) 16.

[3] J. Wang, S. Wasmus, and R. F. Savinell, J. Electrochem. Soc. 142 (1995) 4218.

[4] A. S. Arico, P. Creti, P. L. Antonucci, and V. Antonucci, Electrochem. Solid-State Lett. 1 (1998) 66.

[5] W. J. Zhou, Z. H. Zhou, S. Q. Song, W. Z. Li, G. Q. Sun, Q. P. Tsiakaras, and Q. Xin, Appl. Catal. B 46 (2003) 273.

[6] A. O. Neto, M. G. Giz, J. Perez, E. A. Ticianelli, and E. R. Gonzalez, J. Electrochem. Soc. 149 (2002) A272.

[7] N. Fujiwara, K. A. Friedrich, and U. Stimming, J. Electroanal. Chem. 472 (1999) 120.

[8] F. Vigier, C. Coutanceau, F. Hahn, E. M. Belgsir, C. Lamy, J. Electroanal. Chem. 563 (2004) 81.

[9] E. V. Spinace, A. O. Neto, and M. Linardi, J. Power Sources 124 (2003) 426.

[10] E. V. Spinace, A. O. Neto, and M. Linardi, J. Power Sources 129 (2004) 121.

[11] C. He, H. R. Kunz, and J. M. Fenton, J. Electrochem. Soc. 150 (2003) A1017.

[12] X. Ren, T. E. Springer, and S. Gottesfeld, J. Electrochem. Soc. 147 (2000) 92.

Chapter 10 Summary and Future Work

There are three major themes in this thesis. They are investigating the effects of Nafion loading on the performance of proton exchange membrane fuel cell cathodes, designing a DHE (dynamic hydrogen electrode) reference electrode to separate cell performance losses into individual electrode performance losses, and developing direct ethanol fuel cells.

It was found that cathode performance was strongly dependent on Nafion content and distribution in the cathode catalyst layer. There was an optimum Nafion loading for the best cathode performance, since a balance between the ionic resistance and O_2 transport resistance has to be made.

It has been shown that impedance spectroscopy is a powerful tool to characterize cathode performances. This technique not only revealed the fact that ionic conductivities increased with increasing Nafion loading but also showed that higher Nafion loading led to a significant increase in O_2 transport resistance.

By simulating the experimental data, conductivity profiles and resistance values for the cathode catalyst layer were obtained. The conductivity profiles and resistance values provide valuable information for understanding cathode behavior.

A bilayer cathode has been used to study the effects of Nafion distribution on cathode performance. Future work should focus on the design of a multiple layer cathode to fully study the effects of Nafion distribution.

In order to analyze cell performance losses, we have designed a novel edge-type DHE reference electrode. Both polarization measurements and impedance spectroscopy have demonstrated that this reference electrode is quite stable for the electrochemical study of hydrogen fuel cells and methanol fuel cells. The main advantage of this reference electrode is that it can be conveniently fitted into a commercial cell without the need for any modifications. We have shown that with the aid of the DHE reference electrode, cell performance losses can be resolved into individual electrode performance losses.

With the aid of the DHE reference electrode, we obtained anode polarization curves and impedance spectra for an operating cell. For hydrogen fuel cells, it was found that there were significant anode overpotentials at high current densities, and therefore anode performance losses cannot be treated as negligible at high current densities. By simulating anode impedance data, it was found that the ionic resistance for the anode catalyst layer increased with increasing current density. This provides evidence for the assertion that there was increased dehydration of the anode catalyst layer at higher current density.

For methanol fuel cells, it was found that cell performance losses were due to performance losses at both the cathode and anode. It was found that at high current densities, the rapid decrease of the cell performance was mainly due to the cathode performance loss caused by cathode flooding. In addition, it was found that anode performance was improved at a higher concentration of methanol, while cathode

performance decreased significantly at a higher concentration of methanol. Therefore, balance has to be made between the anode and cathode for the best cell performance.

Since cell performances are influenced by a variety of operating conditions, future work should investigate cell performance losses over broader operating conditions, and therefore provide a clear picture of cell performance losses under different operating conditions.

We have proposed a simplified equivalent circuit to simulate PEMFC electrode impedance behavior. The excellent fit between the experimental data and simulation data indicates that the proposed equivalent circuit is reasonable. Meaningful resistance values have been extracted based on this equivalent circuit. Also, we have used simplified equivalent circuits to explain DMFC electrode impedance behavior. More accurate equivalent circuits should be built in the future to simulate DMFC electrode impedance behavior.

We have prepared a number of Pt based binary and ternary catalysts for electro-oxidation of ethanol. It was found that Pt/Sn, Pt/Ru, Pt/Pb, and Pt/Mo binary catalysts and Pt/Ru/W, Pt/Ru/Pb, and Pt/Ru/Mo ternary catalysts exhibited significant enhancements in catalytic activity for electro-oxidation of ethanol relative to Pt. For the binary catalysts, the Pt/Sn was the best; while for the ternary catalysts, Pt/Ru/W had the highest catalytic activity.

Fuel cell tests demonstrated that a 20% Pt on C based Pt/Sn (4:1) catalyst was quite promising. A current density of 0.1 A/cm^2 was accomplished at a cell voltage of 0.2 V. Product analysis shows that CO_2 was not the main product of ethanol oxidation.

This greatly limits the efficiency of DEFCs. Therefore, future work should focus on developing more active catalysts for complete oxidation of ethanol to CO_2, especially at low temperatures. Obviously this will be a big challenge.

Preliminary results show that deposition of Pt on Ru was an effective way to increase Pt utilization. More detailed work is needed to optimize preparation conditions, since catalytic activities strongly depend on preparation conditions.